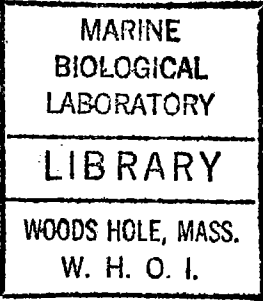# EXPERIMENTAL STUDY OF INTERNAL
GRAVITY WAVES OVER A SLOPE

by

David A. Cacchione

A.B., Princeton University

(1962)

SUBMITTED IN PARTIAL FULFILLMENT OF THE
REQUIREMENTS FOR THE DEGREE OF
DOCTOR OF PHILOSOPHY

at the

MASSACHUSETTS INSTITUTE OF TECHNOLOGY

and the

WOODS HOLE OCEANOGRAPHIC INSTITUTION

September, 1970

Signature of Author .

Joint Program in Oceanography, Woods Hole
Oceanographic Institution and Massachusetts
Institute of Technology, Department of Earth
and Planetary Sciences

Certified by

Thesis Supervisor

Thesis Supervisor

Accepted by

Chairman, Joint Oceanography Committee in the
Earth Sciences, Massachusetts Institute of Technology
- Woods Hole Oceanographic Institution

ABSTRACT

Experimental Study of Internal
Gravity Waves Over a Slope

by

David A. Cacchione

Submitted to the Department of Earth and Planetary Sciences
in partial fulfillment of the requirement for the
degree of Doctor of Philosophy.

A series of laboratory experiments were conducted in a glass wave tank to investigate the propagation of internal gravity waves up a sloping bottom in a fluid with constant Brunt-Vaisala frequency. Measurements of the wave motion in the fluid interior were primarily taken with electrical conductivity probes; measurements in the boundary layer were made with dye streaks and neutrally buoyant particles. The results indicate that, outside of the breaking zone, the amplitude and horizontal wave number of the high-frequency waves increase linearly with decreasing depth; this is shown to agree with existing linear, inviscid solutions. A zone of breaking or runup is induced by these high-frequency waves well upslope. Shadow-graph observations show that, if the wave characteristics are coincident, or nearly so, with the bottom slope, the upslope propagation of the low-frequency waves causes a line of regularly spaced vortices to form along the slope. Subsequent mixing in the vortex cells creates thin horizontal laminae that are more homogeneous than the adjacent layers. These laminae slowly penetrate the fluid interior, creating a step-like vertical density structure.

Available linear theoretical solutions for the velocity in the viscous boundary layer, determined to be valid for certain experimental conditions, are used to develop a criterion for incipient motion of bottom sediment induced by shoaling internal waves. The maximum sediment sizes that can be placed into motion, according to this criterion, are larger than certain mean sediment sizes on the continental margin off New England. This suggests that internal waves might induce initial sediment movement. Speculation about the geological effects of breaking and vortex instabilities is also given. These processes, not definitely measured in the field as yet, might also be conducive to sediment movement.

Thesis Supervisors: John Southard
Assistant Professor of Geology

Carl Wunsch
Associate Professor of Oceanography

TABLE OF CONTENTS

TABLE OF CONTENTS (Cont)

LIST OF SYMBOLS

A	amplitude of the stream function
a	wave amplitude
a_o	input wave amplitude
a_m	measured wave amplitude
$\underline{a}$	fluid acceleration
$\underline{a}_f$	effective fluid acceleration at level of effective fluid velocity
c	slope of internal wave characteristic
D	sediment diameter in Chapter 5
D_m	mean sediment diameter
F_F	fluid resistance force
F_D	hydrodynamic drag
F_G	gravity force
F_L	hydrodynamic lift
F_P	pressure force
F_{VM}	virtual or apparent mass force
g	gravitational acceleration
h	local fluid depth over slope
h_o	fluid depth over horizontal bottom
k	horizontal wave number
k_w	average local horizontal wave number, theoretical
k_m	measured horizontal wave number
N	Brunt-Vaisala frequency
n	mode number in text; index of refraction in Appendix A
p	pressure
R	Reynolds number
R_D	particle Reynolds number
R_W	wave Reynolds number
R_δ	boundary-layer Reynolds number
s	specific gravity when used with a subscript; otherwise, specific gravity ratio

T	internal wave period
t	time
C_D	drag coefficient
C_L	lift coefficient
C_{VM}	coefficient of virtual mass
U	average phase function, theoretical
u	magnitude of the instantaneous horizontal fluid velocity, Chapter 4; magnitude of the instantaneous velocity in boundary layer, parallel to the bottom, Chapter 5
v	magnitude of the velocity of sediment particle
w	magnitude of the instantaneous vertical fluid velocity, Chapter 4; magnitude of the instanteous fluid velocity in the boundary layer, normal to the bottom
x, z	horizontal and vertical coordinates, respectively
x_c, z_c	absolute values of x, z, respectively
x_o	total horizontal projection of the slope
α	slope angle, degrees
β	angle between fluid resistance forces F_F and a line parallel to the slope
γ	bottom slope in radians
δ	boundary layer thickness
δ_m	measured estimate of boundary layer thickness
ϵ	ak; Stokes parameter
ϵ_m	$a_m k_m$; measured estimate of Stokes parameter
θ	phase angle
κ	bed roughness expressed as a particle diameter
μ	molecular viscosity
ν	viscosity
ν_k	kinematic viscosity
ξ, η	coordinates along and normal to the slope
ρ	density

ρ_o mean density; also amplitude of density over the flat bottom, theoretical

ρ' perturbation density, theoretical

ρ_w perturbation density computed from linear, inviscid solutions for progressive internal waves on a slope

σ electrical conductivity

τ shear stress

τ_o shear stress at the bed

τ_c critical shear stress; i.e., that shear stress necessary to initiate sediment movement

ϕ angle of repose of sediment particle

ψ stream function

ψ_T total stream function in boundary layer

ψ_I interior stream function

$\psi_{b.\ell.}$ boundary-layer stream function

ω internal wave frequency

ω_c critical internal wave frequency

ω_T semi-diurnal frequency

b.ℓ.   subscript referring to boundary layer

f   subscript "f" referring to effective kinematic fluid property or to physical property of fluid

m   quantity determined by experimental measurements

max   maximum value of quantity

o   subscript usually denotes those quantities pertinent to the input region; i.e., the portion of the wave tank with horizontal bottom

s   subscript "s" referring to physical property of sediment

T   subscript referring to total value; i.e., interior value plus boundary layer value

*   complex conjugate

| | absolute value of quantity

LIST OF FIGURES Page

LIST OF FIGURES (Cont)

LIST OF FIGURES (Cont)

<div align="right">Page</div>

LIST OF FIGURES (Cont)

ACKNOWLEDGEMENTS

1. INTRODUCTION

GENERAL

The purpose of this research is threefold:

(1) to provide experimental results that describe the changing character of single-frequency, small-amplitude internal gravity waves as these waves propagate over a sloping bottom;

(2) to compare these results with recent theoretical solutions for those conditions which are theoretically tractable, and to examine the physical characteristics of those conditions which are difficult to treat theoretically;

(3) to apply the theoretical and experimental results toward the development of a simple analytical model that prescribes the conditions for the initiation of bottom sediment motion induced by shoaling internal gravity waves.

The motivation for this work was rooted in speculation - a starting point not uncommon in experimental research. The speculation was stimulated by the results of previous work that had indicated the possible significance of internal waves as geological agents and by recent theoretical solutions that predict the intensification of internal wave motion along sloping bottoms.

It was decided early in this research that a clearer physical understanding of the shoaling process for internal waves was needed - particuarly knowledge of the nature of the bottom boundary layer - before the two-phase problem could be considered. The effects of internal waves on sediment particles of various shapes, sizes, and densities were investigated during a preliminary set of experiments. It was concluded from these kinds of experiments that the reliability of the results and the range of test conditions were limited by the experimental difficulties, mainly the difficulty

of attaining large velocities in the small experimental system. The approach to this problem was changed to investigate the movement of sediment by internal waves analytically, based on the results of a detailed laboratory study of shoaling internal waves over a smooth sloping bottom. Recent theoretical analyses had cast a framework for the experimental design (Wunsch, 1969; Keller and Mow, 1969); preliminary laboratory work had established the experimental techniques. Earlier experiments by other researchers had demonstrated the feasibility of some of the techniques (Mowbray and Rarity, 1967; Martin, Simmons, and Wunsch, 1969; Gibson and Schwarz, 1963), and had showed several stimulating results (Thorpe, 1966).

The subsequent work is divided into three sections:

(1) the experimental design, instruments, and techniques are discussed in Chapters 2 and 3;

(2) the results of the experiments and their comparison with theoretical solutions of Wunsch (1969) are presented in Chapter 4. The results are separated into two basic types: experiments with high-frequency waves[*] and experiments with low-frequency waves. The interior wave field and the boundary layer are discussed separately for each;

(3) in Chapter 5 the balance of forces acting on a bed particle is used to derive a simple analytical model for the stability of the particle beneath a train of high-frequency, shoaling internal waves. The approach closely follows that used by Ippen and Eagleson (1955) and Eagleson and Dean (1959) in the development of an analytical model for sediment motion

---

[*] The distinction between high and low frequency waves is discussed in more detail in Chapter 4. Basically the incident energy of the high frequency waves propagates upslope to the corner; i.e., toward the intersection of the slope and the free surface, with no reflection. By contrast, the incident energy of the low frequency waves theoretically is back reflected from the slope.

induced by surface waves. The applicability and limitations of the analysis of internal waves and sediment movement are discussed in Chapter 5, and some speculations are offered concerning the effects of breaking of internal waves and the action of boundary layer instabilities on bottom sediment in the ocean.

BACKGROUND

Internal Wave Theory and Experiment

In two recent papers, Wunsch (1968, 1969) has developed normal-mode solutions for both standing and progressive internal waves in a wedge geometry. The solutions of interest here are for progressive waves propagating into the wedge, i.e., over a linearly shoaling bottom. This theory assumes two-dimensional motion in a stably stratified, inviscid, Boussinesq fluid with constant Brunt-Vaisala frequency N ($N^2 = \frac{g}{\rho_0} \frac{\partial \rho_0}{\partial z}$). The geometry and coordinate system that Wunsch considered is given in Figure 1. Wunsch's solutions are discussed in more detail in Chapter 4; these solutions are presented for comparison with the experimental results. One of the principal features in the solutions is the suggestion of a strong intensification of velocity components along the sloping boundary. Wunsch (1969) conducted a simple experiment in which internal waves were propagated over a linearly sloping, rigid bottom. From photographic determinations of the changes in wave length up the slope, he showed that the results are in agreement with his solutions. The wave length was approximately proportional to the depth. Magaard (1962) presented solutions for a similar problem of standing internal waves except for the density distribution and shape of the bottom profile. He considered a density distribution that can be expressed analytically as:

$$\rho(z) = c_2 (2z + c_1)^{1/2} \tag{1-1}$$

where c_1, c_2 are constants. The bottom profile that he chose for

computational facility and some realism was:

$$h(x) = \frac{1}{2}\left[\frac{1}{(2bx)^2} + \frac{c_1^{1/2}}{bx}\right]$$

(1-2)

where c_1 and b are constants. He developed a linearized characteristic equation for the velocity field and found that the equation was separable in the spatial coordinates only for the case of constant depth. He also showed that for a bottom slope γ less than the slope of the characteristics c, a solution is possible which gives waves that have increasing amplitudes and decreasing wave lengths with depth. Magaard (1962) also found an appreciable intensification of the velocity components along the sloping bottom.

Robinson (1970) has recently considered the effects of a corner (such as the point of transition between slope and flat bottom) upon an internal wave train propagating toward the slope in an infinite medium (i.e., with free surface infinitely far from the horizontal bottom). Robinson provided solutions that consist of incident and reflected waves such that the reflected waves do not violate the radiation condition; i.e., they do not introduce energy from the far field (at $x = +\infty$).

Keller and Mow (1969) obtained an asymptotic solution to the problem of internal wave propagation in a horizontally stratified fluid of nonuniform depth by application of the principles of geometrical optics. Their general solutions apply to the linearized equations of motion, and the wave amplitude and fluid depth are assumed to vary very little over horizontal distances small compared to a wave length. They gave a particular example in which N was assumed constant and the bottom was a small, linear slope. The solutions in this case show that the wave length is proportional to the depth, and the wave amplitude increases linearly with decreasing depth. Keller and Mow noted that their solutions also are in agreement with the experimental results given by Wunsch (1969).

Hogg and Wunsch (1970; also personal communication) derived similar asymptotic solutions using a WKB approach with a two parameter

expansion scheme. Their first order, linear solutions for progressive internal waves over a small, linear slope are equivalent to those of Keller and Mow (1969); both solutions are compatible with the normal mode solutions of Wunsch (1969) for small slopes $(\gamma \ll c)$. Hogg and Wunsch extended their analysis to higher-order terms in the stream function and developed expressions for the wave-induced radiation stress. They showed that a significant set-up of the isopycnals induced by internal waves is possible and demonstrated theoretically the plausibility of "longslope" currents for a line of breaking internal waves oblique to the bottom contours. From the higher order terms Hogg and Wunsch (1970) were also able to demonstrate that in the absence of mixing the net Lagrangian motion of water particles in a two-dimensional stably stratified fluid is necessarily zero for internal wave motion in the proximity of a sloping, rigid boundary.

Fofonoff (1969) also examined analytically the unsteady motion in a horizontally stratified, uniformly rotating ocean. He considered the seaward propagation of an internal baroclinic wave that was generated at the continental shelf edge by the diurnal tide. By examining the characteristics of the solution, he presented a numerical example in which the values of density, latitude, and depth were those measured at site "D" (39° 20'N, 70°W), located about 37 miles south of the 200 meter contour. Fofonoff (1966) showed that north of this location the bottom profile of the continental slope and the path of the characteristic were approximately coincident. Again there is implication of increased bottom shear along the slope.

Sandstrom (1966) derived the reflection properties of internal waves from a sloping, rigid boundary. Both he and Robinson (1970) have noted that the normal-mode solutions derived by Sandstrom from his ray theory solutions for progressive internal waves propagating over a slope violate the radiation condition (i.e., the complete solution requires an anomalous set of reflected waves that introduce energy from the far field). Sandstrom predicted that upon reflection the waves change their wave

number and amplitude; he found that the magnitude of the changes are
dependent on a ratio equivalent to γ/c. Sandstrom (1966) also conducted a
set of experiments in which internal waves were generated by a flap-type
wave maker and allowed to propagate over a planar, inclined bottom. His
experimental results for a gently sloping bottom $(\gamma \ll c)$ showed qualitatively
two features that were also found in the present study, and are discussed
quantitively in Chapter 4: (1) amplification of internal waves traveling
from "deep" into "shallow" water, and (2) intensification of motion near
the slope. Sandstrom (1966) noted, however, that unfortunately the partic-
ular experiment for which these features were observed was complicated
by the presence of a surface mode that was also generated by the wave
maker. Although his apparatus was apparently capable of generating the
first internal mode, there are no experimental results in his work which
indicate that he did this. Sandstrom discussed solutions for the case $\gamma > c$
(steep bottom slope), but did not present experimental results for this
case. He concluded from the linear theory that in the case $\gamma \simeq c$, the motion
close to the bottom becomes very large.

Longuet-Higgins (1968) extended the discussion of reflection prop-
erties of internal waves from rigid surfaces to account for various types
of bottom roughnesses. He has shown that the important parameter is not
the ratio of the scale of bottom roughness to wavelength but instead the
ratio of the scale of roughness to the thickness of the oscillatory boundary
layer. He pointed out that this suggests that small-scale irregularities
can severly affect the transmittance and reflection conditions of the bottom.

In a very thorough theoretical and experimental treatment of finite-
amplitude effects on interfacial and internal waves in a horizontal channel,
Thorpe (1968) also reported some qualitative observations of progressive
internal waves on a slope. In his experimental arrangement, a linearly
sloping, smooth bottom was mainly employed as a wave absorber. How-
ever, during the course of the experimental runs for internal waves in a
linearly stratified salt solution he noted several interesting features over

the slope. These observations are summarized here as a preface to the results shown later in this study:

(1) the wave length decreased upslope;

(2) a large runup was apparent along the upper slope region, and the larger amplitude waves produced a larger runup;

(3) the free surface remained undisturbed;

(4) a "rotor" was observed near the free surface on one occasion;

(5) breaking ("overturning") was observed well upslope on one occasion;

(6) no reflections could be detected.

Thorpe (1968) showed three photographs of the waves over the slope. His method of flow visualization, involving alternating dyed and undyed layers, did not permit detailed observations of the breaking or mixing, but his qualitative observations are quite instructive and essentially agree with the results shown later.

It should also be mentioned here that excellent experimental studies of instabilities and turbulence in a stably stratified fluid, including breaking of interfacial waves, have been carried out by Pao (1968).

Field Observations

Two kinds of field observations are pertinent to this study: (1) measurements that suggest shoreward propagation of internal waves over the continental margin, and (2) observations that indicate, directly or indirectly, the motion of bottom sediment due to passage of internal waves.

Measurements of the first kind have been presented by Lee (1961), Gaul (1961) and Ufford (1947), among others. Their investigations presented time-series measurements of temperature fluctuations taken simultaneously at three stations oriented in various triangular arrays in shallow water (depth <200 feet). The wide geographical distribution of these studies illustrates the ubiquity of internal motions on the continental shelves. Common

internal-wave periods were on the order of 5 to 20 minutes; wave propagation was shoreward with speeds of 0.3 to 1.2 knots. Lafond (1962) has provided similar values. Longer period internal oscillations are described by Lee (1961), Boston (1964), and Summers and Emery (1963). The last study illustrated the refraction of internal waves of semidiurnal period as they propagated shoreward over the continental slope and shelf off Southern California. The estimated wave speed was 7 knots in deep water and slightly less than 1 knot over the shelf.

Isolated asymmetrical internal temperature disturbances resembling the idealized solitary wave profile of surface waves (Ippen, 1966) have also been detected by Lee (1961), Gaul (1961), and Cairns (1967). The common period of this sort of disturbance seems to be approximately 10 minutes, and the propagation direction is again shoreward.

Curves of spectral kinetic energy density versus frequency are available for velocity measurements of internal motion taken with vertical arrays of current meters at site "D" (Fofonoff, 1968). An example of these spectra is shown in Chapter 5.

Direct observations which reliably link the two motions of internal waves and sediment movement are limited to a few isolated instances. This lack of evidence might suggest both the difficulty and the insufficiency of this kind of field measurement. Ideally, one would like to measure simultaneously the internal wave velocity structure and the movement of bottom sediment beneath the wave motion. Either measurement alone is a challenge in the field. Lafond (1965), using underwater television to observe the sediment motion and a vertical array of temperature sensors to measure the internal wave motion, found that the movement of sediment ripples in shallow water (depth about 60 m) was correlated with large fluctuations in the temperature structure. He interpreted this as evidence for sediment transport by internal waves.

Indirect field data that connect the two motions are similarly limited. Revelle (1939) inferred the connection in an attempt to explain an observed

pattern of sediment distribution. Munk (1941) calculated the theoretical standing-wave characteristics in the Gulf of California and found that the nodal-antinodal separation coincided favorably with Revelle's (1939) observed distribution of sediment sizes. That is, the smaller sizes were noticeably lacking beneath the nodes, where larger instantaneous velocities are expected. However, in a subsequent detailed study of the sediment distribution in the Gulf of California Van Andel showed that the sediment pattern described earlier by Revelle was not apparent in the later data. Emery (1956; 1960) suggested that deep, standing internal waves in certain California basins stir the bottom sediments and might produce the observed local concentrations of coarse sediments at the basin sills.

More recent investigations of the large submarine sand waves (average height ≃ 8 meters) near the edge of the continental shelf southwest of Great Britain (water depth ≃ 180 meters) by Stride and Cartwright (1958), Cartwright (1959), Stride and Tucker (1960), and Carruthers (1963) indicate the possibility of interaction between internal waves and bottom sediment. Cartwright (1959) formulated a theory which suggests that these sand waves are maintained by a stationary internal-wave system of tidal period that exists during the presence of the local seasonal thermocline. Measurements of oscillations of the scattering layer (Stride and Tucker, 1960) and towed thermistor records (Carruthers, 1963) support this theory. Carruthers (1963) also measured the currents close to the crest of the sand waves at one-hour intervals over a seventeen-hour period. A plot of current vectors indicated that the predominant flow direction was normal to the crests, with a maximum current of 0.5 knot in this direction. Interestingly, the crests of the sand waves are parallel and adjacent to the shelf edge.

Many investigators have studied the observed sediment distribution on the continental shelf and slope off the East Coast of the United States. Uchupi (1963), Emery (1966), and Schlee (unpublished manuscript) have summarized much of this work. Sand waves and local topographic highs

are abundant on the continental shelf. The type and size distribution of sediment varies both across and along the bottom contours. The seaward variations are generally sharper. For instance, Uchupi (1963) delineated four broad zones parallel to the shelf edge from Cape Cod to Hudson Canyon. He noted that the most seaward zone (about 70 kilometers wide) consists of silty sand, sandy silt, and silt (water depth 60 to 135 meters). Uchupi (1963) claimed that from Hudson Canyon to Cape Hatteras the outermost zone is composed of fine sand of approximately uniform grain size. The surface of the continental slope in these regions consists mainly of silt and clay; however, sand, silty sand, and gravel line the floors of the submarine canyons that cut the slope.

Wave-Induced Bottom Sediment Motion

The writer could find no published results on wave-induced bottom sediment motion in a stratified fluid. However, there are many published studies of sediment motion beneath surface waves in a homogeneous fluid. Most of these studies are empirical or semi-empirical. The obvious lack of theoretical treatment probably stems from the complex form of the governing equations of motion, which are not well established.

One appealing approach to a laboratory and analytical study of the problem was undertaken by Ippen and Eagleson (1955) and later extended by Eagleson, et al (1958), and Eagleson and Dean (1959). A statistical treatment of laboratory data that involved the motion of discrete spherical sediment particles due to shoaling surface waves supplemented their theoretical presentation. Many of the complicating secondary factors, such as (1) nonuniform bed roughness, (2) shape variations of the particles, (3) mutual particle interactions, (4) nonuniform incident wave trains, (5) local channelization and fluidization of the bed, and (6) bed permeability were not included in their work. They were able to derive a force-balance equation for the individual particles. Ippen and Eagleson (1955) described two possible types of particle motion: incipient and equilibrium. Incipient sediment motion was defined by Eagleson et al (1958) as "an instantaneous

condition reached when the resultant of all active forces on the particle intersects the line connecting the bed particle contact points." They also defined established sediment motion as "an oscillatory or quasi-oscillatory condition of motion reached when for some portion of each wave cycle the sum of the instantaneous active forces is greater than that value necessary to initiate motion." The major difficulties in working with these definitions are: (1) the point of application of some of the individual forces is usually not known; (2) the various coefficients, such as those for drag, lift, and virtual mass, are not well defined for unsteady motion; (3) usually the effective fluid velocities acting on the bed particle must be estimated from an approximate theoretical equation, since the exact velocity profile near the rough bed in unsteady motion is not known. Despite these difficulties, Eagleson and Dean (1959) were able to arrive at a semi-empirical relationship for particle size, beach slope, and local wave characteristics. Eagleson et al (1958) compared the analytical results with field data from eight stations on the Atlantic coast of the United States. As these authors put it, the agreement was "fortuitously" remarkable.

The concept of an equilibrium diameter for given wave conditions was first proposed by Cornaglia (Miller and Zeigler, 1964) and has since been labeled the null-point theory. His arguments, as well as those of Ippen and Eagleson (1955) and Miller and Zeigler (1964), are basically simple. In an area of shoaling waves, every bottom sediment particle is affected by the existing sea state. For any given sea state and bottom slope, there will be one size class of particles in a state of equilibrium motion. That is, this size class will move back and forth along the bottom as successive troughs and crests pass, but will oscillate about some mean position. In general, particles larger than the null-point size will move offshore and those smaller will move onshore. Miller and Zeigler (1964) noted that in the field the null point should be regarded statistically, whereas in the laboratory it is convenient to regard it as single-valued. Their field study also indicated the limitations and the modified applicability of this theory in nature. However, at the same time their work showed that

the theory gives a satisfactory prediction of the gross sediment distribution of a nearshore sand bottom.

Other laboratory investigations have produced relationships between the initiation of motion of a given particle size and the associated wave conditions (Manohar, 1956; Goddet, 1960; Vincent, 1958). These investigations were all conducted in a channel with a level bottom. Vincent (1958) observed that the fluid velocity just outside the boundary layer was almost constant at the onset of movement of equal-diameter grains. Abou-Seida (1965) noted that field measurements of radioactive sand tracers conducted by Sato et al (1963) compared favorably with the laboratory relationships deduced by Manohar (1956) and Goddet (1960).

A second approach to this problem is relatively new. Arguing from basic physical principles and certain assumptions, Bagnold (1963, 1966) derived a relationship between bed load transport and the dissipation of energy in the fluid motion. His argument rests on the assumption that a distribution of dispersive and tangential shear stresses exists in a bed of granular material that is subjected to shear deformation. Several summaries of the topic of wave-induced sediment motion are available (Inman, 1963; Abou-Seida, 1965; Raudkivi, 1967). Such presentations of incipient sediment motion usually include a discussion of the various criteria developed for open channel flow. In particular, the work of Shields (1936), White (1940), and Kalinske (1947) is often cited.

2. EXPERIMENTAL SYSTEM

APPARATUS

Wave Tank and Mechanical Components

The rectangular wave tank illustrated in Figure 1 has an open top and 3/8-inch glass side walls and bottom. It is 4.9 m long, 20.5 cm wide, and 38.4 cm deep and consists of two sections of similar dimensions joined end to end by an O-ring seal contained between plastic inserts attached to the sections with epoxy cement. A thin layer of clear silicone sealant (Dow Corning 701 Building Sealant) was applied along the inside seam to form a smooth transition between the two sections. All other joints were also formed with silicone sealant. The ends of the channel are acrylic plastic plates sealed by Neoprene gaskets. A 14-foot length of aluminum angle attached to five vertical aluminum angle supports behind the tank and 3/4 of an inch above the side wall served as an instrument mount.

A filling technique similar to that described by others (Fortuin, 1960; Oster, 1965; Jaffee, 1968) was designed to establish the desired salinity gradients in the wave channel. Figure 1 shows a diagram of the filling system. Owing to the corrosive properties of salt water, the insides of the two 55-gallon containers were coated with epoxy paint, and all seams were caulked with silicone sealant. Wherever the liquid came into contact with bare metal, only stainless steel or brass was used. Flexible Tygon tubing is used throughout the filling system wherever tubing was required.

The filling rate was controlled by a brass needle valve. Each drum was equipped with a Tygon sight tube for visual determination of the level in each barrel. A motor driven stainless stirring rod with two brass stirring vanes was mounted above the fresh water barrel. To prevent solid-body rotation of the water, the stirring rod lay off the axis of the barrel.

The bottom slopes, one of which is shown in position in Figure 1, were cut from Plexiglas sheets. Each slope is beveled at one end to form

1. wave tank
2. Plexiglas slope
3. supporting strut
4. Neoprene gasket
5. Plexiglas end plate
6. Tygon filling tube
7a. fresh water barrel
7b. salt water barrel
8. stirring motor
9. siphon
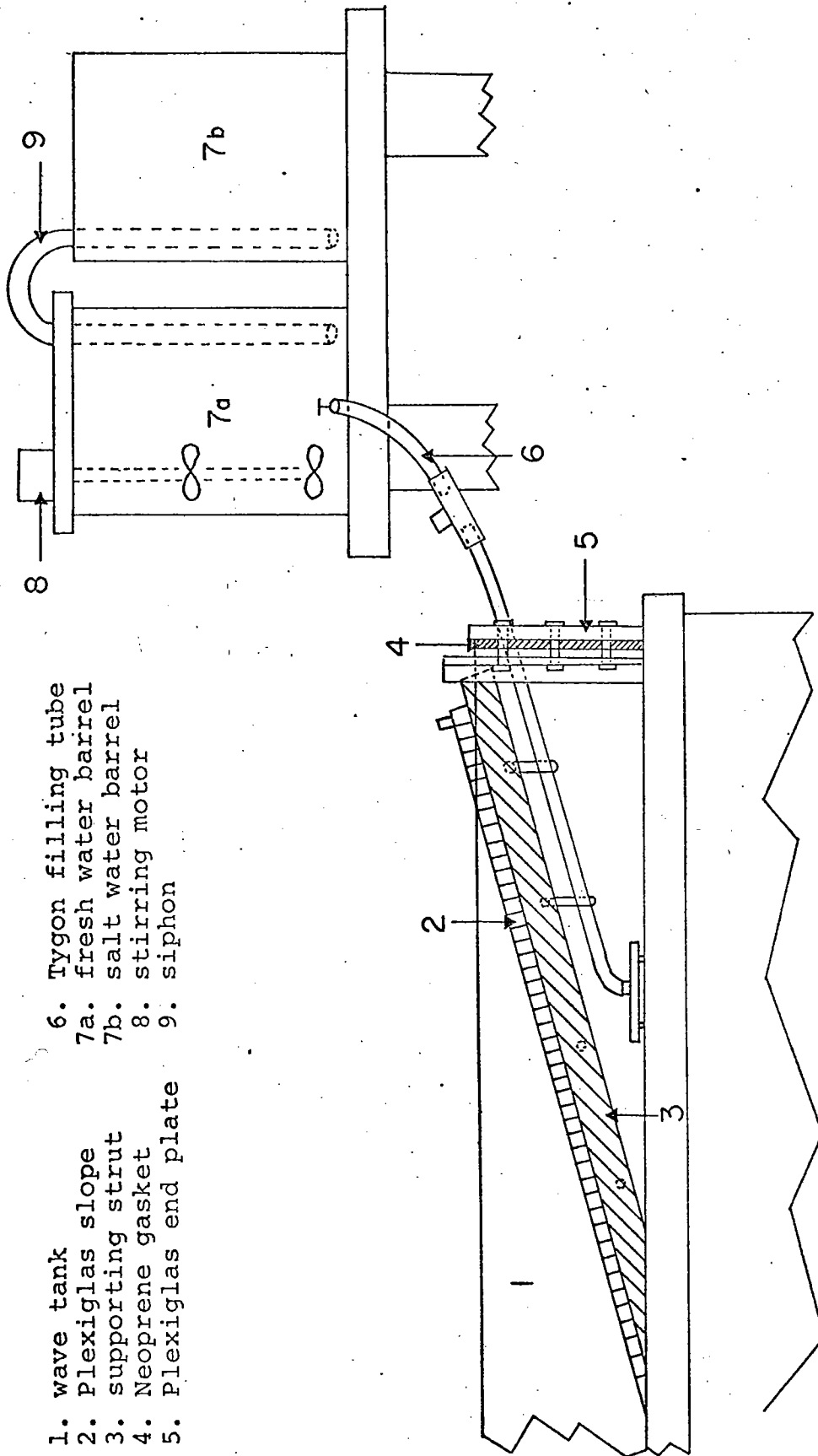
Fig. 1. Wave tank and filling system.

Wave tank dimensions: 4.9 m x 20 cm x 38 cm (not to scale).

a smooth junction with the bottom of the tank. Four slope angles were used, 7, 15, 30, and 45 degrees. During the experiments the slopes were supported by two parallel Plexiglas struts. These struts were positioned at the proper angle along the inner walls of the tank. Four Lexan plastic rods with threaded ends and plastic nuts were used to separate the struts and to maintain their position by forcing them against the channel walls. Neoprene strips were cemented to the outer surfaces of each strut to form a continuous and flexible seal with the side walls of the channel. All materials forming the beach slopes and supports were noncorrodible.

Wave Generating Apparatus

The wave generator had to meet five primary requirements:

(1) smooth and sufficiently powerful motion;

(2) desired frequency range and control;

(3) variable amplitude;

(4) compact size with components stably mounted on a plate above one end of the channel;

(5) long running with low vibration level.

In an effort to meet these requirements the apparatus was modified several times. Availability of various components such as the variable speed drive often aided the choice of parts. The end product was an outgrowth of the usual experimenter's dilemna: getting optimum performance at reasonable cost.

Power unit. Figure 2 is a diagram of the power drive for the wave maker. The entire drive mechanism is rigidly supported above one end of the channel by four 1-1/2-inch pipe legs with foot flanges. The base is a 1/4-inch steel plate. The assembly consists of a Graham variable-speed drive coupled to a 1/4-hp motor. The output shaft is joined to a fixed-ratio gear reducer (9.5:1) via a flexible coupling. This second speed reducer is connected to a Scotch-yoke device that converts the rotary shaft movement into rectilinear sinusoidal motion of a vertical shaft.
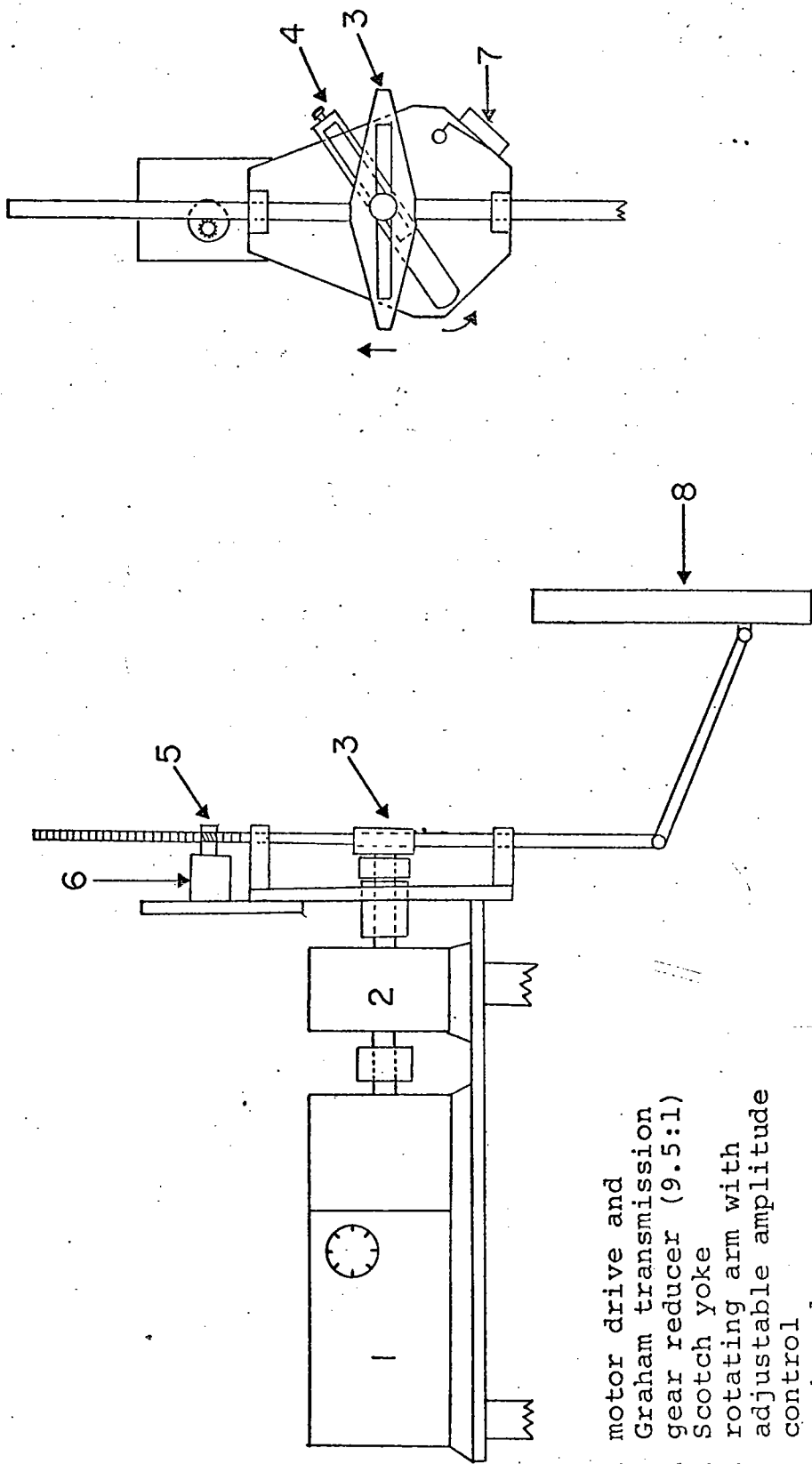
1. motor drive and
   Graham transmission
2. gear reducer (9.5:1)
3. Scotch yoke
4. rotating arm with
   adjustable amplitude
   control
5. rack and spur gear
6. rotary potentiometer
7. microswitch
8. wave maker

Fig. 2. Wave generating apparatus

Wave maker. Figure 3 shows the wave maker in actual location. Several additional considerations were involved in the design of this device. First, a unit was needed that could be inserted into position easily without appreciably disturbing the stratification after the tank had been filled. Secondly, the driving motion had to generate, to a good approximation, first-mode internal waves while minimizing mixing at the wave maker. In addition, the water motion in the section behind the wave maker had to be prevented from interacting with the fluid in the working section of the channel.

Basically, the device consists of a plastic flapper plate free to pivot about its midpoint. Hinges anchor this plate to a supporting frame. A thin flexible rubber gasket covers the entire face of the plate and frame, thus preventing liquid from flowing between the two sections. This gasket is held in position by thin plastic covers cut to the same shape and dimemensions as the frame and flapper plate. The flapper plate is driven by a stainless-steel push rod connected to the vertical shaft of the Scotch yoke by a universal coupling that allows for minor misalignments between shaft and flapper plate.

A closed-cell Neoprene strip was cemented to the sides and bottom of the frame. This afforded an adequate seal between the wave flapper assembly and the glass tank. A test showed that the wave maker could successfully maintain a head difference of at least 6 cm of water between the working section of the channel and the unused portion.

DATA ACQUISITION

This section describes the instruments used to record the experimental data. A more detailed discussion of the quality of the measurements, including calibration curves, error, and reliability estimates, is presented in the next chapter and in Appendix A.

Detection of Wave Motion

The changing properties of the internal waves as they propagated upslope were measured in the Eulerian sense with conductivity probes.
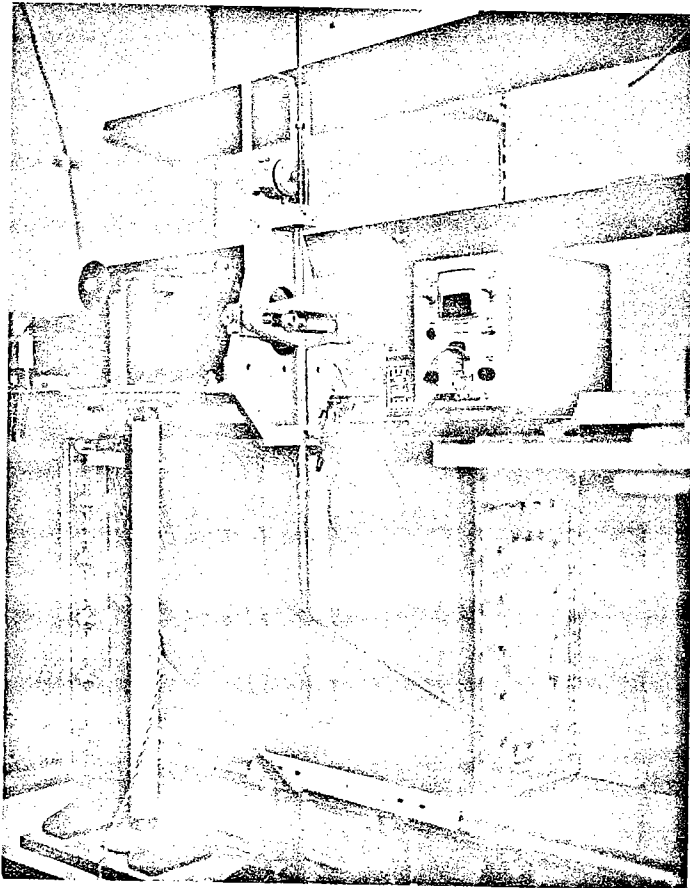
Fig. 3. Wave maker in actual location. Tank
        depth is 38.2 cm.

The basic feature of the water medium was its strong salinity stratification. Also, over the range of salinity values used during this study, salinity is approximately linearly proportional to conductivity. The temperature variations in the water were found to be small (usually less than 0.5°C over the total depth) except in the upper two centimeters, so that below this layer the total change of conductivity at a point is here a valid estimate of the total change of salinity:

$$S = S_0 + \sum (\sigma - \sigma_0)$$

(2-1)

$$\frac{D\sigma}{Dt} = \frac{1}{\sum} \frac{DS}{Dt}$$

where

$\sum$ in $\permil/(\text{ohm} - \text{cm})^{-1}$

S in $\permil$

σ in $\text{ohm}^{-1} \text{cm}^{-1}$

Because the wave-induced fluctuations of conductivity are measured relative to some basic state of rest, only relative changes in conductivity at a point are needed to decode the waves.

The conductivity sensor is a spherical platinum electrode that is the active arm of an A.C. Wheatstone bridge. Design and construction of the probe was inspired by Gibson and Schwartz (1963). Figure 4 shows a probe assembly, including electrode, glass housing, and connecting cable. A detailed description of its construction and an analysis of its performance are presented in Appendix A.

Temperature.

Temperature of the room air and the water in the filling barrels was measured with a mercury-in-glass thermometer which can be read to 0.05°C. Vertical and horizontal temperature profiles of the stratified

5 mm

inner wire of coax

spot weld

3 mm

glass annealed to Pt wire

0.3 mm

5.3 cm
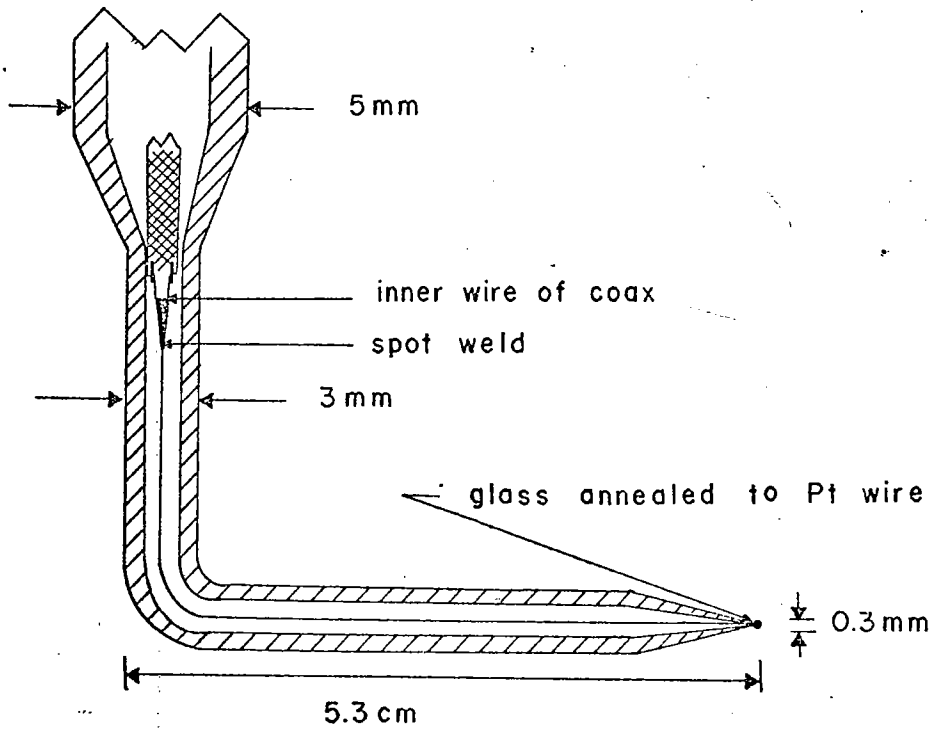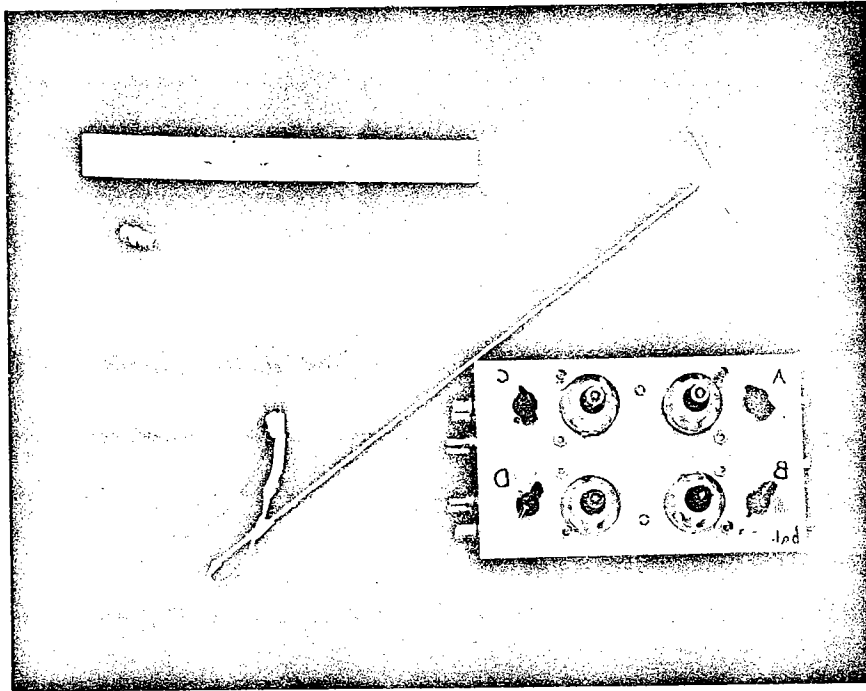
Fig. 4.   Upper: Photograph of conductivity probe
                   assembly and circuit box.
          Lower: Construction of conductivity probe
                   tip.

water column were taken with a glass-coated thermistor bead that is the active arm in a D.C. Wheatstone bridge.

Specific Gravity

Specific gravity measurements of the water in the filling barrels were made with a lead-weighted glass bulb hydrometer. The hydrometer can be read to 0.0005 for any specific gravity in the range from 1.000 to 1.070. Its accuracy is about 0.2 percent of the maximum value in the range.

The basic specific gravity gradient was determined from measurements of the vertical distribution of index of refraction. Figure 5 shows the refractometer and mini-siphon that were used to obtain index of refraction at various depths in the stratified water. These measurements were converted to specific gravity values from calibration curves. The siphon consists of a 0.5 mm diameter stainless steel tube supported vertically by a brass bushing and two locking screws. The bushing is press-fitted into an aluminum bar. Centering pins allow repeatable positioning of the aluminum bar athwart the channel. Markings that are evenly spaced one centimeter apart are inscribed on the steel siphon for vertical positioning. Small-diameter Tygon tubing fits over one end of the siphon tube. A brass pin that can be inserted into the open end of the Tygon tubing is used to stop the flow. Flow rate through the siphon at mid-depth (about 16 cm of water) is about 0.2 m ℓ /sec.

Wave-Maker Motion

A rotary potentiometer in a D.C. voltage-divider circuit transduces the oscillating, rectilinear motion of the Scotch yoke into a fluctuating D.C. voltage signal. A precision gear meshes with a linear rack that is cut into the forward part of the upper vertical shaft of the Scotch yoke (Figure 2). The spur gear is fastened to the shaft of the rotary potentiometer. Vertical movement of the Scotch yoke causes a change in the voltage output of the sensing circuit. The sensitivity is approximately 0.1 volt/cm. This technique establishes a convenient and accurate frequency reference and time
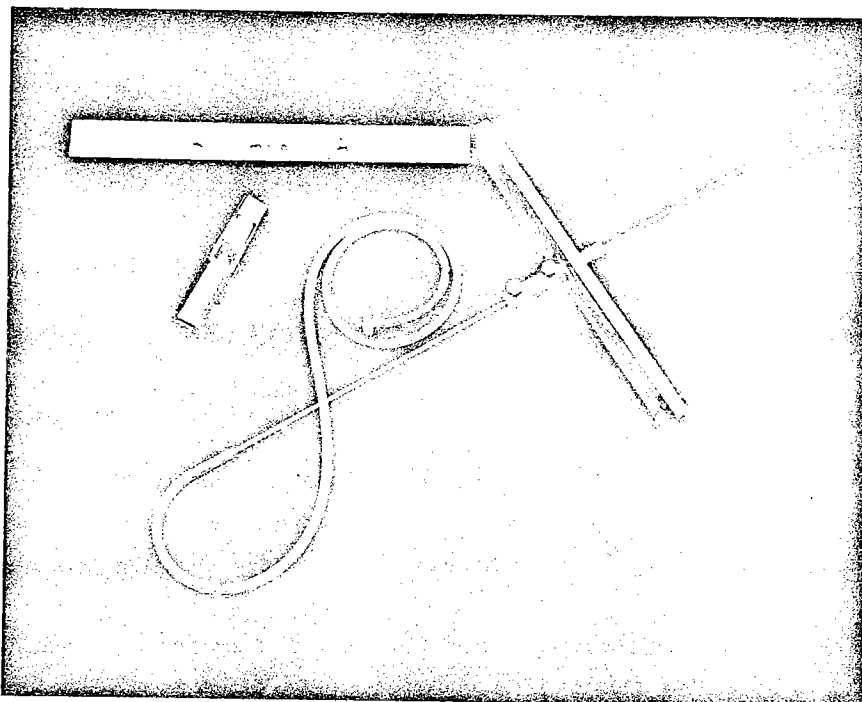
Fig. 5. Refractometer and mini-siphon.

base for the conductivity probe measurements. The accuracy of the circuit as a frequency reference is primarily dependent upon the linearity of the potentiometer. In this case, the linearity of the rotary pot is 0.1 percent (Giannini Control Corporation). Amplitude calibration of the signal also provides a measure of the forcing amplitude of the wave flapper.

The period of the motion is sensed by a microswitch mounted on the lower part of the vertical support plate for the Scotch yoke (Figure 3). This switch is closed once per cycle by a protrusion on the rotating arm, and provides a convenient trigger for a period counter.

Photographic Measurement

Photographic measurements of the wave motion were obtained by recording on film the behavior of neutrally buoyant particles and various dyes. Expandable polystyrene particles (Sinclair-Koppers Company) were chosen because their density was adjustable to the proper range by a technique described by Bohlen (1969). In addition, their milky white color provides an excellent contrast with the surrounding water when used with a black background and overhead lighting. After processing to achieve the desired density range, Bohlen found that their sizes varied over a considerable range. Sieving produced a more uniform size distribution, with median size about 0.2 mm. The range of specific gravity for the lot was 0.990 to 1.040, with an obvious skew toward the heavier limit. The mean specific gravity was estimated at 1.020. These values were adequate for neutral buoyancy in the range of fluid densities used during this study. The particles were used to study orbital velocities and modal structure.

Potassium permanganate ($KMnO_4$) was used to make the vertical dye streaks to determine near-bottom velocities and bottom shear stress. When dropped into a water column, crystals of this substance leave a distinct dark-red dye trace from surface to bottom. The vertical trace was then tracked photographically as it was deformed by wave motion.

Small quantities (one to two cc) of common liquid food coloring or a highly nondiffusive blue dye (Blue Dextran 2000) were injected into the filling tube by means of a 16-gauge hypodermic needle and syringe through a self-sealing rubber membrane at infrequent intervals. The membrane was fitted over one end of a glass T-joint in the Tygon filling line (Figure 1). These injections resulted in thin horizontal dye layers at various levels in the stratified water column. This enabled qualitative measurements of the internal waves by observation of the deformation of the dye layers by the propagating waves. The layers were typically 3 to 5 mm thick for the food dyes and only about 1 to 2 mm thick for the Blue Dextran 2000. The technique also aided in observing flow conditions at the entrance to the main channel during filling. Excessive mixing at this point was indicated by rapid diffusion of the dye, as might be expected in an area of strong turbulence. In such cases, filling rate was decreased. Finally, the dye layers added some aesthetic value to the final stratification.

Shadowgraph images were used to display instabilities in the boundary layer and the violent breaking of waves in the upslope turbulent zone. The shadowgraph system is shown diagrammatically in Figure 6. The two-way diffusive screen is sold by Edmund Scientific Company under the trade name Lenscreen. Its excellent dispersive properties and good transmittance produced clear and evenly lighted images. The merits and techniques of shadowgraph flow visualization are discussed by several authors (Barnes, 1954; Goldstein, 1965; Edgerton, 1958). A Bolex 16 mm camera was used to take motion pictures of the shadowgraph images.

The shadowgraph lighting was provided by a tungsten filament lamp (Beck Company) that contains a dial rheostat for light-intensity adjustments. It also has a circular portal lens that can be moved toward or away from the light source. This lens and an adjustable diaphragm are located in a collimating tube through which the light rays pass. A 500-watt combination flood-spot lamp provided illumination for the dye streak photographs.
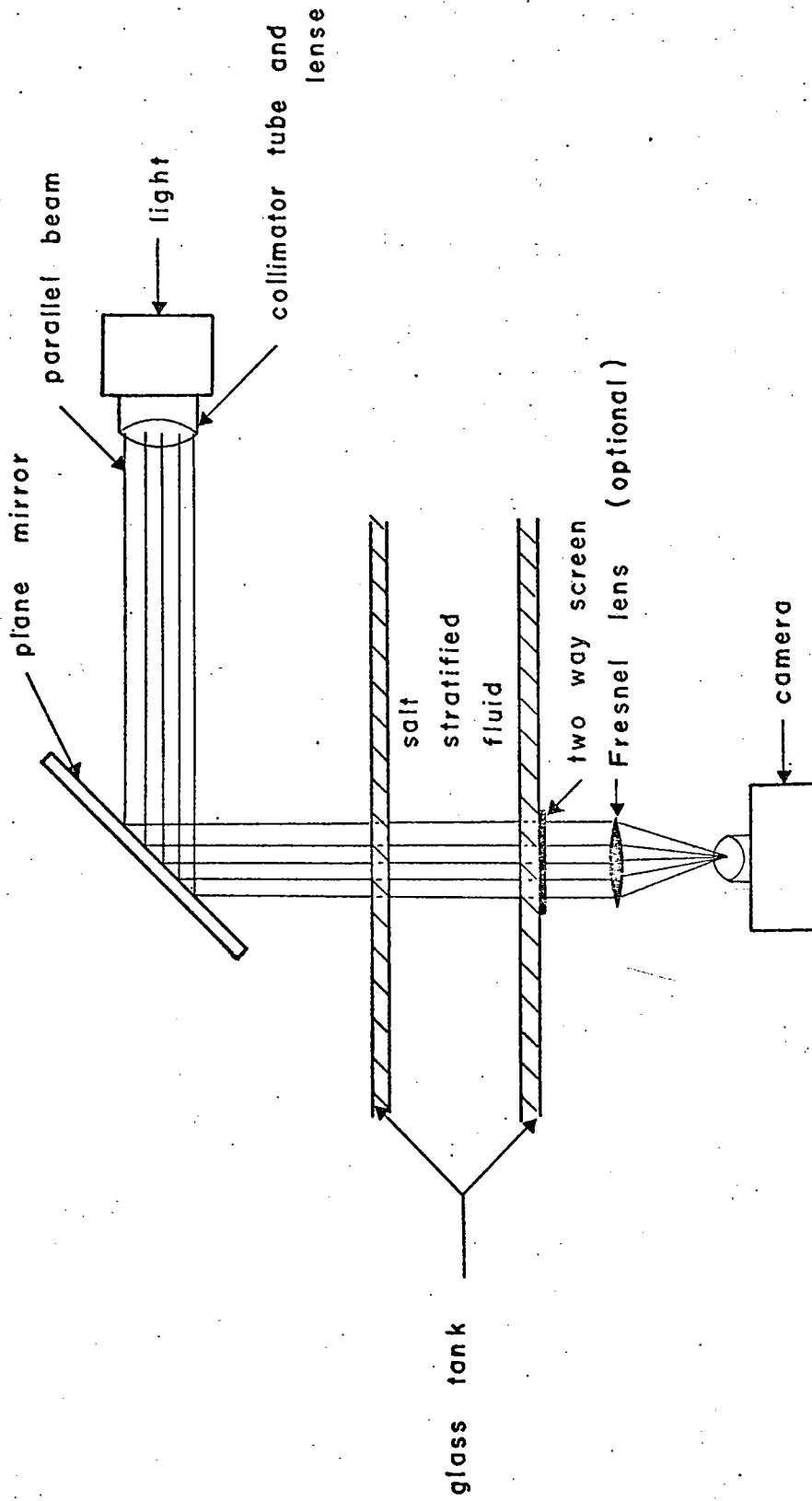
Fig. 6. Schematic of shadowgraph system.

Data Recording and Display

Figure 7 shows some of the instruments used in this study. The oscilloscope at the left of the picture has provisions for dual-channel operation (Tektronix Type 564 Storage Oscilloscope), and was used mainly to display the output of each conductivity bridge when null was set (Appendix A). The instrument at the right is a Brush dual-pen strip-chart recorder. The two charts operate on the same time base but with independent voltage scales. This recorder provided a real-time display of the transduced conductivity fluctuations during the internal-wave runs. Thermistor temperature measurements were also recorded in this way.

The heart of the data recording system, a Wang model 2300 digital readout and recording system (Wang Laboratories), is at the center of the photograph in Figure 7. The fastest available sampling rate (1 cycle per second) was chosen for all phases of this investigation. The system was programmed such that each tape record was in card-image format (≤ 80 characters per record) and represented one second of real time. Included in each record were digital clock time to the nearest second and six sequential channels of data. The data characters contained five measurement digits, decimal point location, and sign; each data point was recorded to the nearest millivolt. The recording format simplified use of the data in the digital computation routines on the IBM 360/67 system and in listing the raw data in decimal format on the IBM 1401.

Several cameras were used to photograph the neutrally buoyant particles and dye lines. General photographic work was done with a Nikon F single-lens 35 mm reflex camera. Another Nikon F camera with an automatic film advance attachment was used to photograph deformations of the dye streaks, and, in some cases, the motions of neutrally buoyant particles. The film advance was controlled by a synchronous timing device that provides continuous one-second trigger pulses to the camera at an accuracy of ±0.1 percent of the timing interval. A Calumet view camera with fast Polaroid film was normally used to photograph the neutrally buoyant particles, which
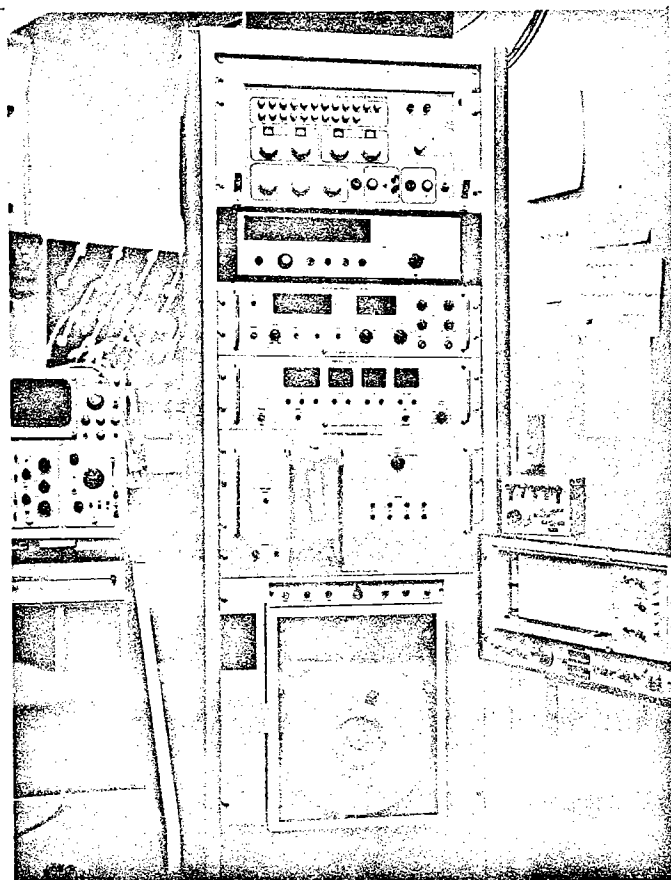
Fig. 7. Data acquisition system
         Left: Tektronix type 564 storage oxcilloscope
         Center: Wang model 2300 digital data system
         Right: Brush dual-pen strip chart recorder

were illuminated by a flashing stroboscope. The strobe flashes were triggered externally by a signal generator (Wave-Tek).

EXPERIMENTAL PROCEDURE

Although the procedure for each experiment varied depending upon the purpose, the following basic procedure was employed throughout the preparation and execution of all experiments. Several days (usually three) prior to the experiment, the two 55-gallon barrels were filled to a predetermined level with hot tap water to which 7 to 10 teaspoons of Alconox laboratory detergent were added. Liberation of dissolved air accompanied the subsequent cooling to room temperature. The detergent inhibited formation of air bubbles along the walls of the drums. The water was also stirred manually as often as possible. On the next day, a predetermined amount of salt was added to one drum. A submersible pump was used to mix the salt into solution and to minimize entrainment of air at the free surface. After the wave tank had been cleaned, the wave flapper assembled and tested, and the slope supports positioned at the desired angle, the siphon connecting the two barrels (Figure 2) was primed, and the stirrer in the fresh water barrel was started. The water temperature in each barrel and the room temperature were then recorded. Readings of specific gravity and index of refraction were taken in both barrels. During filling, the water level was recorded as a function of time, and dye was injected into the filling tube at selected intervals. Room and water temperatures were monitored at one-hour intervals. After filling was completed, about 10 hours later, the final temperature and specific gravity of the water in each barrel were measured. The slope was then inserted very slowly and smoothly by sliding it down the supporting struts until its beveled edge lay flush with the tank bottom. Very little mixing was observed, except at the edge, as the slope moved through the stratified fluid. The coherence of the dyed layers near the slope attested to the small degree of disturbance. The wave flapper, whose bottom had been positioned at mid-depth during the filling, was then inserted through the remainder of the fluid. Its driving rod had been fastened to the vertical shaft of the Scotch yoke prior to filling. This procedure also

caused very little noticeable mixing. The water depth was recorded, and the top of the tank was covered with a thin plastic sheet (Saran Wrap) to minimize evaporation losses at the free surface. (Prior experience showed that these evaporative losses could be quite substantial, 1 - 2 mm of water per day.) In addition, the conductivity probes were cleaned and platinized as necessary (Appendix A). Depth markings were checked and refurbished on all probes.

On the next day, vertical profiles of temperature and index of re-fraction were taken over the flat bottom and at other stations along the slope. The depth was recorded, and the presence of an interface near the surface was investigated with the shadowgraph apparatus. The plastic covering was removed from the slope section of the tank, and the pertinent photographic apparatus was made ready.

Prior to wave generation, the conductivity probes were given static calibration by raising and lowering them vertically by known increments while recording their output at each level; this allowed a comparison with previous calibration values and provided an updated sensitivity coefficient for each probe. Normally, the next group of measurements were taken with the probes all at the same depth over the flat-bottom region. Adjacent probes were separated by equal distances usually 5 to 10 cm, with the probe farthest from the slope at a distance of at least 200 cm from the wave maker. Runs were then conducted in which the forcing amplitude and frequency of the wave maker were varied to include most of the values to be investigated. These data provided a set of reference values with which the later measure-ments over the slope were compared. The procedure used to take the dye-streak measurements is summarized below.

(1) Prior to the initiation of wave motion, a grid marked in milli-meters was gently lowered to the slope in the middle and parallel to the side walls of the tank, photographed in place, and gently removed. The position of the camera relative to the front wall of the tank was carefully measured; this position could be repeated to within 1 percent.

(2) After the disturbances introduced by the grid removal had sub-sided (usually 10 - 15 minutes), and several minutes after the wave-maker had been turned on, several dye pellets were dropped at various locations over the slope (normally four) and at one position over the flat bottom. The pellets were dropped through a small glass tube at the previous position of the grid. By choosing dye pellets that were small (diameter < 0.3 mm) and nearly spherical, irregular motion during descent was minimized. During the rest of the experiment, photographic and conductivity measurements were taken at various locations and times. Each experiment usually lasted from two to four days, depending on the nature of the particular experiment and the physical endurance of the experimenter.

3. DATA ANALYSIS

Several kinds of experimental data were obtained; these included
(1) temperature, (2) mean density gradient, (3) density perturbations,
(4) boundary layer velocities and bed shear stress, and (5) miscellaneous
data including mode number, net particle drift, and measurements of boun-
dary layer instabilities. The instruments and some of the procedures that
were used to obtain the various kinds of data have already been described;
this section presents a summary of the data reduction techniques and the
methods of analysis.

TEMPERATURE

Vertical temperature profiles at several horizontal locations were
made at least once before and after each experiment, and usually several
times in between. Typically the maximum temperature variations were
relatively small ($\leq 0.5°C$) over the fluid interior; more irregular changes
often occurred in the near-surface layer. This layer will be discussed in
more detail in the next section. Figure 8 is a representative temperature-
depth profile.

MEAN DENSITY GRADIENT

A typical density gradient is shown in Figure 9. Measurements of
index of refraction were made at about 2-cm intervals in the vertical and
at closer spacing near the free surface. Index of refraction was converted
directly to specific gravity by applying a calibration constant that included
a correction for the local temperature. Several times during the course of
the experiments the specific gravity values obtained in this way were checked
by carefully weighing a known volume and determining density in g/cc di-
rectly. The maximum difference in the two methods was always found to be
less than 1 part in 10^3 (or about 0.1 percent).
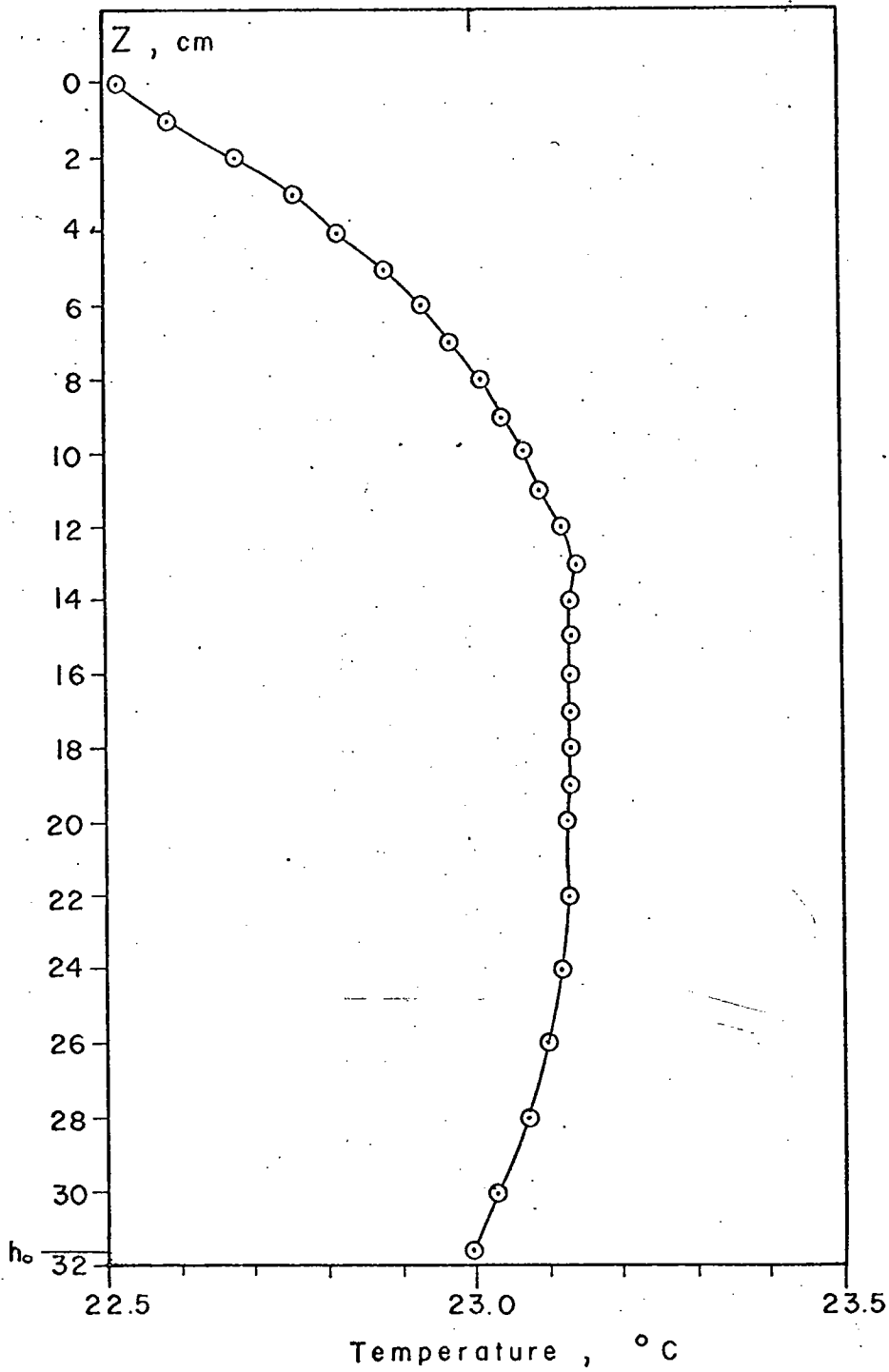
Fig. 8. Typical temperature variation with depth.
Data from exp. group 4.
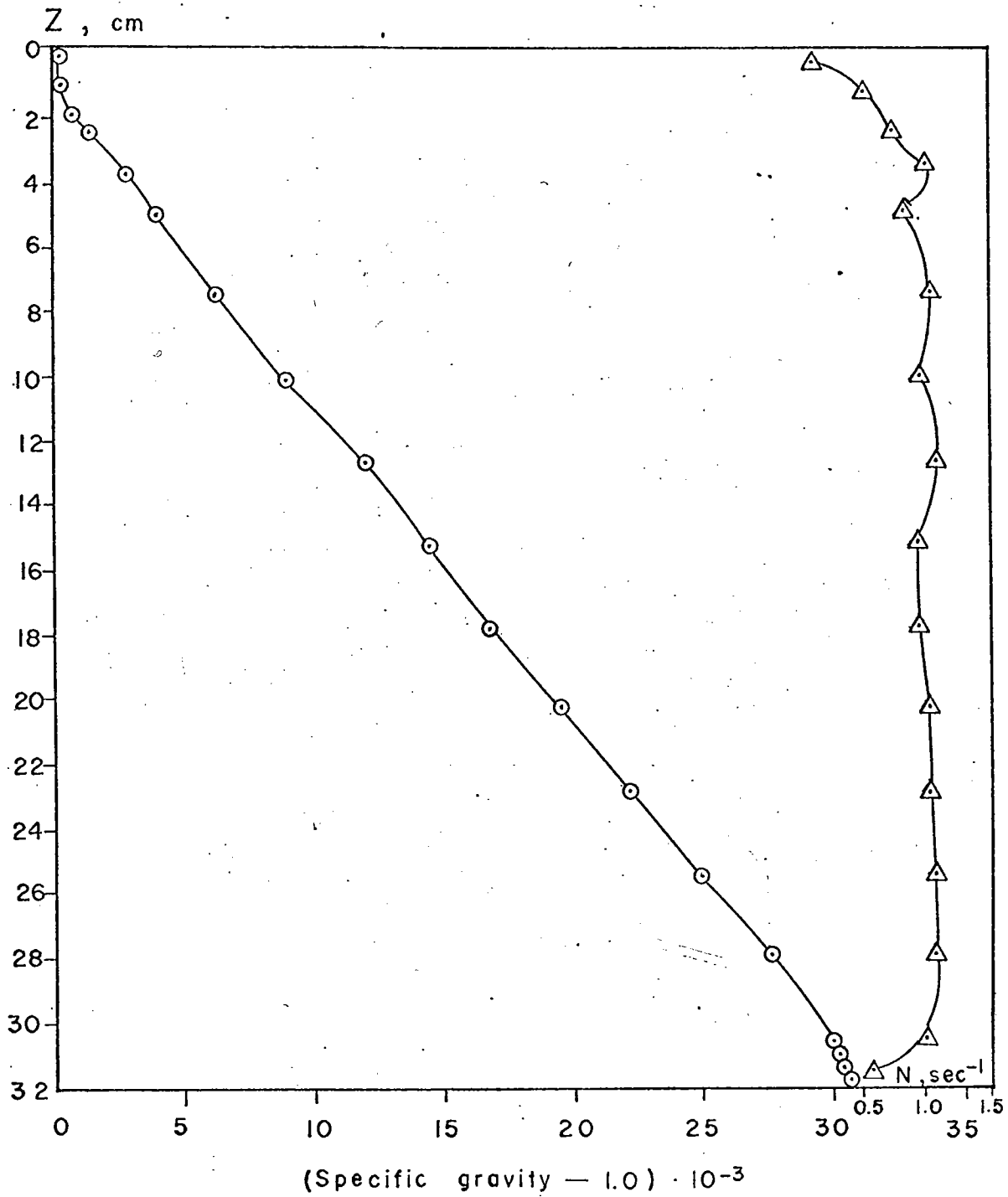
Fig. 9. Typical specific gravity variation with depth.
Data from exp. group 2; computed vertical
distribution of Brunt Vaisala frequency is
also shown.

The linearity of the curve in Figure 9 is quite good over the fluid interior but nonlinear tails are evident near the bottom and the free surface. Evaporative cooling at the free surface, when the plastic wrap was removed from the slope section of the tank during the conductivity runs, tended to increase the density of the water there, countering the effect of lower density due to low salt concentrations. The overall result was a more homogeneous density layer near the free surface. Weak convective motions were observed in this layer in the absence of wave motion by dropping potassium permanganate crystals through the water and tracking the motions of the dye traces in this layer. The amount of evaporation was reduced significantly (to < 1 mm per day) when the plastic cover was used.

The variation of salt concentration with depth as a function of time for a similar experimental arrangement has been derived theoretically from the one-dimensional diffusion equation for a constant coefficient of diffusion and conditions of no flux of salt across the boundaries (Mowbray and Rarity, 1967). The theoretical concentration-depth curves were shown to have a linear interior and nonlinear tails that thickened in time. The point of maximum curvature located between the nonlinear and linear portions of the curves might explain the sharp shadowgraph image that was usually observed a small distance below the free surface and was interpreted as a change in the density gradient (i.e., $\partial \rho_0 / \partial z \neq 0$ at this point). An example of the vertical distribution of Brunt-Vaisala frequency N is shown in Figure 9. The effects of the nonlinear tails cause N to decrease sharply in the small layers. Photographic measurements of the modal structure and of the particle displacements indicate that the basic wave motion was not measureably affected by the small, nonlinear portions of the density distribution.

DENSITY PERTURBATIONS

Perturbations in the density field induced by internal wave motion were sensed with conductivity probes. Voltage variations relative to some

mean or null value and proportional to the conductivity changes were recorded digitally on magnetic tape. The quality of the data was checked by using a real-time display on a strip-chart recorder.

Normally, measurements from all four probes were taken at least one minute before and after the wave motion to establish an instrument drift correction. Each of six data channels was sampled sequentially once per second ($\Delta t = 1$ sec); the channel allocations were four channels for probe data, one for the wave-maker signal, and one for a reference voltage. Samples of the raw data signals from one probe and wave-maker are shown in Figure 10. The length of each data record depended on the particular experimental run. Record durations of least 50 wave periods, often up to 100, were obtained for quasi-steady conditions as determined from the strip-chart output.

The data records on the magnetic tape were then processed on the IBM 360/65 as follows:

(1) average and trend were computed, listed, and removed;

(2) mean square of the data values was computed and listed;

(3) the periodogram was computed for 2N data points using a Fast Fourier Transform algorithm (IBM Manual H20-0205-3) to obtain squares of the real Fourier coefficients a_k, b_k such that:

$$v_j = 1/2 a_0 + \sum_{k=1}^{N-1} \{ a_k \cos \left(\frac{\pi j k}{N} \right) + b_k \sin \left(\frac{\pi j k}{N} \right) \} + \frac{1}{2} a_N (-1)^j$$

$$j = 0, 1, \ldots, 2N-1 \tag{3-1}$$

Normally, the starting point for each computation of the periodogram was selected when it was determined that the data were quasi-steady (transients and other irregular motions were no longer evident on the strip chart). Output listings and selected plots of the squares of the periodogram estimates a_m^2 (in cm^2) and of the phase ϕ_m at each frequency f_m (in cps) were obtained.
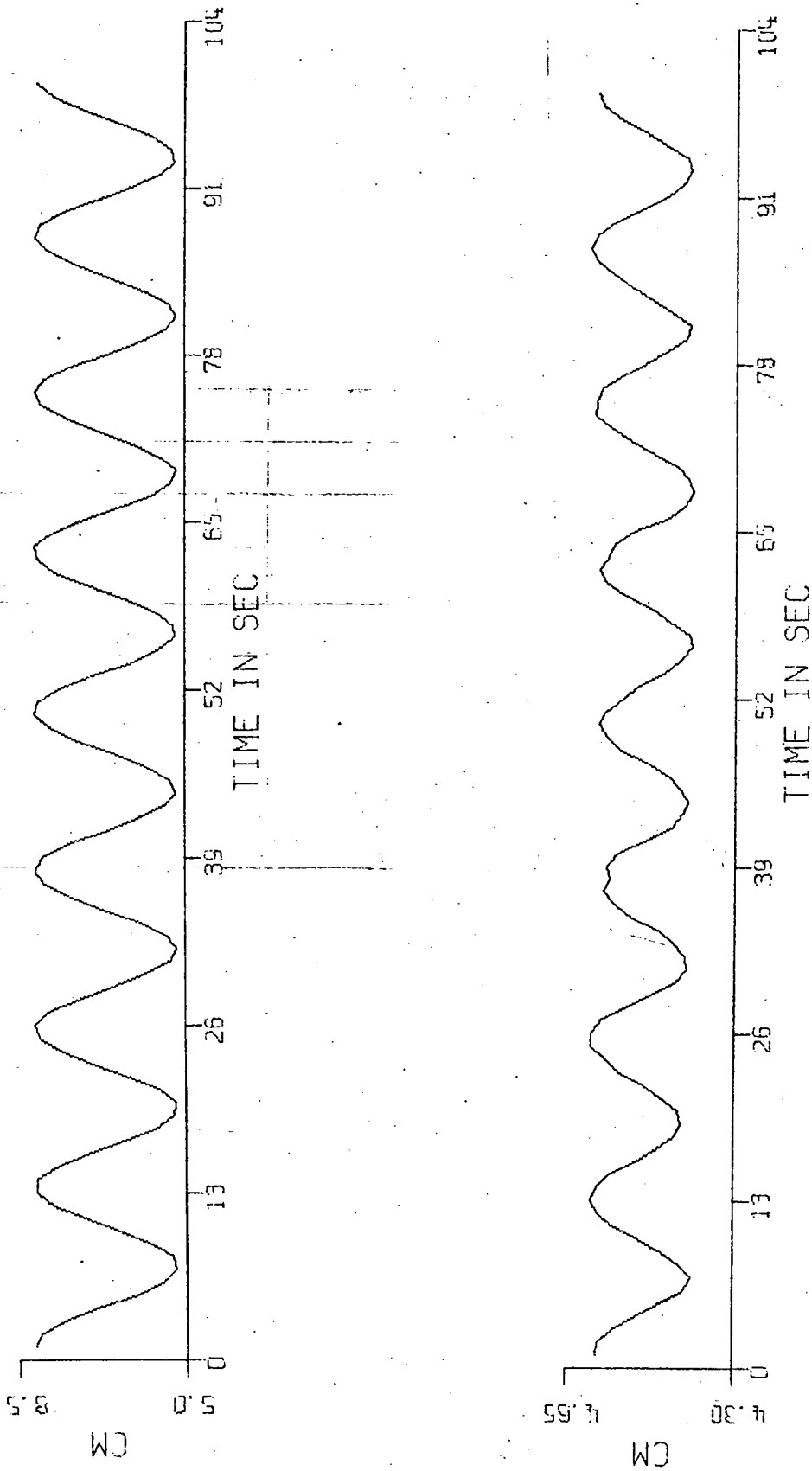
Fig. 10. Raw data plotted for wave maker and conductivity probe output. Mean not removed. (Data from Exp. Group 5)

$$a_m^{\,2} = (a_k^{\,2} + b_k^{\,2})^{1/2}$$

$$\phi_m = \tan^{-1} \frac{b_k}{a_k}$$

$$m = k = 0, 1, \ldots, N-1$$

A sample periodogram computed from the data record represented in Figure 10 is shown in Figure 11. A calibration constant has been applied so that the ordinate is cm^2 instead of $(volts)^2$. The strong peak at the input frequency and the sharp fall-off at adjacent frequencies are typical of these results. The cut-off frequency was lower than the Brunt-Vaisala frequency for all periodogram computations (cut-off frequency = 0.5 cps).

Estimates of the periodogram $a_o^{\,2}$ * were computed for probe data taken over the flat bottom region. These estimates were used as reference values for subsequent estimates $a_m^{\,2}$ for data taken over the slope at similar frequencies. The results are shown in a later chapter in the form $a_m^{\,2}/a_o^{\,2}$ to indicate the change in wave amplitude from flat bottom to slope regions. This normalization also conveniently removes certain calibration constants.

VELOCITIES AND BOTTOM SHEAR STRESS

Time-sequenced photographs of the deformation of potassium permanganate streaks were used to obtain one-second averages of the Lagrangian velocities of these streaks at several levels parallel to the bottom in and near the bottom boundary layer. Reliable measurements of streak displacements were obtained at one-second intervals over at least one full wave period, often down to distances of 0.05 cm above the bottom. Tracks

---

* The subscript "o" signifies a value pertinent to the flat-bottom section of the tank, not to be confused with the general Fourier coefficient a_o in Equation (3-1).

Fig. 11.

Sample Periodograms.

Upper: Periodogram of wave maker signal.

Lower: Periodogram of conductivity probe output.
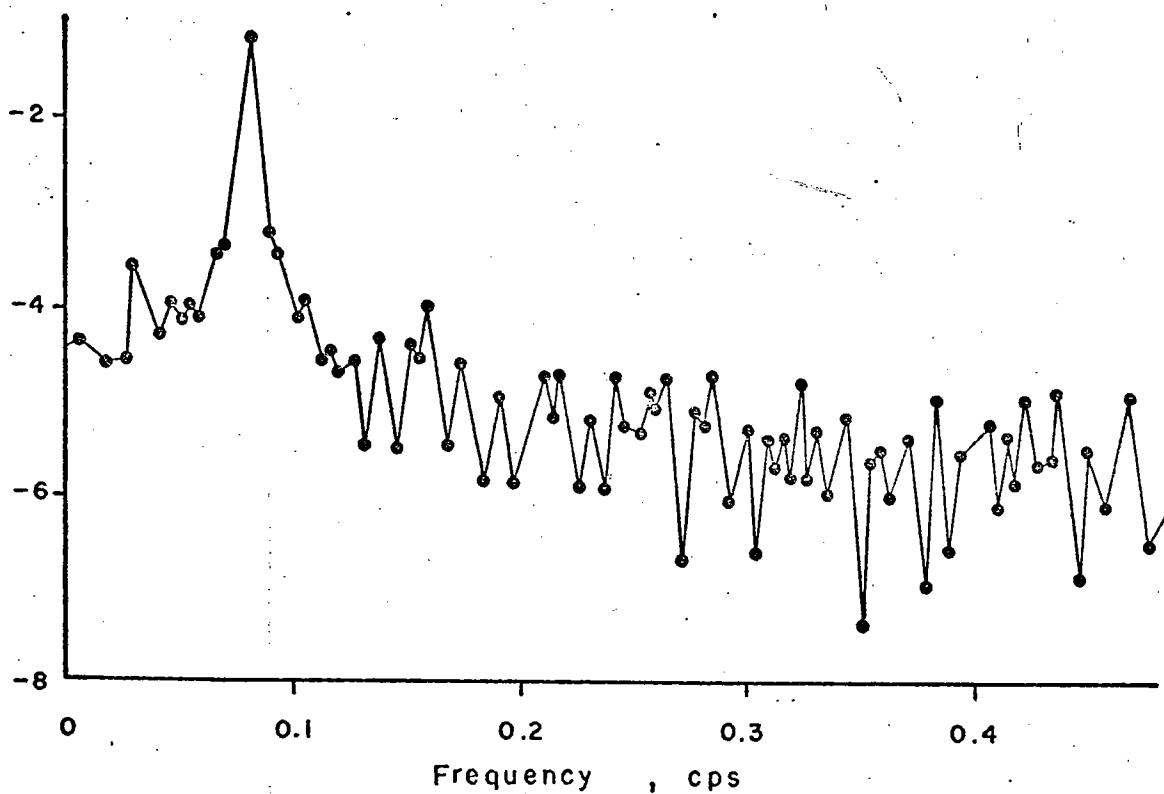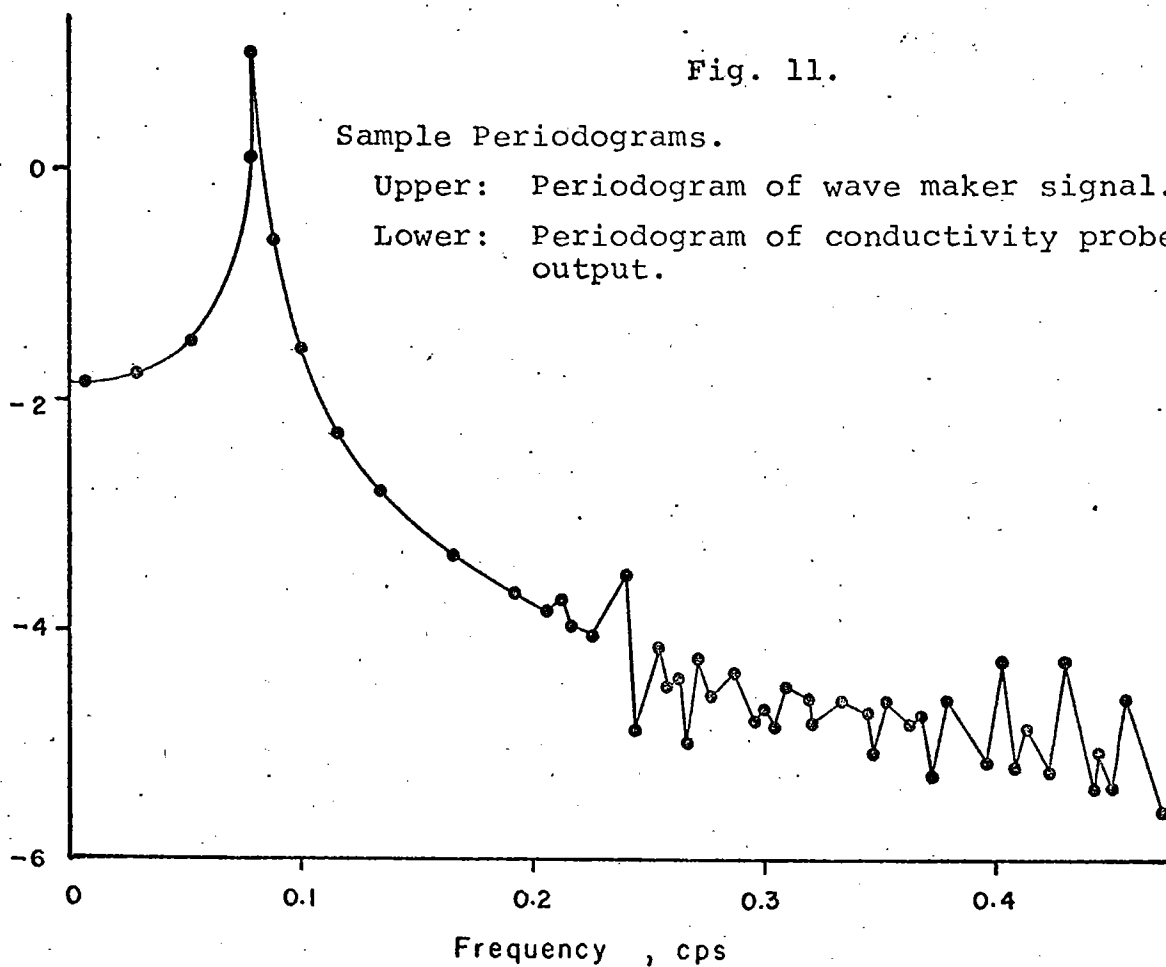
of neutrally buoyant floats near the bottom generally showed very little, if any, motion normal to the bottom, except in the zone of breaking. The dye traces usually remained coherent to the slope, but if instabilities and turbulence were present the streak traces usually developed a wavy structure or dissipated rapidly near the bottom.

The following summarizes the methods used to obtain velocity and bed shear stress data from the streaks.

(1) Photographic negatives which contained a series of one-second positions of the streaks for a particular input wave amplitude and frequency and at each station were enlarged and transferred onto a sheet of tracing paper by using a microfilm reader. A single sheet was produced containing the traces of the successive positions of the dye streak at each station for one-second sampling intervals. Successive displacements of neutrally buoyant particles were recorded simultaneously on the same sheet. Figure 12 is an example of a worksheet that includes the dye streak and particle positions. The numbers represent successive seconds in time relative to t = 1. The streaks and particles were also color-coded; this does not show in Figure 12.

(2) The coordinates of each streak relative to its position at the slope were punched onto IBM cards by a special purpose X-Y digitizer. The streak positions were usually sampled at 0.02 mm increments normal to the bottom in the boundary layer* and at larger increments (0.05 mm to 0.10 mm) above the boundary layer. Each neutrally buoyant particle position was digitized.

(3) Successive displacements of the streaks (or particles) at a particular level above the bottom gave approximately one-second averages of the Lagrangian velocities $u_{j,t}$ at that level;

---

*The thickness of the boundary layer is tentatively defined as the distance of the inflection point in the streak trace to the bottom.
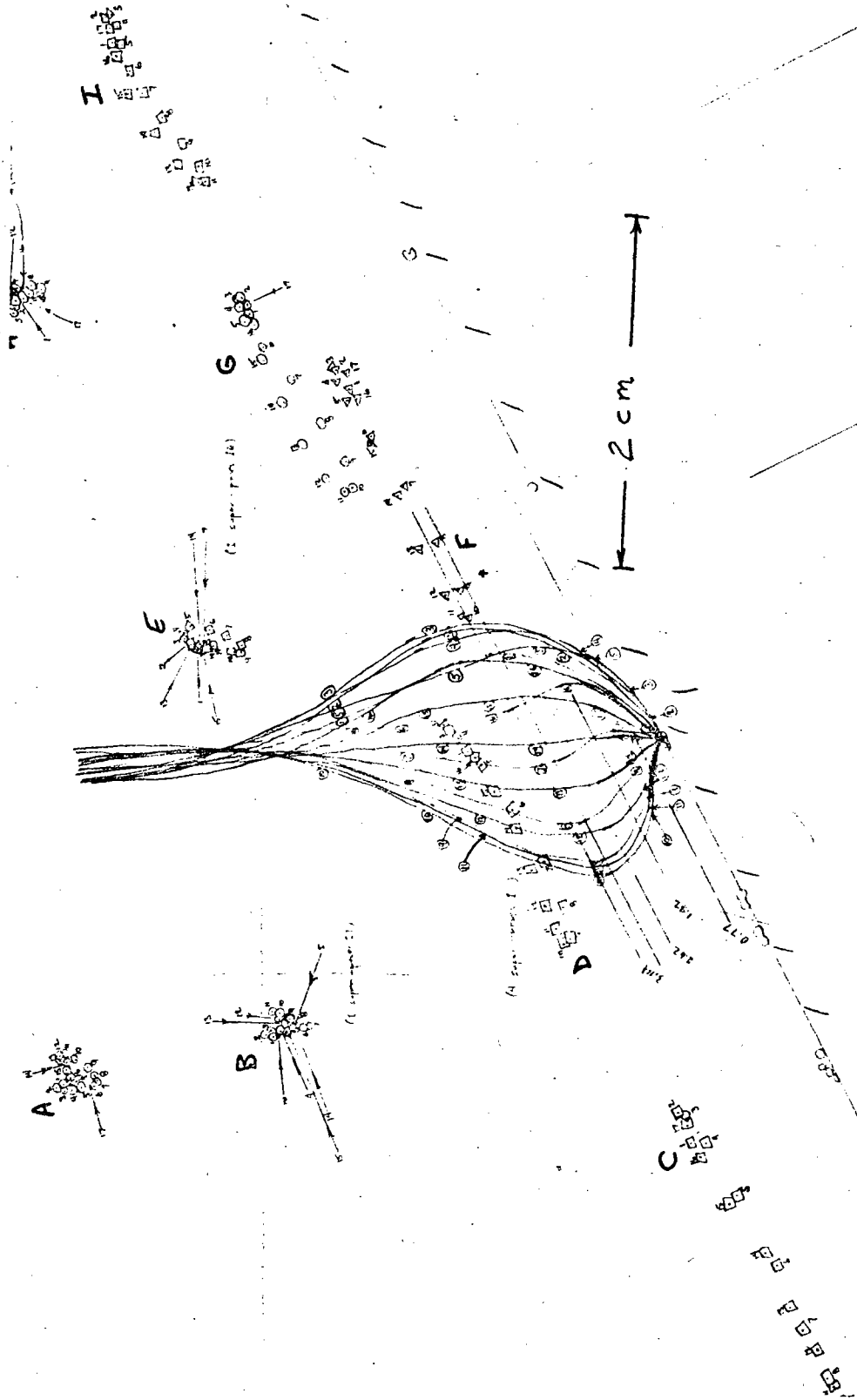
Fig. 12. Sample worksheet with locations of dye streaks and particles plotted at each second during a wave cycle. Time marks (numbers) are relative to t = 1.

$$u_{j,t} = \frac{X_{j,t} - X_{j,t-1}}{\Delta t}$$

$$t = 1, 2, \ldots, T$$

$$j = 1, 2, \ldots, L$$

T is the number of streaks (usually equal to the nearest integer greater than the wave period).

L is the number of vertical levels.

$j = 1$ represents the lowest level for which the data of any particular set are considered reliable.

As stated above, the spacing between the various vertical levels from $j = 1$ was constant in the boundary layer.

(4) Estimates of bottom shear stress (one-second averages) were computed from the velocity values at $j = 1$:

$$\tau_{0,t} = \frac{u_{1,t}}{\Delta \bar{\eta}}$$

$$t = 1, 2, \ldots, T \text{ as before.}$$

$\Delta \bar{\eta}$ is the distance between the bed and the level $j = 1$ measured normal to the bottom.

MISCELLANEOUS

To ascertain that the wave maker was in fact generating primarily the first mode, several photographs of the orbital motion of neutrally buoyant particles over an entire vertical section were taken at various positions along the tank. Figure 13a is a typical section over the flat bottom. The predominantly vertical motion near the center of the water column and the horizontal pattern near the free surface and at the bottom are characteristic of internal wave motion of the first mode. The photograph was taken with Polaroid film that was exposed by flashing a strobe through a thin slit
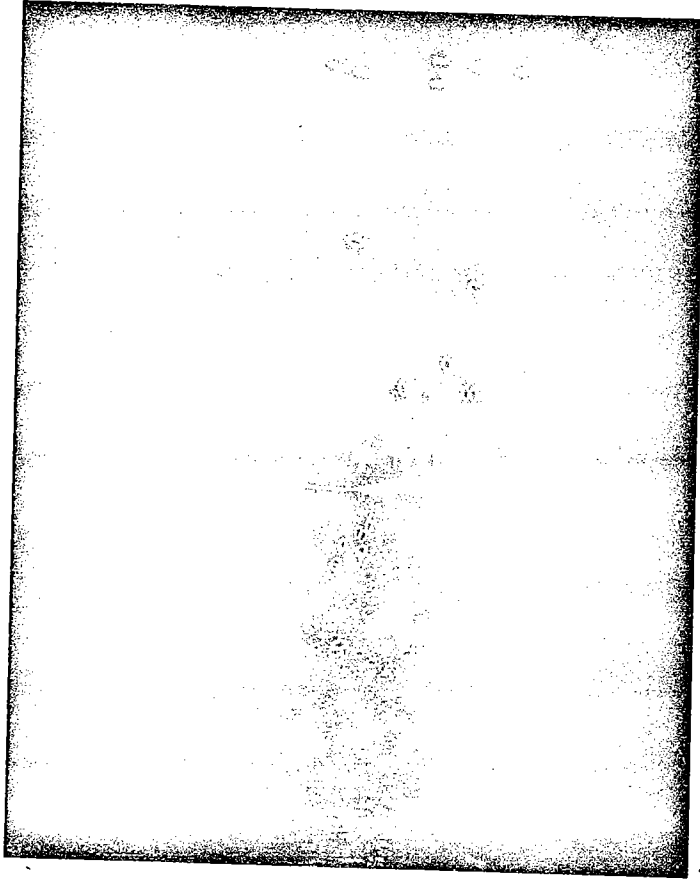
Fig. 13 a. Time sequence of neutrally buoyant
            particle positions over horizontal bottom.
            Modal structure approximately equal to the
            first internal mode (n = 1).
            Pointer depth: 16.0 cm.
            Bright horizontal section on pointer: 1.0 cm.
            Brunt-Vaisala period: 6.5 sec.
            Wave period: 12.0 sec.
            (Strobe: 1 flash/sec; Polaroid 4x5 film,
            ASA 3000)

from above the tank at 2 cps. The illuminating flash was a rectangular beam about 1.5 cm wide and approximately centered between the side walls of the tank. Similar photographs were taken at various positions over the slope. Figure 13b shows a close-up view of successive displacements of neutrally buoyant beads near the bottom of a relatively low slope ($\alpha \simeq 15$ degrees). Note the amplification in the particle displacements nearer the bottom.

Shadowgraph images were used to visualize the boundary layer instabilities and breaking of the high frequency waves. Both of these phenomena are discussed in Chapter 4; several photographs of the shadowgraph images are shown in that chapter.

The net drift patterns of neutrally buoyant particles were determined by two methods:

(1) The positions of selected particles were marked on the glass side walls of the tank over long durations (up to 30 minutes).

(2) The positions of the particles were traced from 16 mm movies of the shadowgraph images that were projected onto a screen of large grid paper. By counting the frames between position marks, the approximate time that had elapsed was estimated and a net velocity computed.
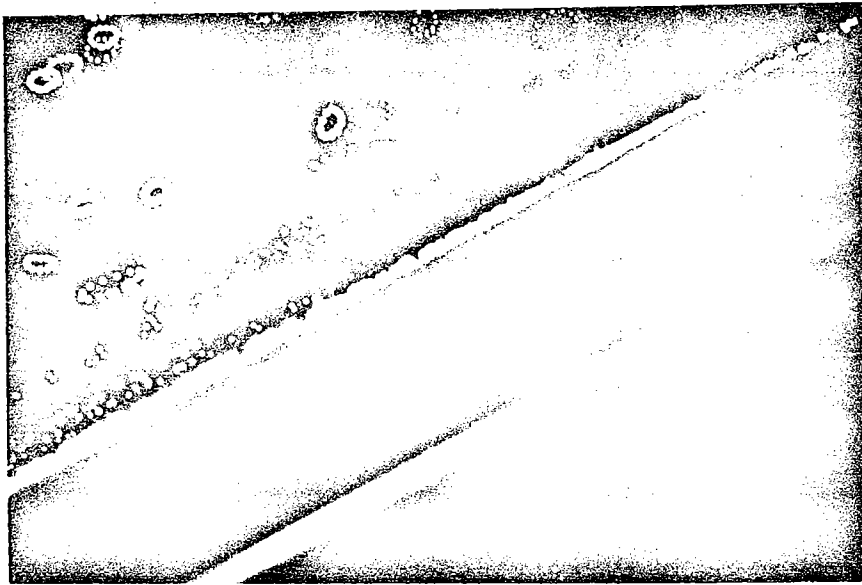
Fig. 13 b. Time sequence of neutrally buoyant
particle positions over slope (=30 deg).
Note intensification of motion near bottom.
Brunt-Vaisala period: 6.0 sec.
Wave period: 9.6 sec.
Input wave amplitude: 0.2 cm.
(Strobe: 1 flash/sec; Tri-x 35mm film.)

4. EXPERIMENTAL RESULTS

GENERAL DISCUSSION

This section describes the organization of the results and presents an overview of the hydrodynamics. Subsequent sections discuss the results in more detail and compare them with the predictions of recent theories. The results are separated into two basic categories: (1) one that describes the interior wave field (wave number and wave amplitude); (2) another that describes the activity at the boundaries (wave breaking and boundary layers).

It is useful to define two distinct hydrodynamic regimes on the basis of the reflection conditions for internal gravity waves from a smooth, rigid slope (Phillips, 1966; Sandstrom, 1966). This subdivision is based on the ratio of bottom slope γ to the slope of the input wave characteristics c. Figure 14 illustrates the classification and shows that regime II can be further subdivided into two cases. Phillips (1966), among others, has shown the slope of the characteristics to be a function only of the stability frequency N and the frequency of the input waves ω, provided that N is constant with depth:

$$c = 1/(N^2/\omega^2-1)^{1/2} \tag{4-1}$$

Since N and γ were essentially constant during each experiment, the ratio γ/c could be altered by changing ω. In this way, both hydrodynamic regimes $\gamma/c<1$ and $\gamma/c\geq1$ were investigated during several experiments.

Tables B1 and B2 in Appendix B summarize the experimental parameters for the various measurements that were made with the conductivity probes. Table B1 is divided into experimental groups that each have a similar Brunt-Vaisala frequency and bottom slope. This table is a reference for Table B2, which lists the various input wave frequencies that were generated during the experiments. The experimental conditions for each frequency can be found by matching the second number in the first column of Table B2 with

Regime	Case	Designation	γ/c	Reflection Properties
I	A	subcritical	$</$	transmissive; all energy propagates into corner
II	B	critical	$=/$	marginally transmissive; energy propagates parallel to bottom slope
	C	supercritical	$>/$	nontransmissive; energy is back-reflected
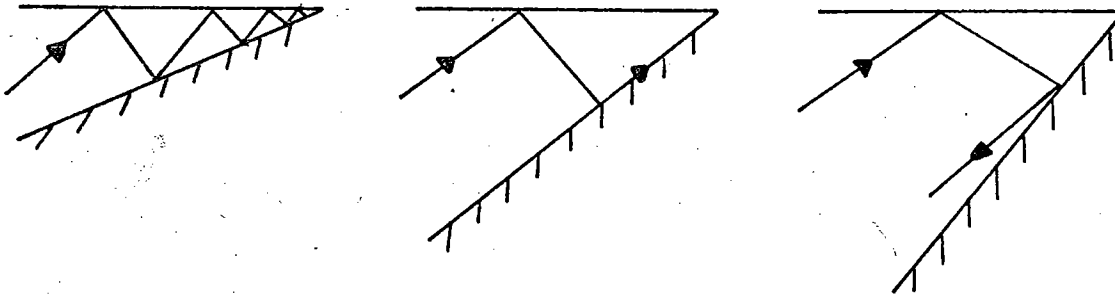
Fig. 14. Classification of internal waved based on reflection
from a smooth, rigid slope. Slope of wave charac-
teristics = c; bottom slope = γ.

the number of the experimental group in Table B1. Those frequencies
which belong to hydrodynamic regime II are identified by a dash in column 7.
An asterisk is located above those frequencies for which more than one ex-
perimental run were made.

The emphasis on two hydrodynamic regimes is supported by the re-
sults. The subcritical case was examined extensively, since the results for
this case are pertinent to the later analysis of sediment motion and since
this case is important for certain oceanic conditions (Chapter 5). The
data for this case suggest a further classification into two wave types
based on the frequency of the input waves. This distinction is more justified
for the measurements that were taken over the low slope angle (15 degrees)
than those measurements taken over steeper slopes. The experimental re-
sults indicate that the high-frequency input waves decrease in wave length
and increase in wave amplitude as they propagate upslope until at some lo-
cation near the corner and below the free surface they dissipate by breaking.
The low-frequency waves in this case $(\gamma < c)$ initially steepen like the high-
frequency waves, but the effects are less pronounced. The steepening
diminishes upslope as these waves form an internal surge that produces a
large runup with little breaking. The water motion near the bottom is am-
plified for both wave types. The bottom shear stress is increased over the
slope and is greatest in and near the zones of breaking and runup. In addi-
tion, there is considerable vertical motion near the bottom in the breakers.

The experimental results for case B and case C $(\gamma/c \geq 1)$ indicate
that the interior wave motion is very complicated. The conductivity-probe
measurements show that during most experimental runs the wave amplitude
over the slope was a maximum at or near a depth $z = -cx$. (The geometry
is defined in Figure 15.) In the critical case, a line of small, regularly
spaced vortices forms along the slope. The vortices have diameters on the
order of 1 cm and axes that are normal to the side walls of the tank. They
oscillate along the slope with the wave motion, collapsing and reforming
over a half-cycle. The distance from the vortex core to the slope is about
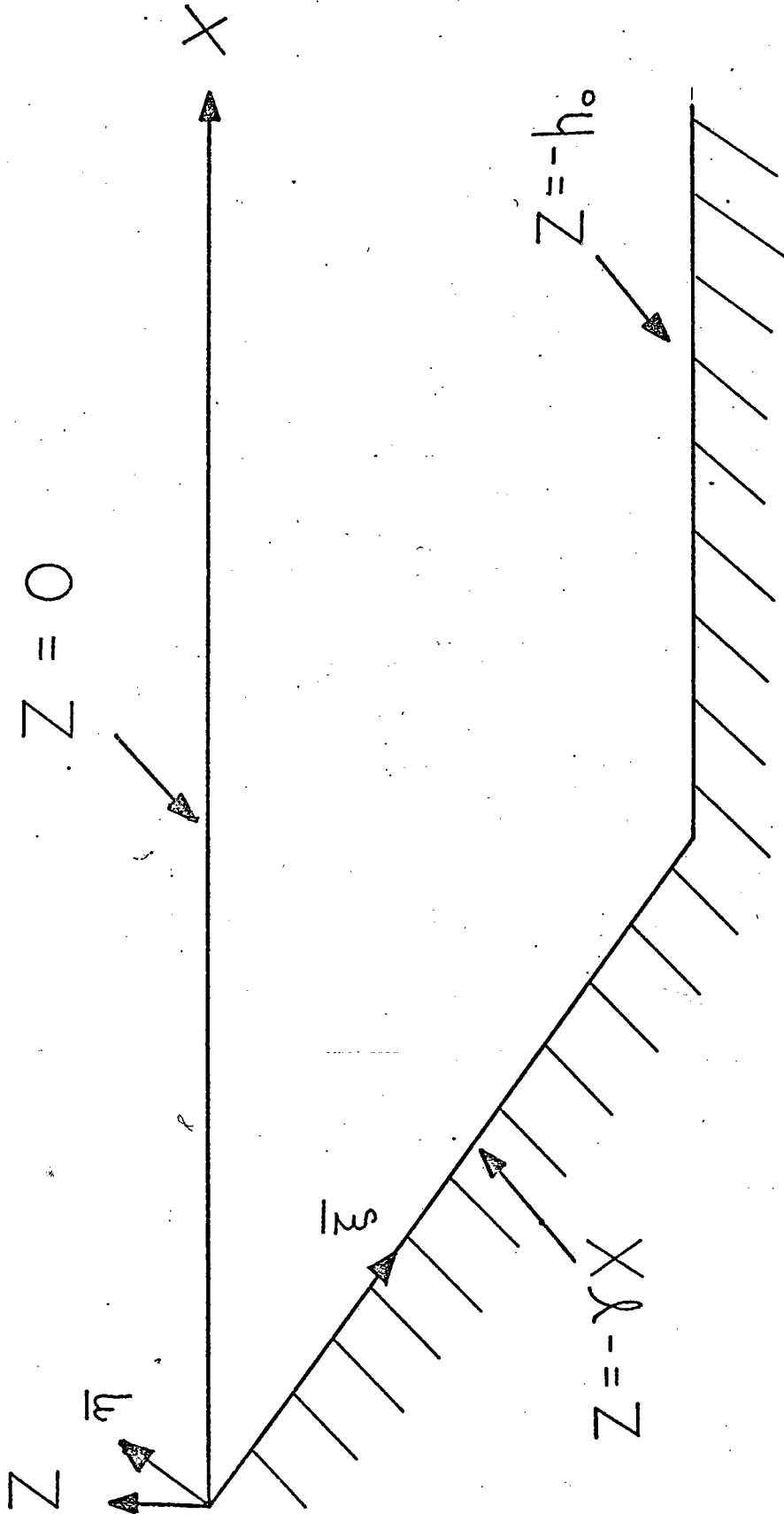
Fig. 15. Geometry and coordinate system.

7 to 10 mm. Several wave cycles after the formation of the line of vortices, thin horizontal layers appear in the fluid. Each layer is associated with a vortex near the slope and represents a modification to the density structure over the slope. Wave breaking near the corner accompanies the vortex activity. These features are discussed in more detail later in the chapter.

THEORETICAL DISCUSSION

The experimental results presented in this chapter are compared to the theoretical solutions of Wunsch (1969). Preliminary measurements indicated that the exact linear solutions for the interior wave field fitted the experimental data. The experimental conditions and the assumptions implicit in the theory were compatible except for the boundaries. Wunsch (1969) solved the problem for a wedge geometry bounded above by a rigid horizontal top and below by a rigid bottom slope that extends indefinitely far from the corner (the term corner refers to $x = z = 0$ in Figure 15). The rigid bottom slope used in the experiments terminated a finite distance from the corner at the transition to a horizontal bottom. The possible effects of this discrepancy between theoretical model and experimental conditions are mentioned in the discussion of results for cases B and C and in the boundary layer section for case A. Although a free surface was permitted in the experiments, the observed vertical motions of this surface were small. In the sense that $w \approx 0$ at $z = 0$, the use of a free surface was compatible with the rigid top in the theoretical model.

For a viscous Boussinesq fluid of mean density $\rho_0(z)$ the two-dimensional perturbation equations (after Wunsch, 1969) are:

$$u_t = -p_x/\rho_0 + \nu\nabla^2 u \qquad (4\text{-}2)$$

$$w_t = -p_z/\rho_0 - g\rho'/\rho_0 + \nu\nabla^2 w \qquad (4\text{-}3)$$

$$u_x + w_z = 0 \qquad (4\text{-}4)$$

$$\rho'_{\underline{t}} + w\rho_{o_{\underline{z}}} = 0 \qquad (4\text{-}5)$$

where ρ' is the perturbation density, and a bar denotes partial differentiation.

Interior Wave Field

The interior equations are given by the inviscid forms of Equations (4-2) through (4-5) above. The pertinent linear solution (Wunsch, 1969) for small-amplitude internal waves of frequency ω traveling toward the corner is composed of two progressive waves:

$$\psi = A\left[e^{-iq\ln(cx - z)} - e^{-iq\ln(cx + z)}\right]e^{-i\omega t} \qquad (4\text{-}6)$$

$$q = \frac{2n\pi}{\ln\Delta} \quad , \quad \Delta = \frac{c + \gamma}{c - \gamma} \qquad (4\text{-}7)$$

where n is the mode number. This solution is singular at $x = z = 0$ for case A $(\gamma < c)$. The phases of the two waves in Equation (4-6) are arithmetically averaged to give an average phase function U:

$$U = q/2\left[\ln(cx - z) + \ln(cx + z)\right] \qquad (4\text{-}8)$$

It follows that an average local horizontal wave number is defined by k_w:

$$k_w = \partial U/\partial x = q\left(\frac{c^2 x}{c^2 x^2 - z^2}\right) \qquad (4\text{-}9)$$

The corresponding wave number k_m that was determined from the conductivity probe measurements is $\Delta\theta_m/\Delta x$ (Chapter 3).

For a time dependence of $e^{-i\omega t}$, the incompressibility condition condition, (Equation (4-5)) yields:

$$\rho = -i/\omega \; \partial\rho_o/\partial z \; w \qquad (4\text{-}10)$$

(the prime on ρ has been dropped for convenience).

The vertical velocity w is obtained from the stream function in Equation (4-6), $w = \partial\psi/\partial x$:

$$w = Aiqc\left[-\frac{1}{M}e^{-iq\ell nM} + \frac{1}{N}e^{-iq\ell nN}\right]e^{-i\omega t} \tag{4-11}$$

$$M = cx - z \quad , \quad N = cx + z$$

Applying Equation (4-11) into Equation (4-10) and taking the time average of the product of ρ and its complex conjugate $\rho*$, we obtain an expression for the square of the amplitude variation with coordinate position:

$$\rho_w^2 = \frac{1}{2}\overline{\rho\rho*} = \frac{1}{2}A^2\left(\frac{qc}{\omega}\right)^2 (\partial\rho_0/\partial z)^2$$

$$\times \left[\frac{1}{M^2} + \frac{1}{N^2} - \frac{2}{NM}\cos\left\{q\ell n(\frac{N}{M})\right\}\right] \tag{4-12}$$

The comparative experimental value is the square of the spectral amplitude, a_m^2, as determined from the periodogram of the conductivity-probe measurements. The method of comparison between a_m^2 and ρ_w^2 was discussed in Chapter 3.

It is useful to point out here that for $\gamma << c$, Wunsch's solutions are the asymptotic solutions for internal waves propagating over a small slope (also given by Keller and Mow, 1969). The dependence on local depth h for local values of horizontal wave number k_x and amplitude a is

$$k_x = \frac{n\pi c}{h} \quad , \quad a = \frac{a_0 h_0}{h} \tag{4-13}$$

where the subscript "o" signifies "deep" water values (i.e., constant values of wave amplitude a_0 and depth h_0). Hogg and Wunsch (1970) have shown that the nonlinear terms are significant when ϵ becomes order one,

$$\epsilon = ak_x = \frac{a_0 h_0}{h}cn\pi \tag{4-14}$$

That is, the amplitudes of the next higher order term in the velocity expansion grows as ϵ^2. This suggests that the linear solutions are no longer

valid over the small slope at some depth h given by ϵ of order one in Equation (4-14).

For the case $\gamma > c$, Wunsch (1969) showed that the apparent singularity at $z = -cx$ in Equation (4-6) could be removed. Wunsch rewrote q in the form*

$$q = r + is \qquad (4-15)$$

and showed that the expression for the stream function for waves propagating upslope could be rewritten

$$\psi = A \left[e^{(s - ir)\ell nM} - e^{(s - ir)\ell nN} \right] e^{-i\omega t} \qquad (4-16)$$

where

$$r = \frac{2n\pi \ell n |\Delta'|}{[(\ell n |\Delta'|)^2 + \pi^2]}$$

$$s = \frac{-2n\pi}{[(\ell n |\Delta|)^2 + \pi^2]}$$

$$\Delta' = \frac{c - \gamma}{c + \gamma} = 1/\Delta$$

and n is a negative integer. (Note that ℓnN is complex for $cx + z \leq 0$.)

---

*The notation here does not conform to that of Wunsch (1969) in order to avoid later confusion. He wrote the complex form of q as $q = \eta + i\delta$, and gave an analogous expression for Equation (4-16) in which the real part of the exponential group was written in a power of s(i.e., δ in his notation).

In order to have the velocities and their first derivatives continuous, Wunsch derived the requirement that $s > 2$ or

$$-n > \frac{(\ell n |\Delta'|)^2}{\pi^2} + 1 \tag{4-17}$$

$-n$ represents the lowest, nonsingular inviscid mode permissible for these solutions. The vertical velocity is obtained from Equation (4-16):

$$w = Ac(s - ir) \left[\frac{1}{M} e^{(s - ir)\ell nM} - \frac{1}{N} e^{(s - ir)\ell nN} \right] e^{-i\omega t} \tag{4-18}$$

An expression for ρ_w^2 analogous with that in Equation (4-12) can be obtained in principle from Equation (4-10) and Equation (4-18) and compared to the measured amplitude a_m^2 for specific coordinate positions by the method described in Chapter 3. However, it is not simple in this case to obtain a physically meaningful phase function that is analogous to Equation (4-8) owing to the complicated wave forms in Equation (4-18). The amplitude dependence on the spatial coordinates indicates that these are not simple plane waves. By writing

$$w = f(x, z) e^{ig(x, z, t)} \tag{4-19}$$

where f and g are complex, a phase function U can be defined as

$$U = \tan^{-1} \frac{I(w)}{R(w)} \tag{4-20}$$

where $I(w)$ and $R(w)$ are the imaginary and real parts of w, respectively. This form of U will be used in the later discussion of theoretical and experimental results for cases B and C.

Boundary Layer

The full set of perturbation Equations (4-2) through (4-5) were used by Wunsch (1969) to obtain linear boundary-layer solutions for case A

$(\gamma < c)$. The solutions match those for the inviscid interior just outside the boundary layer. The stream function can be written:

$$\psi_T = \psi_I + \psi_{b.\ell.} \tag{4-21}$$

where ψ_I and $\psi_{b.\ell.}$ are the interior and boundary layer contributions, respectively. In terms of the coordinates $\bar{\xi}$, $\bar{\eta}$ shown in Figure 15, the expression for $\psi_{b.\ell.}$ given by Wunsch (1969) can be rewritten

$$\psi_{b.\ell.} = \frac{Aq}{\bar{\xi}} P \left[F\, e^{-iq\,\ell n(B\bar{\xi})} - G\, e^{-iq\,\ell n(D\bar{\xi})} \right]$$
$$\times e^{-(i+1)\,\bar{\eta}/\delta}\, e^{-i\omega t} \tag{4-22}$$

where

$$P = \frac{1}{i-1} \left(\frac{2\omega\nu}{\omega^2 - N^2 \sin^2\alpha} \right)^{1/2}$$

$$\delta = (i-1)\,P$$

$$B = c\cos\alpha + \sin\alpha, \qquad\qquad D = c\cos\alpha - \sin\alpha$$

$$F = \frac{c\sin\alpha - \cos\alpha}{B}, \qquad\qquad G = \frac{c\sin\alpha + \cos\alpha}{D}$$

The component of velocity parallel to the slope (in the $\bar{\xi}$ direction) is given by

$$u_T = u_I + u_{b.\ell.} = -\partial\psi_T/\partial\bar{\eta} \tag{4-23}$$

or from Equation (4-6), after it has been expressed in $\bar{\xi}$, $\bar{\eta}$ coordinates, and Equation (4-22),

$$u_T = V(\bar{\xi}) \left| 1 - e^{-(i+1)\,\bar{\eta}/\delta} \right| e^{-i\omega t}$$

(4-24)

$$V(\bar{\xi}) = \frac{iAq}{\bar{\xi}} \left| F\,e^{-iq\,\ell n(B\bar{\xi})} - G\,e^{-iq\,\ell n(D\bar{\xi})} \right|$$

The behavior of the velocity component u_T parallel to the bottom with variations in $\bar{\xi}$ and $\bar{\eta}$ is obvious: (1) u_T grows to infinitely large values as $\bar{\xi} \to 0$; in fact, at $\bar{\eta} = \bar{\xi} = 0$, the solution is singular, as might be expected since the interior solution is singular at the origin for $\gamma < c$; (2) for $\bar{\eta} = 0$, $\bar{\xi} \neq 0$, the solution reduces to that of the interior field; and (3) as $\bar{\eta} \to +\infty$, the boundary-layer part ($u_{b.\ell.}$) becomes infinitesimally small and $u_T \to u_i$. The solutions for w_T can be derived in principle from $w_T = \partial\psi/\partial\bar{\xi}$, but are not presented here since the measured values of w_T were very small in the boundary layer (this is discussed later in this chapter).

For cases B and C ($\gamma \geq c$), Wunsch (1969) found that the boundary-layer equation for $\psi_{b.\ell.}$ was nonseparable in the spatial coordinates. In fact, Wunsch showed that when the slope is near critical the scale of the boundary-layer thickness is proportional to $R^{-1/3}$, in contrast to $R^{-1/2}$ for $\gamma < c$, where R is a local wedge Reynolds number and h is the local depth:

$$R = Nh^2/\nu$$

INTERIOR WAVE FIELD — RESULTS

Subcritical Case

Table B3 (Appendix B) summarizes the periodogram amplitudes and wave numbers that were determined from the conductivity-probe measurements as described in Chapter 3. The notation in the column headings is discussed in the following sections. The experimentally determined values are organized into columns by input wave amplitude.

Wave number. As was described in Chapter 3, an experimental wave number k_m was computed from the measured phase differences between adjacent probes ($k_m = \Delta\theta_m/\Delta x$). Columns 9, 10, and 11 of Table A3 contain the appropriate values of k_m divided by q, i.e., $\frac{1}{q} \Delta\theta_m/\Delta x$ (q is defined in Equation (4-7)). This parameter is convenient since $\frac{1}{q} k_m$ corresponds to the theoretical value $\frac{1}{q} k_w$ given by Equation (4-9):

$$\frac{1}{q} k_w = \frac{1}{q} \frac{\partial U}{\partial x} = \frac{x}{x^2 - (z/c)^2} \qquad (4-25)$$

The right-hand side of this equation is evaluated for the appropriate values of c, and the average is computed for the two probe positions. The value listed in column 7 is

$$\frac{1}{q} k_{w_{1,2}} = \frac{1}{2} \left[\frac{x}{x^2 - (z/c)^2} \right]_{1,2} \qquad (4-26)$$

in which the subscripts 1 and 2 indicate that the function is evaluated at the coordinate positions for each probe and then the average is taken.

The theoretical curves in Figures 16 and 17 are straight lines with slope of 1. The data in Figure 16 are taken from the values for relatively high-frequency waves in Table B3. The upper right portion of the diagram corresponds to the corner region of the slope. Figure 17 is a similar plot for the data of the low-frequency waves. Both plots show that the wave number decreases with increasing distance from the corner.[*] The agreement of the results with the theoretical curve is best for waves over the lower section of the slope, well away from the corner. Toward the corner,

---

[*]The behavior of the abscissa, $\dfrac{x}{x^2 - (z/c)^2}$, is approximately like $1/x$ for constant z. (This is obviously true for $x \gg z/c$.)

$$\frac{1}{q} \cdot \frac{\Delta \Theta m}{\Delta X}$$

$\cdot 10^2$

High Frequency Waves	
EXP group	$a_0 = 0.2$ cm
1	⊙
2	⊡
3	△
5	⊙

$$\frac{X}{X^2 - \left[\frac{Z}{C}\right]^2} \cdot 10^2$$
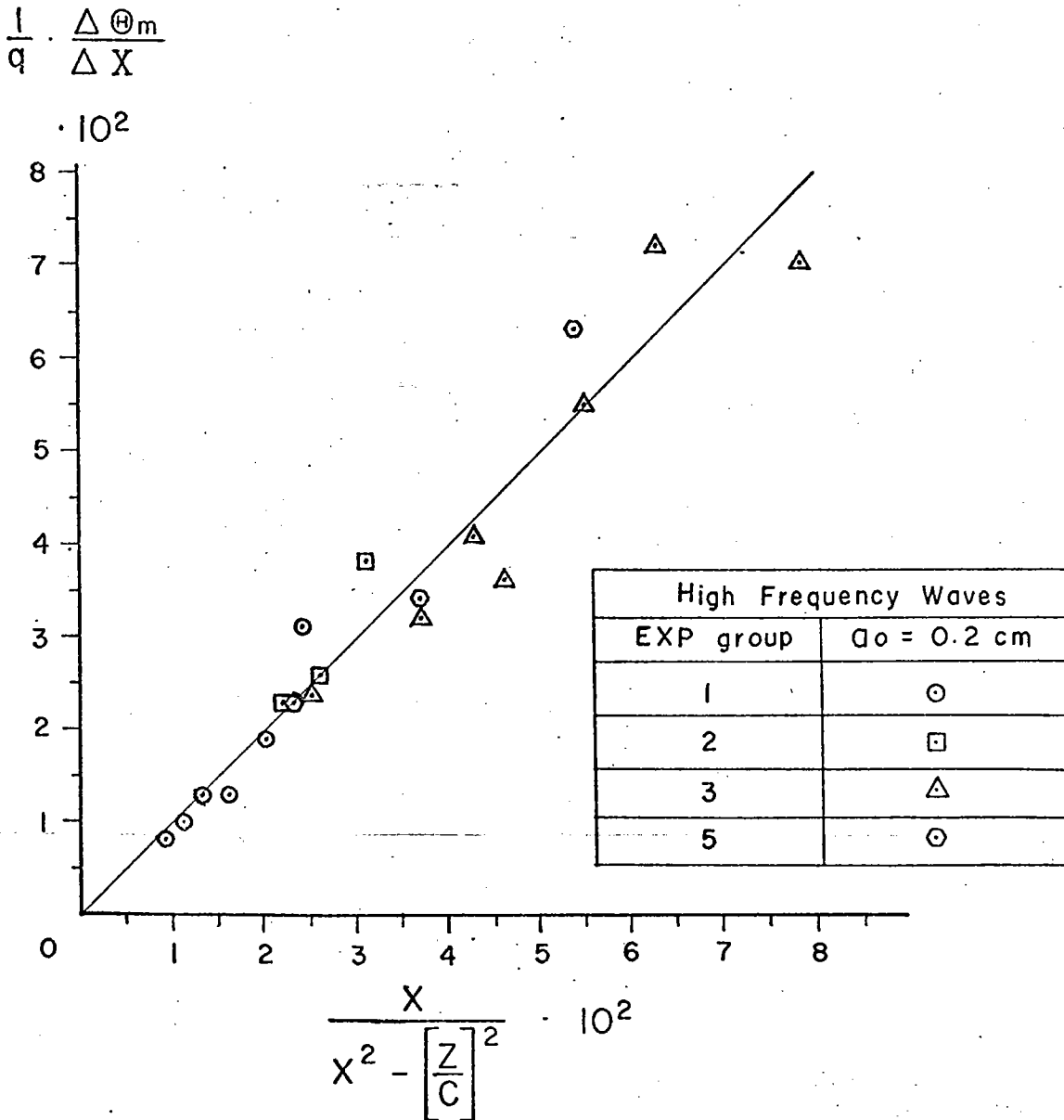
Fig. 16.

Upslope variation of wave number, $\gamma < c$

$$\frac{1}{q} \cdot \frac{\Delta \Theta_m}{\Delta X}$$

-10^2

Low	Frequency	Waves
EXP group	$a_o = 0.2$ cm	
1	⊙	
2	⊡	
5	⊙	
6	◇	

$$\frac{X}{X^2 - \left[\frac{Z}{C}\right]^2} \cdot 10^2$$
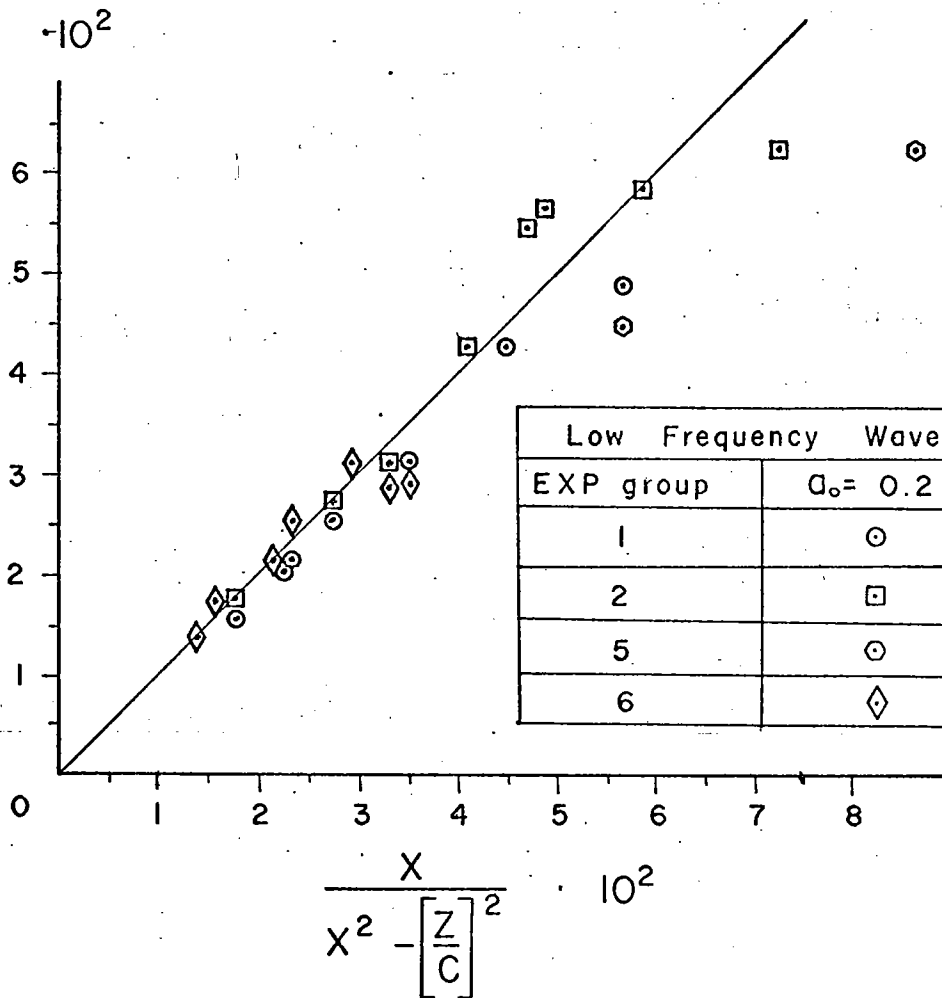
Fig. 17.

Upslope variation of wave number, $\gamma < c$.

the data points in Figure 16 depart significantly from the theoretical curve. It is also evident that the value farthest to the right for each experimental group in Figure 16 is displaced toward higher wave number than that predicted by theory. This trend is illustrated in Figure 18, which includes data for the high-frequency waves ($\omega = 0.094$ cps) in Group 1 (Table B3). The upslope increase in wave number is similar for both input waves ($a_o = 0.2$ cm and $a_o = 0.1$ cm). However, the greater increase in wave number for the larger waves ($a_o = 0.2$ cm) at the most cornerward position (i.e., closer to $x = 0$) suggests that the upslope variation in wave number might depend on amplitude. The experimentally determined value of ϵ at this most cornerward position is approximately 0.15; this might indicate that nonlinear effects are beginning to have a significant effect on the motion.

In Figure 17 there is good agreement between theory and measurement for the low-frequency waves, although most of the data values tend to be lower than the theoretical curve in the right-hand side of the diagram (near the corner). This suggests that the wave length of these lower frequency waves decreases more slowly with decreasing distance to the corner than theory predicts.

Another type of comparison between theoretical and experimental values of wave number is shown in Figures 19 through 21. The data are taken from columns 12 through 14 in Table B3 (Appendix B). Experimental wave numbers k_m and k_o were determined for each input wave from probe measurements taken over the slope and over the flat bottom, respectively. The ratio k_m/k_o is the ordinate in Figures 19 through 21 ($k_m = \Delta\theta_m/\Delta x$). A comparative theoretical ratio is used as the abscissa in these figures; i.e., k_w/k_{w_o} where k_w is the theoretical wave number computed from Equation (4-9) for coordinates established by the probe locations over the slope, and k_{w_o} is similarly computed for coordinates at the entrance to the slope region ($k_w = \Delta\theta_w/\Delta x$). (The depth z used in the computation of k_{w_o} is equal to the probe depth during the determination of k_m and k_o.)
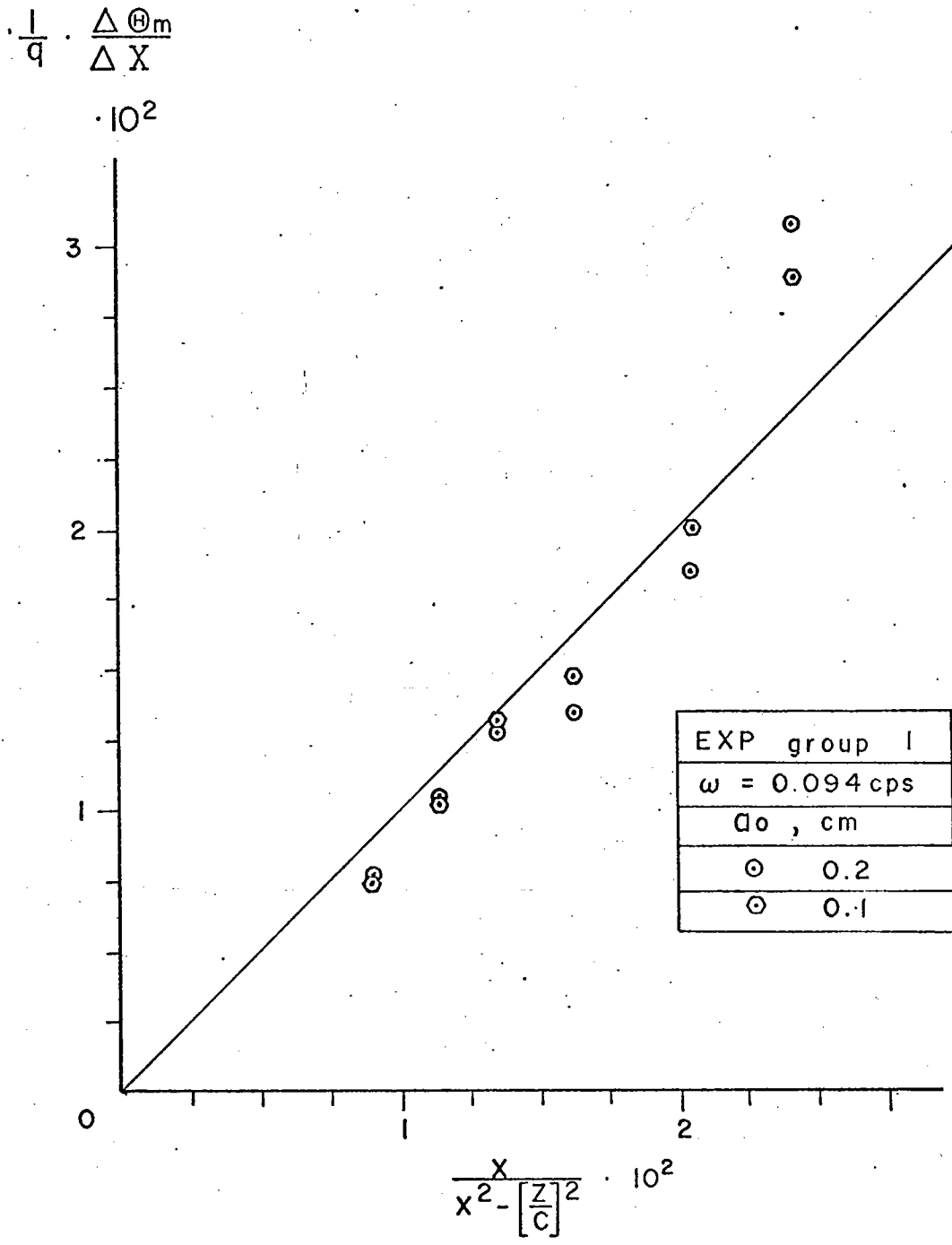
Fig. 18.

Upslope variation of wave number, $\gamma < c$.
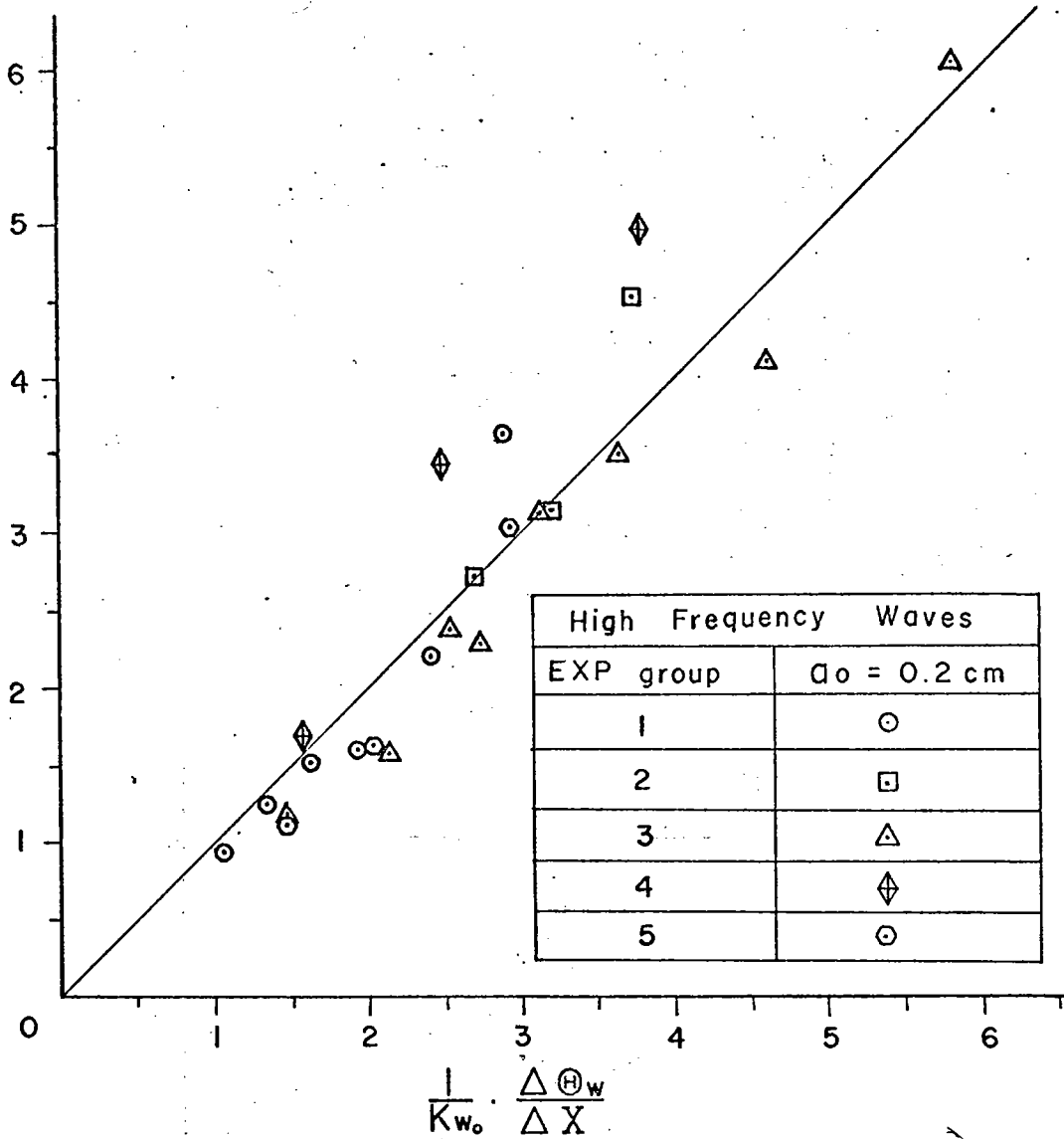
Fig. 19.

Measured versus computed values of wave number, $\gamma < c$.

Fig. 20.

Measured versus computed values of wave number, $\gamma < c$.

$$\frac{1}{K_o} \cdot \frac{\Delta \Theta_m}{\Delta X}$$

EXP group	1	
$\omega = 0.094\,cps$		
a_o , cm		
⊙	0.4	
⊙	0.2	

$$\frac{1}{K_{w_o}} \cdot \frac{\Delta \Theta_w}{\Delta X}$$
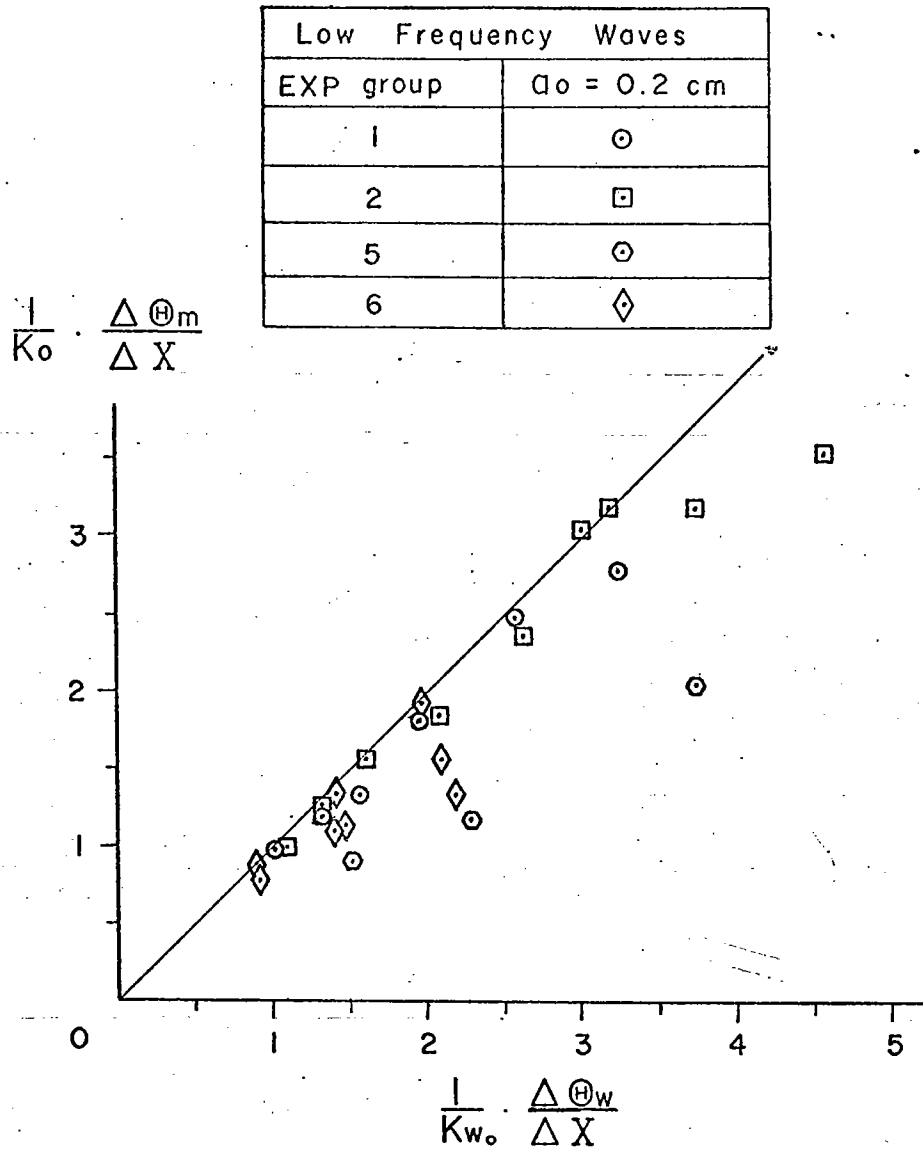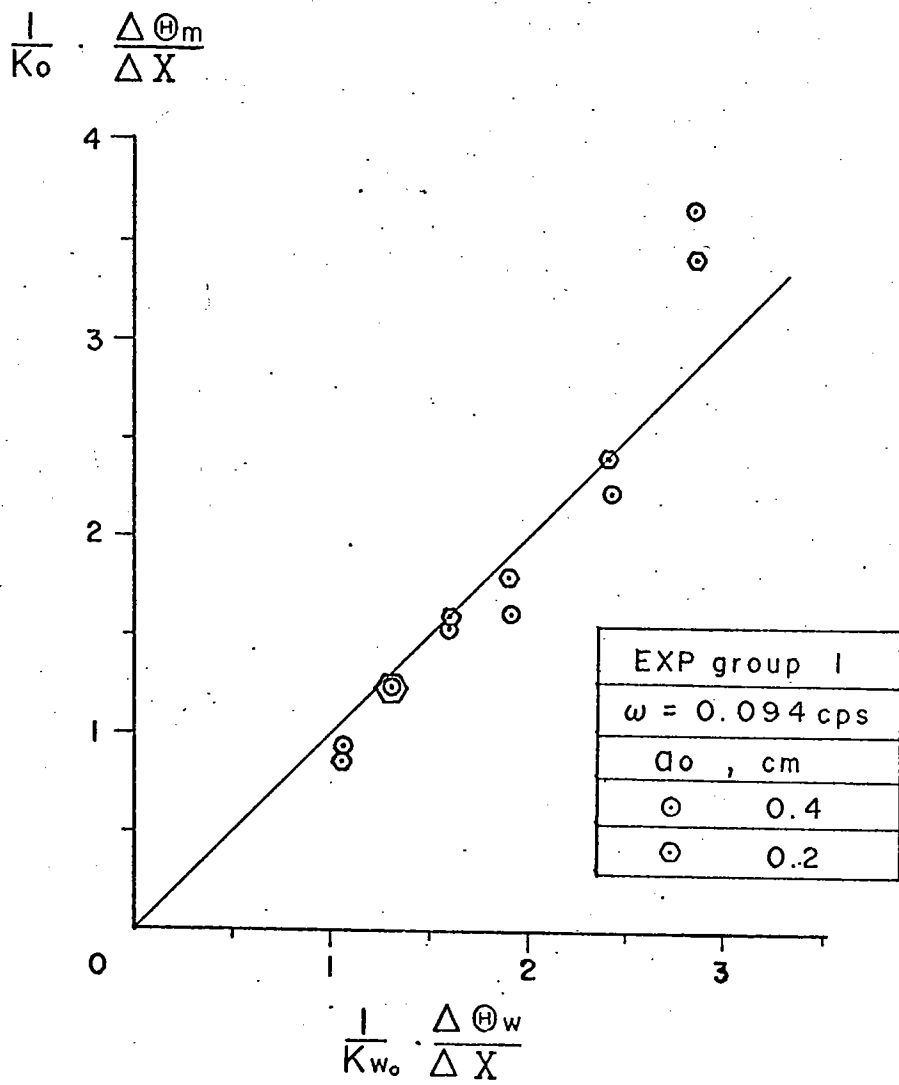
Fig. 21.

Measured versus computed values of wave number, $\gamma < c$.

Figure 19 and 20 also show better agreement between experiment and theory for the smaller wave numbers over the lower slope sections. Farther upslope the data for the higher frequency waves in Figure 19 tend toward larger values of wave number relative to the theoretical values; by contrast, the lower frequency waves in Figure 20 generally tend toward smaller wave number. The effect of input wave amplitude on wave number is indicated in Figures 21 and 22, for high and low frequency waves, respectively. The values for the larger amplitude waves in Figure 21 appear to deviate from theory more significantly than the smaller waves. Significant departures from theoretical estimates are also shown for the larger input waves of low frequency (Figure 22). In this case, however, the measured wave numbers are smaller than the predicted values at locations farthest to the right in Figure 22. This behavior corresponds to the previous observations (Figure 17) that the wave lengths of the lower frequency waves apparently decrease less than theory predicts at positions well upslope.

Wave amplitude. The results of the conductivity-probe measurements for case A, concerning the effects of shoaling on wave amplitude, are summarized in Table B4 (Appendix B). The experimental group numbers correspond to those in Table B1. Experimental determinations of the periodogram amplitudes a_m^2 and a_o^2 for each input wave were made from probe measurements over the slope and over the flat bottom, respectively (for more detail see Chapter 3). The value a_o^2 was determined for each of the four probes so that each ratio a_m^2/a_o^2 represented data taken with a particular probe. This procedure was convenient since it removed the necessity of introducing calibration constants relating one probe to another. That is, the measured amplitude ratios could be compared to one another without applying relative gain factors. This method of normalization also simplified the detection of measured changes in wave amplitude relative to the input wave amplitude a_o. The comparative theoretical values ρ_w^2 and ρ_o^2 were computed from Equation (4-12) for coordinates of the probe locations over the slope and at the entrance to the slope region, respectively.
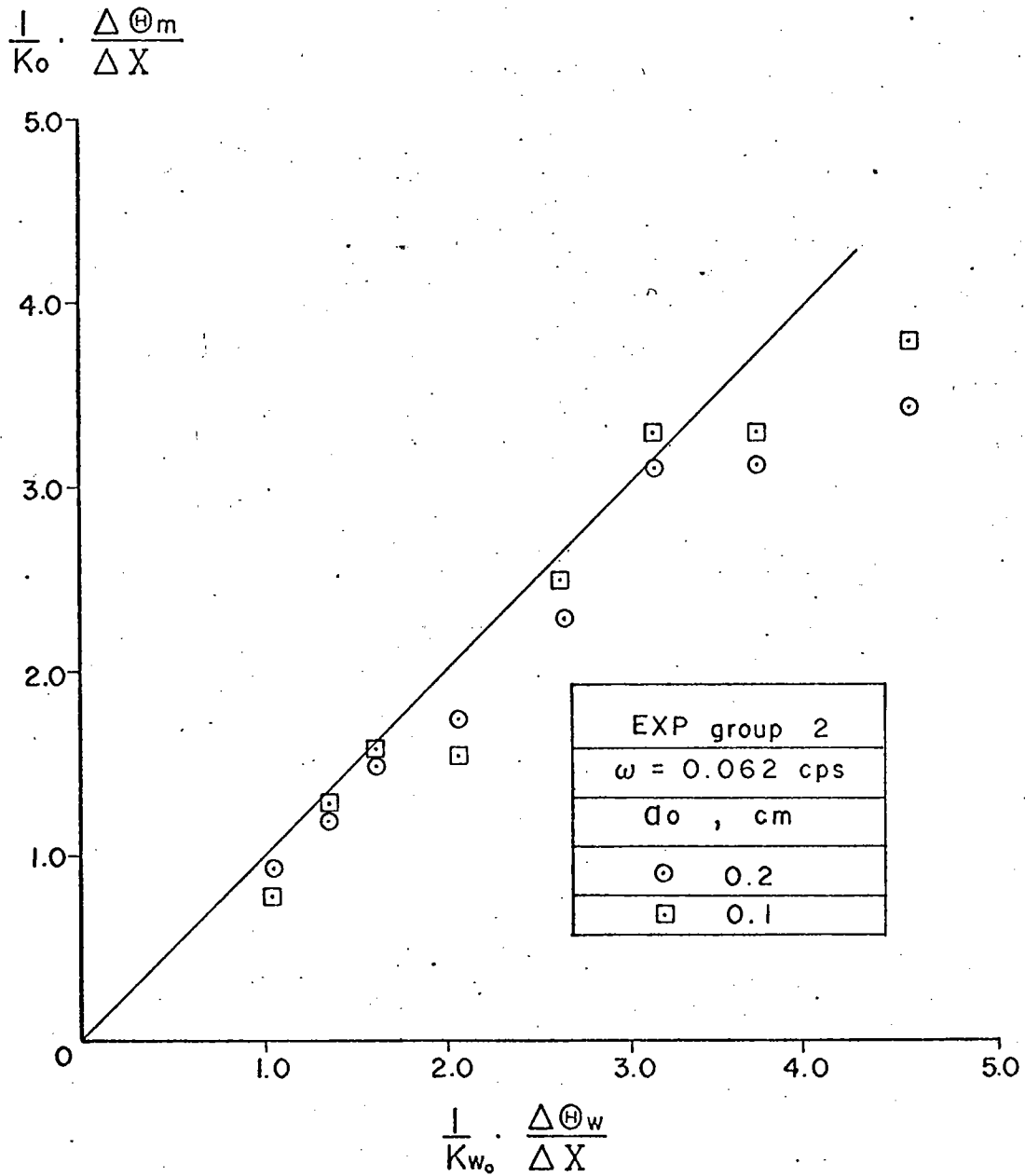
Fig. 22.

Measured versus computed values of wave number, $\gamma < c$.

The ratio $\rho_w{}^2/\rho_o{}^2$ was equally convenient, since its use circumvented a conversion from density ρ_w to the units of a_m and permitted direct comparison with the experimental ratio a_m^2/a_o^2.

The results shown in Figures 23 and 24, for the high-frequency and low-frequency waves, respectively, suggest that the agreement between theory and experiment is best for the lower values of $(a_m/a_o)^2$, i.e., for the wave motion on the lower and middle sections of the slope. This is in agreement with the results for wave number. The solid lines in these figures were drawn for reference and represent points where measurement and theory coincide. The deviations of the points from the straight line in Figure 23 are significant for $(\rho_w/\rho_o)^2 > 20$, but no consistent pattern is apparent in the variations. The values for lower frequency waves show earlier departures from theoretical values than do the higher frequency waves. For example, the measured and theoretical values shown for low-frequency waves in Figure 24 are significantly different for $(\rho_w/\rho_o)^2 > 10$. There is strong indication in the trend of the points that the actual amplitudes are much lower than predicted on the middle and upper sections of the slope. At these slope sections it was also found that the measured values of steepness $a_m k_m$ (or ϵ_m) are considerably less than those estimated from theory.

Measured amplitude growth is further compared with theoretical estimates in Figures 25 through 30. In these figures the variation of wave amplitude is examined as a function of horizontal distance x_c to the corner at various fixed depths z_c. The data are again taken from Table B4 (Appendix B).[*] In each of these figures the theoretical and experimental ratios of

---

[*]The actual wave amplitude in centimeters at a point along the slope can easily be found from the graphs. If the correct wave amplitude (in centimeters) for the flat bottom region is multiplied by the square root of the measured value $((a_m/a_o)^2)$, the measured estimate of the actual amplitude is obtained.
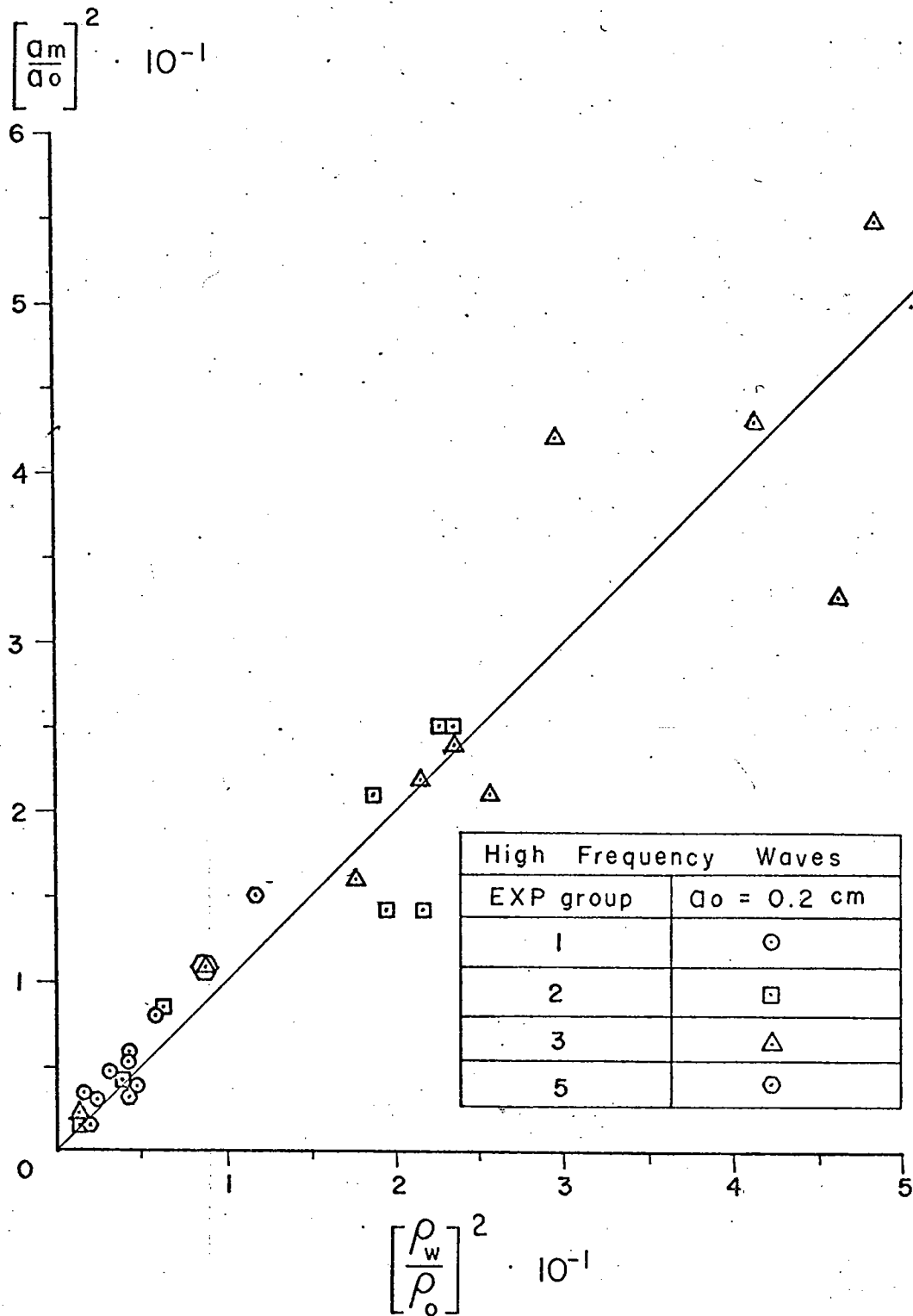
Fig. 23.

Measured versus computed values of wave
amplitude, $\gamma < c$.

Fig. 24.

Measured versus computed values
of wave amplitude, $\gamma < c$.

$$\left[\frac{\rho_w}{\rho_o}\right]^2 \text{ or } \left[\frac{a_m}{a_o}\right]^2$$

EXP group 1		
ω = 0.094 cps		
⊙	a_o= 0.2 cm	
▣	ρ_ω	

$$\frac{X_c}{X_o} \cdot 10^1$$
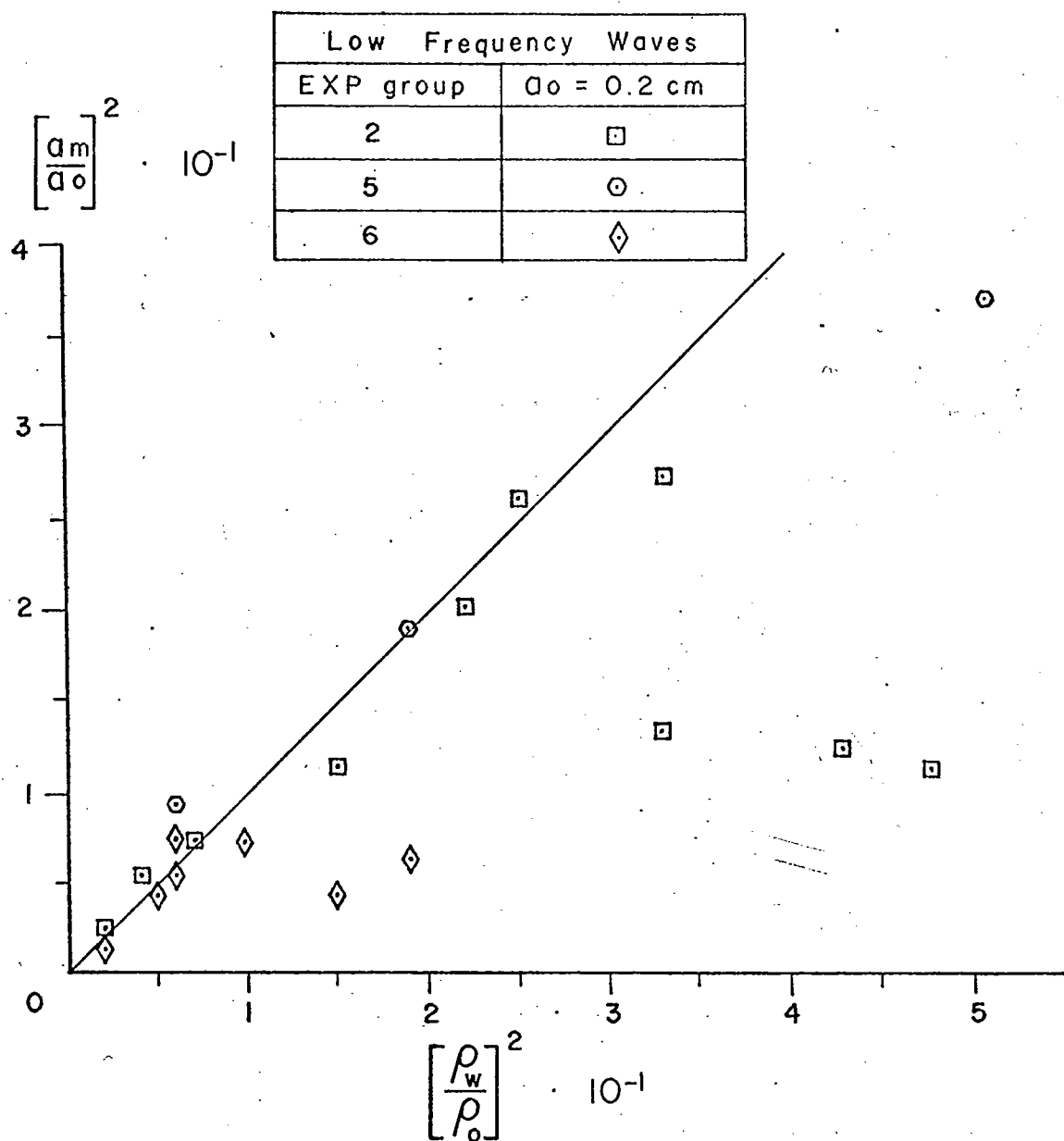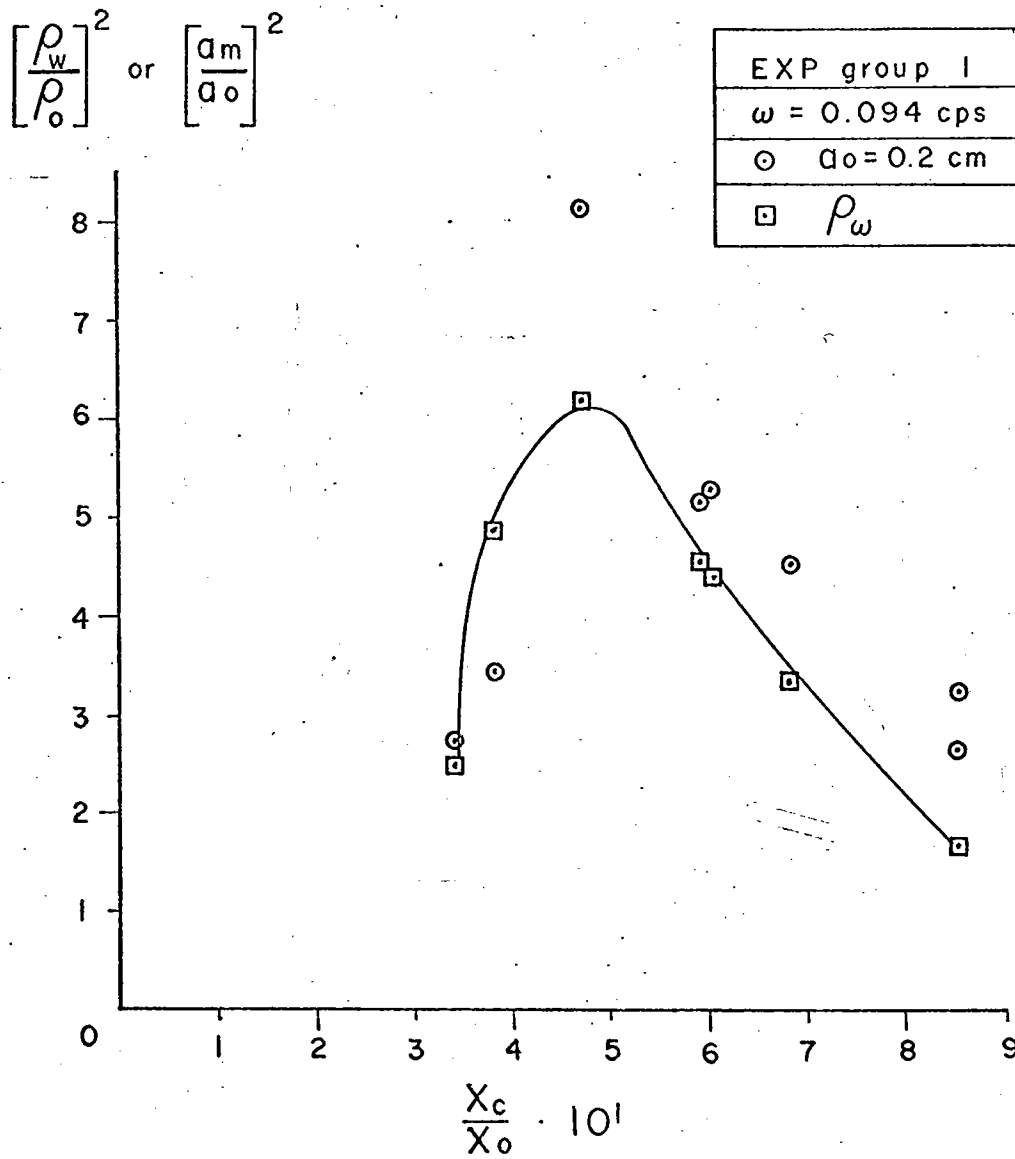
Fig. 25.

Upslope variation of wave amplitude, $\gamma < c$.
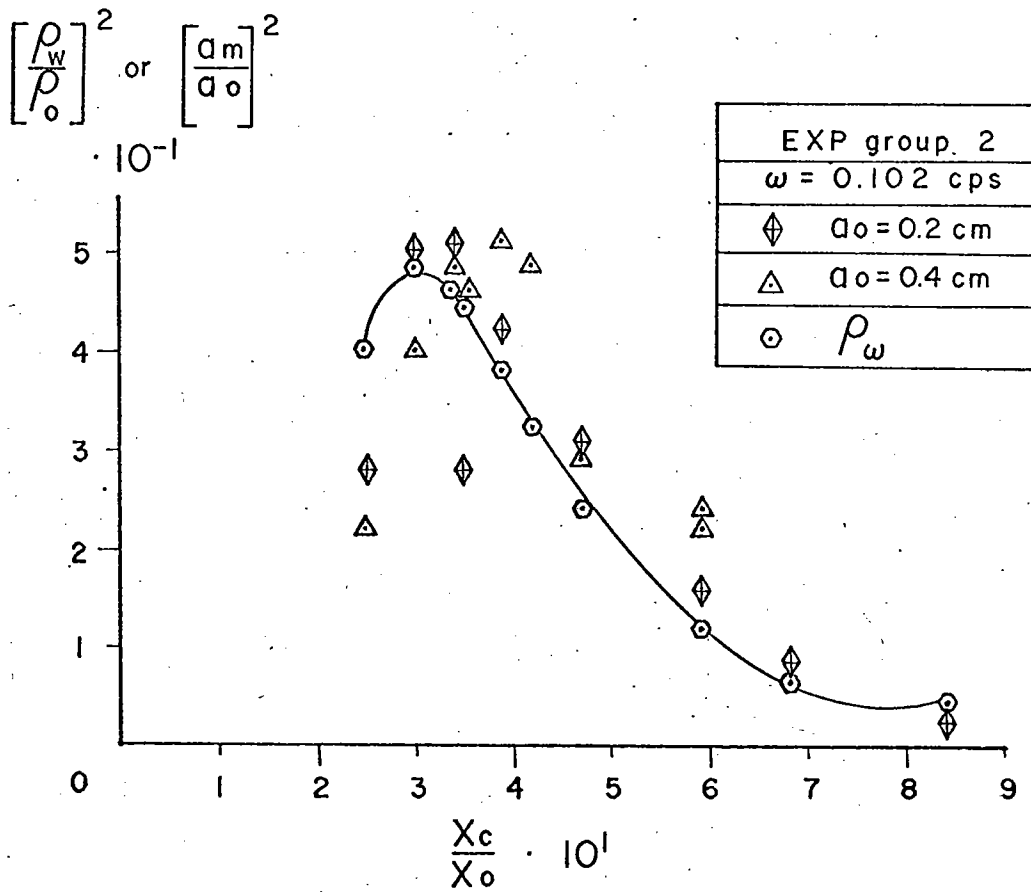
Fig. 26.

Upslope variation of wave amplitude, $\gamma < c$.
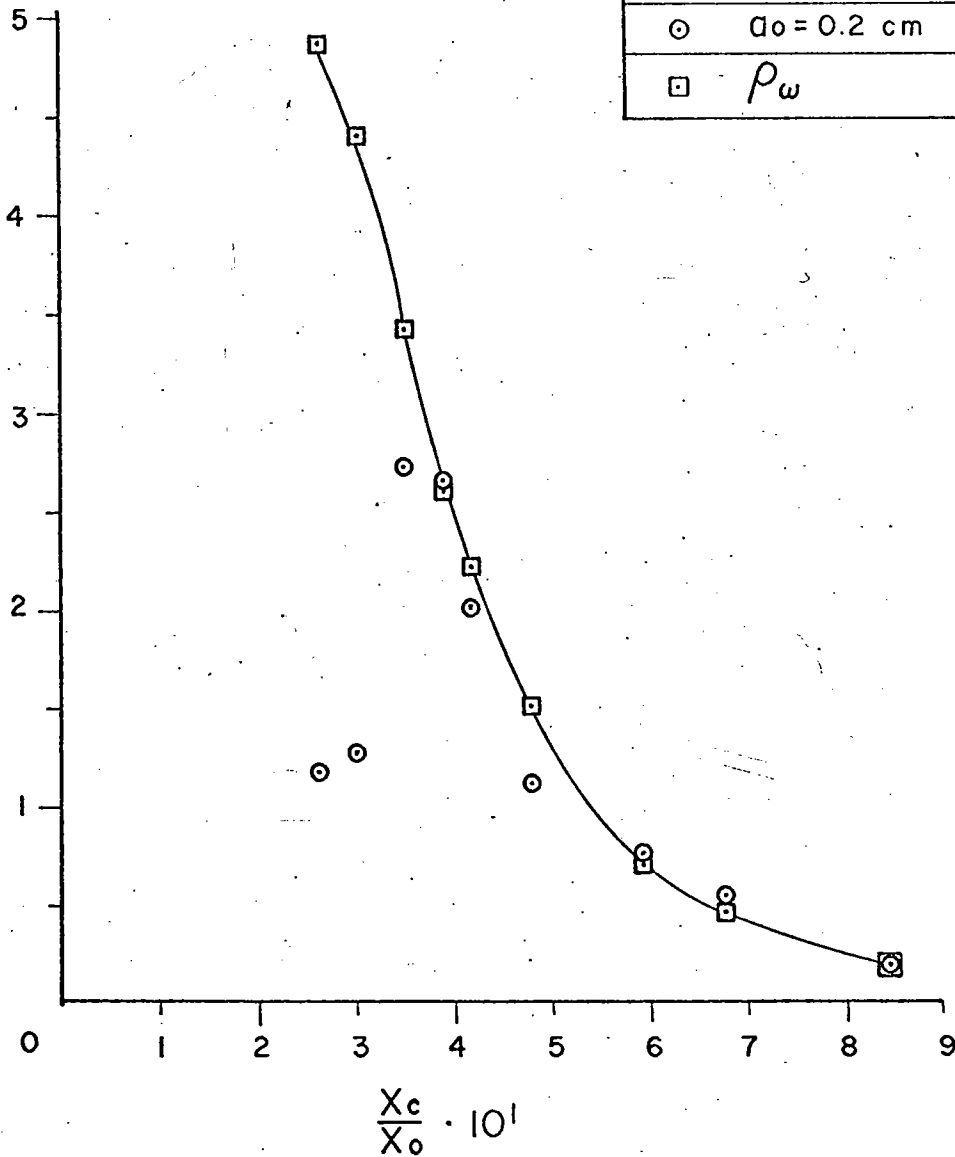
Fig. 27.

Upslope variation of wave amplitude, $\gamma < c$.
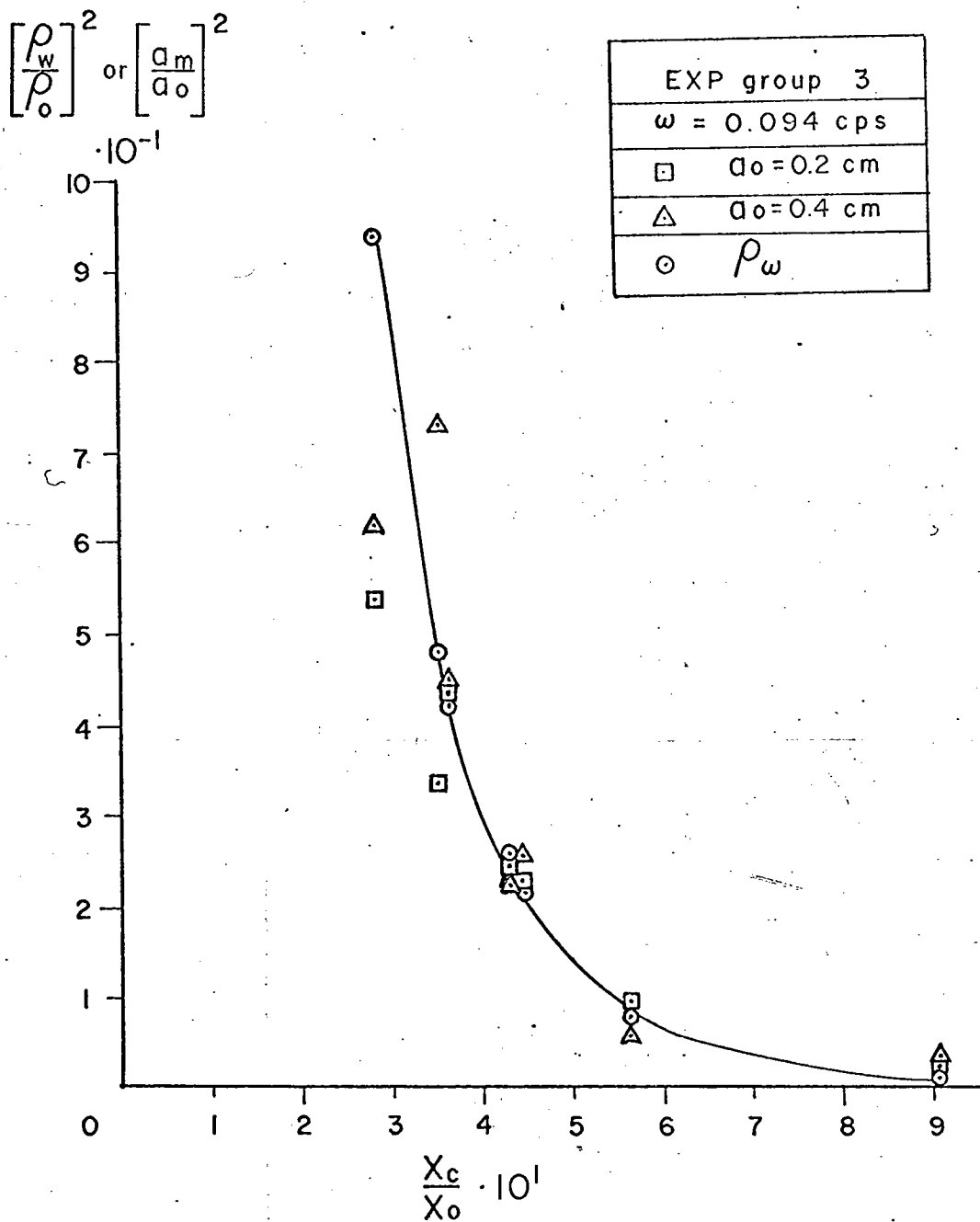
Fig. 28.

Upslope variation of wave amplitude, $\gamma < c$.

$$\left[\frac{\rho_w}{\rho_o}\right]^2 \text{ or } \left[\frac{a_m}{a_o}\right]^2$$

$\cdot 10^{-1}$

EXP group 5	
$\omega = 0.098$ cps	$\omega = 0.082$ cps
$-\odot$ $a_o = 0.2$ cm	$\odot$ $a_o = 0.2$ cm
$-\boxdot$ ρ_ω	$\boxdot$ ρ_ω

$$\frac{X_c}{X_o} \cdot 10^1$$

Fig. 29.

Upslope variation of wave amplitude, $\gamma < c$.

$$\left[\dfrac{\rho_w}{\rho_o}\right]^2 \text{ or } \left[\dfrac{a_m}{a_o}\right]^2$$

EXP group 6		
ω , cps	a_o	ρ_ω
0.062	⊙	⬦
0.047	⊡	⊙
0.043	△	◇
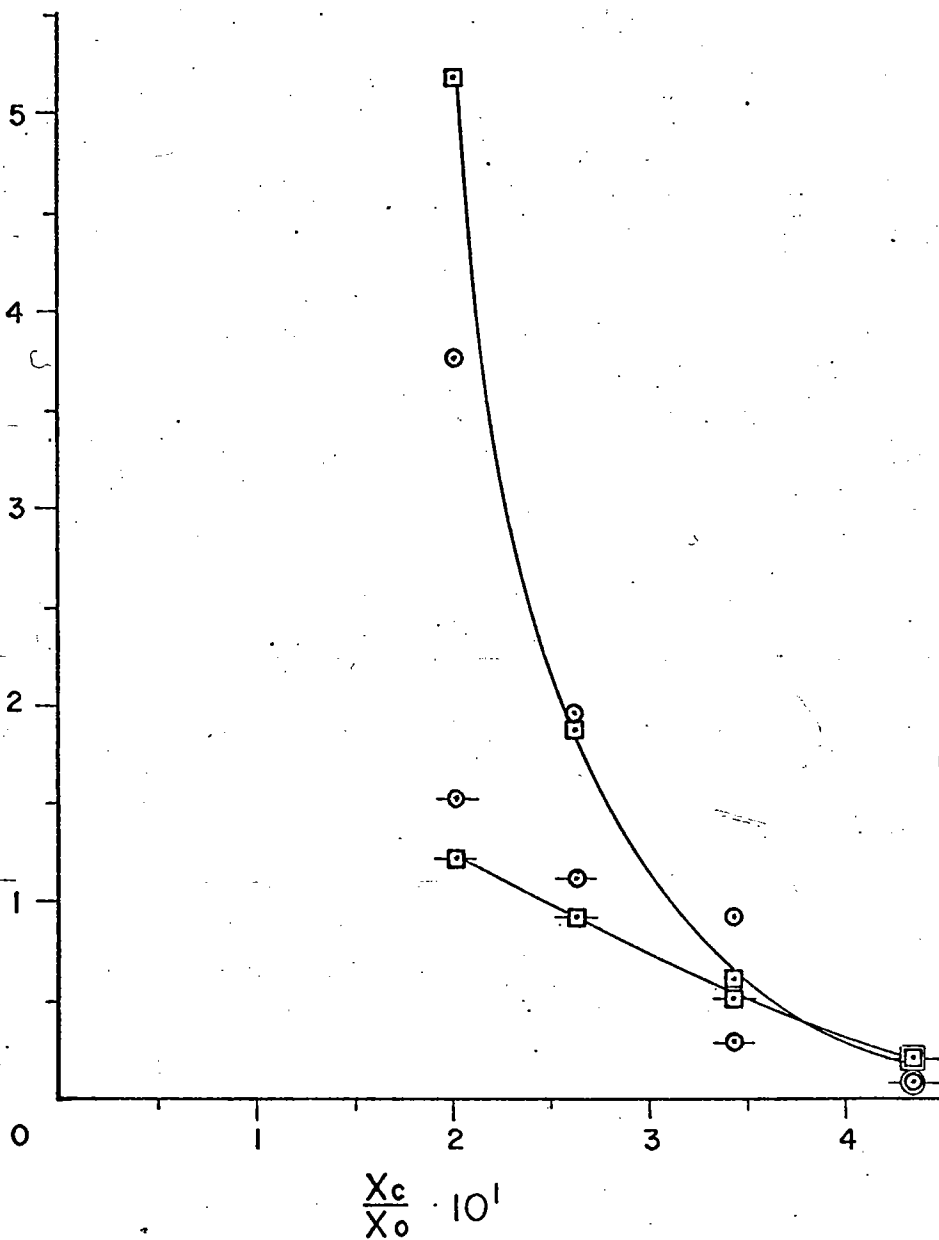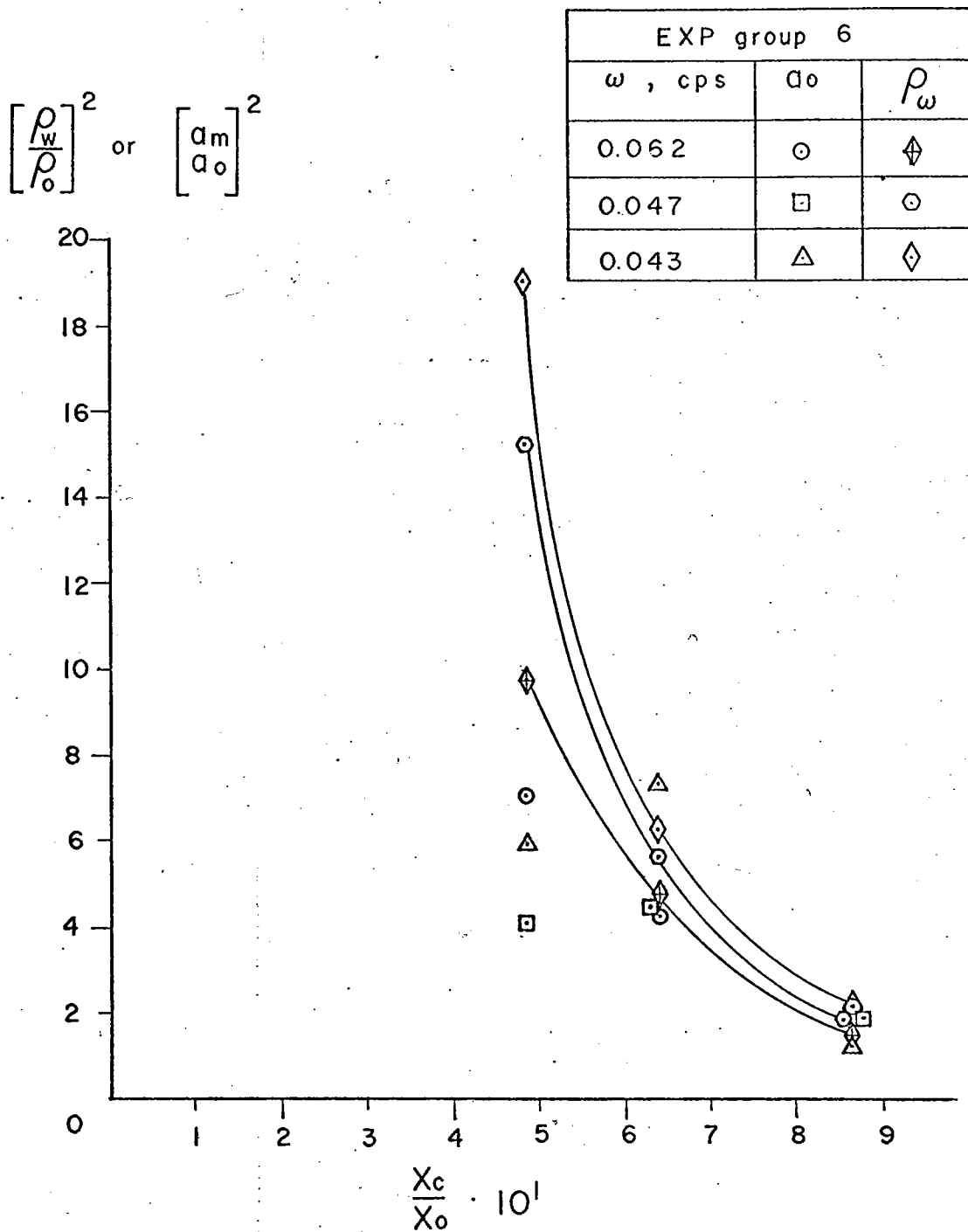
Fig. 30.

Upslope variation of wave amplitude, $\gamma < c$.

amplitude variations $(\rho_w/\rho_o)^2$ and $(a_m/a_o)^2$, respectively, are plotted along the ordinate; the ratio of the horizontal distance between the probe and the corner x_c to the total horizontal projection of the slope x_o is plotted along the abscissa. The depth of the probe measurements is constant for any one of the figures, but as shown in Appendix B, Figure B4, it generally varies for each experimental group. In Figures 25, 26, 27 and 30 the results pertain to the slope angle of 15 degrees, for which the distinction between high and low frequency waves appears most applicable. Two effects of the method used to display the results must be mentioned here:

(1) the deviations between the theoretical and measured estimates of amplitude are exaggerated in the graphs, since squares are plotted as the ordinate;

(2) the peaking of the waves is a function of the vertical position z_c of the probes as well as distance from the corner x_c. This latter effect is subtle; since the internal waves are of the first mode, the amplitude should be largest near the center of the water column at any position over the slope if the modal structure remains intact.[*] Consequently, the amplitude is expected to vary along a horizontal line (constant depth) due to the modal structure as well as to the amplification during shoaling.

To the right of the peak values (i.e., away from the corner) in Figures 25 and 26 (high-frequency waves), the variations are essentially parallel, although the experimental values are consistently higher than the predicted. The maximum measured values are slightly higher than predicted, with an indication that the larger input waves (a_o = 0.4 cm, Figure 26) peak sooner than the smaller waves. There is also evidence

---

[*]For this case $(\gamma < c)$, photographic measurements indicate that the mode is preserved at least over the lower and middle slope areas.

that the measured values fall off to lower values than the theoretical values to the left of the zone of peaking (i. e., toward the corner).

The high-frequency waves over the steeper slope (Figure 28) conform closely to the predicted behavior for $x_c/x_o > 0.35$, but nearer the corner the amplitudes of these waves grow less than predicted. This is probably a result of the anomalously large growth of the theoretical solutions near the corner (recall that for $\gamma < c$ Equation (4-6) is singular for $x = z = 0$). The larger input waves ($a_o = 0.4$ cm, Figure 28) show a tendency to peak earlier than predicted. The measured value at $x_c/x_o = 0.35$ for $a_o = 0.2$ cm is suspiciously low.

Figures 27 and 30 illustrate the behavior of wave amplitude during shoaling of the lower frequency waves for a low slope angle (15 degrees). The measured values obviously do not achieve the high predicted values well upslope ($x_c/x_o < 0.4$ in Figure 27 and $x_c/x_o < 0.5$ in Figure 30). The departure from theoretical estimates is most noticeable for the very low frequencies ($\omega = 0.047$ cps and $\omega = 0.043$ cps) in Figure 27. This suggests that the waves increase in amplitude as they propagate upslope until at some point near the half-distance of the horizontal projection of the slope the rate of growth decreases. It was indicated earlier that these waves tend to surge as they approach the corner. Possibly a transformation from the sinusoidal wave form to a different wave structure (such as a solitary wave) that is continually losing energy to viscous dissipation along the slope accounts for the nature of the experimental data for these kinds of waves. In any event, the amplitude of these lower frequency waves is not as large as predicted, and there seems to be evidence of a more gradual dissipation of these low frequency waves with the formation of runup.

Critical and Supercritical Cases

The experimental runs for the critical and supercritical cases are indicated by a dash in column 6, Table B2 (Appendix B). A comparison of the input wave frequency with the critical frequency for each of these runs shows that $\omega \leq \omega_c$, a necessary condition for this regime. A brief description of the reflection properties that define this regime was presented in the first section of this chapter. In particular, for case C (supercritical) two features are suggested by the reflection properties: (1) the presence of back reflected wave energy; (2) concentration of this back-reflected energy in a zone bounded by the bottom slope and the characteristic that intersects the corner. Figure 31 further illustrates these features. This figure shows that wave characteristics which are incident to the slope from above, i.e., those with a downward-pointing vertical component, upon reflection from the slope will remain below the characteristic (defined by z = -cx) that intersects the corner. The energy flux associated with these characteristics enters the slope region in a relatively broad band and exits in a confined, triangular zone (for example, the triangular area AOB in Figure 17). As Figure 31 indicates, there is a smaller influx of energy which, upon reflection from the flat bottom, propagates upslope within the narrow bottom zone (for example, the path of the characteristic "b" in triangle AOB). The characteristics associated with this latter energy flux have upward-pointing vertical components as they enter their slope regions; upon reflection they preserve the sense of the upward-directed vertical components. In both cases (characteristics "a" and "b" in Figure 31) once the characteristics reflect from the slope the horizontal direction of energy is away from the corner.

Critical conditions (case B) were difficult to achieve experimentally for two reasons: (1) $\gamma = c$ required that the wave-maker frequency be tuned precisely; (2) it was difficult to determine the Brunt-Vaisala frequency accurately during an experiment. In addition, the experimental groups which involved the 15 degree slope angle had critical frequencies
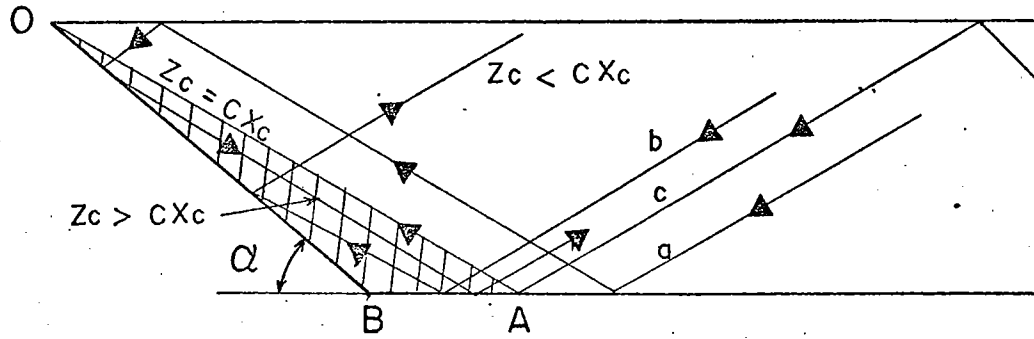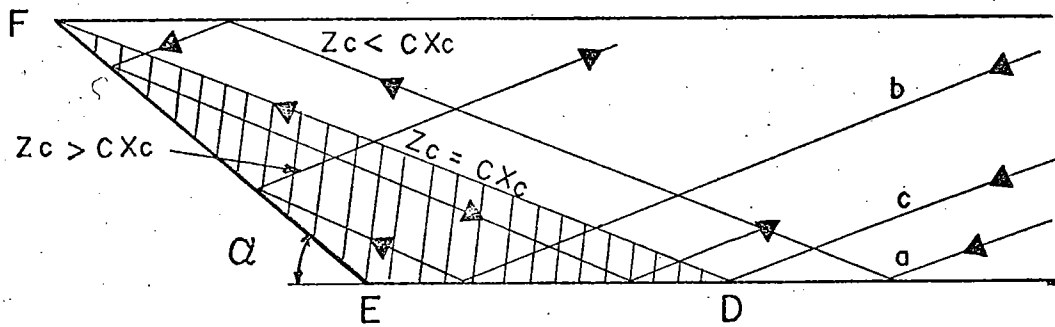
FIG. 31. Reflection of characteristics for case C, $\gamma > c$ where $\gamma = \tan \alpha$, $z_c = |z|$, $x_c = |x|$ and characteristics are labeled a, b, c. Characteristic c is "critical" i.e., passes directly to the corner at O in (1) and at F in (2). The increased concentration of characteristics in the triangular zones (hatched areas) is illustrated by the path of characteristic a.

that corresponded to long horizontal wave lengths over the flat bottom (on the order of the tank length). Data for only six runs at the critical frequency are considered reliable. During each of these runs the input wave frequency was held to within two percent of the calculated critical frequency.

Table B5 (Appendix B) summarizes the experimental results from the conductivity-probe measurements for this regime ($\gamma \geq c$). Like the organization in Table B3, the frequency, period, and probe coordinates $(x_c, z_c)^*$ are given for each experimental run. The experimental runs having the same N and γ are again collected into groups; as before, the experimental parameters for each experimental group are listed in Table B1. An asterisk in column 2 of Table B5 again indicates that the experimental run was repeated at least once. The local depth h is shown in column 6 of Table B5, and the parameter $\dfrac{x}{x^2 - (z\,c)^2}$ in column 10 is analogous to the parameter in column 7 of Table B3.

The experimental method of determining wave number and wave amplitude was discussed in Chapter 3. These quantities are plotted as functions of x_c/x_0 and z_c/cx_c in this section to examine their dependence on (1) horizontal distance from the slope at a fixed depth, and (2) nearness to $z_c = cx_c$ (i.e., distance to the theoretical position of the critical characteristic). The pertinent theoretical curves were computed from Equations (4-18) and (4-20) and are presented in several of the figures for comparison with the data.

It must be pointed out here that qualitative considerations of the linear, inviscid solution for $\gamma > c$, given by Equation (4-16) suggest a priori that these solutions might fail to fit the experimental data. It can be shown that the velocity components derived from Equation (4-16) become anomalously large for large coordinate values (x, z). This behavior was not

---

*In this discussion and in Table B5 $x_c = |x|$ and $z_c = |z|$ for x, z as shown in Figure 15.

observed in the experiments. In addition it is shown later that the theory (in particular, Equation (4-17)) selects $|n| = 2$ as the lowest nonsingular inviscid mode permissible over the slope region for each of the experimental conditions tested. In the particular experimental geometry, it was not apparent that the second mode was present over the slope; it was found most often that the modal structure was approximately that of the input mode ($|n| = 1$). In spite of these qualitative objections, the following discussion of the experimental results is done quantitatively by comparison with the theoretical predictions and by consideration of the reflection properties (Figure 31). It is felt that this method of presentation aids the interpretation of the results.

Wave number. Figure 32 and 33 illustrate the complicated behavior of the experimentally determined wave numbers for this case. Data from three experimental groups and for frequencies $\omega = 0.051$ cps and $\omega = 0.066$ cps are represented in these figures. The calculated positions of the critical characteristic (determined by $z_c = cx_c$) for two of the experimental groups are shown along the horizontal axes. The two theoretical curves shown in each figure were computed for two different values of the mode number (see qualitative discussion at end of previous section). Equation (4-20) was used to determine the minimum permissible nonsingular mode number for the curves labeled $n = 2$. The mode number $n = 1$ was preselected for the theoretical curves labeled $n = 1$. Although this latter choice violated the condition necessary for finite values of the velocity components and their first derivatives at $z = -cx$ (Equation (4-20)), it nevertheless forces the theoretical mode number over the slope to be equal to the input mode of the experiments.

It is apparent in the figures that there is no straightforward relationship between linear theory ($n = 2$) and the data. There is only qualitative indication that the curves for $n = 1$ have the same trend as the experimental results for $x_c/x_o \leq 0.035$ in Figure 32 and for $x_c/x_o \leq 0.45$ in Figure 33. It is obvious that the theoretical estimates for $n = 1$ grow toward very large values at the critical points (for example, $x_c/x_o = 0.26$, Figure 33). The
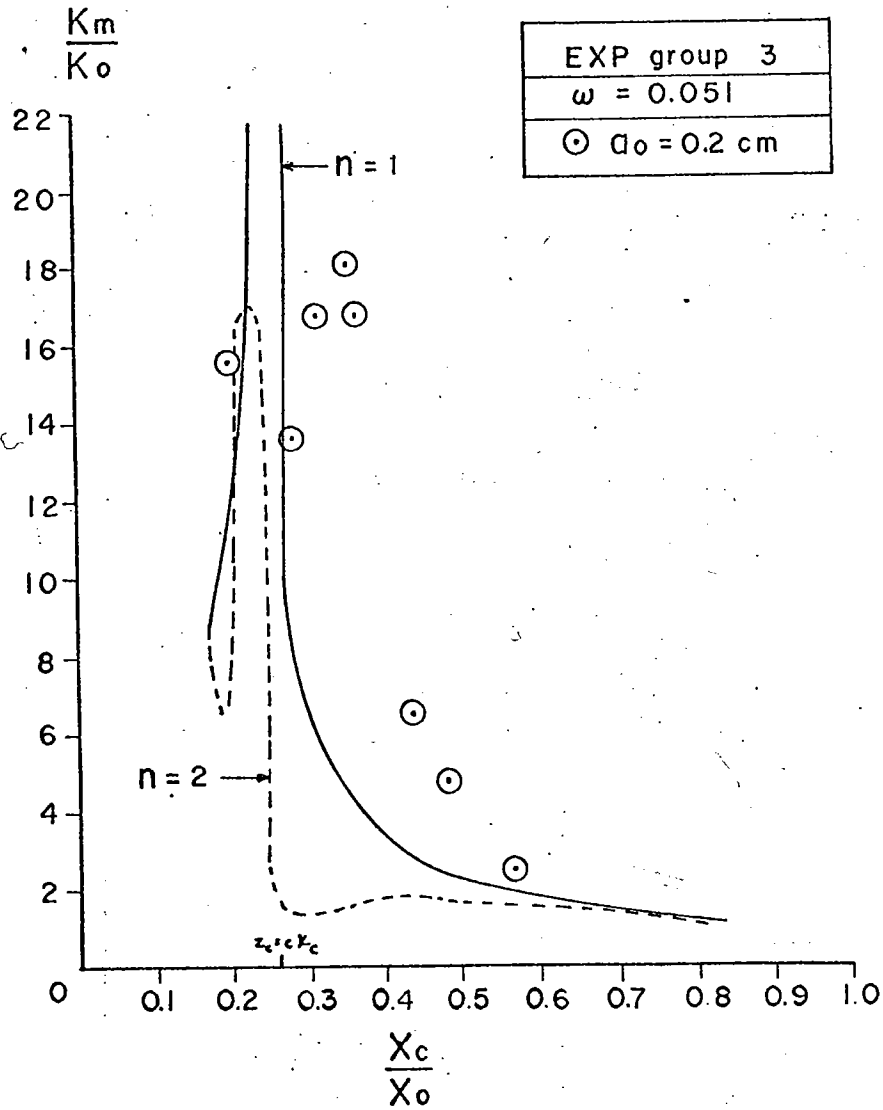
Fig. 32.

Upslope variation of wave number, $\gamma > c$.
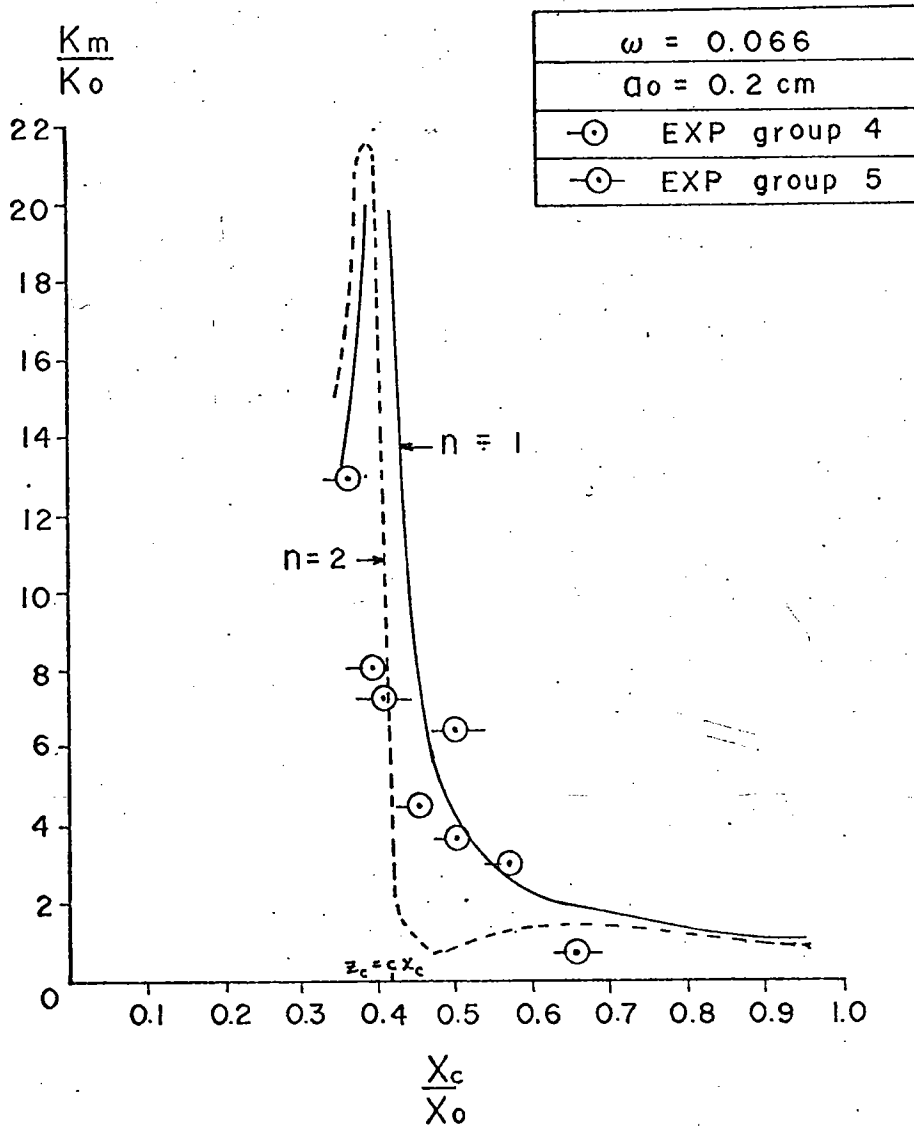
Fig. 33.

Upslope variation of wave number, $\gamma > c$.

experimental values near the calculated critical points are apparently bounded. The dip in the data in Figure 32 for x_c $x_o \simeq 0.30$ is not apparent in Figure 33. Possibly the absence of the dip in the data from experimental group 4 (Figure 33) can be explained by considering nonlinear effects. The measured value of ϵ_m (Table B5) for this particular data set is approximately 0.5 at $x_c/x_o = 0.36$. This suggests that nonlinear amplitude growh might be significant near these positions. By comparison, the measured value of ϵ_m for the data in Figure 32 is only 0.13 for $x_c/x_o \approx 0.2$ (Table B5). It should also be noted that there is a significant shift in the peak value to the right of the calculated critical point in Figure 32. Possible this shift indicates that the singularity is removed by nonlinear or fiscous processes and tha that the linear inviscid solutions are not valid in this particular physical situation.

Data from experimental groups 3 and 4 are plotted on log-log scales in Figures 34 and 35, respectively. Theoretical curves for n = 1 are again shown in these figures. The qualitatively similar trend between the theoretical curve and the data is apparent, particular in Figure 12. Values of wave number for the larger amplitude input waves ($a_o = 0.4$ cm) tend to be higher than those for the smaller waves ($a_o = 0.2$ cm) in experimental group 3 (Figure 34).

Figure 36 shows the results of experimental group 3 plotted as a function of z_c/cx_c. It is obvious that the theoretical curve for n = 1 grows toward infinite values of k_m/k_o at $z_c = cx_c$; the theoretical curve for n = 2 (obtained from Equation (4-17)) is finite at this point. The trend in the data values reverses at about $z_c/cx_c \simeq 0.80$, and again at $z_c/cx_c \simeq 1.0$. No simple relationship between the data and the theoretical curves are apparent from this figure.

Figure 37 summarizes the experimental results of wave number for case B ($\gamma = c$). The log-log plot emphasizes the steep rise toward larger values of wave number for decreasing distance to the slope. It is interesting that the magnitudes of wave number for the larger input waves ($a_o = 0.4$ cm)
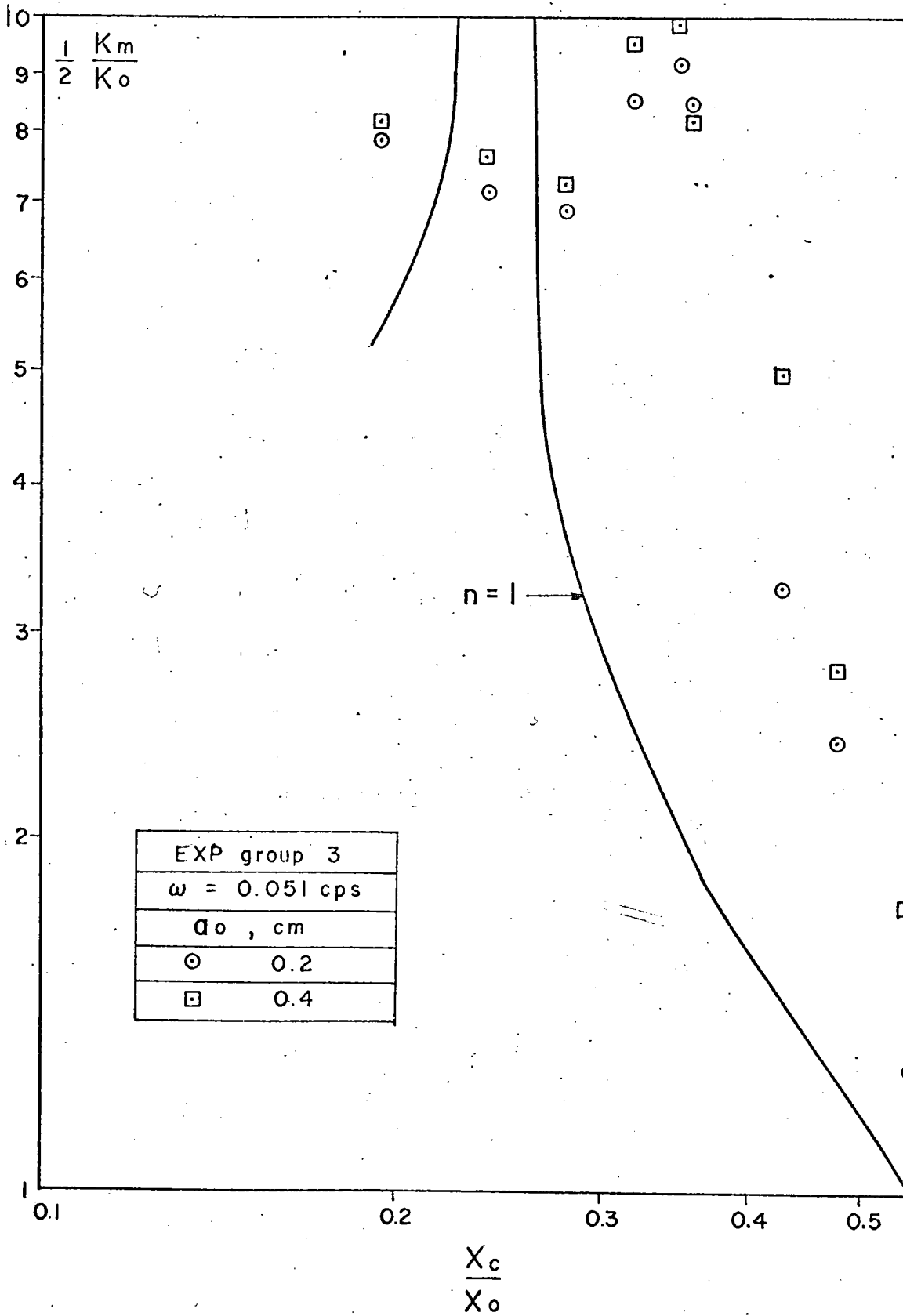
Fig. 34.

Upslope variation of wave number on log-log plot, $\gamma > c$.
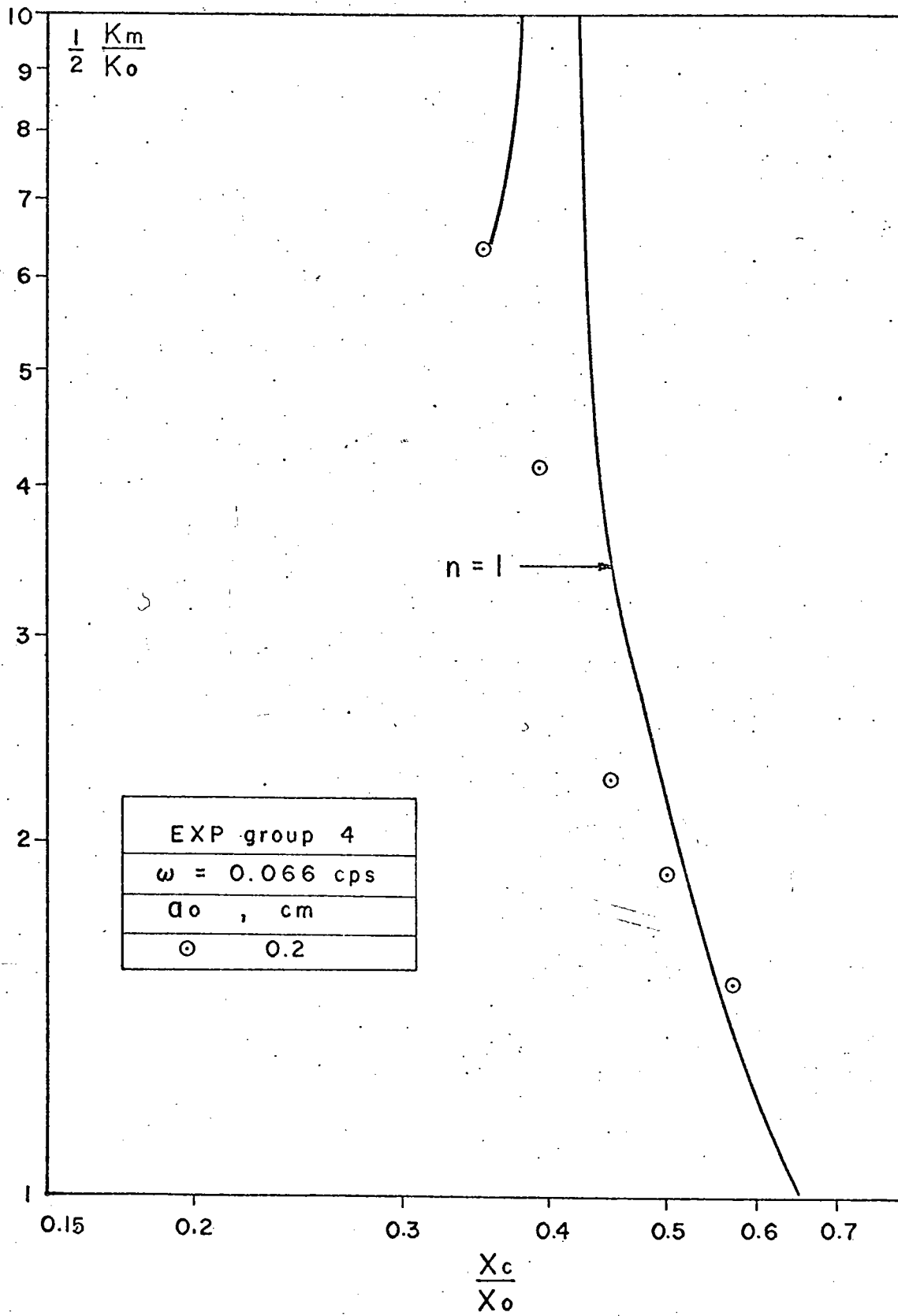
Fig. 35.

Upslope variation of wave number on log-log plot, $\gamma > c$.
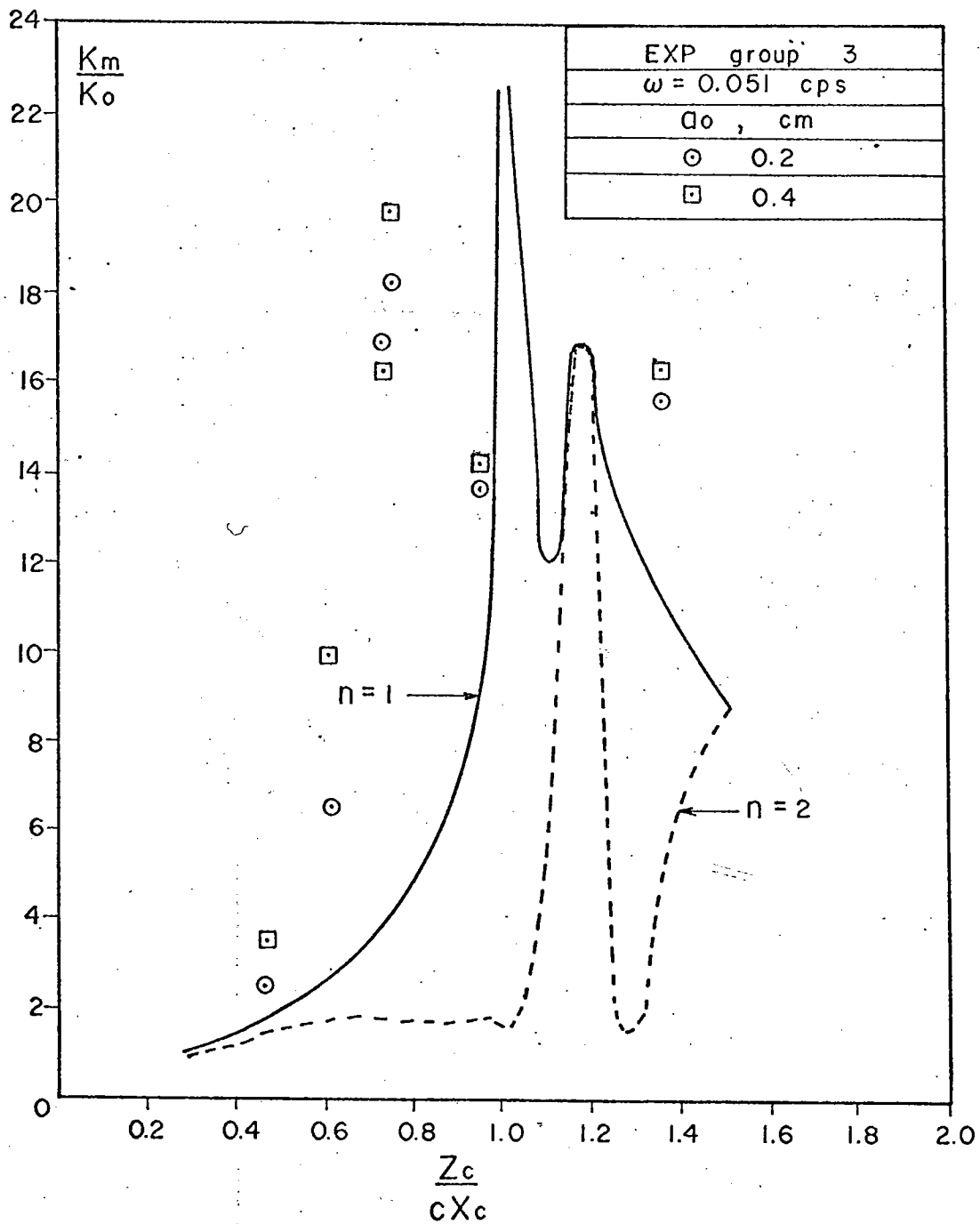
Fig.36.

Wave number versus magnitude of z_c/cx_c, $\gamma > c$.

$\frac{1}{2} \frac{Km}{Ko}$

EXP group 3	EXP group 4
$\omega = 0.073$ cps	$\omega = 0.079$ cps
Zc = 5.5 cm	Zc = 11.1 cm
ao , cm	ao , cm
⊙ 0.2	△ 0.2
▣ 0.4	

$\frac{Xc}{Xo}$
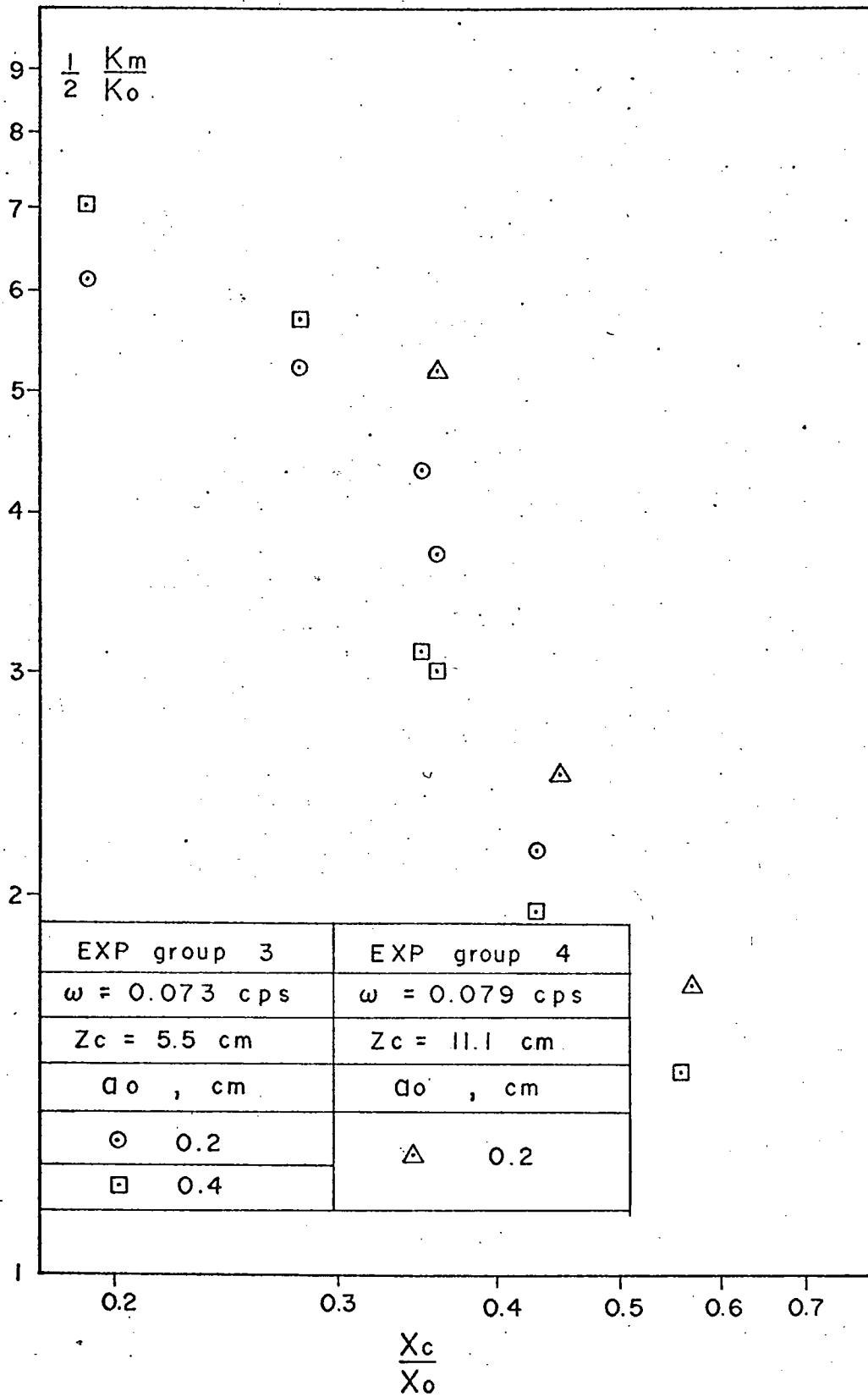
Fig. 37.

Upslope variations of wave number, $\gamma = c$.

in experimental group 3 are larger than the corresponding values of the smaller input waves for $x_c/x_o < 0.3$, but for $x_c/x_o > 0.3$ the wave numbers of the larger waves are consistently less than those of the smaller waves. In general, the wave number variations with distance to the slope for this case are similar to the variations shown in Figure 34 for the supercritical case. No theoretical comparison is shown, since for $\gamma = c$ the minimum permissible nonsingular inviscid mode over the slope, given by Equation (4-17) is infinite.

In summary, the results show a complicated relationship between wave number and position over the slope. There is evidence in Figures 34 and 35 that the wave number increases rapidly as the waves pass over the lower and middle sections of the slope for the supercritical case, but there does not appear to be a systematic pattern to the data near $z_c = cx_c$. The variations in wave number for the critical case are qualitatively similar to those for the supercritical case; a large increase in the wave number for smaller x_c/x_o is apparent. The trends of the theoretical values of wave number computed for $n = 1$ are similar to the measured values for $z_c/cx_c < 1$. It is obvious that the unbounded theoretical values at $z_c = cx_c$ for $n = 1$ are removed when the condition given by Equation (4-17) is satisfied. For both cases, the measured values of ϵ_m (Table B5) are greater than 0.1 for the most of the measurements taken closest to the corner. This suggests that nonlinear effects might be important near these positions.

Wave amplitude. The experimental estimates of wave amplitude were obtained from the periodograms of the conductivity-probe measurements (Chapter 3). The results are presented as ratios of the square of the wave amplitude over the slope to the square of the wave amplitude over the flat bottom for various frequencies of the input waves. Like the earlier presentation for wave number, these results are illustrated graphically with z_c/cx_c and x_c/x_o used as the horizontal axes.

The results for wave amplitude are easier to interpret in terms of
the reflection properties of the slope than were the results for wave number.
Earlier theoretical discussion indicated that near the characteristic defined
by $z_c = cx_c$ and in a zone between this characteristic and the bottom slope
(Figure 31) there is a possible region of concentrated energy flux. Figure
38 shows that the measured values of wave amplitude are highest near
$z_c/cx_c = 1.0$ for each frequency tested in this group except $\omega = 0.039$ cps.
However, it is not conclusively shown in this figure that the amplitudes peak
exactly at $z_c = cx_c$. This figure also shows that the ordinate values for the
various frequencies at equal values of z_c/cx_c generally increase with de-
creasing frequency. In the light of Figure 31, back-reflected wave energy m
might contribute smaller amounts to the total energy at locations above the
critical characteristic (i.e., at positions given by $z_c < cx_c$) for frequencies
nearer to critical. This in turn might account for the lower measured
levels of $(a_m/a_o)^2$ for the frequencies nearer to critical in Figure 38.
Figure 39 is a similar plot for data from experimental groups 3 and 4;
two input wave amplitudes are represented in the values from experimental
group 3. Also shown in Figure 39 are theoretical curves for $(\rho_w/\rho_o)^2$ de-
rived from Equations (4-10) and (4-18) by the methods described earlier.
The mode number $|n|$ was determined from the condition in Equation (4-17)
for curve $n = 2$ in this figure. The theoretical values $(a_m/a_o)^2$ decrease
toward the slope and undergo a smooth transition through the critical point
$z_c/cx_c = 1.0$, where they then begin to increase toward the slope. The
theoretical curve with $n = 1$ has increasing values toward the slope until the
critical point $(z_c = cx_c)$ is approached; a sharp dip in the theoretical values
at this point followed by a rapid rise suggests that the solutions are not well
behaved at this critical point. The ordinate values for the two input ampli-
tudes of group 3 in Figure 39 agree within 10 percent of one another for
values of $z_c/cx_c < 1.0$; in general, the larger input waves have slightly
higher measured amplitudes in this range. It is also apparent that the
larger input waves grow more rapidly as the value $z_c/cx_c = 1.0$ is approached.
Owing to the larger values of ϵ_m (Table B5) for the waves of larger input

Fig. 38.
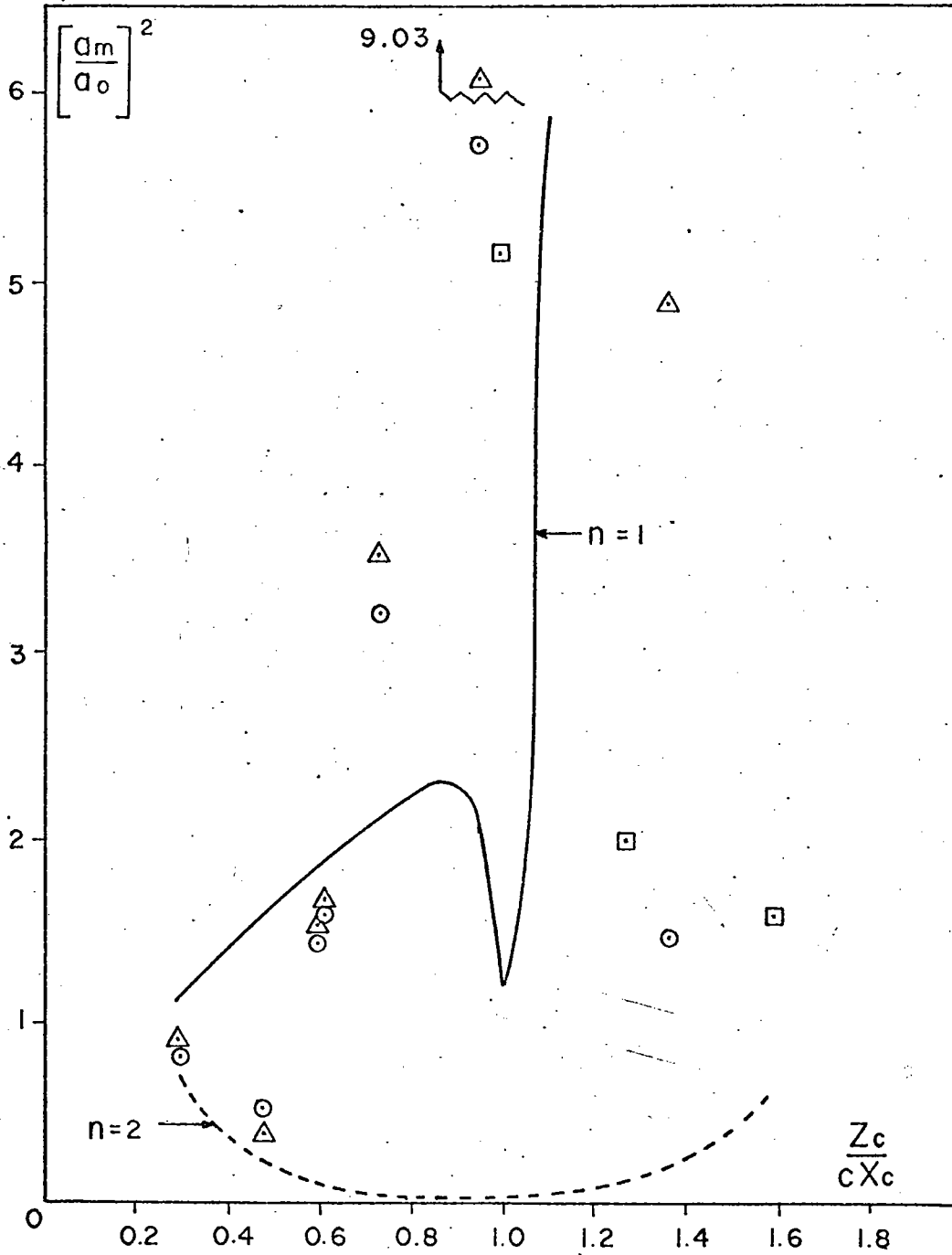
Wave amplitude versus magnitude of z_c/cx_c, $\gamma > c$.

Fig. 39.

Wave amplitude versus magnitude of z_c/cx_c, $\gamma > c$.

amplitude (a_o = 0.4 cm), the increased disparity in the measured amplitude values for input waves of 0.4 and 0.2 cm, respectively, at values of $z_c/cx_c \geq 1.0$ in Figure 39 might be the result of nonlear effects.

Figure 40 shows the experimental results and theoretical curves for ω = 0.051 cps (group 3) on a log-log scale; the horizontal axis id distance x_c to the corner normalized by the total horizontal projection of the slope x_o. The rapid increase in amplitude upslope for $0.28 < x_c/x_o < 0.60$ is readily apparent in the data; however, the theoretical values for n = 2 show an opposite trend, toward lower values for decreasing distance to the slope. The measured amplitudes below the indicated position of the critical point remain relatively high; this suggests amplification of the motion near the bottom. Nonlinear effects also might be important near the corner (x_c/x_o = 0.19)

The results for the probe measurements of wave amplitude at critical frequencies are shown in Figure 41. The increase in amplitude over the range $0.28 < x_c/x_o < 0.60$ is similar to the increase shown in Figure 38 for the same range. However, the maximum amplitude measured for these waves is considerably less than the corresponding value for the supercritical case (Figure 40). Larger viscous dissipation along the slope in the critical case might explain the smaller peak amplitude levels.

In summary, the data indicate that the wave amplitudes generally increase toward the slope; the higher frequency waves (i. e., those closer to ω_c) for these cases show rapid growth during shoaling over the middle sections of the slope. Peak levels of amplitude were generally found near $z_c/cx_c \simeq 1.0$, with lower measured peak values for waves of critical frequency. In both cases the motion is relatively large near the slope. In general, the conductivity-probe measurements of amplitude agree qualitatively with the reflection properties of internal waves from a rigid, sloping bottom. There is some indication from the measured values of ϵ_m that nonlinear amplification of the amplitude occurs for small values of x_c/x_o.
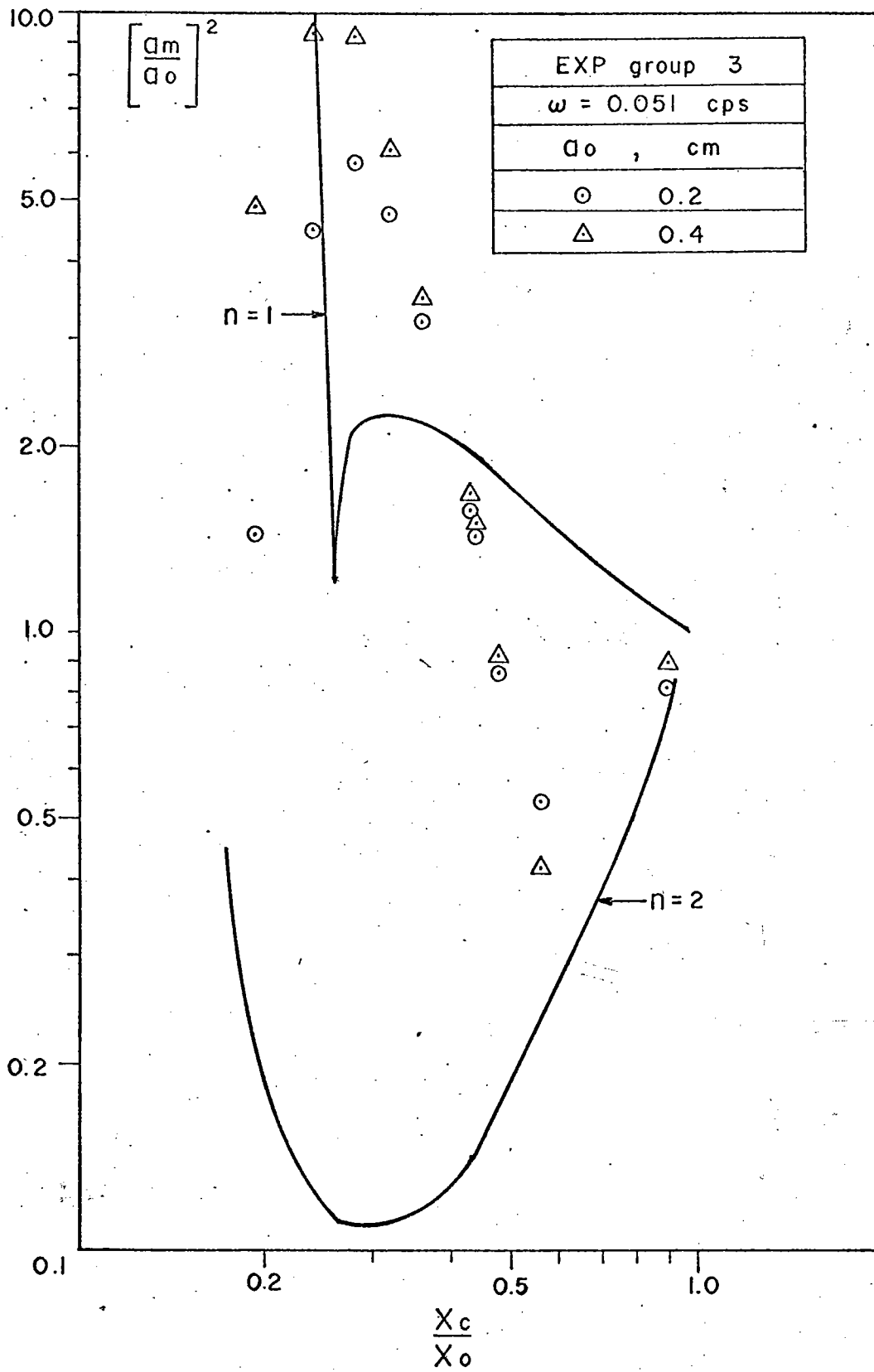
Fig. 40.

Upslope variation of wave amplitude, $\gamma > c$.
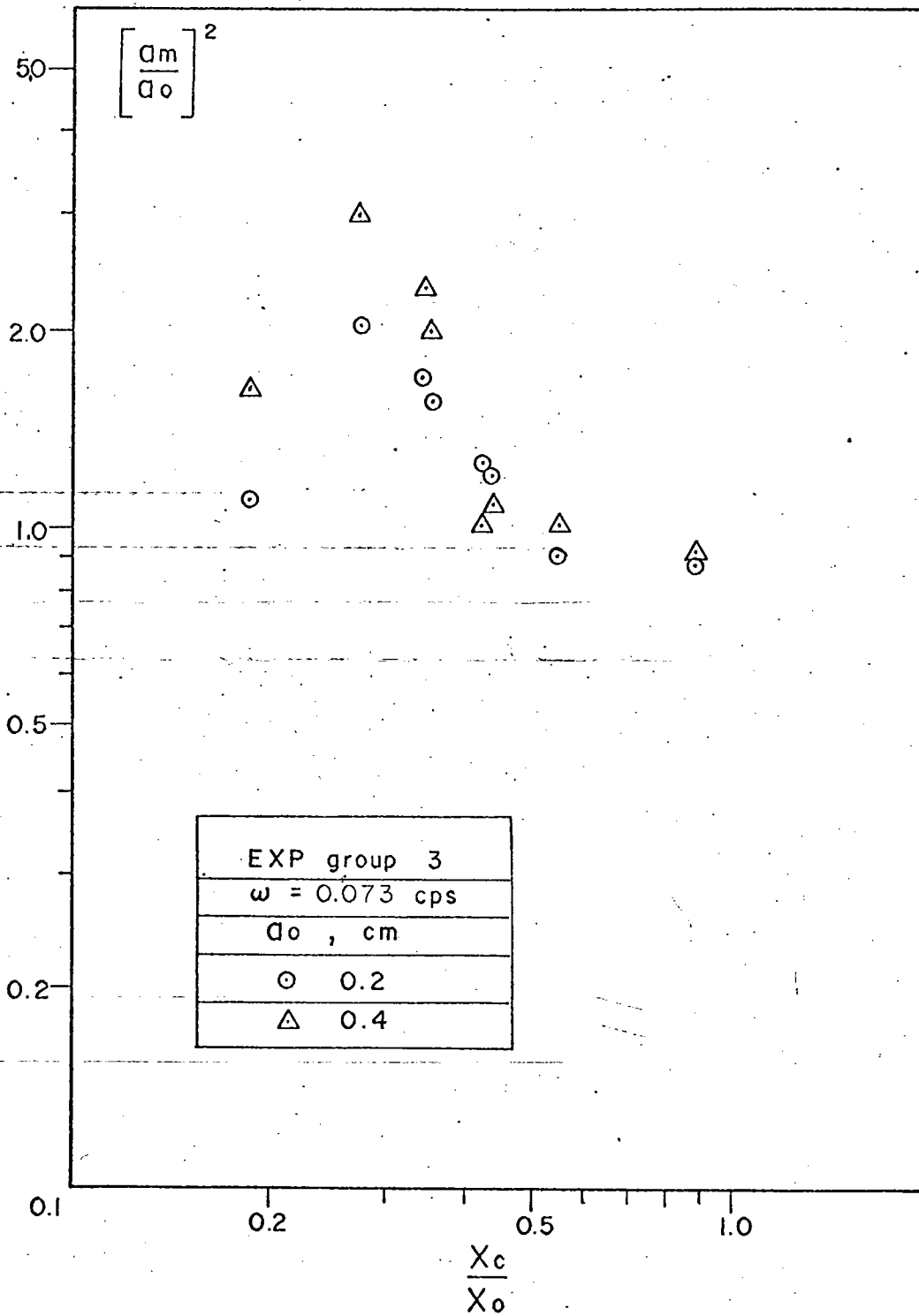
Fig. 41.

Upslope variation of wave amplitude, $\gamma > c$.

It might be added here that the bounded experimental values at $z_x = cx_c$ suggest that viscous dissipation and nonlinear processes might act to remove the singularity at the critical characteristic. For example, the shift in the measured peak wave number in Figure 32, mentioned earlier in th this section, and the formation of vortices near the bottom for these cases, discussed in the next section, suggest that the linear inviscid model is not properly tested by these experimental results. Nonlinear and viscous effects in the interior, particularly in the vicinity of the critical characteristic, should be examined in future analytical treatments of this problem.

BOUNDARY ACTIVITY

The discussion of the bottom boundary layer and the zone of breaking follows the procedure of separating the experimental results into two hydro-dynamic regimes (I $\gamma < c$ and II $\gamma \geq c$). The distinction between these two regimes was defined in Figure 14. Qualitative features observed during the experiments and illustrated by several photographs are presented at the outset as an introduction to the later discussion of quantitative results. In the discussion of quantitative results, experimentally determined velocities in the bottom boundary layer at several positions along the slope are shown to agree with theoretical values computed from the linear solutions in Equation (4-24) for case A. On the basis of the good agreement between experiment and theory for the conditions tested in case A, Equation (4-24) is used in Chapter 5 to develop a model for sediment movement induced by shoaling internal waves.

Case A: $\gamma < c$

Qualitative results. The shadowgraph images and the motion of neutrally buoyant floats permitted excellent real-time observations of the oscillatory flow in the boundary layer and breaking zone. One obvious major feature of this flow was its intensification near the bottom along the slope as com-pared with the flow along the horizontal bottom. The maximum velocities generally increased at positions farther upslope, with a sharp growth in the

velocities near the zone of breaking. The oscillatory flow remained laminar in the boundary layer up to the zone of breaking.

The breaking of waves on the relatively steep slopes (30 and 45 degrees) is characterized by considerable turbulence and vertical motion below the free surface and by the generation of spatially irregular fine structure in the density field. This kind of breaking is also observed for relatively high-frequency waves on the smaller slopes (7 and 15 degrees). In contrast, the lower frequency waves (i.e., those waves with frequencies closer to ω_c) break much less violently, and typically form surges that run up the slope for relatively long distances.

More detailed observations of the higher frequency waves indicate that shortly after the first arrival of the waves near the top of the smaller slopes (α = 7 and 15 degrees), a small vortex forms along the slope beneath the crest of the advancing wave form. Figures 42 and 43 illustrate the onset of this instability beneath the wave crest. In Figure 43 the maximum amplitude of the incoming wave at the entrance to the slope region was approximately 0.4 cm, whereas the corresponding amplitude in Figure 42 was 0.2 cm. The time that had elapsed from the start of the wave maker is shown in the guide sheet preceding Figure 42. Subsequent development of the instability in Figure 42 is shown in Figures 44a and 44b, and later stages of the instability in Figure 43 are shown in Figure 45a and 45b. The lamellar structures in these photographs represent small-scale departures from the constant vertical index-of-refraction gradient characteristic of the stratified fluid with no wave motion. A constant index-of-refraction gradient (or equivalently, constant density gradient) produces a uniform uninteresting shadowgraph image (see center of field in Figure 42). In spite of the apparently chaotic density structure, the basic wave-form can still be discerned in the photographs. Qualitatively, the larger amplitude waves show a higher intensity of breaking, as evidenced by the contrast between Figure 44b and Figure 45b. Not shown in this series of photographs is the protrusion of thin horizontal layers back into the interior region

over the slope. The protrusions lose their intensity (as measured by photographic contrast) over very short horizontal distances (5 to 10 cm) and are confined to the upper vertical levels, where the breaking occurs. The protrusions, thin tonges of mixed fluid that are weakly converted back into the interior, are probably caused by mixing in the zone of breaking.

In contrast to the higher frequency waves, the waves of lower frequency on a small slope (7 degrees or 15 degrees) show less mixing and fewer laminae in the zone of breaking. Each wave forms a surge in which the velocities of neutrally buoyant particles within the surge become approximately equal to the wave celerity as the wave progresses upslope, somewhat analogous to solitary surface waves. The surging motion eventually produces a runup and backwash zone along the bottom very near the corner. The runup appears as a thin streamer in the shadowgraph image and represents a protrusion of fluid of higher density into the near-surface layer. Figures 46a through 46c illustrate the development of this phenomenon for waves whose initial amplitude is 0.4 cm, Figures 47a through 47c show waves whose initial amplitude is 0.2 cm. Vortex instabilities initially form beneath the wave crests and propagate upslope with the wave form. The quasi-steady development for the 0.4 cm and 0.2 cm waves is shown in Figures 46c and 47c, respectively. In these figures, the surging motion essentially fills the water column in the left portion of the photographs. Farther upslope a vortex forms and eventually dissipates into runup.

Figures 48a throuch 49c show a corresponding development of breaking for waves of 10.7 sec period and 0.4 cm initial amplitude over a 30-degree slope. The mixing becomes very intense after the collapse of the initial vortex (Figure 48a). It is interesting to note the reversal in the circulation of the lead vortex as it propagates upslope and collapses. The reversal is a consequence of the shear between the surging motion near the bottom and the opposing flow above the vortex. The following sketch in Figure 50 illustrates this pattern.

Figs. 42 through 49. Guide to photographs of shadowgraph images in the following figures.

Fig. Number	Input Wave Amplitude, a_o (cm)	Wave Period, T (sec)	Slope, α (deg)	Time Elapsed From Start Of Wave Maker (min sec)
42	0.2	8.5	15	04 00
43	0.4	8.5	15	04 00
44a	0.2	8.5	15	06 00
44b	0.2	8.5	15	06 00
45a	0.4	8.5	15	05 20
45b	0.4	8.5	15	05 20
46a	0.4	16.0	15	02 10
46b	0.4	16.0	15	02 30
46c	0.4	16.0	15	05 15
47a	0.2	16.0	15	03 20
47b	0.2	16.0	15	04 30
47c	0.2	16.0	15	08 30
48a	0.4	10.5	30	02 20
48b	0.4	10.5	30	02 30
49a	0.4	10.5	30	02 40
49b	0.4	10.5	30	02 55
49c	0.4	10.5	30	06 20
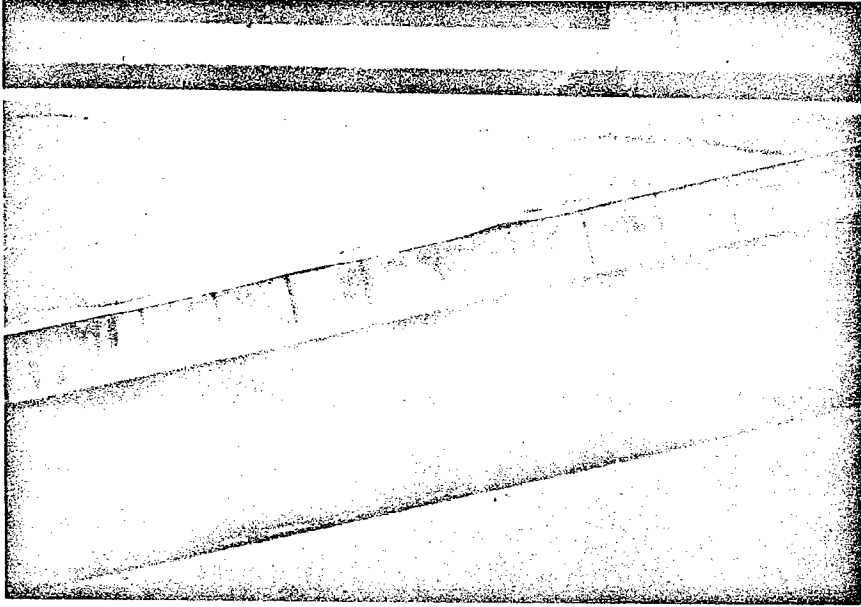
Fig. 42.
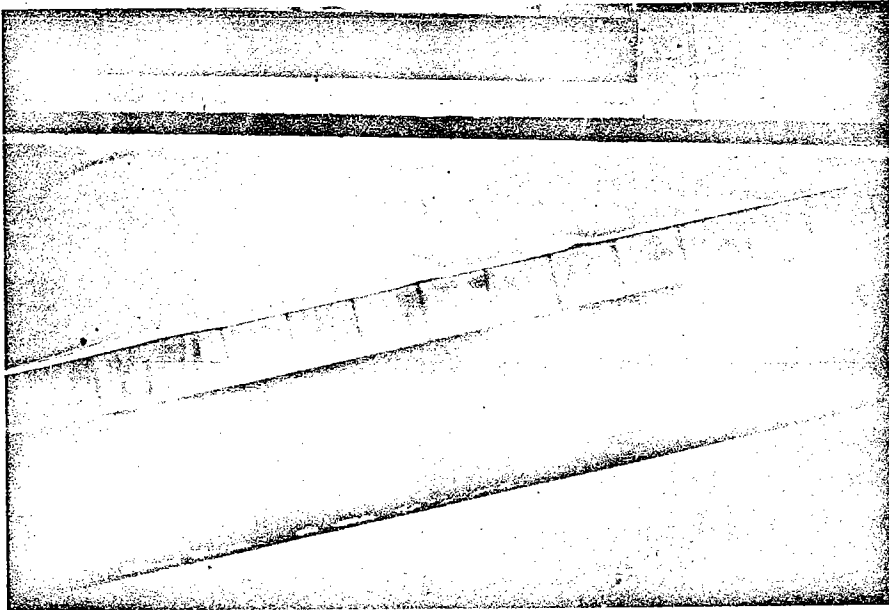
Fig. 43.
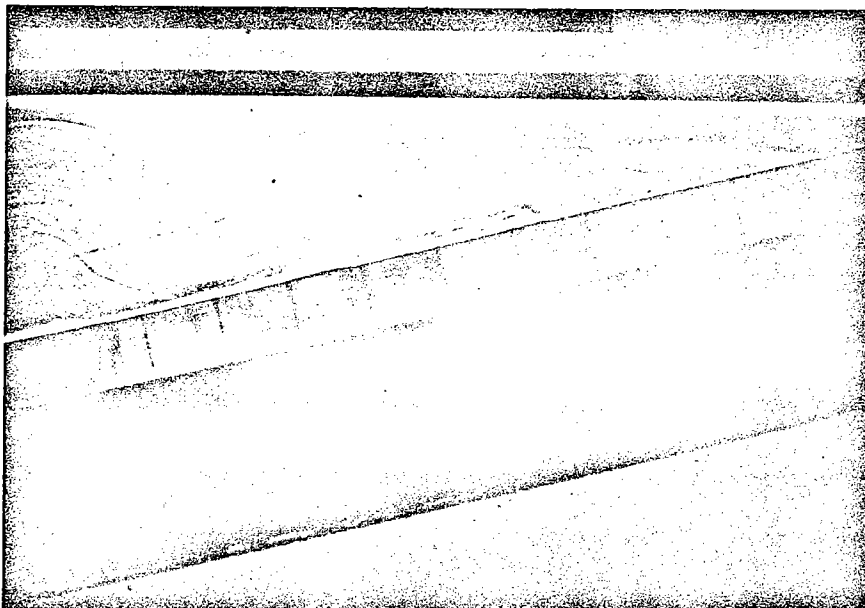
Fig. 44a.
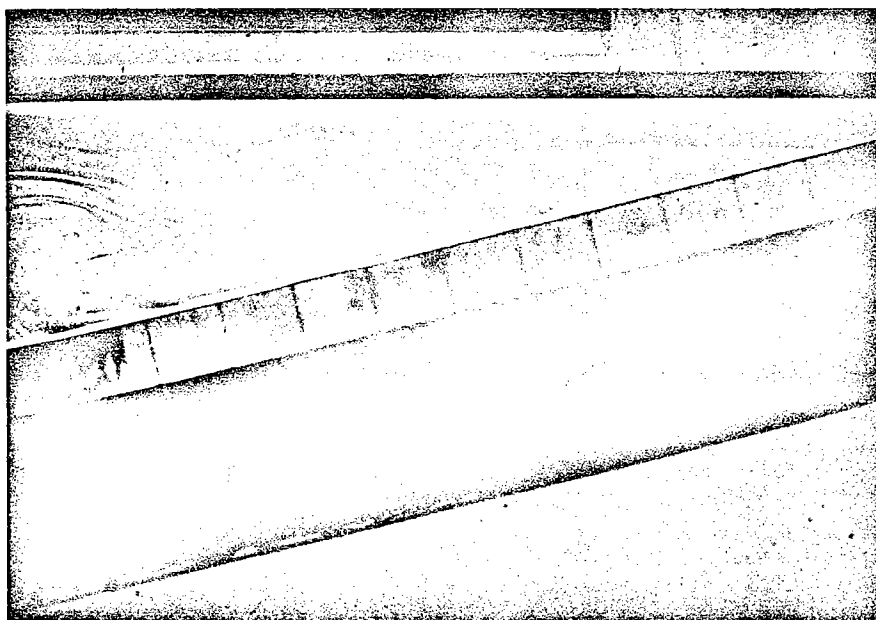
Fig. 44b.
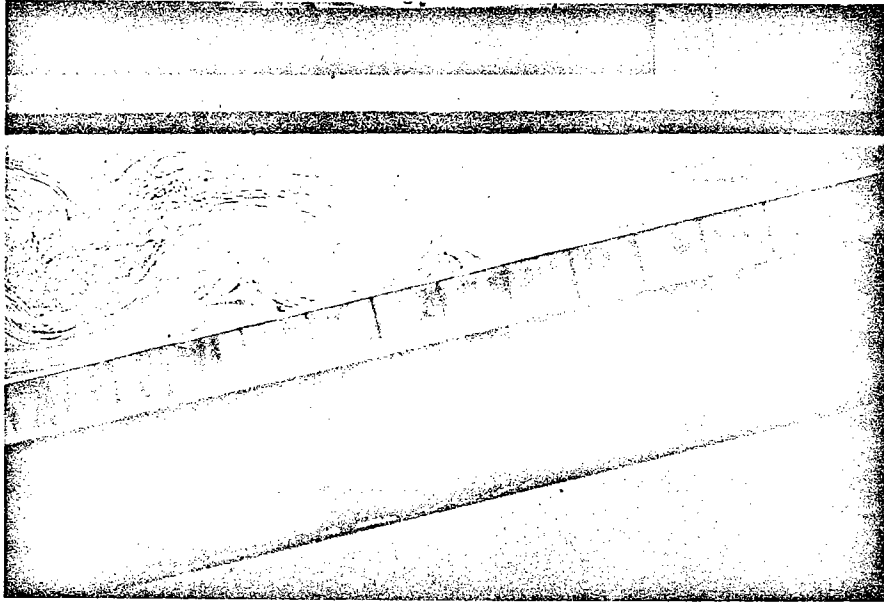
Fig. 45a.
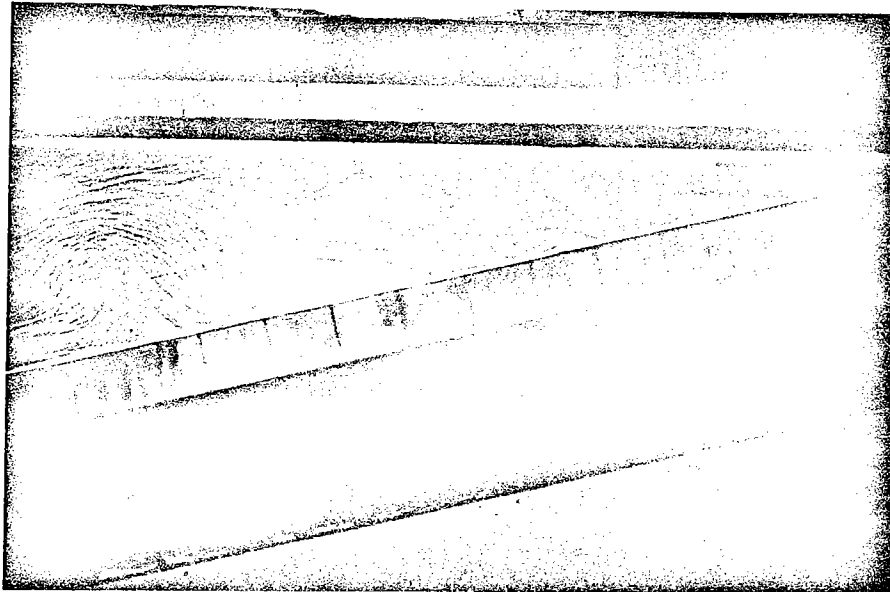
Fig. 45b.

Fig. 46a.

Fig. 46b.

Fig. 46c.
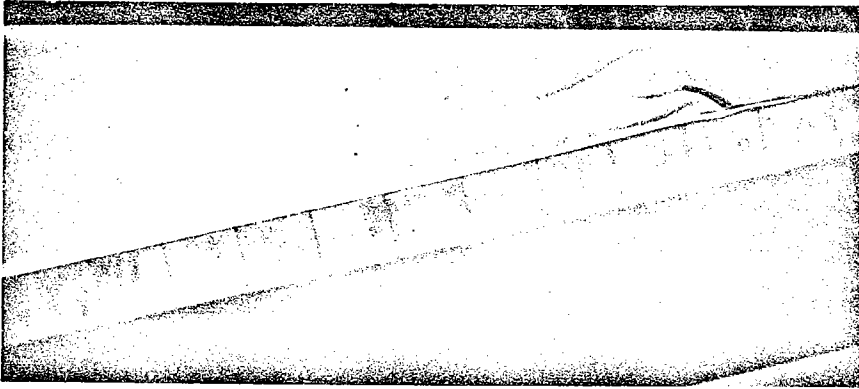
Fig. 47a.
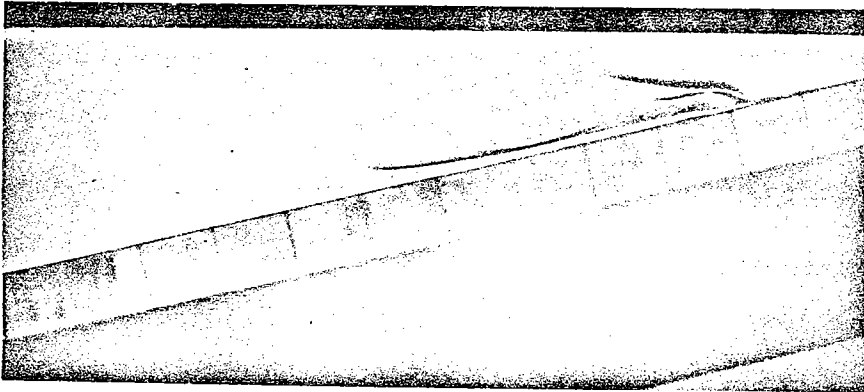
Fig. 47b.
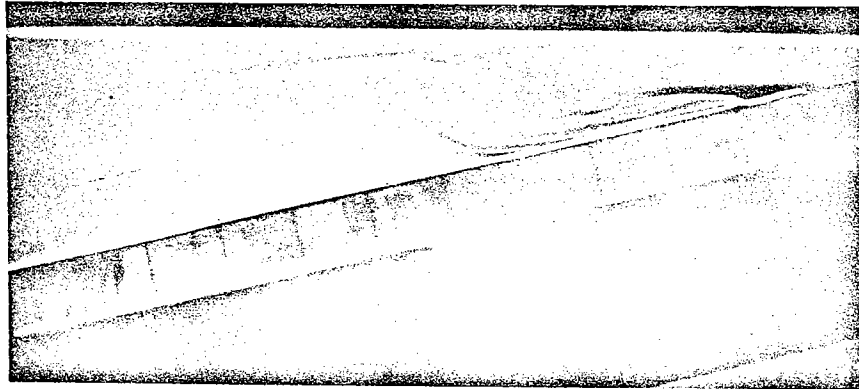
Fig. 47c.
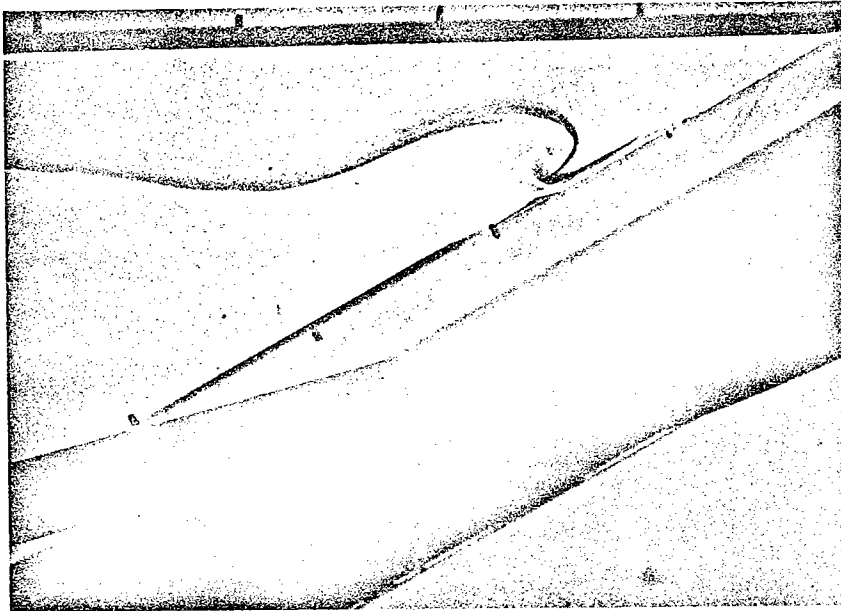
Fig. 48a.
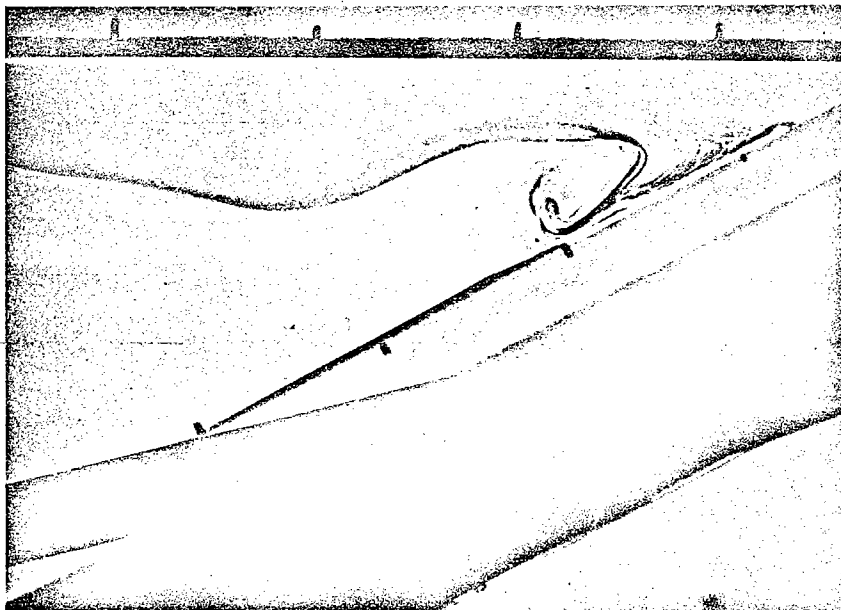
Fig. 48b.
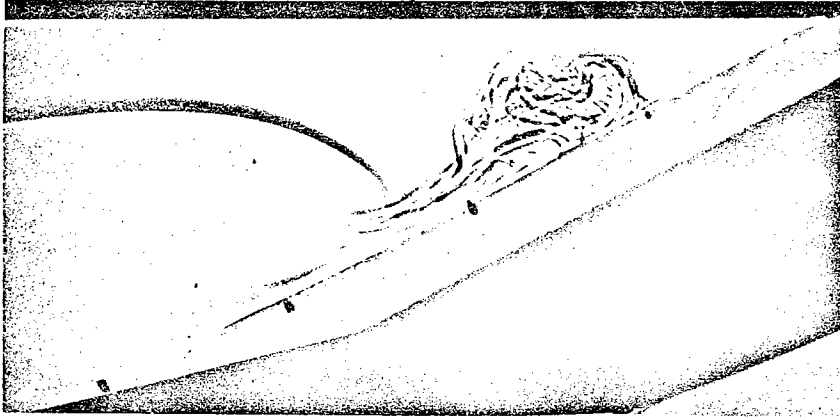
Fig. 49a.
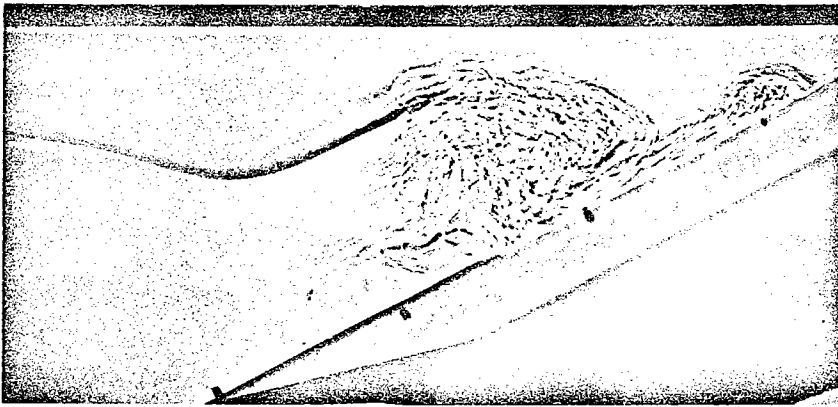
Fig. 49b.

Fig. 49c.

FIG. 50. Advancing initial vortex at successive locations A, B, and C.
Note observed reversal in circulation at position C.
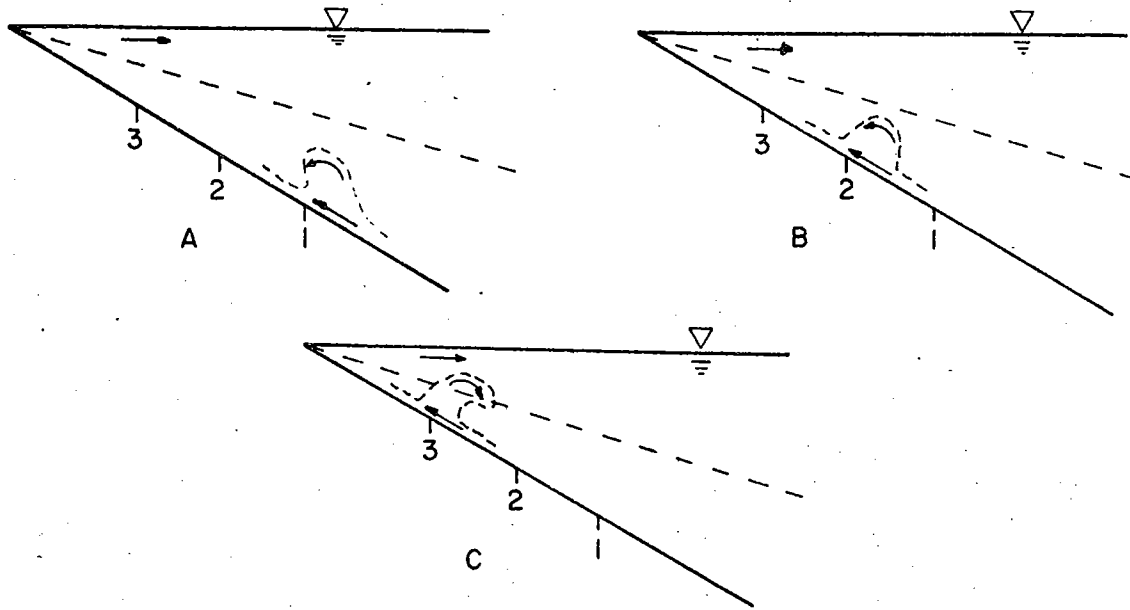
The outflow above the vortex balances the flow of water that is advected
toward the corner along the bottom by the wave motion.

As indicated by the well developed lamellar structures in Figures
49b and 49c, the steeper slopes appear to produce a high intensity of breaking.
The formation of a surge with associated runup was not observed for the
steeper slopes (30 degrees and 45 degrees) for any wave frequency tested.

Figure 51 presents a summary of the observed positions of breaking
on slopes of 30 degrees. The accuracy of the distance L_b is low, owing to
the difficulty in defining the point of breaking; however, the relative order
of the values of L_b for the waves of different frequencies shown in the figure
is reliable. The general trend indicates that for a given N, the higher fre-
quency waves break first, i.e., in deeper water.

FIG. 51. Position of breaking

α = 30°, N = 0.97

ω, sec^{-1}	T, sec	L_b, cm	
		$a_o = 0.2$ cm	$a_o = 0.4$ cm
0.722	8.7	13.4	14.0
0.668	9.4	12.5	12.9
0.593	10.6	10.6	11.1
0.561	11.2	9.9	10.5
0.537	11.7	9.0	9.5
0.515	12.2	8.2	8.6
0.495	12.7	7.7	8.2
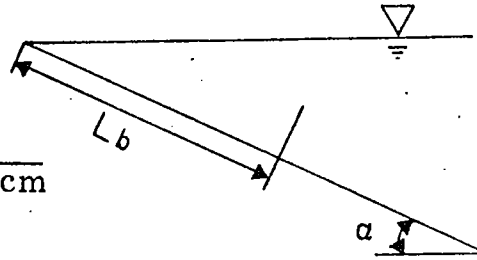
Quantitative results. The experimental techniques that were used to measure the motion in the boundary layer are discussed in Chapter 2. The results of these measurements are compared with the predictions of the linear, viscous boundary layer solutions in order to check the validity of these solutions for certain conditions and provide some empirical estimates of the motion where the theory does not apply.

Since successive displacements of the dye streaks and neutrally buoyant particles were measured at one-second time intervals, the velocity values computed from these measurements are essentially one-second time averages in the Lagrangian sense. Equation (4-24) provides a linear, Eulerian solution for the velocity field parallel to the bottom in the viscous boundary layer; this solution is identical with the Lagrangian one to first order in ϵ. The Lagrangian velocity $\vec{u}_L$ can be determined in principle from the Eulerian velocity $\vec{u}_E$:

$$\vec{u}_L (\vec{a}, t) = \vec{u}_E (\vec{a}, t) + \int_{t_o}^{t} \vec{u} (\vec{a}, t') \, dt' \cdot \nabla_{\vec{a}} \vec{u}_E \qquad (4\text{-}27)$$

where $\vec{a}$ is a position of the dye streak, say, at time to, $t - t_o$ is small compared to the wave period T; and ∇ is the gradient operator. (Phillips, 1966)

This expression for $\vec{u}_L$ is correct to $O(\epsilon^2)$ if $\vec{u}_E$ is correct to this order.
Let

$$\vec{u}_E = \epsilon \vec{u}_E^{(1)} + \epsilon^2 \vec{u}_E^{(2)} \tag{4-28}$$

where $\vec{u}_E^{(1)}$ is the linear solution for the velocity field. It is easy to show that there are two second order contributions to $\vec{u}_L$ in Equation (4-27): (1) $\vec{u}_E^{(2)}$ and (2) $(\int_{t_o}^{t} \vec{u}_E dt') \cdot \nabla \vec{u}_E$. The first contribution (1) is due to the nonlinear terms in the equations of motion; the second (2) is commonly referred to as the Stokes velocity and can be computed in principal from Equation (4-21). Hogg and Wunsch (1970) have shown that to order ϵ^2 the time average of $\vec{u}_L$ for this problem is zero. This implies that there is no net transport of water particles induced by internal waves near a sloping boundary. It also implies that since $\overline{\vec{u}_E^{(1)}} = 0$, then

$$\overline{\vec{u}_E^{(2)}} = -\overline{(\int_{t_o}^{t} \vec{u}_E^{(1)} dt') \cdot \nabla \vec{u}_E^{(1)}} \tag{4-29}$$

where the bar denotes a time average over one wave period.

A complete analysis of the data was carried out for three wave frequencies in regime I ($\gamma < c$). Two of these analyses involved waves on a 30 degree slope ($\omega = 0.105$ cps and $\omega = 0.094$ cps, group 7, Figure B1, Appendix B) and one involved waves on a 15 degree slope ($\omega = 0.105$ cps, group 2). For the sake of brevity, and without any appreciable loss of detail, only the results from $\omega = 0.105$ cps will be discussed at length. Instances where measurements from the other runs showed significant features of deviations from this one will be mentioned in the discussion. The results for regime II ($\gamma \geq c$) are discussed in a later section.

A time-sequenced series of streak and particle positions from which velocity information was obtained is shown in Figure 12. The streaks are numbered according to consecutive, one-second time marks relative to the initial one. The numbers on the particles correspond to those for the streaks. The increase in displacement of the streaks nearer to the bottom agrees qualitatively with the amplification predicted by Wunsch (1969) for $\gamma < c$ (Figure 52).

Figure 53 summarizes some of the relevant parameters that were estimated from the measurements. The five station marks in the diagram show the locations of dye pellets. The coordinates for these locations are given in columns 2 and 3. The definitions of the various Reynolds numbers and estimates of boundary-layer thickness are given in the legend. The approsimate maximum error in the measured estimates of the boundary-layer thickness (δ_m) is 10 percent of the listed value.

The boundary-layer behavior for steep slopes (30 degrees) is anomalous on the lower portion of the slope. The data at station 4 for $\omega = 0.105$ cps (Figure 57) and $\omega = 0.094$ cps both reveal erratic streak displacement. The estimates of boundary-layer thickness at this location were slightly larger or approximately equal to those at station 3. The measured thickness of the boundary layer at corresponding positions on the smaller slope (15 degrees) generally increased in an upslope direction to the zone of breaking. The anomalous behavior for steeper slopes was probably associated with an adjustment in the modal structure as the waves progressed from the flat-bottom region to one of appreciable slope. The irregularities in the motion at station 4 are discussed later in this section.

The larger values of δ_m as compared with δ_2 at stations 1, 2, and 3 represent significant departures of the measured estimates from the theoretical values. In addition, the theoretical value is constant over the entire slope, whereas the measurements indicate that δ_m varies slightly with slope positions. Over the flat bottom, δ_m is slightly larger than the value given by $(2\nu/\omega)^{1/2}$, although this difference was not significant for

Z

0.6   0.8   1.0   X

w (z)

C = 1.0

γ = 0.5

n = 1

0.6   0.8   1.0

u (z)
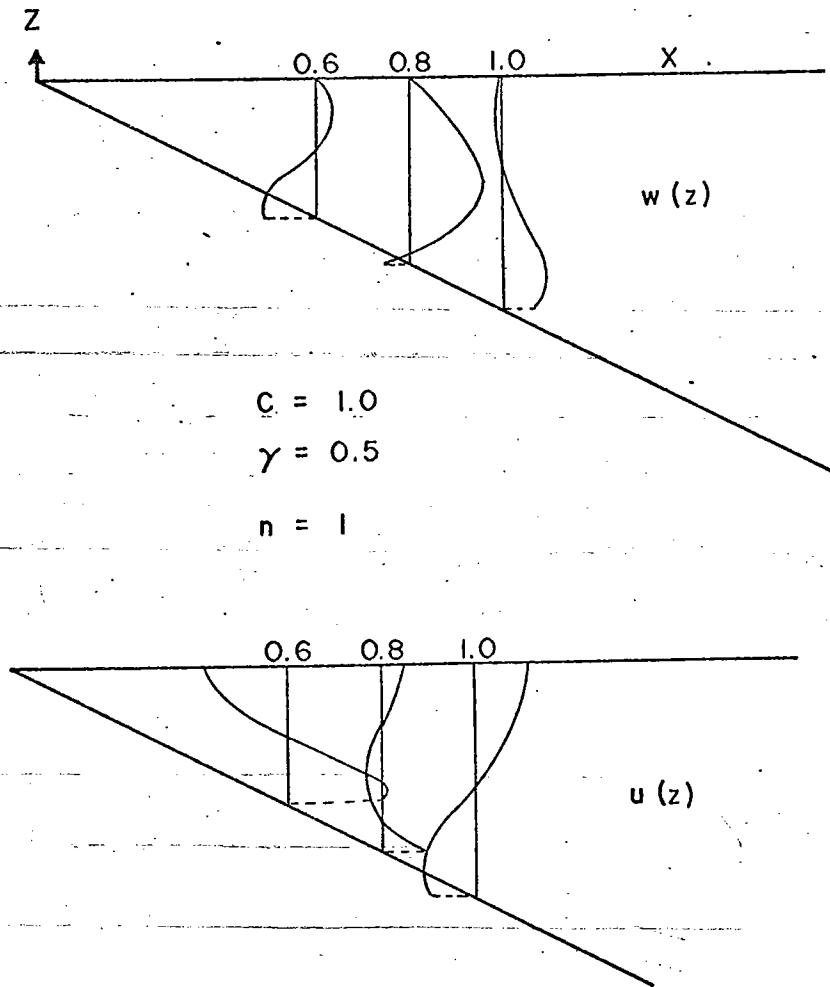
Fig. 52.   Theoretical prediction of increase in
velocity components along the slope.   Units
are arbitrary (after Wunsch, 1969).

There is no page 123

ω = 0.66 rad/sec, T = 9.5 sec
N = 0.97 rad/sec, C = 0.93
α = 30 deg γ = 0.577
a_0 = 0.2 cm
k_0 = 0.097 cm^{-1}, λ_0 = 64.7 cm
h_0 = 30.0 cm
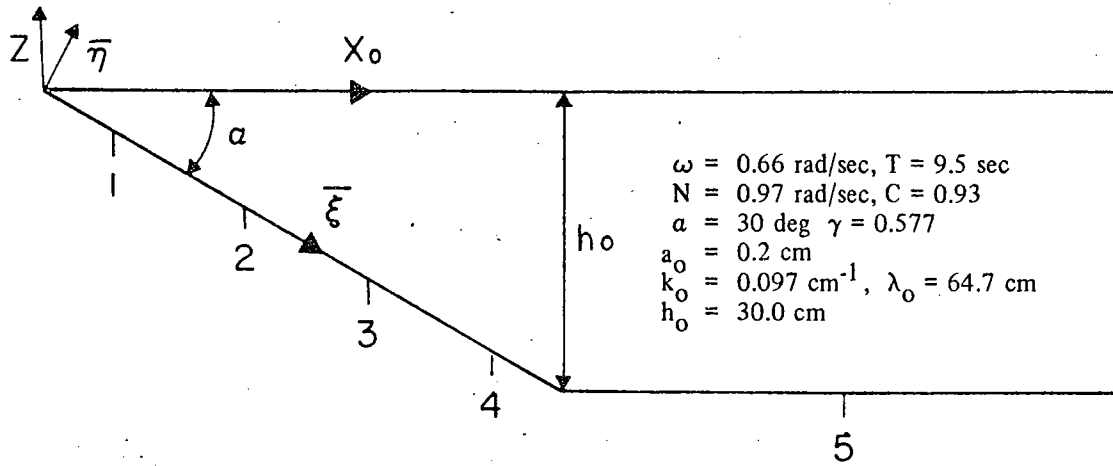
1	2	3	4	5	6	7	8	9	10	11	12
Station No.	x_c (cm)	h (cm)	R_L $\times 10^{-3}$	R_W	R_B	δ_1 cm	δ_2 cm	δ_m cm	δ_s cm	a_m cm	ϵ
1	8.7	5.0	2.4	209.0	41.2	0.17	0.26	0.35	0.17	1.78	0.52
2	23.0	13.3	17.2	32.4	21.7	0.17	0.26	0.47	1.16	0.70	0.08
3	36.0	20.8	42.0	19.3	13.0	0.17	0.26	0.39	2.17	0.54	0.04
4	51.0	29.4	83.8	62.2	25.0	0.17	0.26	0.39	1.74	0.97	0.05
5	100.0	30.0	87.3	4.1	3.6	0.17	0.26	0.22	8.70	0.25	0.01

$R_L = Nh^2/\nu$ = local wedge Reynolds number

$R_W = a^2\omega/\nu$ = local wave Reynolds number

$R_B = a\omega\delta_m/\nu$ = local boundary layer Reynolds number

$\delta_1 = (2\nu/\omega)^{1/2}$

$\delta_2 = (2\nu/N)^{1/2} (\sigma/(\sigma^2 - \sin^2\alpha)^{1/2}$, $\sigma = \omega/N$

$\delta_s = \delta_1/\epsilon$

$\epsilon = a_m k_m \sin\alpha$

FIG. 53. Estimated of boundary layer thickness and
Reynolds numbers. $\gamma < c$.

the experiments in which $\omega = 0.105$ cps, $\alpha = 15$ degrees. It appears that the boundary layer thickness given by linear theory gives the correct order, mm rather than cm, but the measured values tend to be significantly higher. However, it must be recalled that the definition of boundary layer thickness for the purposes of measurement, i.e., the distance between the bottom and the point of inflection in the velocity profiles, is somewhat arbitrary, and might account for the discrepancies with the theoretical values.

It should also be mentioned here that at station 1, the computed value of ϵ is relatively high ($\epsilon \simeq 0.5$); nonlinear effects are probably important there. It was mentioned earlier that Wunsch (1970) recently showed theoretically that there can be a mean upwelling velocity independent of wave motion in a layer whose thickness is δ_w:

$$\delta_w \sim (\nu \, \kappa)^{1/4}/N^{1/2}$$

where ν and κ are the vertical diffusivities of momentum and heat, respectively. In terms of molecular processes, $\nu \sim 10^{-2}\,\text{cm}^2/\text{sec}$ and $\kappa \sim 10^{-3}\,\text{cm}^2/\text{sec}$. Using the value of N given in Figure 53, $N \sim 1\,\text{sec}^{-1}$, we can estimate $\delta_w \sim 0.06$ cm for this particular experiment.

The curves in Figures 54 through 58 show velocity versus depth for all five stations. Each curve represents a one-second time average of the Lagrangian velocity parallel to the bottom. The consecutive numbers on the curves indicate the time history of this velocity over one wave cycle. The curves were computed only to the vertical level nearest the bottom for which the streak data was considered reliable. The horizontal velocity scales are uniform in each of the figures except for the expanded scale of the flat bottom results (Figure 58) and the condensed scale at station 1; the vertical scales are the same for all figures.

It is important to note that at each of these stations the observed motion in and near the boundary layer was essentially parallel to the bottom.
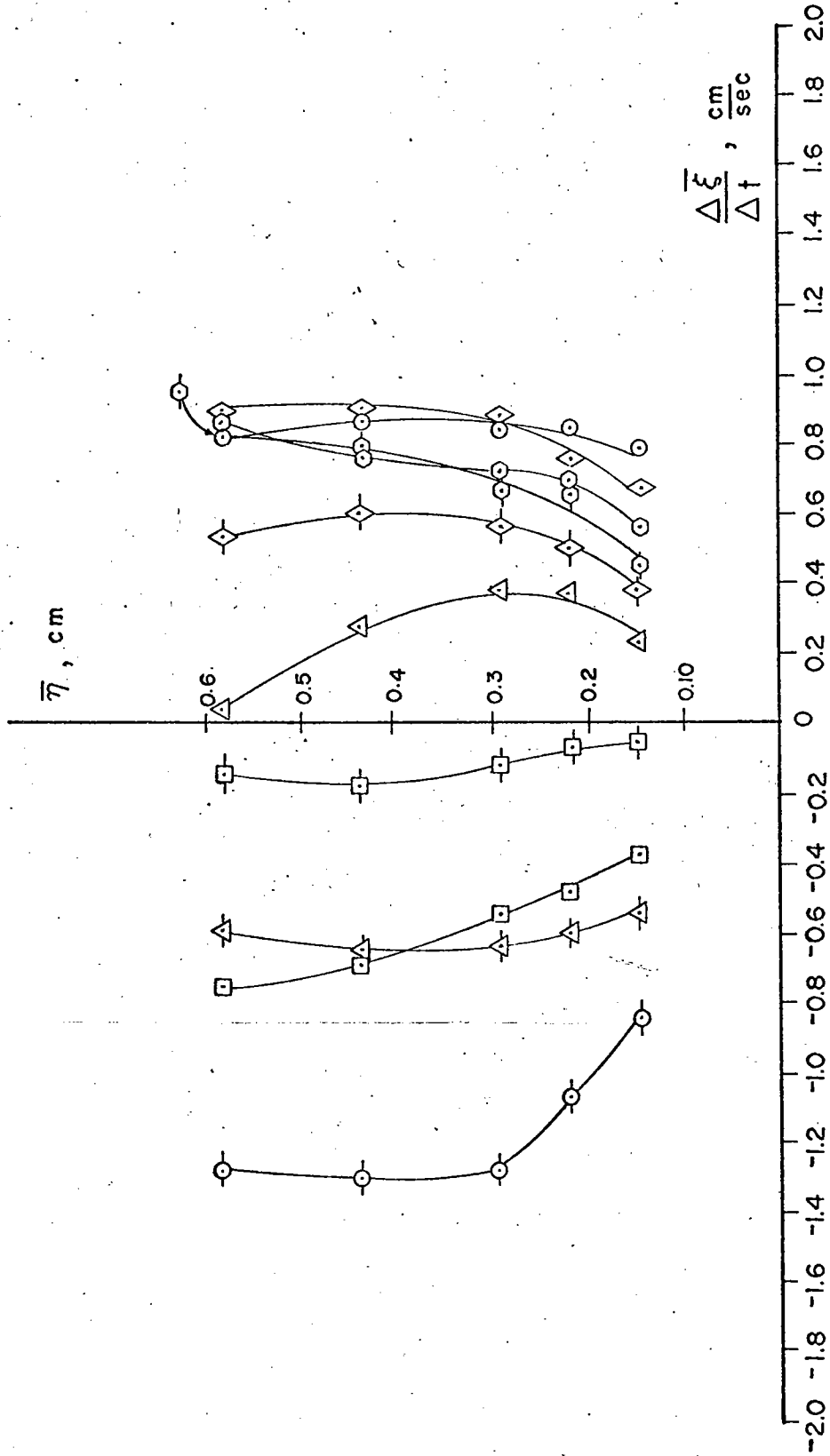
Fig. 54. Vertical distribution of velocity near the bottom at station 1.
$a_0 = 0.2$ cm, $\omega = 0.105$ cps, $N = 0.155$ cps, $\alpha = 30$ deg,
$x_c = 8.7$ cm.
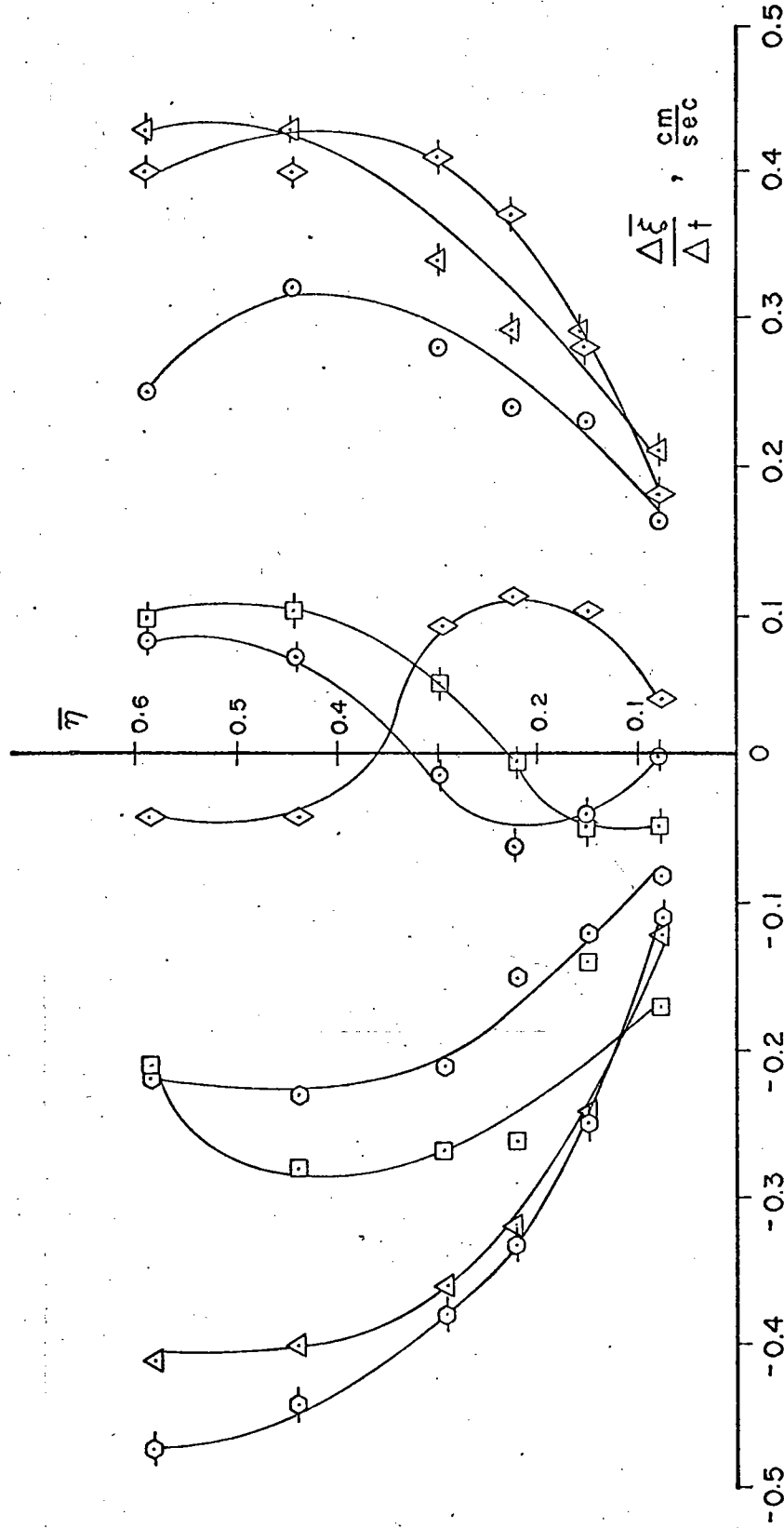
Fig. 55. Vertical distribution of velocity near the bottom at station 2.
$a_o = 0.2$ cm, $\omega = 0.105$ cps, $N = 0.155$ cps, $\alpha = 30$ deg,
$x_c = 23.0$ cm.
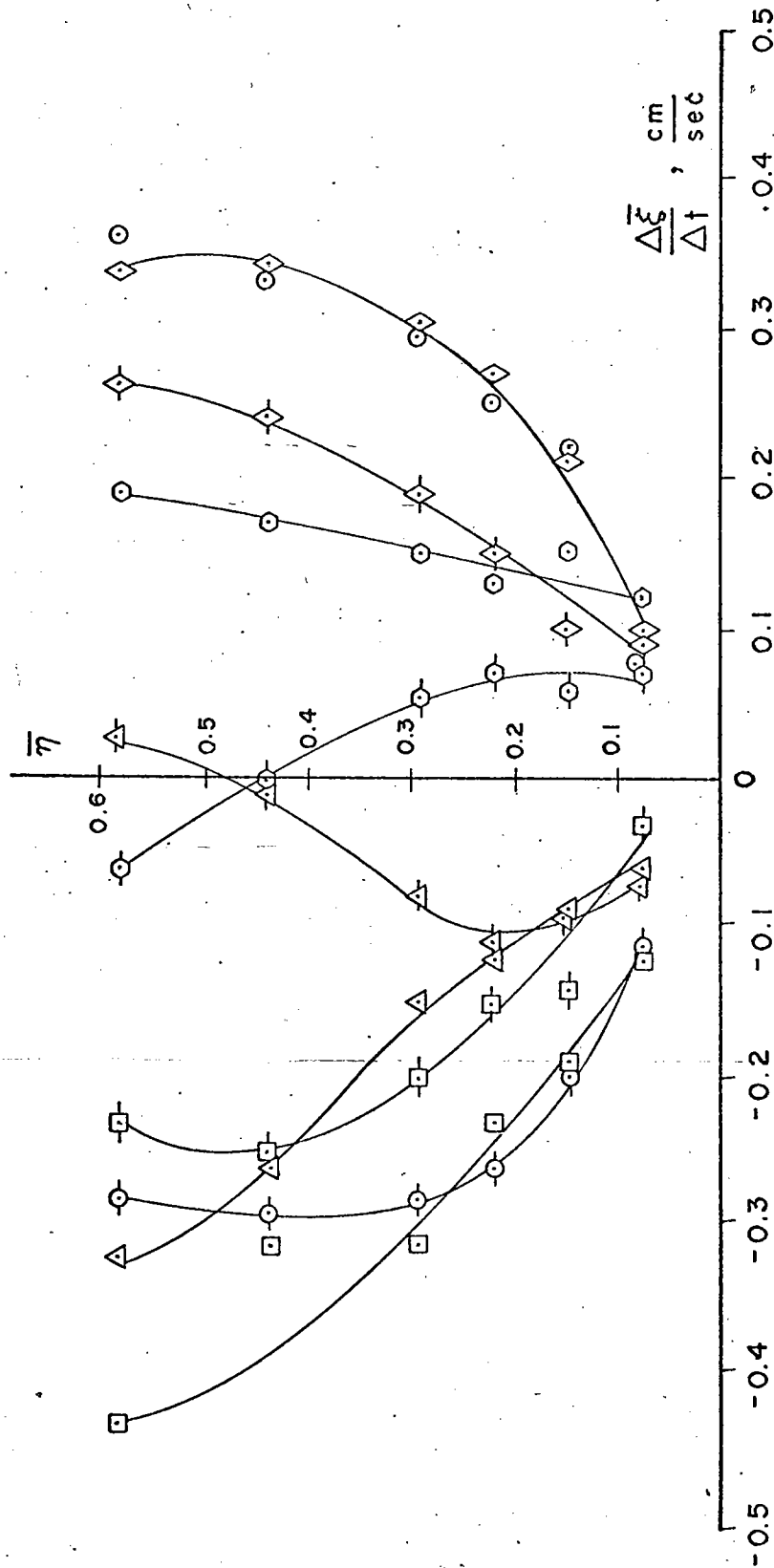
Fig. 56. Vertical distribution of velocity near the bottom at station 3.
$a_o = 0.2$ cm, $\omega = 0.105$ cps, $N = 0.155$ cps, $\alpha = 30$ deg,
$x_c = 36.0$ cm.
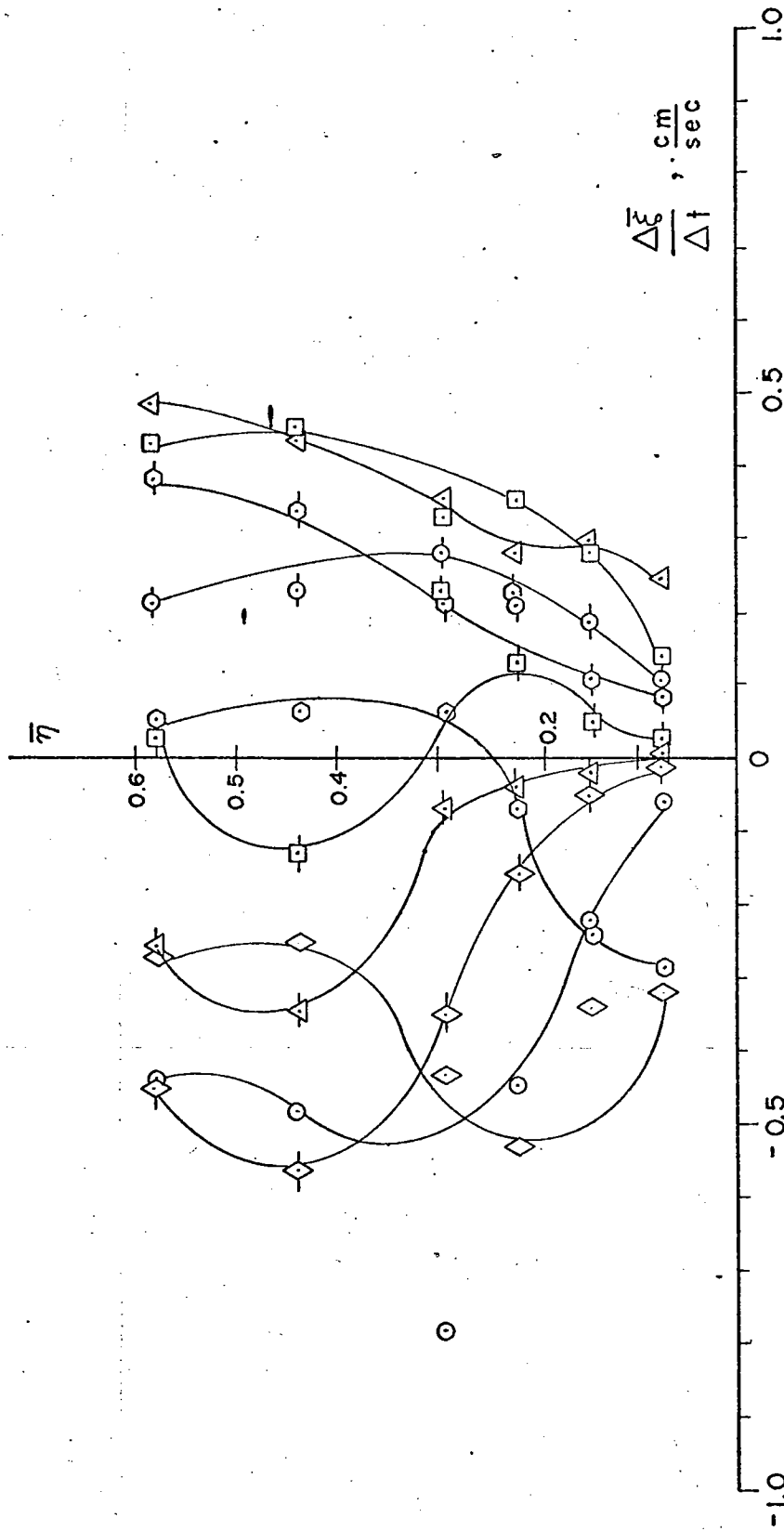
Fig. 57. Vertical distribution of velocity near the bottom at station 4.
$a_o = 0.2$ cm, $\omega = 0.105$ cps, $N = 0.155$ cps, $\alpha = 30$ deg,
$x_c = 51.0$ cm.
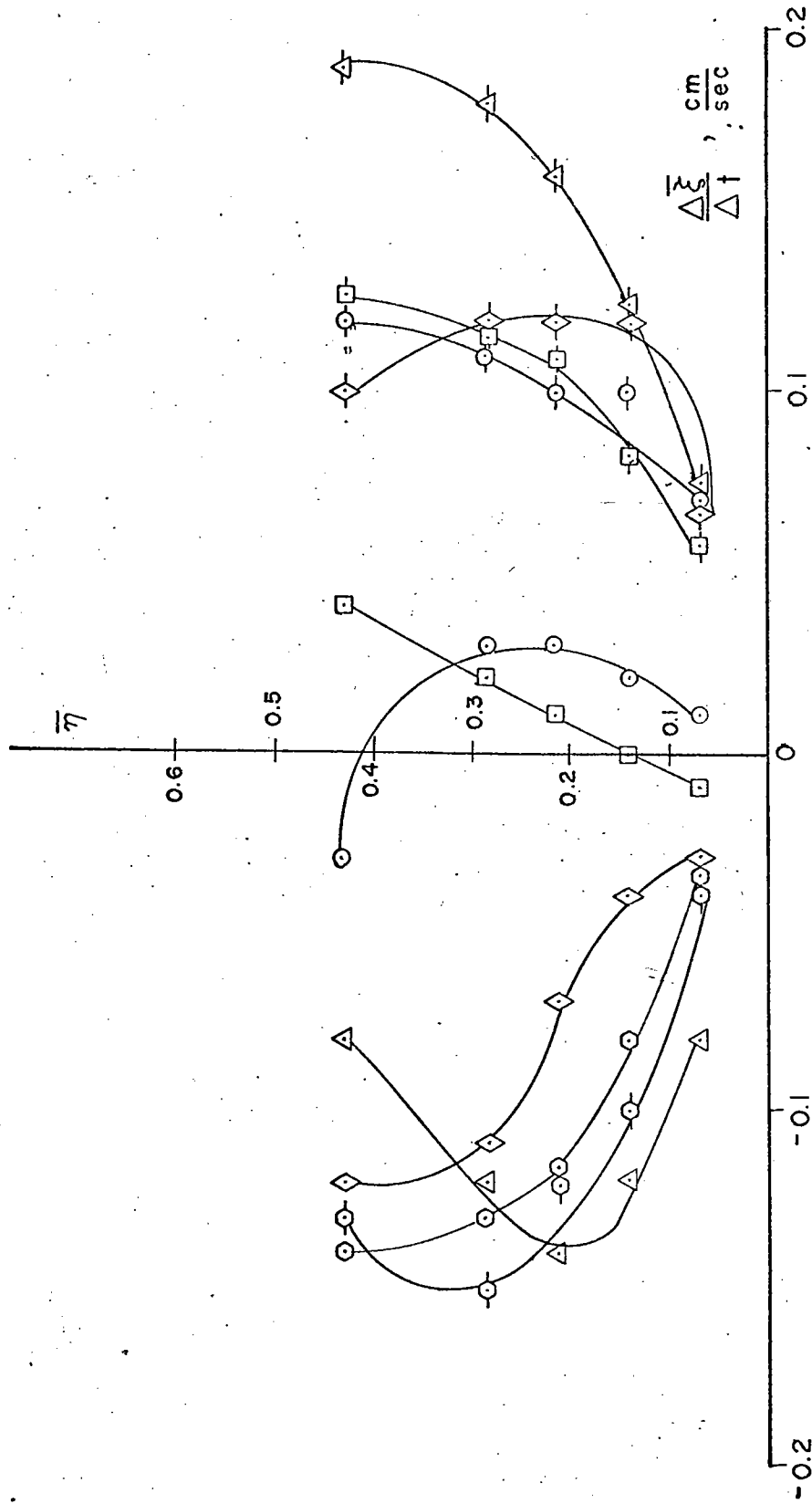
Fig. 58. Vertical distribution of velocity near the bottom at station 5.
$a_o = 0.2$ cm, $= 0.105$ cps, N = 0.155 cps, $= 30$ deg,
$x_c = 100.0$ cm.

Only very small velocities normal to the bottom were detected from the motion of the plastic beads, and this vertical motion was usually confined to regions adjacent to and in the zone of breaking.

A reason for the anomalous behavior of the velocities at station 4 (Figure 57) was hypothesized earlier in this section. An alternative explanation is that the abrupt change in bottom geometry acts as a source of diffracted waves which locally affect the pattern of motion. However, since the density did not vary linearly with depth at the bottom (for example, Figure 9), but instead gradually became more homogeneous in a small layer near the bottom, the dynamics in this transition region are probably quite complicated. Visual observations of the motion of neutrally buoyant particles and dye patches that were placed at the transition in bottom geometry during several experiments (for 15 and 30 degrees slop angles) did not disclose any significant patterns other than those already mentioned.

Figure 59 shows a comparison between the theoretical and experimental RMS values of the velocities at selected vertical levels shown in Figures 54 through 58. The experimental RMS value at each level was computed as:

$$u_{RMS} = (u_{MS})^{1/2}$$

where

$$u_{MS} = \sum_i (u_i^2)/T \quad , \quad i = 1, 2, \ldots\ldots, T$$

and T was chosen as the smallest integer greater than the wave period. For this particular set of data, $T = 10$ (wave period $\simeq 9.5$ sec). For stations on the slope, theoretical RMS values were obtained from the Eulerian expression for the boundary layer velocity component parallel to the slope (Equation (4-24)):

$$u_{RMS} \text{ (theory)} = (1/2 \, u_E \cdot u_E)^{1/2}.$$

These RMS values are listed in Figure 59 as first order theoretical estimates of the RMS Lagrangian velocities.

Qualitatively, we might expect that the measured values are more accurately represented by the sum of the first order Eulerian values and the second order values consisting of the Stokes velocity component and the nonlinear component, particularly farther upslope where ϵ become larger.

When the various sources of uncertainty in the measurements of velocity and experimental parameters (A_o, N, ω, h, etc.) are considered, a rather good comparison would require that the theoretical and experimental values fall within 15 percent of one another at each level $\bar{\eta}$. The results in Figure 59 show that excluding station 4 there is excellent agreement (within 10 percent) between the measured RMS values and the corresponding first order, theoretical values. The excellent comparison at station 1 is particularly remarkable, considering that the estimated value of ϵ is approximately 0.5 there. The high measured values at station 4 are a consequence of the anomalous motion that has already been discussed.

The results for the maximum velocity $|u|$ max parallel to the bottom at the selected levels (columns 6, 7, 8, Figure 59) also show good agreement between experiment and theory. Theoretical estimates of the maximum values of this velocity component were again obtained from Equation (4-24). The maximum computed Stokes velocity is shown in column 8. The experimental values are generally higher than the theoretical first order values. The large deviations between experiment and theory at station 4 are again obvious. The results for the other analyses of this kind show similar, good

FIG. 59

Station No.	$\bar{\eta}$, cm	u, RMS, cm/sec		|u| max, cm/sec		|τ| max, dynes/cm^2	
		Exp.	Linear Theory	Exp.	Linear Theory	Exp.	Theory $\times 10^2$
1	0.15	0.598	0.54	0.85	0.70	5.67	6.79
	0.22	0.73	0.69	1.07	0.93	5.67	6.79
	0.29	0.81	0.79	1.28	1.11	5.67	6.79
	0.44	0.85	0.91	1.30	1.28	5.67	6.79
2	0.15	0.20	0.20	0.28	0.23	1.87	2.56
	0.22	0.26	0.26	0.37	0.27	1.87	2.56
	0.29	0.29	0.30	0.41	0.28	1.87	2.56
	0.44	0.32	0.34	0.44	0.26	1.87	2.56
3	0.15	0.15	0.13	0.22	0.16	1.40	1.61
	0.22	0.19	0.16	0.27	0.22	1.40	1.61
	0.29	0.19	0.19	0.31	0.26	1.40	1.61
	0.44	0.25	0.22	0.39	0.30	1.40	1.61
4	0.15	0.21	0.09	0.34	0.07	2.27	1.16
	0.22	0.29	0.12	0.53	0.08	2.27	1.16
	0.29	0.36	0.14	0.78	0.08	2.27	1.16
	0.44	0.36	0.15	0.75	0.06	2.27	1.16
5	0.15	0.09	0.00	0.12	0.01	0.60	0.08
	0.22	0.11	0.01	0.16	0.02	0.60	0.08
	0.29	0.12	0.01	0.18	0.02	0.60	0.08
	0.44	0.12	0.00	0.19	0.01	0.60	0.08

agreement between theory and experiment. The velocity values for station 4 with the 15 degree slope are more in agreement with the theoretical values (within 25 percent) than are the results in Figure 59 and did not show anomalously large velocity values for this station.

The asymmetry in the velocity profiles at station 1 (Figure 54) contrasts with the more symmetrical curves for the other stations. Station 1 is located well upslope and only a few centimeters from the zone of breaking. The skewness toward positive velocities suggests that there might be a measurable net upslope motion of the water particles over one wave cycle. Although the maximum velocity is directed downslope (curve 1, Figure 54), the magnitudes of the upslope component are quite high (approximately 1 cm/sec) for a considerable fraction of the wave cycle. The local measured value of ϵ is about 0.5 at this station, which suggests that nonlinear effects might be important. It is also interesting to note that δ_m at this station shows a decrease from that at station 2 (Figure 53).

Experimental estimates of net drift at the outer edge of the boundary layer were computed at each station by algebraically averaging the measured velocity values at the estimated level of δ_m in Figures 54 through 58, respectively. The average is for one wave cycle (sampling interval of one second) and represents a single estimate of mean streaming at each station. No statistical significance can be inferred from this method, but the measured results in Figure 60 show that the streaming is insignificant at all slope stations except station 1. Here the net drift is approximately 1.3 mm/sec. This drift is probably induced by mixing in the nearby (3 - 5 cm) zone of breaking. As discussed earlier, protrusions of thin fluid laminae slowly advect into the interior over the slope from the zone of breaking. The direction of the drift measured at station 1 is toward the breaker, possibly indicating that this flow compensates in part for the mass efflux in the protrusions. The observed direction net drift near the free surface above this station is also toward the zone of breaking.

FIG. 60. Measured values of mean streaming at $\overline{\eta} = \delta_m$
stations 1 through 4 on slope.

Station No.	x_c, cm	$\overline{\xi}$, cm	μ_s, cm/sec
1	8.7	10.05	+0.13
2	23.0	26.6	-0.07
3	36.2	41.8	-0.003
4	51.0	58.9	-0.023

Owing to the poor reliability of the raw streak data very near the wall (<0.07 cm), the best experimental estimate of bed shear stress, τ_o, was obtained by extending the reliable portion of the velocity-depth curves to the zero point at the bottom. The shear stress was then computed from a simple straight-line fit between the zero point and the lowest point on the velocity curve. This gives a low estimate of the bed shear stress, since the actual shape of the velocity curves in the boundary layer are more exponential. The maximum bed shear stress $/\tau_o/$max measured at each location is listed in column 9 of Figure 59; the time variations in τ_o over one wave cycle corresponding to the time variations in the velocities in Figures 54 through 58 are shown in Figure 61(a - d). The theoretical values of bed shear stress were computed from Equation (4-24):

$$\tau_o = \bar{\mu} \, \partial u / \partial \bar{\eta} \quad , \quad \bar{\eta} = 0$$

where

$$\mu = 0.01 \, \frac{gm}{cm\text{-}sec^2} \cdot$$

The maximum theoretical value is shown in column 10, Figure 59, for comparison with the corresponding measured value. Since the theoretical estimates were made from the linear Eulerian expression of velocity at each station, they correspond to the experimental Lagrangian estimates only to first order in ϵ. It can be shown that μ varies by only 4 percent over the density range for the particular experimental conditions shown in Figure 53. In spite of the poor comparison of the estimates of boundary layer thickness given by linear theory and experiment, the theoretical estimates of maximum bed shear stress at stations 1 - 3 compare reasonably well with the measured values. This is apparently the consequence of the higher experimental values of maximum velocity as compared to the first-order theoretical values for levels near the boundary. Figure 61 also shows the excellent fit of the theoretical curve computed from first order solutions to the experimental values at stations 1, 2, and 3.
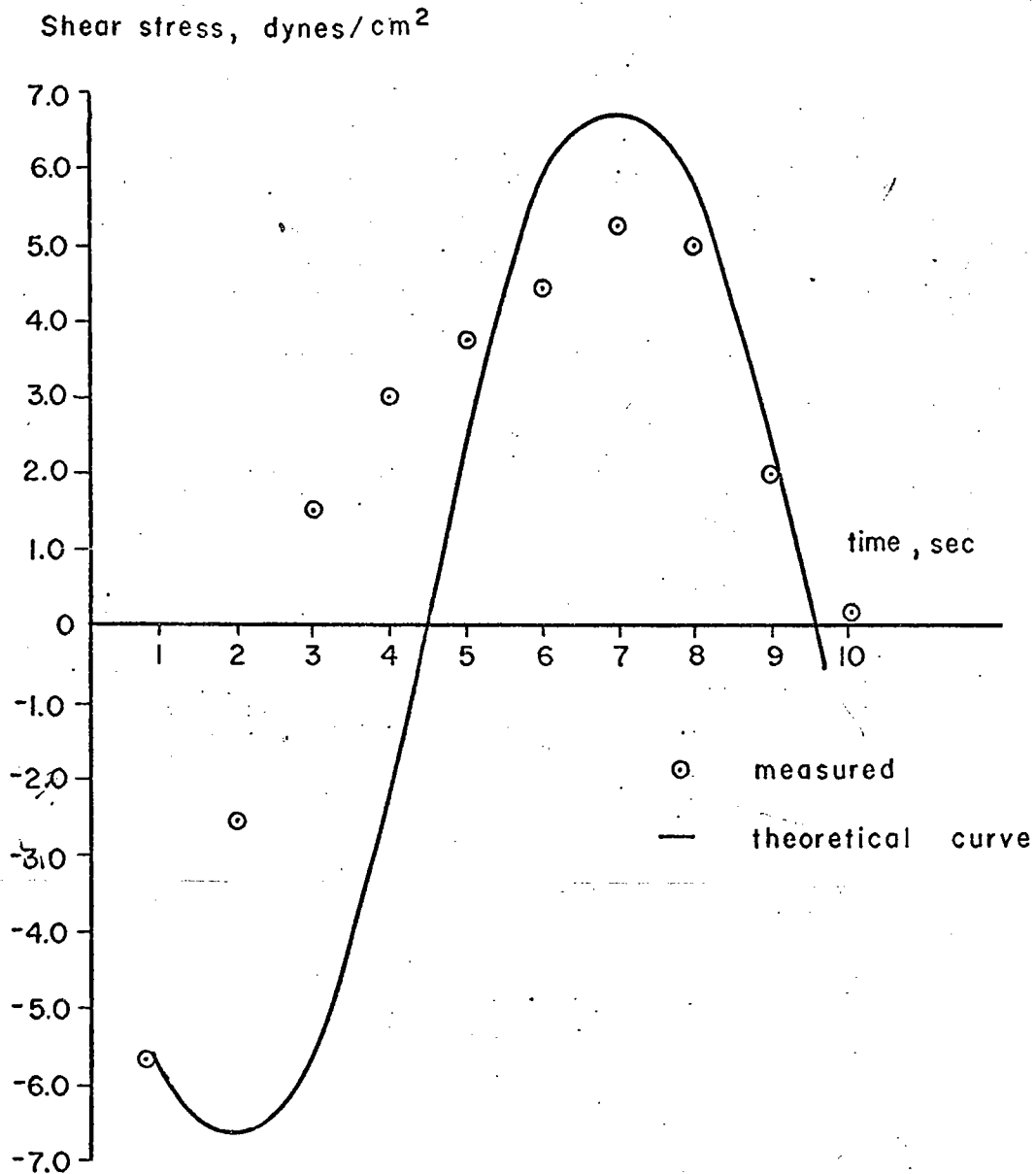
Fig. 61 a. Experimental and theoretical values of bed
shear stress τ_O at station 1. The experi-
mental values were obtained for each
second of time t during one wave cycle.

Shear stress, dynes/ cm^2
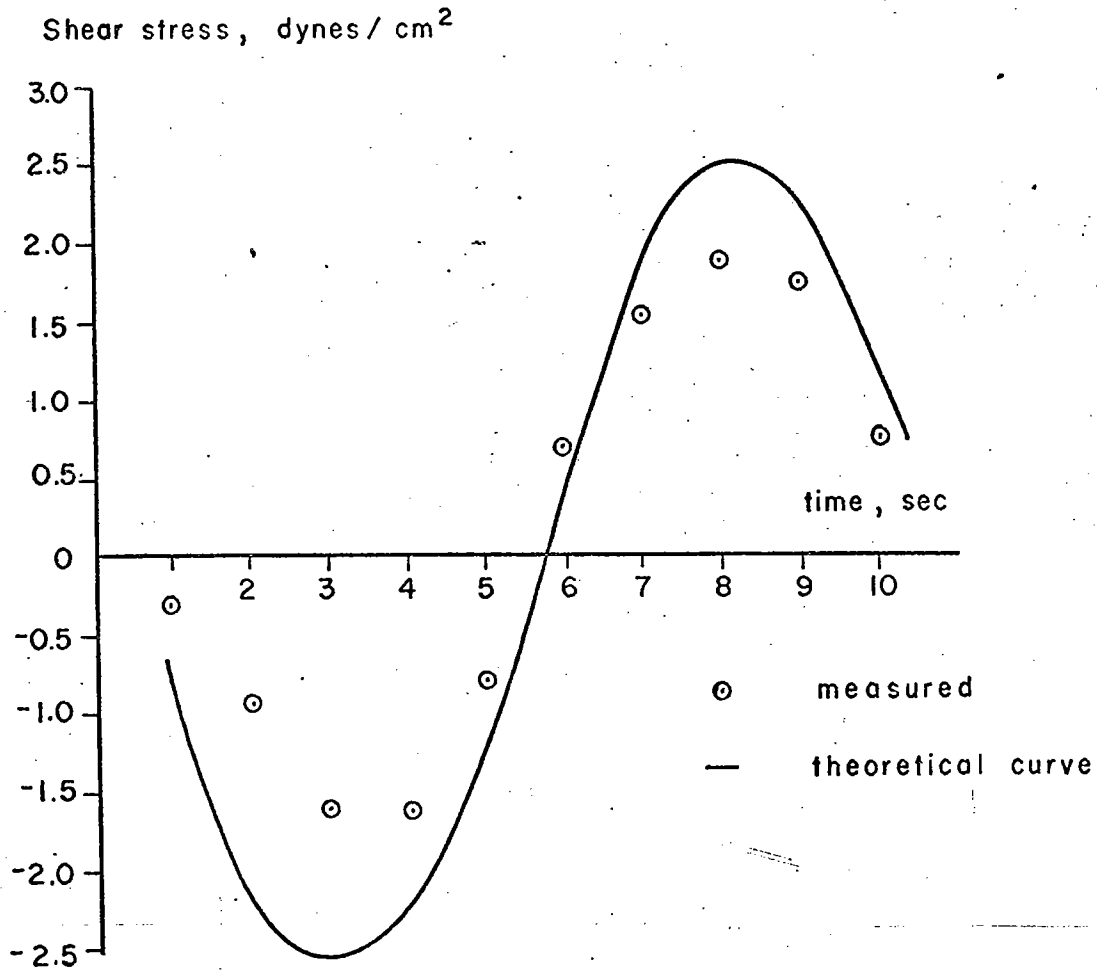
Fig. 61 b.   Experimental and theoretical values of bed
shear stress τ_O at station 2.   The experi-
mental values were obtained for each second
of time t during one wave cycle.
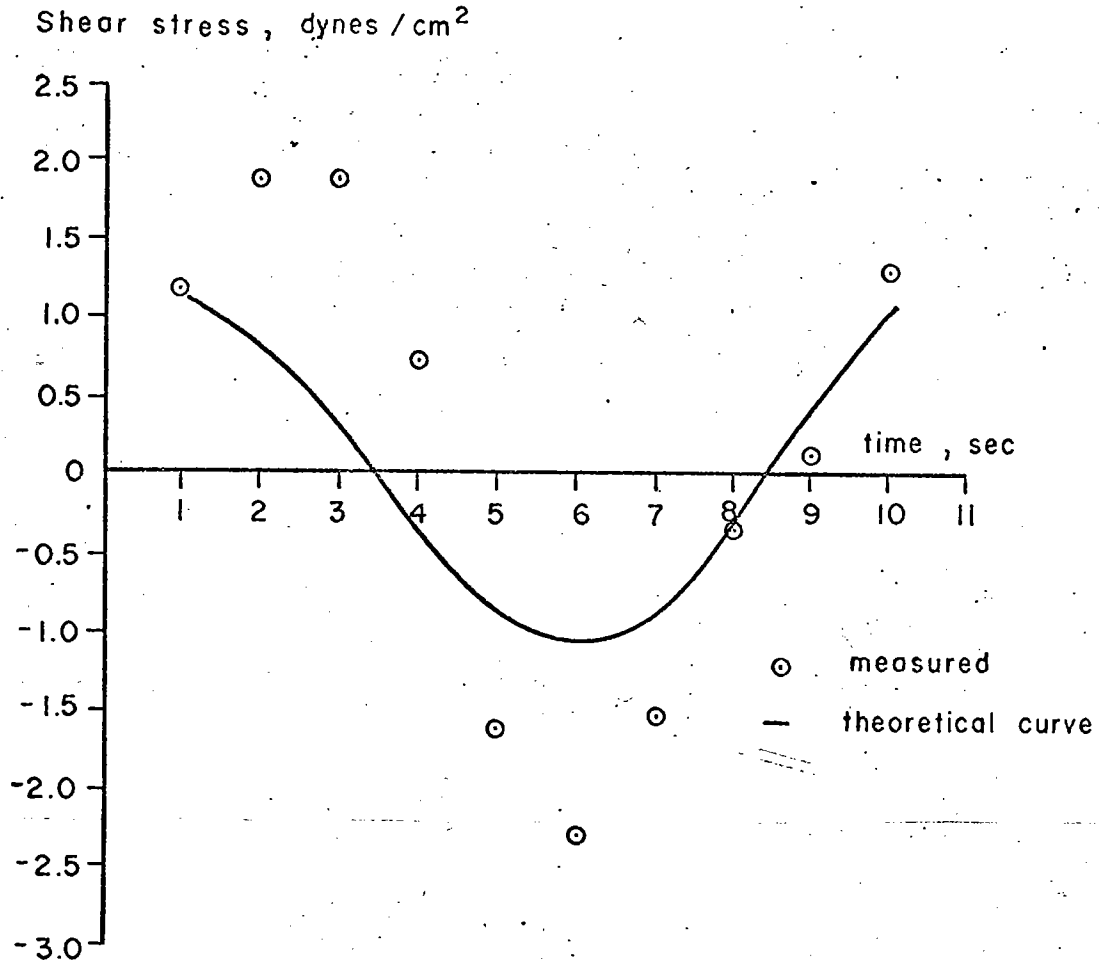
Fig. 61 c. Experimental and theoretical values of bed shear stress τ_O at station 3. The experimental values were obtained for each second of time t during one wave cycle.
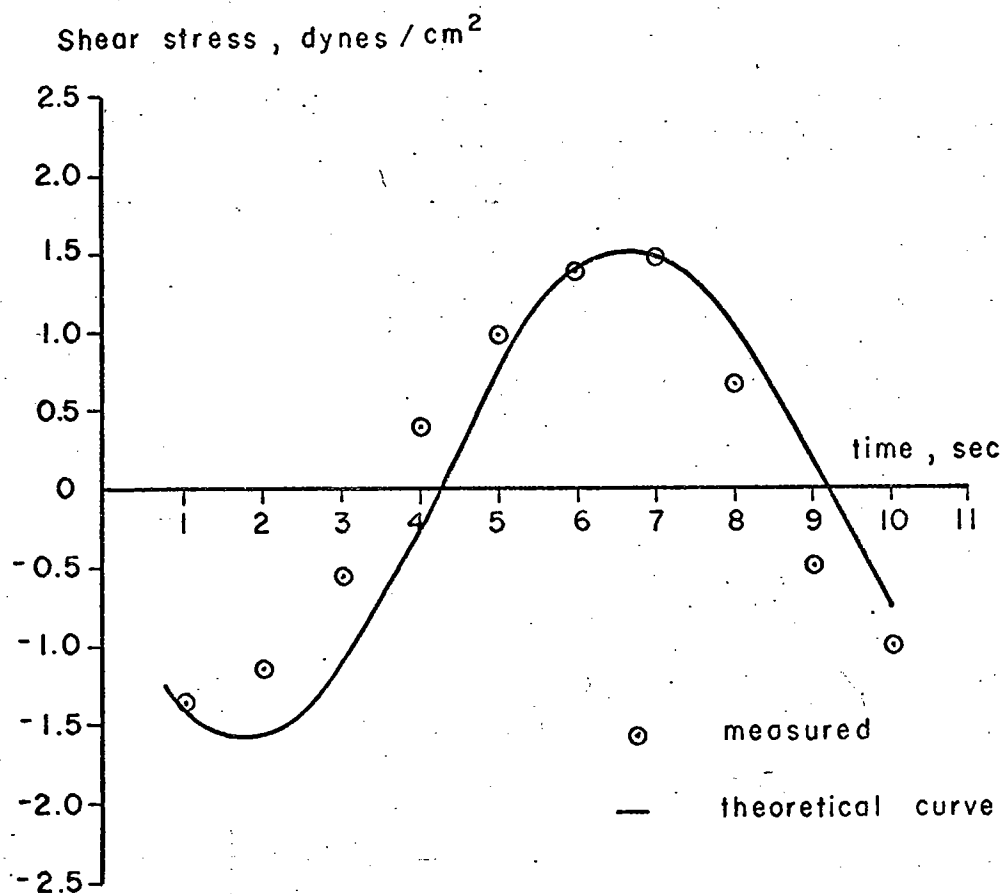
Fig. 61 d. Experimental and theoretical values of bed shear stress τ_0 at station 4. The experimental values were obtained for each second of time t during one wave cycle.

Cases B and C: $\gamma = c$ and $\gamma > c$

The description of the boundary-layer motion in this section follows a format similar to that presented in the discussion of boundary activity for case A ($\gamma < c$). The qualitative remarks deal mainly with the observations and photographs of shadowgraph images, whereas the quantitative results were derived from the measurements of the motion of dye streaks and neutrally buoyant particles.

Qualitative   During those runs for the critical case ($\gamma = c$) with moderately steep slopes (30 and 45 degrees), the zone of breaking near the corner was characterized by intensive mixing as evident in the shadowgraph images, similar to that described for the high-frequency waves on a 30 degree slope (see earlier discussion for $\gamma < c$ in this chapter). For runs with a slope of 15 degrees, each wave, for both the critical and supercritical cases, formed a surge that usually ended with a short runup. This runup usually occurred at the bottom of the more homogeneous near-surface layer, if present, and appeared like a gentle, lapping motion with much smaller upslope penetration than the runup for the subcritical case, which persisted over a much longer distance. In summary, the intensity of breaking and runup for $\gamma \geq c$ is decreased as compared with the experimental observations of these processes for the subcritical case.

Figures 62 through 64 illustrate in a very striking way that the internal wave motion for these cases ($\gamma \geq c$) is associated with the growth of an instability along the slope. The shadowgraph observations of the instability illustrated in these figures indicate that a line of regularly spaced vortices forms near the bottom. These vortices grow and decay over each half cycle as they oscillate along the slope at the frequency of the input waves. It appeared that on the downslope propagation during the wave cycle, the vortices would "flatten", indicating that they form only during the upslope movement of the water particles. This is indicated in Figures 63a and 63b. The circulation of adjacent vortices has the same sense;

Figs. 62 through 64.   Guide to photographs of shadowgraph images in the
                        following figures.

Fig. Number	Input Wave Amplitude (cm)	Wave Period (sec)	Slope (deg)
62a	0.2	12.7	30
62b	0.2	12.7	30
63a	0.2	13.0	30
63b	0.2	13.0	30
64a	0.2	12.1	30
64b	0.2	14.5	30
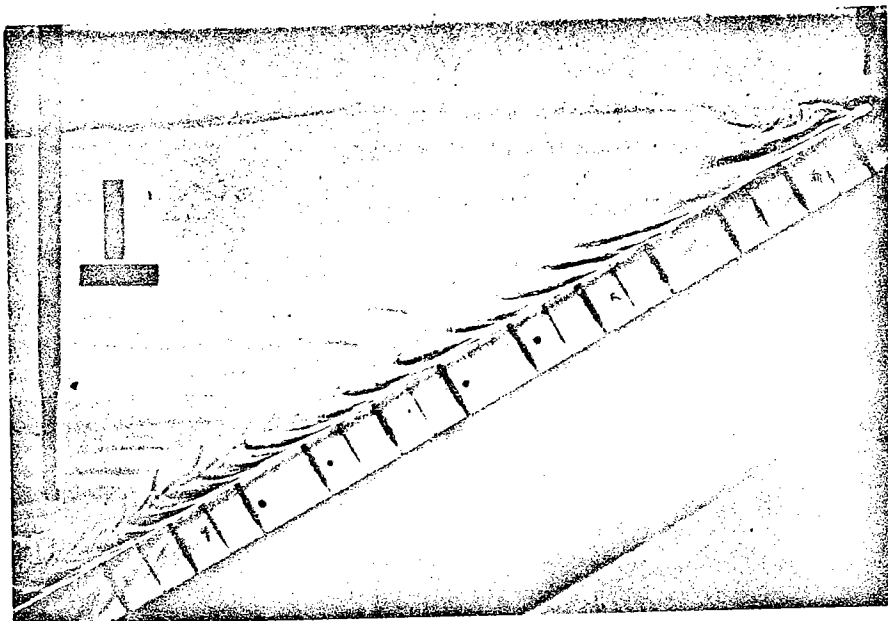
Fig. 62a.
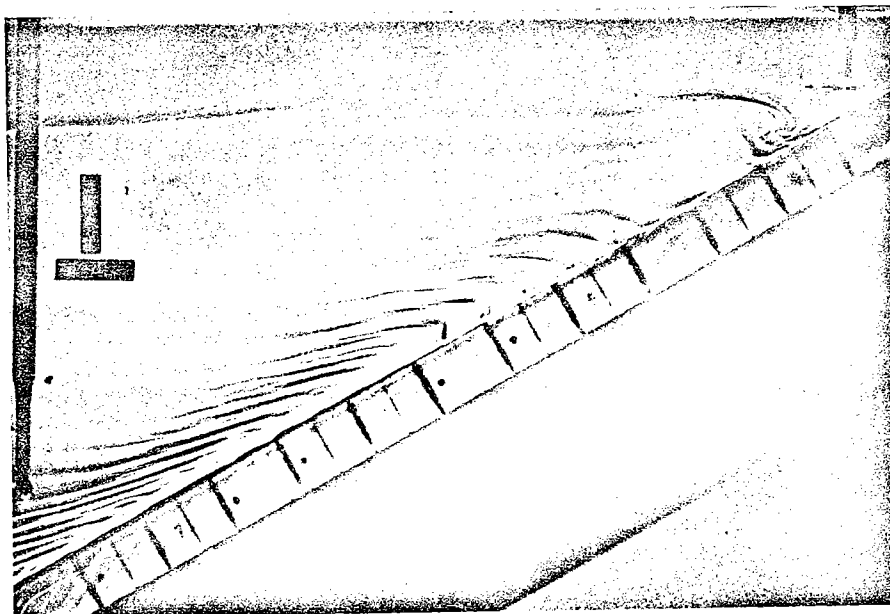
Fig. 62b.
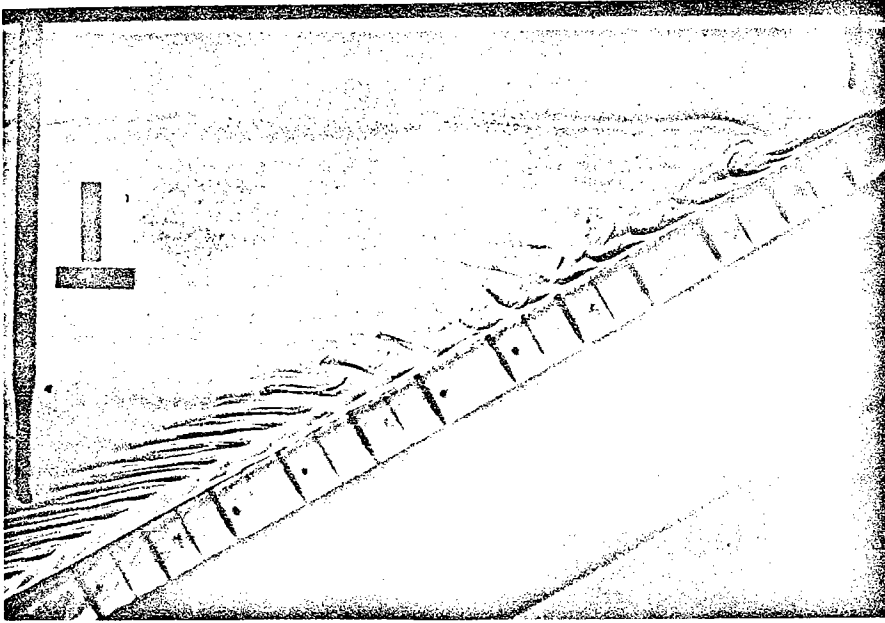
Fig. 63a.
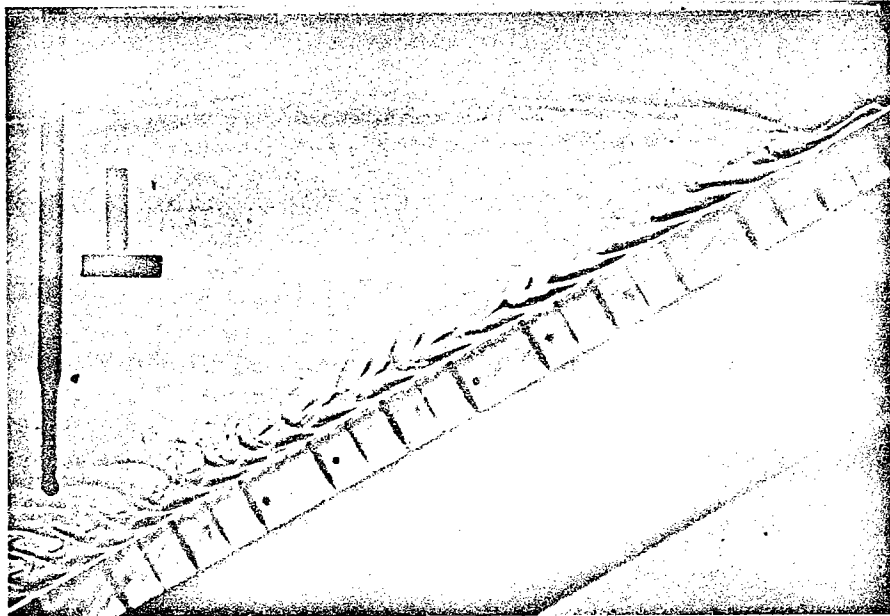
Fig. 63b.
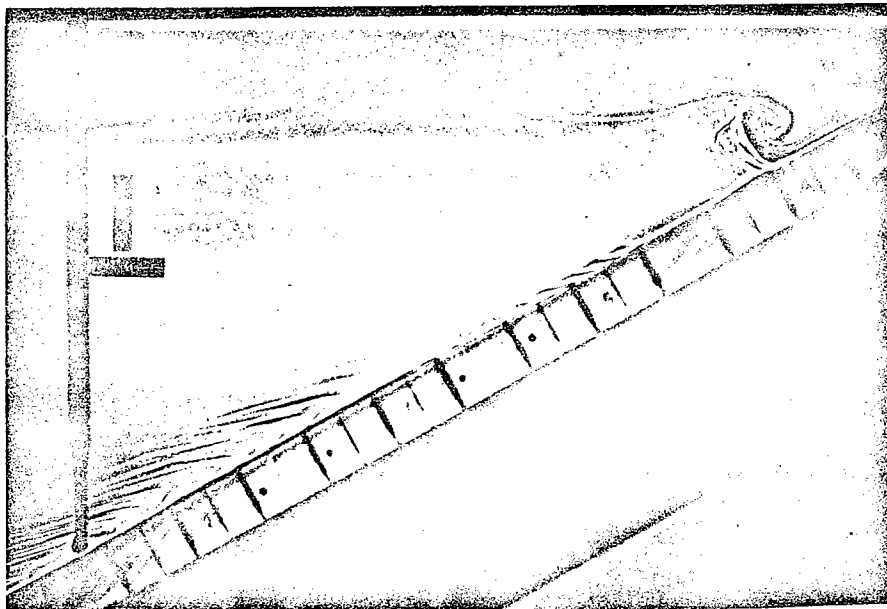
Fig. 64a.
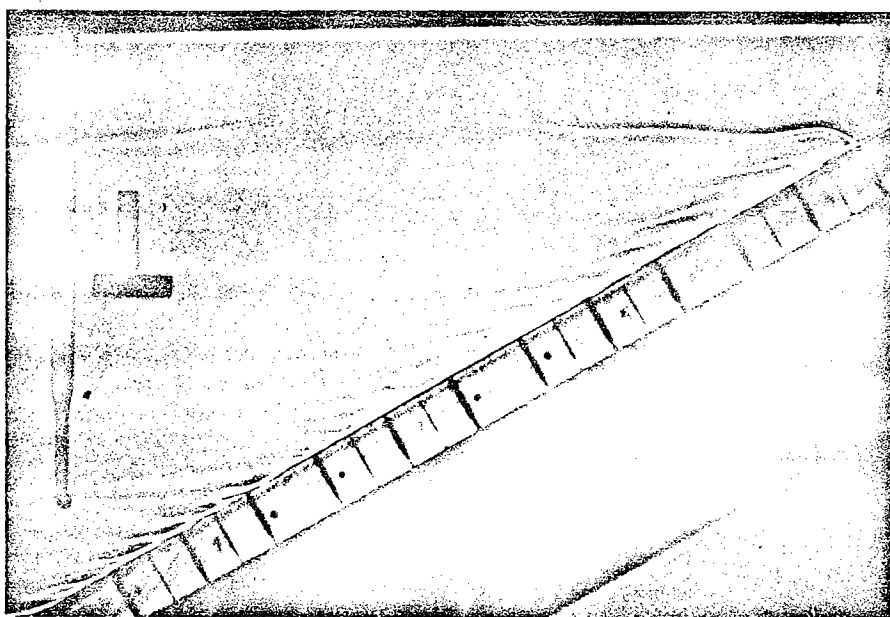
Fig. 64b.

this circulation is indicated diagrammatically below. The axis of each
vortex is oriented approximately normal to the side walls of the tank,
and the maximum distance observed between the core of adjacent vortices was
was about 2 cm. Unlike the vortices which form beneath the shoaling,
high-frequency waves well upslope and which precede the violent breaking
(Figure 45), these vortices retain their cyclic growth and decay pattern
for the duration of the input wave motion. Their regular spacing was much
shorter than the wave lengths of the input waves, particularly at the middle
and lower slope regions.
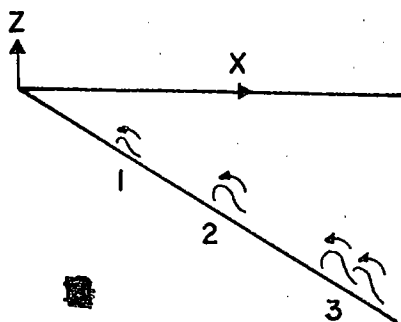
Circulation in Vortices

Shortly after the formation of the line of vortices, thin streamers or
wisps appear near the cusp of each vortex and penetrate horizontally back
into the interior of the fluid (note the thin lighter bands that alternate with
the darker bands in Figures 62 through 64). Qualitatively, it appears that
fluid of slightly different densities from vertical levels adjacent to each
vortex cell is mixed in the cell and returns to the interior as a thin streamer
at a new equilibrium level. The result of this process is alternate layers of
thin, nearly homogenous streamers and thicker, linearly stratified laminae.

<u>Quantitative</u> (1) Vortices and Layering. The onset of vortex activity for any particular run normally occurs within 10 to 20 wave periods following the arrival of the first wave motion at the corner region of the slope. The initial vortex generally appears somewhere along the middle section of the slope, and the instability spreads gradually toward the corners. The initiation of vortex activity was observed as a function of input frequency for experimental groups 4 and 5; the results are shown in Figure 65. These results indicate that, for this set of experiments, (1) the vortices occur earliest (in time measured from the start of the wave maker) for $\omega \simeq \omega_c$ even though the lower frequency waves have a higher group velocity; (2) there is some $\omega < \omega_c$ for which the vortices do not appear, and (3) there is a small range of ω slightly greater than ω_c (i.e., waves in the subcritical range) for which vortices form.

The diameters of the vortices were difficult to measure accurately from the shadowgraph images because of the constant process of either growth or decay during each half cycle. From dtat taken from various photographs, the size of the vortex diameters is largest for $\omega \simeq \omega_c$ and generally decreases for lower and higher frequencies. Figure 66 shows the size variation of maximum vortex diameters measured at midslope positions during experimental group 4. The corresponding input wave frequencies are listed in column 1.

The position of the vortices relative to the bottom also varies over each half cycle of the wave motion. As a vortex grows in diameter it also appears to move away from the boundary; conversely, as its diameter diminishes its distance from the bottom decreases. The maximum distance measured between the center of a vortex and the bottom was approximately 1.2 cm.*

---

*It is worth noting here that the alternate motion toward and away from the boundary by a diminishing and enlarging vortex cell gives the impression of a periodic pumping in a direction normal to the bottom.

$$\frac{t_c}{t}$$

$\omega_c = 0.495$ sec

$t_c = 250$ sec.

delimit the range
of observed vortex
formation.

$$\frac{\omega}{\omega_c}$$
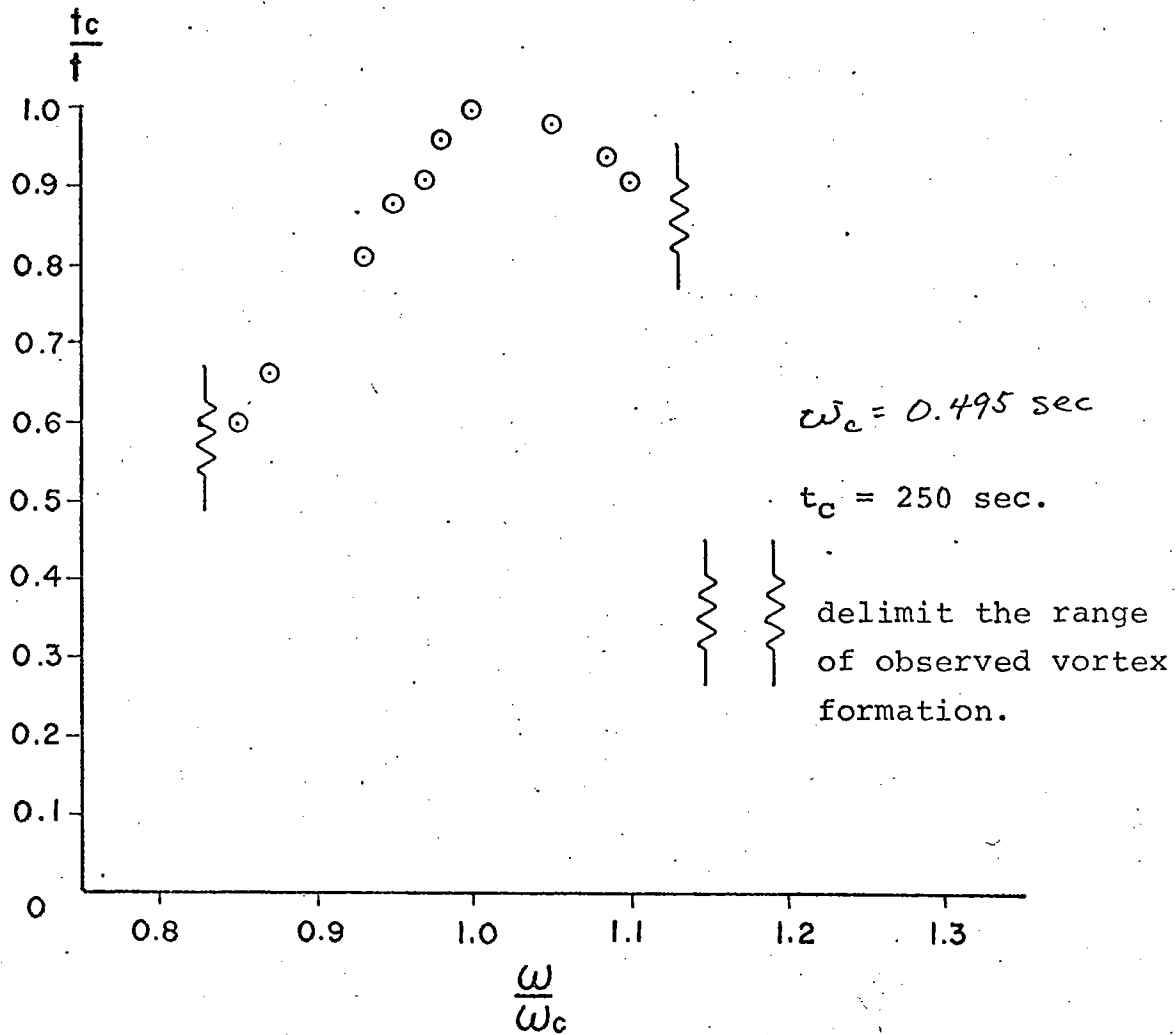
FIG. 65. Onset of vortex motion as a function of input
wave frequency.

ω, sec^{-1}	T, sec	d, cm
0.546	11.5	0.32
0.547	11.7	0.39
0.519	12.1	0.43
0.495	12.7	0.52
0.487	12.9	0.51
0.480	13.1	0.52
0.468	13.4	0.47
0.458	13.7	0.47
0.430	14.6	0.43

FIG. 66. Maximum size of vortex diameters
as a function of frequency

$$\omega_c = 0.495 \text{ sec}^{-1}$$
$$N = 0.99 \text{ sec}^{-1}$$

Shadowgraph images of the thin, horizontal streamers (for example, Figure 62b) usually intensify with time if the wave motion continues. Their initial appearance generally varies with frequency much in the same way as the onset of the vortices. The streamers are usually sharply outlined as shadowgraph images near the vortices, but within short horizontal distances from the slope (order of 2 - 4 cm) their images weaken. Although they can be detected out to distances of 20 cm from the bottom from the shading variations on the shadowgraph, the contrast between the images of the streamers and adjacent layers becomes very indistinct at distances greater than 20 cm from the slope. Their deepest observed penetration of the interiro was approximately 25 cm, measured horizontally away from the slope. This particular measurement was made after one hour of continuous wave motion at the critical frequency for a run during experimental group 4 (α = 30 degrees). The thickness of the streamers during this particular run was 2 mm near the boundary, and the vertical distance separating two streamers was typically 5 mm. Normally the vertical separation between streamers is approximately equal to the diameter of the nearest vortex. The shadwograph images of the streamers are most distinct for wave frequencies near ω_c.

Several conductivity probe traverses through short vertical sections (3 and 4 cm) were made in order to detect changes in the linear density-depth profiles that might be associated with the streamers. Figure 67 shows the measured structure for a typical vertical traverse of a probe after the formation of the streamers. Small scale irregularities in the curve (after the wave motion) are typical of these traverses. The values along the horizontal axes represent changes in output voltage relative to the null position that was chosen approximately at the center of the traverse; the vertical axis is actual tank depth in cm. Changes in equivalent density determines from the calibration curves are also shown along the horizontal axis. Although sharp changes in density at the edges of the streamer are apparent from the photographs, some conductivity probe and specific gravity
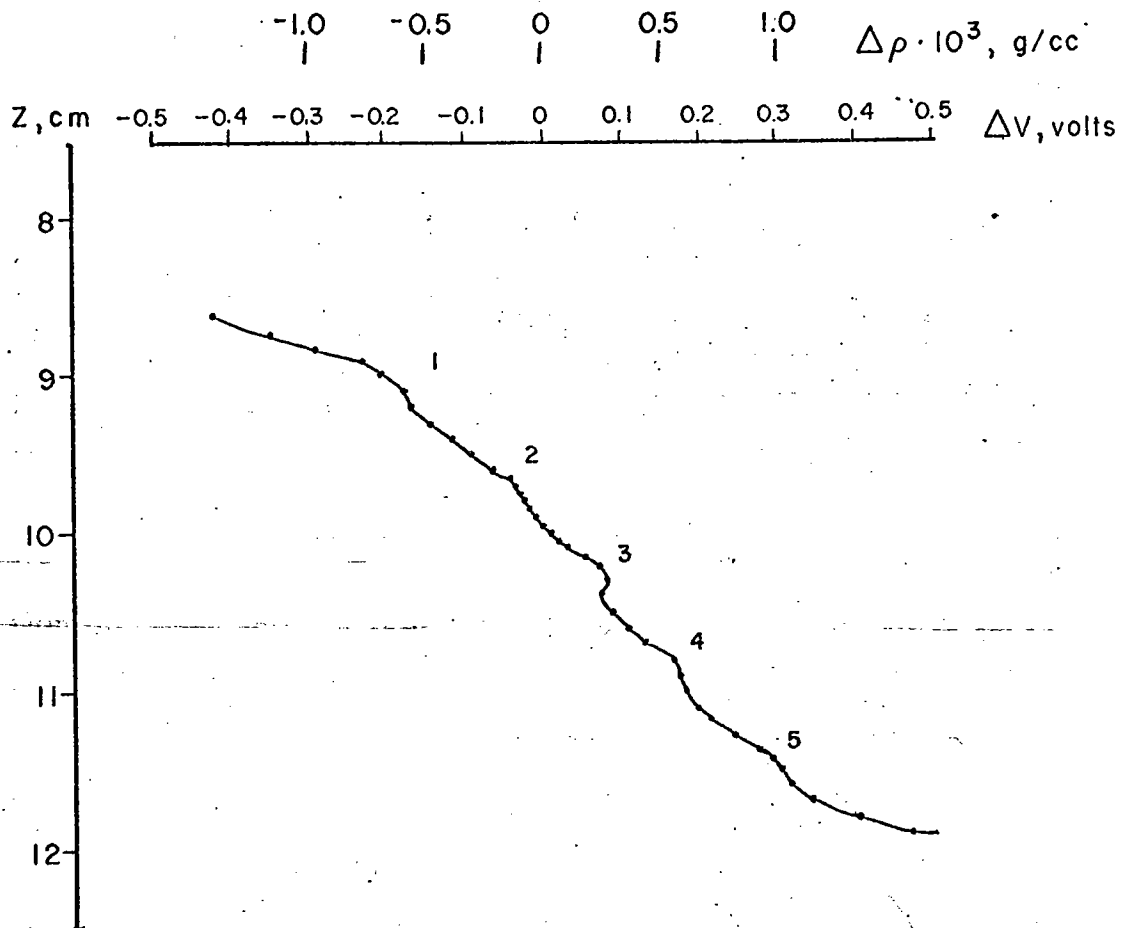
Fig. 67.

Density-depth profile through a region of
streamers (numbered) and intervening layers.

measurements suggest that the density is not homogeneous within the streamer, but has a small, nonzero gradient there. This latter remark is based on only six measurements within two streamers (not shown in Figure 67), and these were taken near the associated vortex cell close to the slope, where the streamer could easily be identified from shadowgraph observations. The apparent density inversion at layer "3" in Figure 67 is not significant.

The net movements of neutrally buoyant particles in the streamers and in the invervening layers were observed for several runs. The typical net motion (away from the slope in the streamers and toward the slope in the intervening layers) is indicated diagrammatically in Figure 68. Averages of the net velocity measurements in the streamers and layers are listed in the table in Figure 68. Each individual determination of net motion that went into the computation of this average involved tracking particles for a minimum of 10 wave periods. The differences among the various numbers are not significant; however, a magnitude of about 0.1 mm/sec in each zone is reliable.

Case	Average net velocities in mm/sec	
	Streamer	Intervening Layer
Critical $(\gamma = c)$	0.14	0.21
Super Critical $\gamma > c$	0.17	0.13
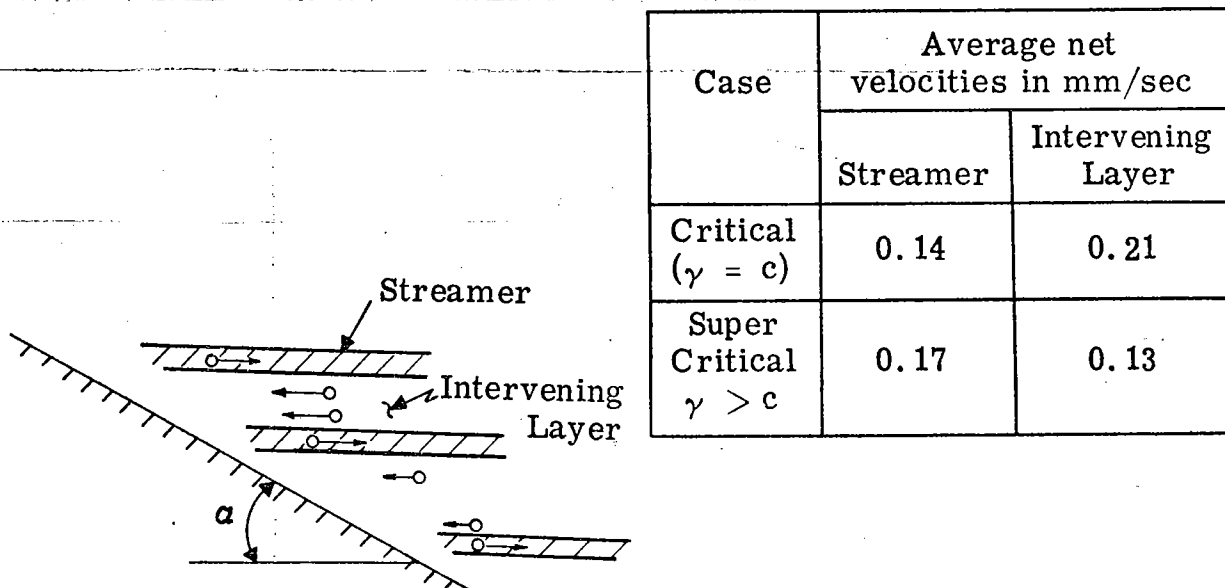
Fig. 68. Average net velocities in streamers and intervening layers.

(2) Boundary-layer description. Owing to the complicated near-bottom motion caused by waves of frequencies at or near critical, it was difficult to choose a level that accurately described the physical extent of the boundary layer. The height above the bottom of the inflection point in the streak curves was selected as an approximate measure of the boundary-layer thickness. Admittedly, the choice is somewhat arbitrary; however, the change in curvature in the streaks was generally well defined at this point during at least the total time of sampling. In any event, this estimate of δ_m should be regarded as only approximate. In addition to the values of δ_m, other estimates of the boundary-layer thickness are presented in Figure 69 for comparison.*

The values of δ_2 and δ_3 represent two estimates of the boundary-layer thickness that result from scaling considerations. Wunsch (1969) found that for $\omega \simeq \omega_c$ there is a balance in the governing boundary-layer equation over a distance proportional to $R^{-1/3}$. He also showed that the equation is nonseparable in the spatial coordinates. This type of balance $(R^{-1/3})$ is represented by δ_2 in column 8. The value of δ_3 represents a boundary-layer thickness of Stokes type ($\delta \alpha R^{-1/2}$) and is presented for comparison in column 9. Firm conclusions based on quantitative comparisons between the scaling estimates and δ_m are not justified here since δ_m is only approximate for each slope station.

Similar results for a representative run of the supercritical cases are shown in Figure 70. For these measurements, the boundary-layer motion at each station was very regular, and the dye-streak profiles generally resembled those described for the subcritical case. There was no evicence of vortex activity with the associated generation of thin streamers

---

*The estimates of δ_1 and δ_2 differ approximately by a factor of 2; this is obvious from their definitions.

ω = 0.495 rad/sec, T = 12.7 sec
N = 0.97 rad/sec, C = 0.593
a = 30 deg γ = 0.577
a_o = 0.2 cm
k_o = 0.056 cm^{-1}, λ = 113.0 cm
h_o = 33.5 cm
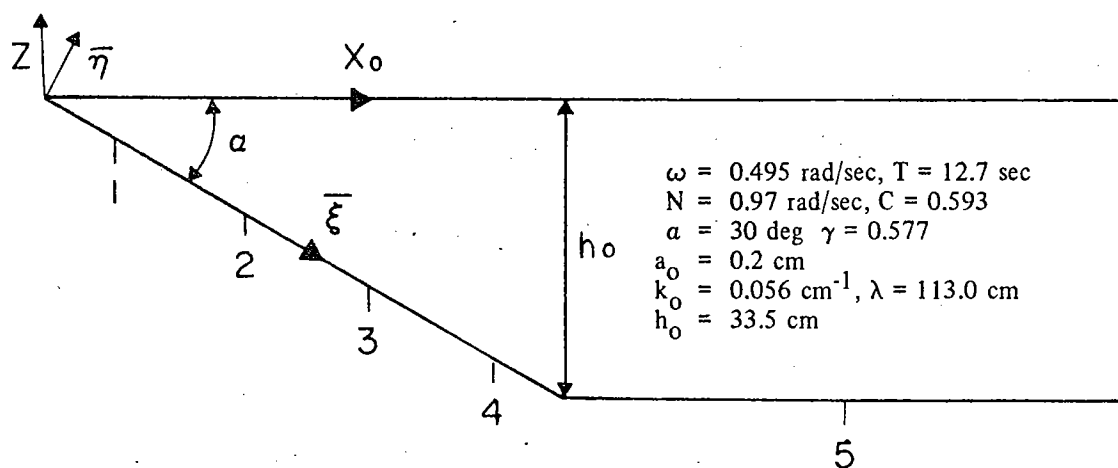
1	2	3	4	5	6	7	8	9	10	11	12
Station No.	x_c (cm)	h (cm)	R_L $\times 10^{-3}$	R_W	R_B	δ_1 (cm)	δ_2 (cm)	δ_3 (cm)	δ_m (cm)	a_m (cm)	ϵ
1	15.6	9.0	7.86	68.98	21.14	0.201	0.45	0.10	0.362	1.18	0.12
2	24.2	14.0	19.03	92.91	26.51	0.201	0.52	0.10	0.391	1.37	0.09
3	43.3	25.0	60.63	102.64	29.08	0.201	0.64	0.10	0.408	1.44	0.05
4	53.7	31.0	93.2	25.66	14.65	0.201	0.68	0.10	0.411	0.72	0.04
5	110.0	33.5	109.2	7.15	5.27	0.201	0.70	0.10	0.283	0.38	0.02

$$R_L = Nh^2/\nu \qquad = \text{local wedge Reynolds number}$$

$$R_W = a_m^2 \omega/\nu \qquad = \text{local wave Reynolds number}$$

$$R_B = a_m \omega \delta_m/\nu \quad = \text{local boundary layer Reynolds number}$$

$$\delta_1 = (2\nu/\omega)^{1/2}$$

$$\delta_2 = h R_L^{-1/3}$$

$$\delta_3 = h R_L^{-1/2} \quad = (\nu/N)^{1/2}$$

$$\epsilon = a_m k_m \sin \alpha$$

FIG. 69. Estimates of boundary layer thickness
and Reynolds numbers. $\gamma = c$.

ω = 0.405 rad/sec, T = 15.5 sec
N = 0.97 rad/sec, C = 0.460
α = 30 deg γ = 0.577
a_0 = 0.2 cm
k_0 = 0.043 cm^{-1}, λ_0 = 145.7 cm
h_0 = 33.5 cm
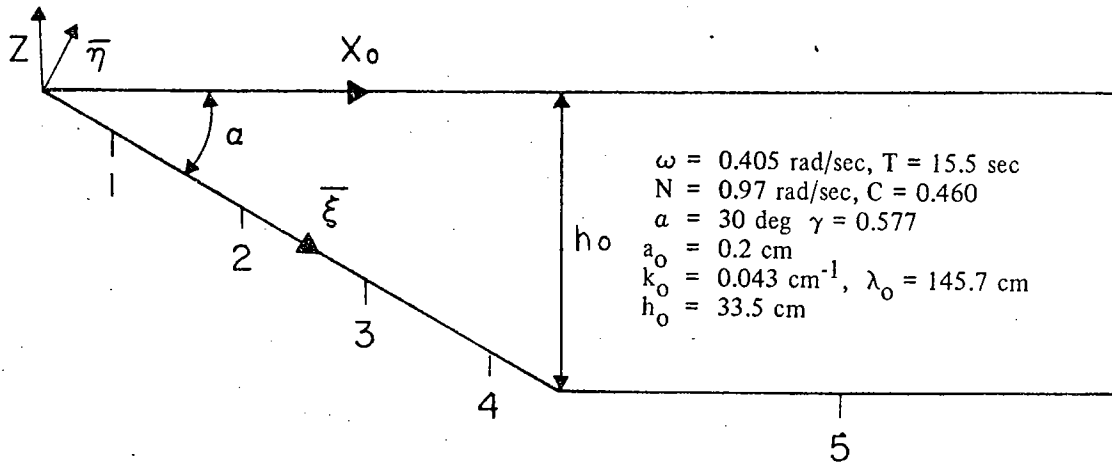
1	2	3	4	5	6	7	8	9	10	11	12.
Station No.	x_c cm	h cm	R_L $\times 10^{-3}$	R_W	R_B	δ_1 cm	δ_2 cm	δ_3 cm	δ_m cm	a_m cm	ϵ
1	12.1	7.0	4.75	15.1	11.4	0.22	0.42	0.10	0.46	0.61	0.06
2	22.5	13.0	16.39	61.3	22.4	0.22	0.51	0.10	0.45	1.23	0.07
3	38,1	22.0	46.95	30.7	17.3	0.22	0.61	0.10	0.49	0.87	0.03
4	48.5	28.0	76.05	31.4	11.8	0.22	0.66	0.10	0.33	0.88	0.02
5	100.0	33.5	108.86	1..3	1.5	0.22	0.70	0.10	0.21	0.18	0.004

$$R_L = N h^2 / \nu \qquad = \text{local wedge Reynolds number}$$

$$R_W = a_m^2 \omega / \nu \qquad = \text{local wave Reynolds number}$$

$$R_B = a_m \omega \delta_m / \nu \quad = \text{local boundary layer Reynolds number}$$

$$\delta_1 = (2\nu/\omega)^{1/2}$$

$$\delta_2 = h R_L^{-1/3}$$

$$\delta_3 = h R_L^{-1/2} = (\nu/N)^{1/2}$$

$$\epsilon = a_m k_m \sin \alpha$$

FIG. 70. Estimates of boundary layer thickness and
Reynolds numbers. $\gamma > c$.

or breaking along the entire slope. Unlike the subcritical case, with slopes of 30 degrees, the displacements of dye streaks and neutrally buoyant particles at station 4 did not show any irregularities or anomalous behavior. The measurements of the boudary-layer thicknesses at each station are considered to be as reliable as those given for the subcritical case (figure 53).

(3) Velocity and Shear Stress. One-second velocity averages were again computed from the streak displacements; for the critical case these values are shown only for one vertical level: that described above for the measurements of δ_m. This level was chosen since it normally was the vertical position closest to the slope for which the streak curves remained coherent over the entire wave cycle during sampling. The dye streaks usually became quite distorted above this level (probably due to the motion in the wisps and streamers), and generally the streaks were very faint adjacent to the slope (probably due to mixing). These velocity measurements for the various stations on the slope are presented in Figure 71; the experimental conditions at the time these values were determined are listed in the upper right-hand section of Figure 69.

The values of velocity in Figure 71 are plotted along the vertical axis in cm/sec, and the successive seconds of time during the wave cycle are shown along the horizontal. The phase has been adjusted artificially so at time t = 1 the velocity is nearly zero. The average distance above the bottom for which these measurements were taken is indicated for each station. This distance is approximately equal to δ_m (Figure 69). A summary of the maximum and RMS values of velocity is given in Figure 72 for each station (including the velocity variations on the flat bottom not shown in Figure 71).
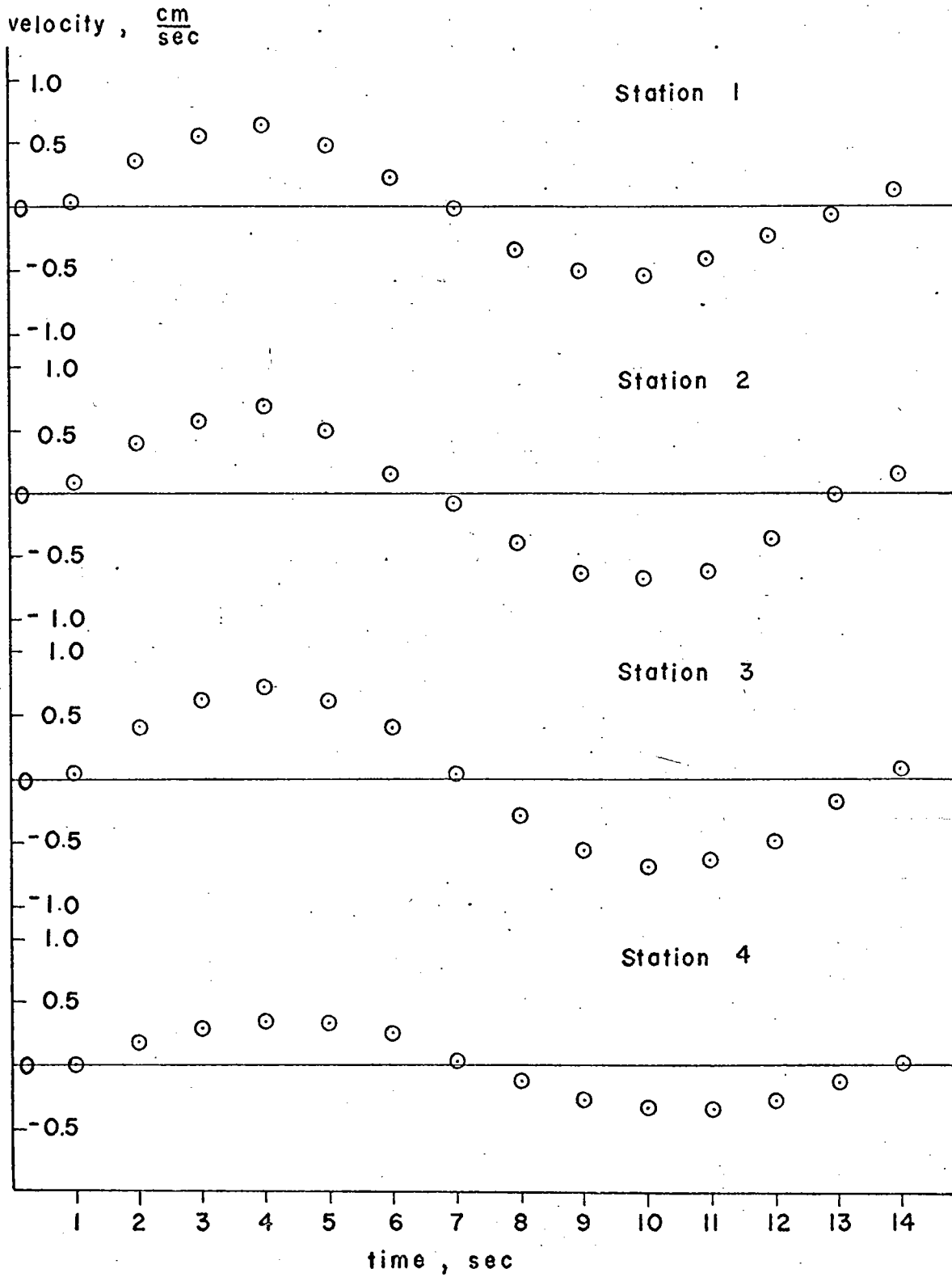
FIG. 71

The last column of Figure 72 gives rough estimates of the maximum bed shear stress,

$$|\tau_0| \; max \simeq \bar{\mu} \; \frac{|u| \; max}{\delta}$$

where $\bar{\mu}$ = 0.01 gm/cm-sec, that were computed at the level of the inflection point ($\bar{\eta} = \delta_m$) described above. This kind of estimate assumes a laminar velocity distribution that remains essentially linear with distance above the bottom over the wave cycle. This assumption is not accurate for two reasons: (1) the actual profiles of velocity are probably not linear, and (2) the observed dissipation of the dye streaks below δ_m indicates possible turbulence in this region. The estimates of $|\tau_0|_{max}$ are intended only as approximate lower bounds on the local maximum bed shear stress; the actual values are probably larger due to a nonlinear velocity distribution with superimposed turbulent fluctuations near the bed.

Fig. 72. Summary of velocity and bed shear stress values for critical case ($\gamma \simeq c$) measurements.

Station (see Fig. 11)	$|u|_{max}$ cm/sec	u_{RMS} cm/sec	$|\tau_0|_{max}$ dynes/cm^2 ($\times 10^{-2}$)	cm δ_m
1	0.65	0.38	1.80	0.36
2	0.68	0.44	1.74	0.39
3	0.72	0.45	1.76	0.41
4	0.35	0.25	0.85	0.41
5	0.18	0.13	0.64	0.28

The velocity measurements show that the magnitude of the maximum oscillatory motion at the selected level of measurement is nearly uniform at the middle and upper slope stations. The value of $|u|_{max}$ on the lower slope (station 4) is smaller than that farther upslope (stations 2, 3, and 4) by about

a factor of 2. The increase in maximum velocity between the flat bottom and station 1 is approximately a factor of 4. This is considerably lower than that found between similar locations for the subcritical-case measurements shown in Figure 59. The measured bed shear stress (as defined above) at station 1 is greater by only a factor of 3 than that for the flat bottom. A striking feature in the results is the smooth sinusoidal appearance of the velocity1time curves in Figure 71. The apparant lack of irregularities in these curves suggests that in spite of the vortex-streamer production, the basic harmonic motion of the input waves is still quite recognizable.

The Lagrangian velocity measurements for the supercritical case are represented by the results in Figures 73a and 73b. These velocity-depth profiles are analogous to those shown in Figures 54 through 58 for $\gamma < c$. Only the results at tow stations (1 and 4) are shown here to illustrate the regularity of the motion. The absence of the vortices and thin streamers for this frequency ($\omega < \omega_c$) was also accompanied by a return to an apparent periodic motion of the dye streaks and particles near the bottom. No wave breaking was observed near the corner. The maximum and RMS velocity values that were taken from selected levels in the velocity-depth curves at each station are listed in Figure 74. The maximum value of bed shear stress is also shown in the last column of this figure.

The velocity curves at all stations are quite symmetrical and do not indicate any measureable net motion; the measured net displacement of neutrally buoyant particles over several wave periods corroborate this finding. It is also evident that $|u|_{max}$ at the selected levels increases only slightly from station 4 to station 2, and then decreases at station 1, which is farthest upslope. This behavior contrasts sharply with the large increase in $|u|_{max}$ at station 1 for the high-frequency waves ($\gamma < c$, case A). The estimated bed shear stress at the slope locations increases by a factor of 4 or 5 from that over the flat bottom. In this case, δ in Equation (4-7a) was chosen as the smallest $\bar{\eta}$ for which the dye streak data were considered to be reliable (see first value of $\bar{\eta}$ for each station in Figure 74).
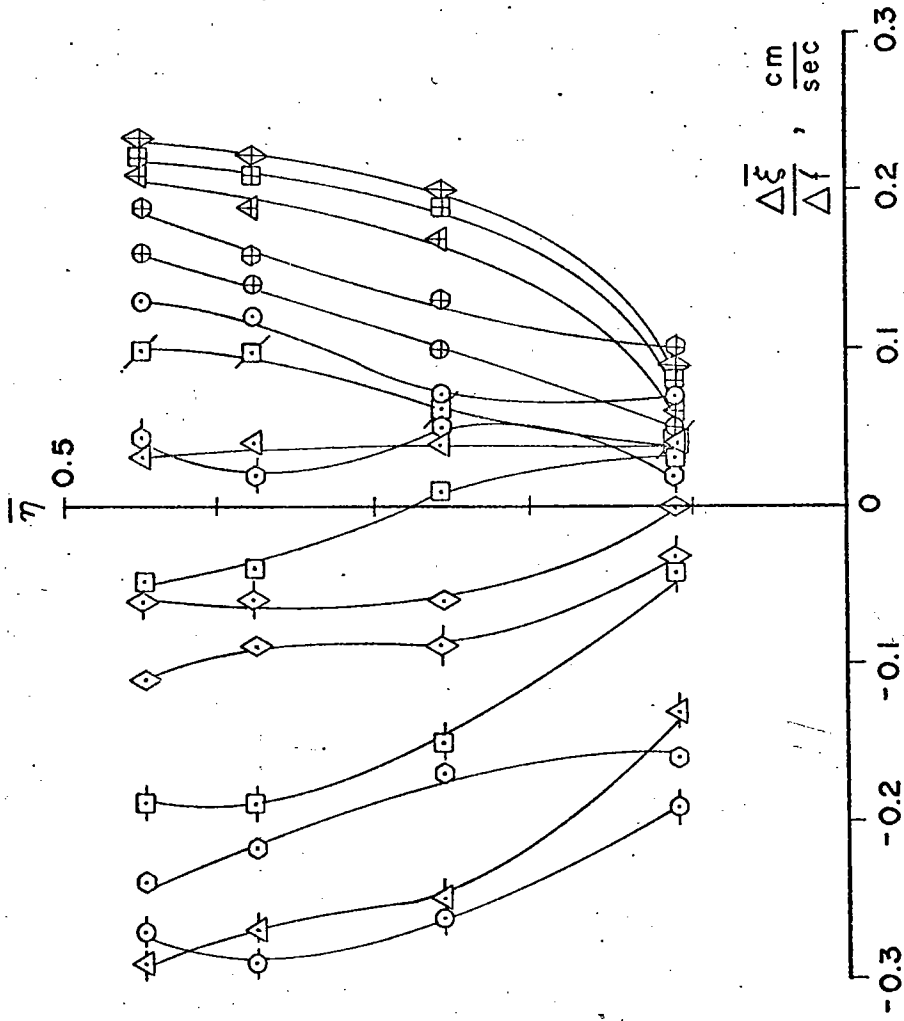
FIG. 73a. Velocity - depth profiles at station 1, $\gamma > c$.
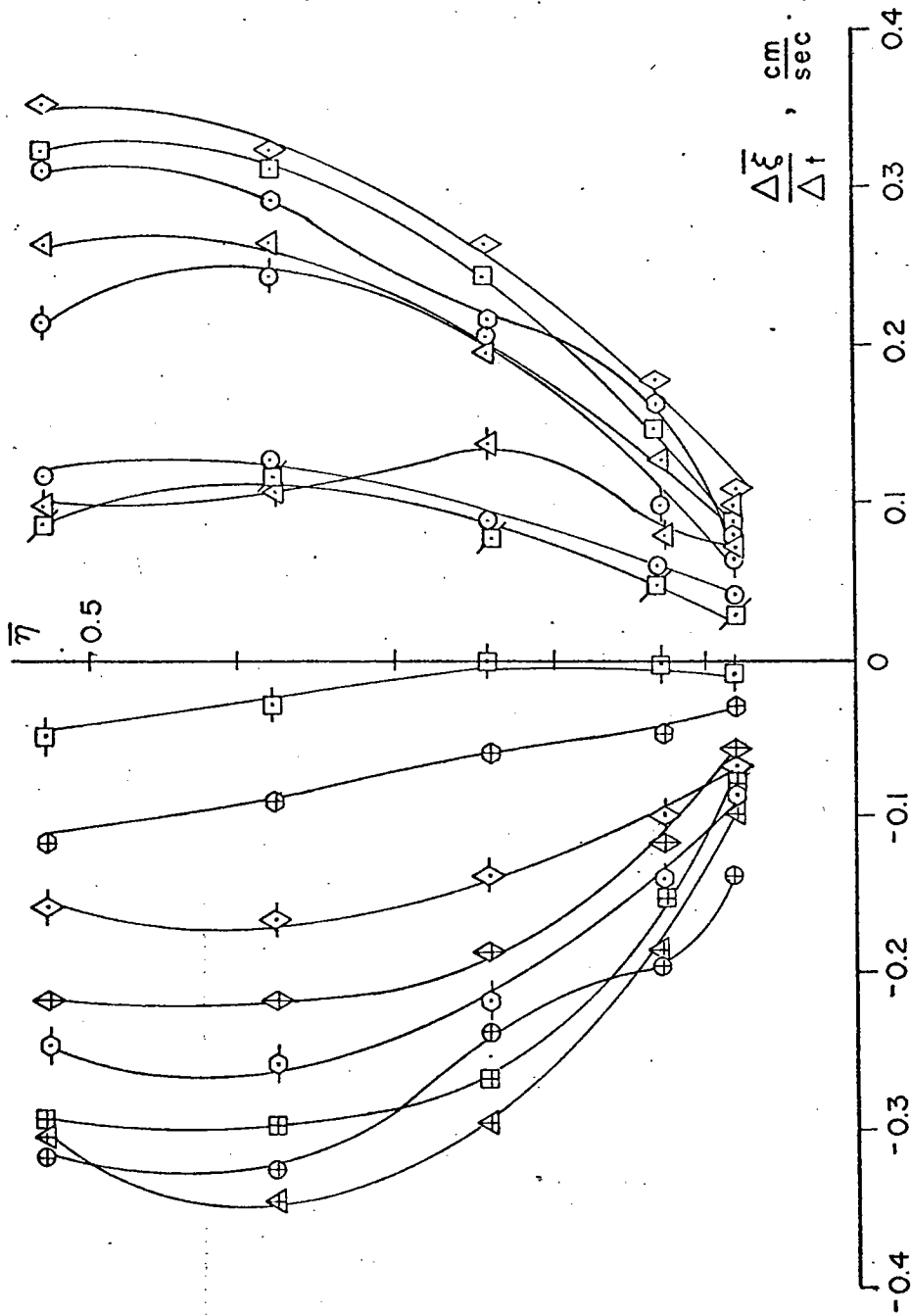
FIG 73b. Velocity - depth profiles at station 4, $\gamma > c$.

FIG. 74. Velocity and bed shear stress at selected levels

Station No.	$\bar{\eta}$ cm	$|u|_{max}$ cm/sec	$|u|_{RMS}$ cm/sec	$|\tau_0|\,max$ $(\times 10^2)$ dynes/cm^2
1	0.11	0.18	0.08	1.64
	0.26	0.26	0.14	
	0.38	0.29	0.17	
	0.45	0.28	0.17	
2	0.16	0.32	0.22	2.00
	0.30	0.44	0.30	
	0.45	0.48	0.33	
	0.66	0.50	0.33	
3	0.13	0.20	0.13	1.54
	0.24	0.30	0.20	
	0.38	0.35	0.24	
	0.53	0.36	0.24	
4	0.13	0.25	0.17	1.92
	0.24	0.35	0.23	
	0.37	0.38	0.25	
	0.51	0.35	0.23	
5	0.12	0.05	0.03	0.42
	0.21	0.07	0.04	
	0.32	0.11	0.06	
	0.46	0.11	0.07	

DISCUSSION

The experimental results can be summarized briefly. The measurements of the wave motion in the subcritical range $\gamma < c$, indicate that the linear theoretical solutions (Wunsch, 1969) accurately represent the data for the higher frequency waves in the interior and in the boundary layer over the slope for ϵ less than approximately 0.5. The data for the lower frequency waves in the subcritical range do not agree with these solutions as well as the data for the higher frequency waves. For both of these wave types, no significant reflections were measured; the wave energy dissipates primarily in a narrow upslope zone. The higher frequency waves break turbulently in this zone, where mixing generates laminae of various thicknesses that protrude back into the interior. By contrast, the lower frequency waves form surges that dissipate in runup near the corner. Large intensification in the velocities parallel to the slope were measured for all waves in this range.

The critical case, $\gamma \simeq c$, is characterized by less violent breaking near the corner. Regularly spaced line vortices form along the slope during the upslope motion of the water particles. The mixing in these vortices generates thin streamers of fluid that penetrate horizontally back into the interior over most of the depth. Intesification of the near-bottom oscillatory velocities was also evident; however, the flow pattern in the vortices complicated the kinematics near the bottom.

In the supercritical case, $\gamma > c$, no breaking was seen near the corner. The vortices and streamers persisted until the wave frequency reached low values, below which the vortex production subsided. The motion in the boundary layer was very regular in the absence of the instabilities. In the fluid interior the measurements show that the wave motion intensifies near the critical characteristics, whose position is given by $z = -cx$.

5. SEDIMENT MOVEMENT BY INTERNAL WAVES

GENERAL DISCUSSION

This chapter attempts to assess the role of shoaling internal gravity waves in the initiation of bottom-sediment movement in the ocean, in the light of the theoretical and experimental results discussed in the previous chapters. Although the concept of internal waves as an effective geological agent in the ocean is not new, very few published studies have dealt specifically with the erosion, transportation, or deposition of sediments on submarine slopes. Chapter 1 has provided some historical background on this subject. Several explanations for the apparent lack of attention are possible: (1) our knowledge of the mechanics of sediment movement beneath the more familiar oceanic surface waves is still incomplete; (2) the wide spatial separation of available data on bottom sediment types on the continental margins hampers understanding of local sedimentary processes; (3) reliable measurements of oceanic internal waves, particularly those taken in conjunction with a sediment-sampling program, are few; (4) until very recently, theoretical and experimental studies of internal waves passing over a bottom with variable depth were virtually nonexistent.[*] In spite of these problems, there have been inferences to the potential importance of this process (Lafond, 1962; Hulsemann, 1968). There exists a body of internal-wave measurements (see Chapter 1) which indicate that internal waves propagate shoreward normal to the bottom contours. (Wunsch, 1969, has also shown theoretically that these waves can refract, in the sense that their crests tend to align parallel to the bottom contours.) These measurements, together with the results of the previous chapters, promote the following discussion about the interaction of these waves with bottom sediment.

_____

[*]Defant (1961) gives two illustrations of the experimental work of Zeilon (done in 1934) in which interfacial waves incident onto a model shelf-slope configuration were studied.

The first section in the following discussion presents various examples of internal-wave measurements in the ocean and discusses qualitatively some features of sediment distribution on the continental margins, particularly off the northeastern United States. The purpose of this section is to provide some background material on ocean conditions relevant to the later discussion and to demonstrate the wide range of values of the various hydrodynamic and sediment properties. The second section develops a criterion that describes the initiation of bottom-sediment motion. This criterion is basically an extension of the analysis developed by Eagleson, et al (1958) for incipient motion of discrete bottom-sediment particles induced by surface waves. The analysis for shoaling internal waves over a constant bottom slope is then specialized for the case of small slopes $(\gamma << c)$, which is shown to be particularly appropriate for high-frequency internal waves in the ocean. Another criterion (the Shields curve, with a later extension by Vanoni, 1964), which represents the more traditional approach to the problem of incipient motion of bottom sediment and is based primarily on dimensional analysis and empirical results, is also discussed. This latter criterion is shown to be approximately equivalent to the first.

The analysis is then applied to specific oceanic measurements, and the results are discussed in a final section, in light of the various limitations. Qualitative remarks concerning the effect on sediment movement by breaking internal waves and critical slope conditions $(\gamma \simeq c)$ are also given in the last section. Throughout the subsequent discussion, consideration of the interaction between internal waves and sediment particles is only an initial attempt to evaluate the possibilities of incipient motion induced by this interaction; the actual importance, or even existence, of this process under real conditions must await future field studies.

Oceanic Conditions

Chapter 1 provides several references to actual measurements of internal wave motion in the ocean, including studies of the directional

properties of these waves (for example, Summers and Emery, 1963). In most cases the measurements were made either by recording fluctuations of temperature or horizontal velocity at fixed positions from a moored buoy or anchored ship or by sampling the vertical distribution of temperature with devices like the bathythermograph. Since the frequency content of the internal wave field is not known a priori, a common means of distinguishing the contributions to the measured changes by the various frequency components is the energy spectrum.[*] Figure 75 illustrates kinetic energy spectra at several levels computed from horizontal velocity data taken at site "D" (location shown in Figure 76) and described by Fofonoff (1969). The large values of spectral energy density at the inertial and tidal frequencies are typical of this location. Frequencies and amplitudes of vertical temperature fluctuations have been measured by others (Chapter 1). Figure 77 demonstrates the wide range of amplitudes and frequencies represented in previous measurements of internal waves in the ocean. The measurements by Gaul (1961) and Ufford (1947) taken over the outer continental shelf and continental slope suggest that wave amplitudes of 1 meter to 5 meters are not unreasonable for the higher frequency internal waves.

----

[*] Time series of measurements of vertical velocity or temperature fluctuations can be used to compute frequency spectra of potential energy. Measurements of horizontal velocities like those taken at side "D" (location given in the following text) are the basis for kinetic energy spectra. Fofonoff (1969) discussed the spectral ratio of potential energy to kinetic energy in terms of a linear internal wave model and found that this ratio is approximately unity for low frequencies (near inertial frequency), but approaches infinity for $\omega \to N$. He noted that this latter behavior is probably caused by the exclusion of the advective terms in the linear model. Voorhis (1968) measured vertical internal motions near site "D" with neutrally buoyant floats. After comparing the frequency spectra of potential energy and vertical kinetic energy (obtained from the measurements) with the spectra of horizontal kinetic energy computed from the site "D" records, Voorhis found that there is an approximate equipartition of potential and kinetic energies for frequencies between inertial and Brunt-Vaisala. He interpreted this equipartitioning to indicate the predominance of internal wave motion in the measurements.
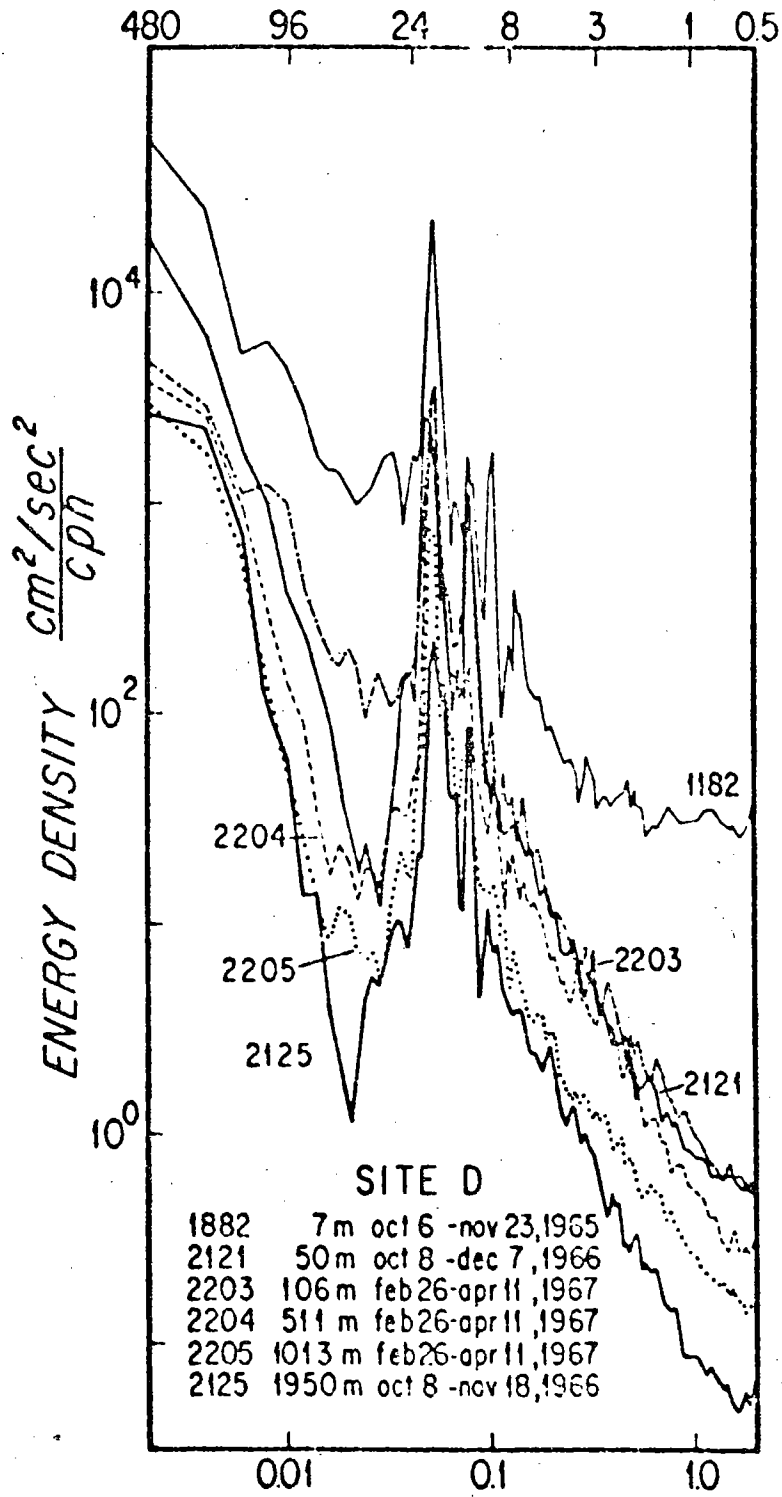
Fig. 75. Frequency spectra of horizontal kinetic energy
density computed from current meter records at
site "D" (after Fofonoff, 1969).
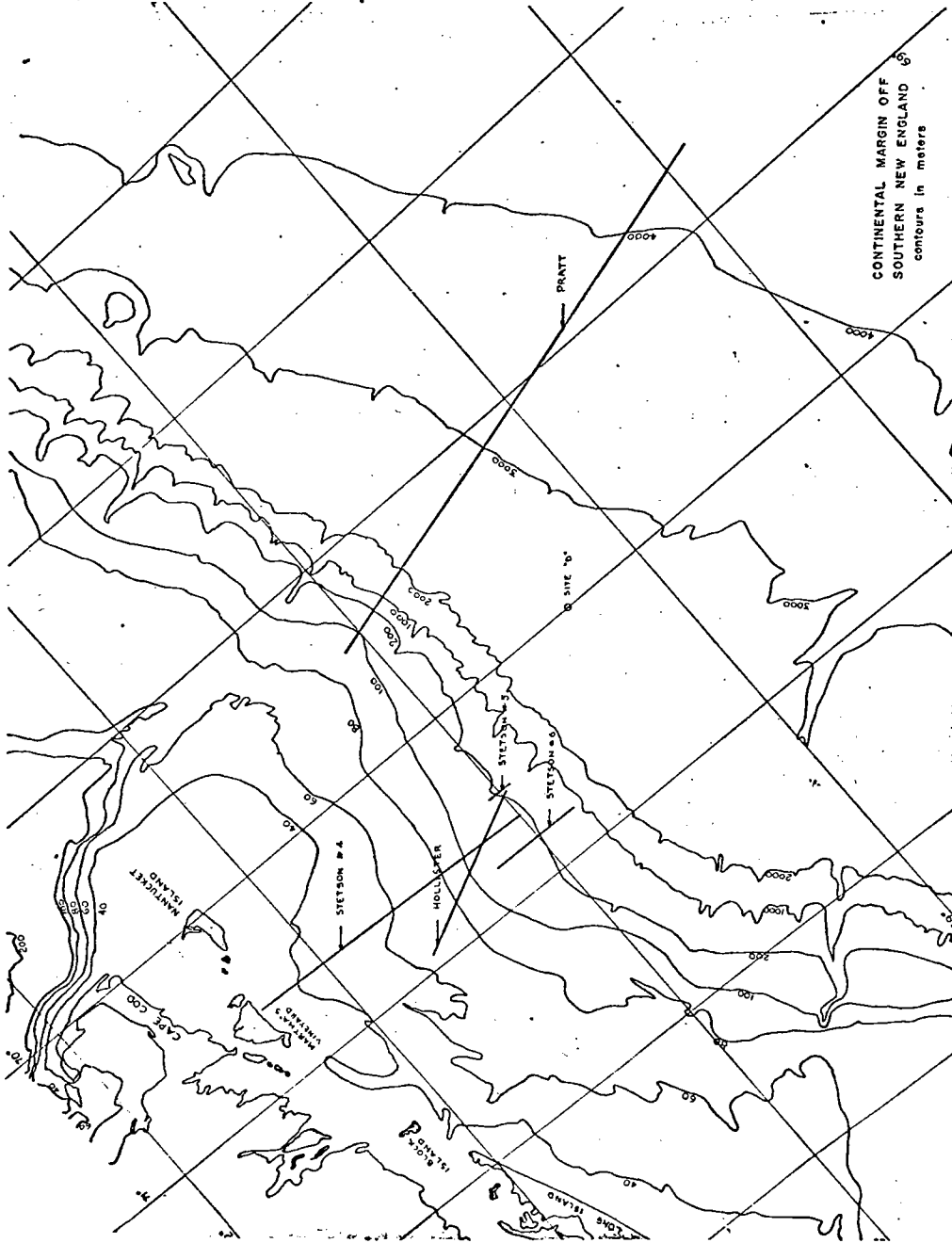
Fig. 76. Bathmetry off southern New England.

FIGURE 77

INTERNAL WAVE MEASUREMENTS ON CONTINENTAL MARGINS

Source	Water Depth (meters)	Wave Height (meters)	Wave Period	Celerity* (knots)
1. Lafond (1963)	20	7 (max.)	7 min. to 12 hr.	0.11 - 0.6
2. Boston (1964)	20, 33	8	12 hr.	
3. Gaul (1961)	62	1 - 3	10 min.	0.5 - 1.5
4. Ufford (1947)	40, 100	1 - 30	9 min. - 2 hr.	0.08-0.68
5. Emery (1956)	1350	130 - 200	12 hr.	(standing)
6. Lee (1961)	20	3 - 7	5 - 15 min.	——
7. Summers and Emery (1963)	10 - 1500	30	12 hr.	1 (shallow) 7 (deep)

*In all cases, the dominant direction of propagation was shoreward.

In order to describe internal wave motions in the ocean, an estimate of the vertical distribution of Brunt-Vaisala frequency is needed. The average vertical distribution of Brunt-Vaisala frequency for locations seaward of the continental slope (near site "D", for example) is typically characterized by relatively large values of N in the seasonal thermocline, if present and in the deeper main thermocline. Figure 78 shows measured values of Brunt-Vaisala frequency N versus depth for stations near site "D"; the hydrographic data were provided by Volkmann (personal communication). An idealized distribution of Brunt-Vaisala frequency with depth is also shown in this figure. The idealized case consists of three distinct vertical layers; in each layer the density gradient is assumed to be constant (i. e., $N \simeq$ constant) This hypothetical vertical distribution of N is later used with the idealized topography also shown in Figure 78 as a basis for various models of sediment movement induced by internal waves.

The generalized topographic cross-section in Figure 78 is not construed to be representative of any particular area, but is taken as an idealized case in which the slopes are linear and the boundaries between the three provinces (shelf, slope and rise) are well defined. Each idealized spatial province in this figure is similar to the experimental conditions described in previous chapters in the sense that N and γ are constant in each.

The actual bottom topography of the various provinces comprising the continental margins of the oceans not only varies markedly with geographic position but also can be quite complicated locally. Featureless and even bottom slopes are probably rare. In his summary of the continent shelves and slopes of the world, Shepard (1963) remarks that it is exception to find a shelf that has a constant slope out to the shelf edge; constancy of slope usually implies widely spaced sample points. The values for bottom slopes shown in Figure 78 are recommended averages taken from Shepard (1963) and Heezen, et al (1959). More detailed descriptions of the physiography, structure, and sedimentology of the continental margin off the east
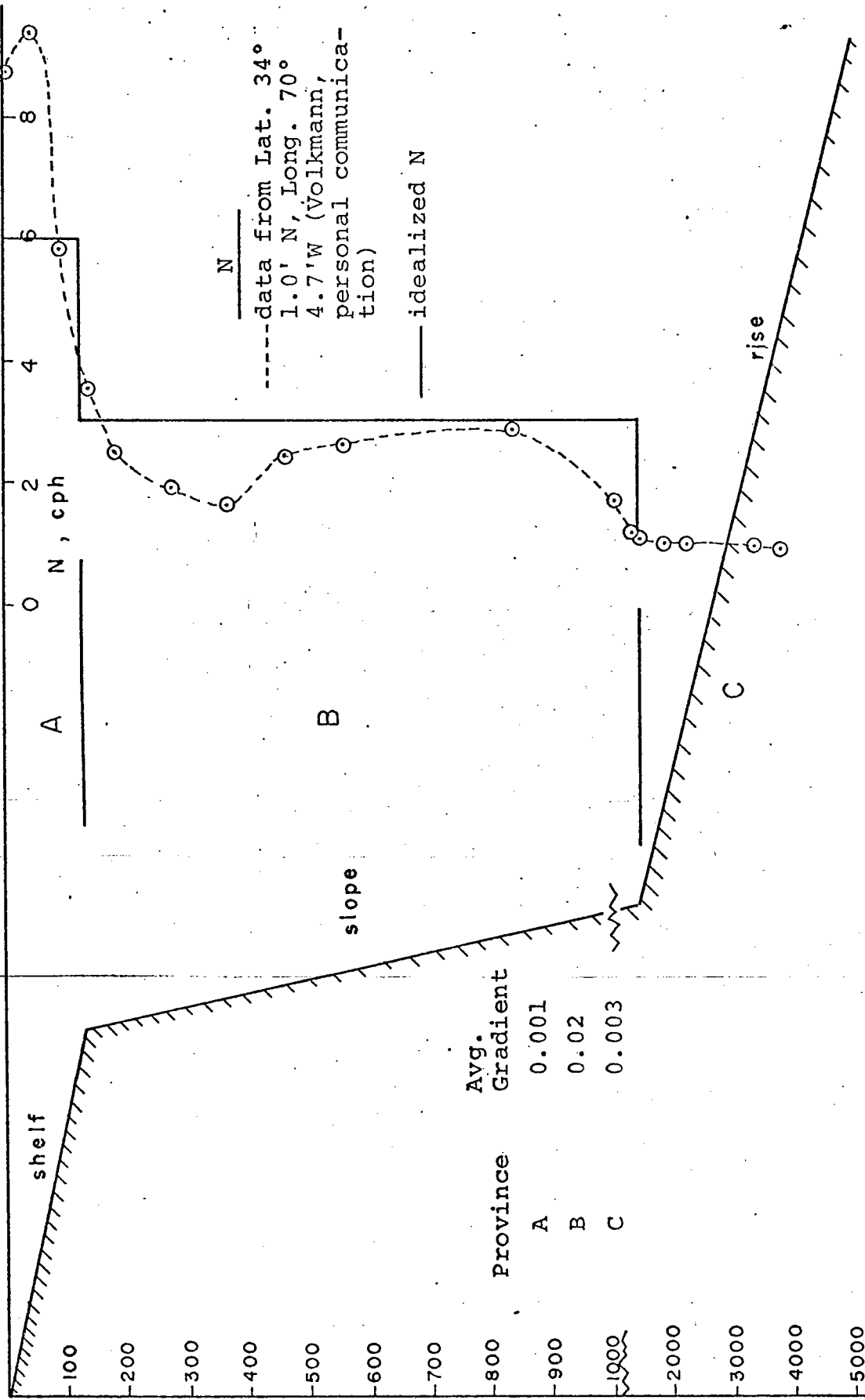
FIG. 78. Idealized cross section of continental margin. Actual and idealized distribution of Brunt-Väisälä frequency are also shown.

coast of the United States is presented by Uchupi (1963, 1968), Emery (1966) Pratt (1968), Schlee (unpublished manuscript), and Emery, et al (1969).

At this point it is instructive to compare average values of the oceanic slopes γ with hypothetical estimates of the slopes of the internal wave characteristics c in order to determine which case ($\gamma < c$, $\gamma \simeq c$, or $\gamma > c$) in Figure 1, if any, is predominant. Figure 79 summarizes the relative values of c and γ for typical values of Brunt-Vaisala frequency N, wave frequency ω, and a constant value of Coriolis frequency (f = 0.042 cph). The results show that the continental shelves are approximately critical (i.e., $\gamma \simeq c$) for internal wave frequencies near inertial for each of the values of N shown; for frequencies greater than the frequency of the semi-diurnal tide ω_T, the shelf is subcritical.

The assumption that the average gradient of the continental shelf is small compared to the slope of characteristics c for normally incident internal waves (i.e., $\gamma << c$) appears to be reasonable for high-frequency internal waves. For example, if $\omega > 0.1$ cph and N $\geq$ 1.0 cph, or if $\omega > 0.5$ cph and N = 6.0 cph, then $\gamma << c$ is approximately valid according to Figure 79. The average gradient of the continental slope might be critical for a relatively wide range of internal wave frequencies depending on the local values of N and f. For example, in Figure 79 for N in the range considered (0.5 cph $< N <$ 6.0 cph), the range of critical frequencies is approximately 0.045 cph $< \omega <$ 0.03 cph; this range includes the semi-diurnal tide. The average gradient of the continental rise is approximately critical for frequencies between inertial and tidal (semi-diurnal) for 0.5 cph $< N <$ 3.0 cph.

It is tempting to speculate about the consequences of $\gamma \geq c$ for oceanic conditions; this is done later and only touched upon here. The experimental results show that for internal wave frequencies equal to or slightly less than critical, vortex instabilities form along the slope. If this occurs along submarine slopes, the mixing in these vortices, with consequent formation of thin streamers that might advect fluid horizontally

C or γ

N= 0.5

N = 1.0

N = 3.0

N= 6.0

OCEANIC ISLANDS

SLOPE

RISE

$$C = \left[\frac{\omega^2 - f^2}{N^2 - \omega^2} \right]^{1/2}$$

OUTER SHELF

.04

f

ω_τ

.1

ω cph

1.0
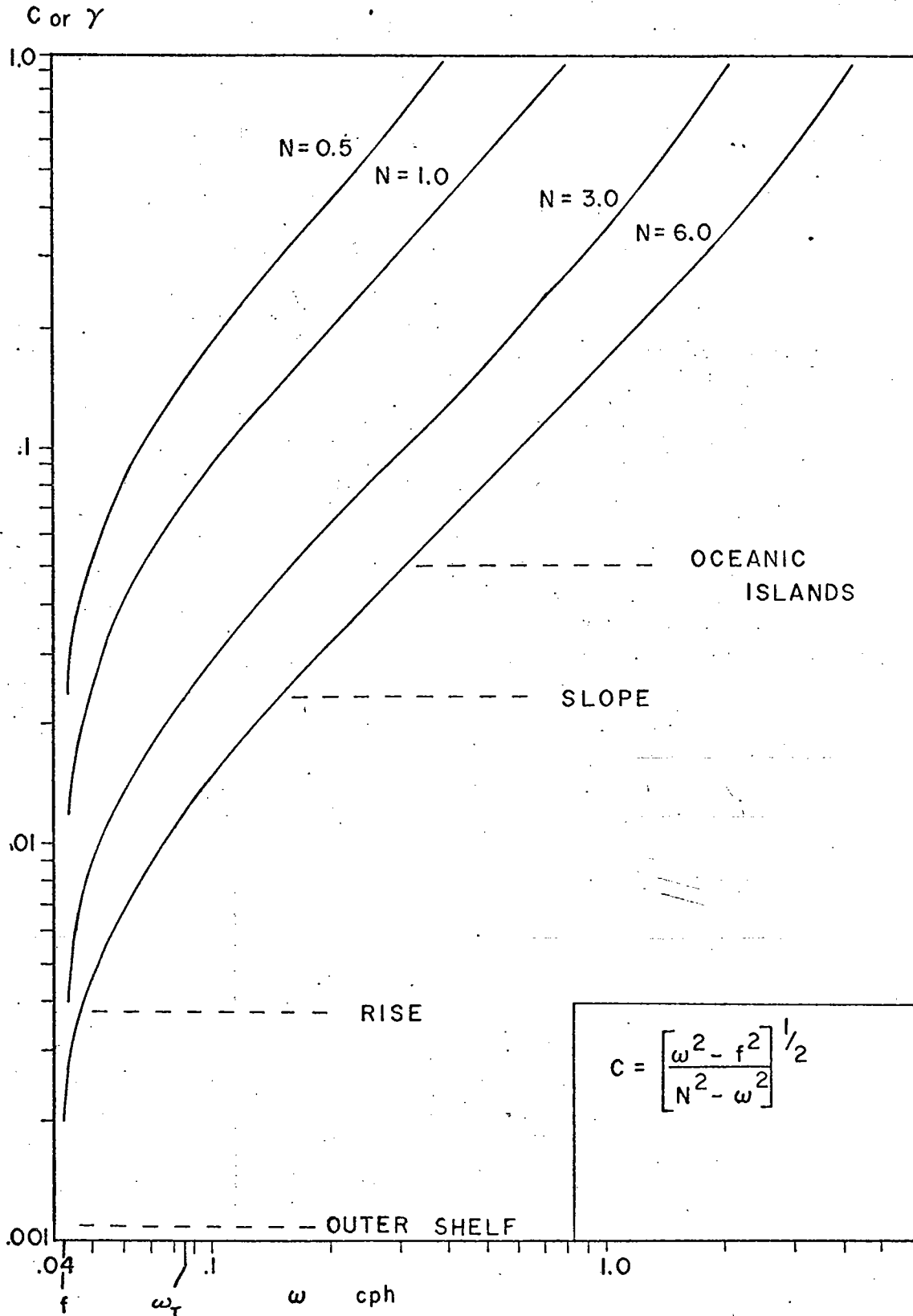
FIG. 79. Characteristic slope c (ordinate) computed for various frequencies ω and selected Brunt Vaisala frequencies N. Average oceanic slopes γ are also shown.

back into the interior, might provide a means of stirring the fluid near the bottom and moving the very fine suspended matter seaward. This agitation might inhibit or prevent deposition of fine suspended matter, and thus maintain a relatively turbid and well-mixed fluid layer near the bottom. However, it is dangerous to extrapolate the laboratory observations to unobserved natural phenomena.

The intention of the above discussion of average gradients of the oceanic slopes was to present the gross features of these slopes in relation to an idealized hydrodynamic structure (Figure 79); local bottom features such as animal markings, sediment ripples, depressions, and rock outcrops were intentionally left out of consideration. It is realized that these additional features might locally affect the internal wave motion by causing complicated reflection patterns of the internal wave characteristics (Longuet-Higgins, 1969) and by influencing the flow in the boundary layer.

The actual scales of bottom roughness on oceanic slopes are quite variable. Spatial variations of these scales have been illustrated by several excellent photographic and echo-sounding studies of submarine topography. A series of camera stations spaced two miles apart on a line extending south of Martha's Vineyard and lying approximately normal to the bottom contours was described by Northrup (1951). Sediment samples were taken at most of the camera stations. Northrup noted that there was good evidence for the action of bottom currents on the outer shelf. Others (for example, Uchupi, 1963) have described topographic features such as sand waves with heights of 5 to 25 meters on the continental shelf. Owen and Emery (1967) cited photographic evidence for intensive erosion of the continental slope south of of Martha's Vineyard by strong bottom currents. They found several unusual features in their photographs including small masses of sediment that protruded a centimeter or so above the general level of the bottom; in this instance they described the overall appearance as "sand-blasted". Bowin, et al (1967) made an extensive photographic and sediment survey of the western and southern slopes of Plantagenet Bank (near Bermuda) in water

depths of 60 meters to 2000 meters. The height scales of the various sand ripples that are clearly shown in some of their stereo-photographs appear to be on the order of 10 cm. (The ripples were observed at various depths, but especially between 950 and 1200 meters.)

The effects these local variations in bottom roughness actually have on the internal wave motion have not been determined. In fact, what role internal waves might have in forming or maintaining features such as ripples or sand waves is uncertain, and must await field studies of this problem. The analysis and discussion in the subsequent sections deals only with the simpler problem of a linearly sloping bottom, mainly for reasons of analytical tractability. It is probably true that the wide variations in the hydrodynamic and topographic features of the ocean include this case; its consideration might provide some insight into more complex situations.

A general discussion of the distribution of sediments on the various continental shelves and slopes is given by Shepard (1963). For the purposes of this discussion, only a brief summary of the sediment types in the area shown in Figure 76 will be given. Uchupi (1963) and Schlee (unpublished manuscript) presented detailed descriptions of the bottom sediments in this region. In his report Schlee noted that although the sediments on the shelf are dominantly quartzose sands that are moderately sorted, many of the sediment samples from the continental shelf (about 20 percent) showed sizable silt-clay fractions. Schlee also noted that there is some evidence for a seaward reversal in the median sand sizes (i.e., fine to coarse in a seaward direction) at limited sections of the shelf break southeast of Cape Cod. This seaward reversal has been found by others.

Several studies have indicated that the sediments on the outer shelf shown in Figure 76 are predominantly Tertiary, and that modern sediments are either lacking or the result of reworking of the older material (Donahue, et al 1966). The dynamics of the by-passing of the shelf by much of the silt and clay of modern sediments, particularly on that part of the shelf below surface wave base, are not well known. Emery (1966) states that waves

and currents on the continental shelf produce enough motion to cause much of the silt and clay of modern sediments to travel across the outer shelf and come to rest in deeper waters. It is suggested later in this chapter that near-bottom velocities induced by internal waves might be partly responsible for the sediment transport in this region.

Pratt (1968) described the continental slope off the eastern coast of the United States as a complex feature whose surface is generally more irregular on the upper parts. In the area under consideration the median diameter of the surface sediments is in the silt range; quartzose sands are locally predominant on the upper slope (Schlee, unpublished manuscript). The continental rise has been described as a depositional apron sloping seaward from depths of about 2000 m to about 5000m at a gradient of between 1:100 and 1:700 (Heezen, et al 1959). The surface is covered with fine well-sorted sands and coarse silts interbedded with clays. Emery (1966) suggests that these sediments were deposited by turbidity currents; however, Heezen, et al (1966) maintain that ocean bottom currents flowing parallel to the contours are responsible for most, if not all, continental rise sedimentation.

Actual sediment data that are later compared with the analytical results were obtained from the work of Hollister (personal communication), Stetson (1939), Pratt (1968), and Emery and Ross (1968). The geographic locations of the sampling sites are shown in Figure 76. These results are particularly useful, since the sample locations are on lines extending offshore near site "D". The hydrodynamic data at and near site "D" provide convenient inputs to the models considered in a later section in which incipient-motion criteria are discussed for the various sediment data.

Before proceeding to the analysis of sediment movement by internal waves, some consideration of the boundary layer along oceanic slopes would be worthwhile. Studies of sediment movement in rivers and beneath surface waves have indicated the importance of the flow characteristics (laminar or turbulent) in this layer in determining the motion of bottom sediment. Linear solutions due to Wunsch (1969) for the boundary layer beneath internal waves on a sloping bottom were discussed in Chapter 4. Wunsch (1970) also

considered theoretically oceanic boundary mixing for quasi-steady conditions in a stratified fluid adjacent to a sloping boundary, and showed that a mean vertical velocity is induced at the sloping boundary to satisfy the no-flux condition. He found that the effect is confined to a boundary layer of thickness

$$\delta = (\nu \kappa)^{1/4}/N^{1/2}$$

where

ν is the eddy momentum coefficient

κ is the eddy heat coefficient

N is the Brunt-Vaisala frequency, as before.

He also pointed out that the various estimates of the mixing coefficients ν , κ in the ocean are unreliable, and showed that for ν , $\kappa \sim 1 \text{ cm}^2/\text{sec}$, and $N = 2 \times 10^{-3} \text{ sec}^{-1}$, then $\delta \sim 20$ cm.

Attempts to define ν for various oceanic processes are abundant (Defant, 1961); however, near a sediment-strewn bottom that is disturbed by periodic and quasi-steady currents, such a definition is elusive. Based on measurements of suspended matter near the bottom of the continental slope east of Chesapeake Bay (Ewing and Thorndike, 1965), Ichiye (1966) computed an eddy diffusivity from a linearized version of the Fickian diffusion equation. He arrived at a figure of $0.12 \text{ cm}^2/\text{sec}$ for the eddy viscosity. Others have shown photographically that the bottom along the submarine slopes can be quite turbid; high concentrations of suspended matter in this near-bottom zone might increase both the viscosity and the density of the fluid. By contrast, many photographs show remarkable clarity and suggest low concentrations of suspended material near the bottom. It therefore appears that the local conditions along oceanic boundaries are sufficiently variable to preclude a single, all-inclusive value of ν . The above discussion suggests that many processes are operative along the oceanic slopes (currents, animal stirrings, etc.); internal waves are only

one possible kind. The actual viscosity near the bottom must be the result of the composite effects of the processes.

INCIPIENT MOTION CRITERIA

The various approaches to the formulation of analytical criteria that adequately describe the initiation of motion of bottom sediment due to water waves are limited owing to the complexity of the process. Several authors (Inman, 1963; Raudkivi, 1967; Abou-Seida, 1965) have summarized these approaches and discussed some of the limitations of each method.

Prior to the development of an analytical model, it might be helpful to present a dimensional analysis of the problem of initiation of sediment motion induced by internal waves, in order to show the large number of independent variables and dimensionless groupings of these variables that are possible. The specific problem is to relate functionally the incipient diameter* of the movable sediment particles to the pertinent hydrodynamic, geometric, and sediment variables. It is assumed that internal gravity waves of a given mode number in a continuously stratified fluid propagate over a bottom slope that has a sedimentary bed. The density stratification is approximately linear and stable, and the bottom slope is constant. The bed is assumed to consist of noncohesive particles with mean diameter D_m; the roughness is arbitrarily described by a length scale . Figure 80 shows the idealized geometry and particle relationships; this figure is similar to that given by Eagleson and Dean (1959).

---

*Incipient diameter is the largest size within a local size-frequency distribution of particles that can be placed into motion by the action of the hydrodynamic and gravitational forces. The condition of incipient motion induced by surface waves on beaches has been described as follows. At some point on the offshore slope, the instantaneous hydrodynamic forces may become sufficiently large to cause static instability of bed-sediment particles of a given size. The diameter of this size is referred to as the incipient diameter (Johnson and Eagleson, 1966).
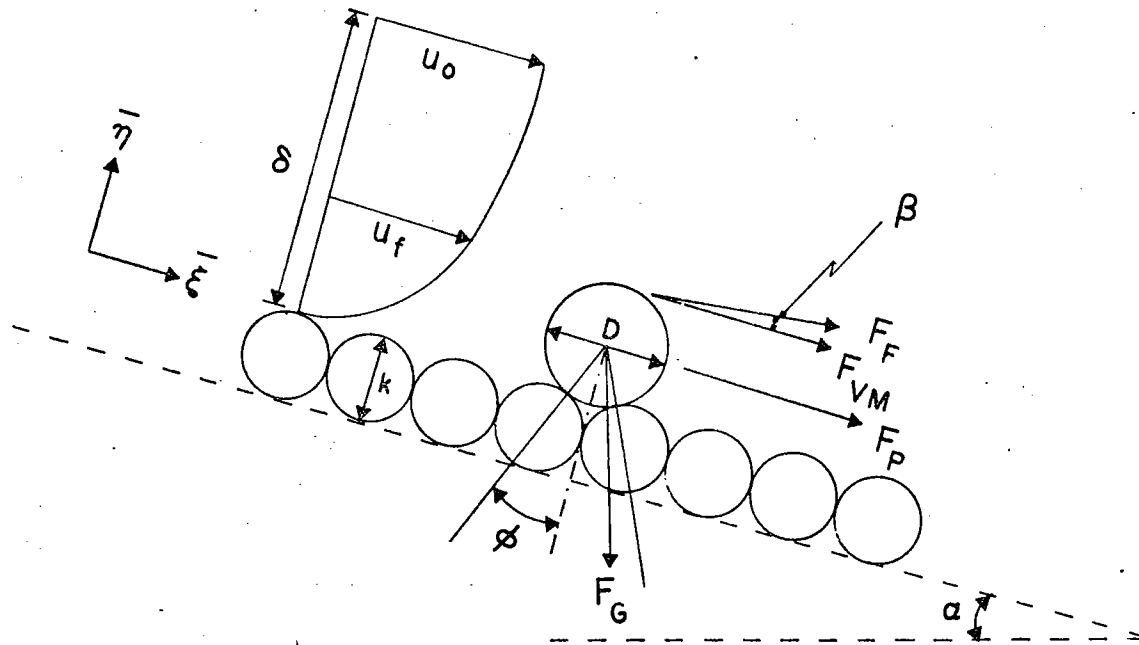
FIG. 80. Definition sketch of sediment particles; forces and geometry.

symbol	name	definition	point of application
F_G	submerged weight	$\pi D^3/6 \; \rho_f g \; (s_s - s_f)$ gravity - buoyancy	center of mass
F_F	fluid resistance	$C_F \; \rho_f \; \pi D^2/8 \; u_f^2$ dynamic pressure and viscous shear acting over surface of particle	top
F_P	pressure force	$\pi D^3/6 \; \rho_f \; \underline{a}_o$ instantaneous pressure gradient force present in fluid whether or not particle is present. Equal to the inertial force of the displaced fluid.	center of mass
F_{VM}	virtual mass force	$C_M \; \pi D^3/6 \; \rho_f \; \underline{a}_f$ force required to accelerate fluid due to presence of particle	top

Eleven independent variables are selected a priori as being important in determining the incipient diameter D_i for this problem. The functional relationship can then be expressed as

$$D_i = f(a, \omega, N, n, \rho_f, \nu, h, \gamma, D_m, \rho_s, \kappa) \tag{5-1}$$

(The symbols are defined in the front section of this paper.) By dimensional analysis the functional relationship can be expressed equivalently in terms of eight independent dimensionless groups:

$$D_i/D_m = f\Big(\underset{(1)}{a/h}, \ \underset{(2)}{\omega/N}, \ \underset{(3)}{n}, \ \underset{(4)}{\gamma/c}, \ \underset{(5)}{a\omega D_m/\nu}, \ \underset{(6)}{a\omega/[(s-1)gD_m]^{1/2}},$$

$$\tag{5-2}$$

$$\underset{(7)}{\frac{1}{N}[(s-1)g/D_m]^{1/2}}, \ \underset{(8)}{D_m/\kappa}\Big)$$

where $s = s_s/s_f$.

The first four expressions on the right in Equation (5-2) relate to the local wave field[*]; the remaining groups relate either to the wave-sediment interaction or to the sediment properties alone. Dimensionless groups (5) through (8) resemble those developed by Carstens, et al (1969) in his analysis of incipient motion due to surface waves. The large number of dimensionless groups indicates the complexity of the process and the potential difficulties in developing accurate dynamic models of this process. Several other variables have purposefully been omitted; these include measures of sorting and packing. These factors would increase the complexity of the process.

If the problem is simplified to consideration of the balance of forces acting on a single, protruding bed particle such as shown in Figure 80, an

---

[*] a/h is proportional to the local Stokes parameter ϵ, since $k \simeq cn\pi/k$ and $\epsilon = ak$ (Chapter 4).

expression can be derived for the incipient diameter in terms of the local, wave-induced velocity field in the viscous boundary layer, certain resistance coefficients, bottom slope, and sediment properties. Furthermore it is postulated that incipient conditions hold when the sum of all hydrodynamic and gravitational moments acting on the particle at any instant is equal to zero. Such a condition can be represented (similar to Eagleson and Dean, 1959) by

$$\sum M = 0 = (F_F \sin \beta \sin \phi \pm F_F \cos \beta (1 + \cos \phi) \qquad (5\text{-}3)$$

$$\pm F_{VM} (1 + \cos \phi) \pm F_P \cos \phi - F_G \sin (\phi \mp \alpha)) \frac{D}{2}$$

Brief definitions of each force and its assumed point of application for this model are given in Figure 80. The points of application follow from the discussion in Ippen and Eagleson (1955) and Eagleson and Dean (1959). Ippen and Eagleson (1955) give a more detailed discussion of the various forces and their representation. The fluid resistance can be rewritten in terms of components normal to and parallel to the bed; these components are commonly referred to as lift and drag, respectively (Schlichting, 1955):

$$F_L = F_F \sin \beta = C_L \, \rho_f \, \pi D^2/8 \, u_f^2$$

$$F_D = F_F \cos \beta = C_D \, \rho_f \, \pi D^2/8 \, u_f^2$$

To obtain an expression for the incipient diameter from Equation (5-3), the following assumptions are made.

(1) The magnitude of the acceleration is small compared to the magnitude of the effective velocity ($|\underline{a}_o|$, $|\underline{a}_f| << |u_f|$). If the advective accelerations are neglected (this is a linearized model), then the instantaneous accelerations are approximately equal to ω times the instantaneous velocity. Their neglect is reasonable for internal waves in the ocean (say $\omega \simeq 10^{-3} \sec^{-1}$).

(2) The lift coefficient is approximately equal to the drag coefficient. The actual relationship used in this model ($C_L \simeq 0.85\, C_D$) was obtained from Chepil (1958). It is recognized that this relationship was found for particles in a turbulent boundary layer; its applicability to laminar conditions has not been verified.

Applying assumptions (1) and (2) above and the lift and drag expressions for the fluid resistance in Equation (5-3) and solving for D, the incipient diameter is expressible as

$$D_i = \frac{3}{4} \frac{u_f^2\, C_D}{g} \, |\Gamma| \qquad (5\text{-}4)$$

where

$$\Gamma = \frac{\pm\,(1 + \cos\phi) + 0.85\,\sin\phi}{(s_s/s_f - 1)\,\sin(\phi \mp \alpha)}$$

The sign convention necessitates the use of absolute value for Γ; if u_f is directed upslope the choice of the bottom signs would give a negative value of Γ. The value of D_i represents the largest diameter that can be moved for particular sediment and internal-wave conditions.

The quantity Γ is dependent on ϕ, s_s/s_f, and α. Since emphasis is placed here on noncohesive particles in sea water, the choice of $s_s = 2.65$ (quartz) and $s_f = 1.027$ appears reasonable. The density variation in the water column over the continental margins off the northeastern United States is < 1 percent. The angle of repose ϕ for both well-rounded and very angular grains of sizes ≥ 0.3 mm was shown graphically by Albertson, et al (1963). There is strong evidence from the nature of the curves for rounded and angular grains of small diameters (< 0.3 mm) that ϕ approaches 30 degrees (± 3 degrees). Eagleson, et al (1958) showed that for the idealized situation similar to Figure 80 this angle can be derived geometrically:

$$\tan\phi = \frac{0.866}{\left[(D/\kappa)^2 + D/\kappa - 1/3\right]^{1/2}} \qquad (5\text{-}5)$$

If the diameters of the bed grains are approximately equal to the equivalent diameters of the roughness ($D/\kappa \simeq 1$), $\tan \phi = 0.53$ or $\phi \simeq 28$ degrees. If these values of s_s, s_f, and ϕ are used and α is assumed to be small, such that $\alpha << \phi$, then $|\Gamma| \simeq 2.01$ for upslope motion and $|\Gamma| \simeq 3.08$ for down-slope motion.

Consequently, on small slopes ($\alpha << \phi$),

$$D_i = 2.31 \frac{u_f^2 C_D}{g} \qquad \text{(downslope incipient motion)} \qquad (5\text{-}6a)$$

and

$$D_i = 1.51 \frac{u_f^2 C_D}{g} \qquad \text{(upslope incipient motion).} \qquad (5\text{-}6b)$$

The problem now remains to obtain a value u_f in Equation (5-6a) or (5-6b) that is the maximum velocity which effectively acts at the uppermost point of the grain surface ($\overline{\eta} = D_i$). The boundary-layer velocity at this point can be expressed as the real part of Equation (4-24)

$$u_f = \frac{Aq}{\xi} [\{F \sin\theta_1 - G \sin\theta_2\} - e^{-D_i/\delta}$$

$$\times \{F \sin(\theta_1 + D_i/\delta) - G \sin(\theta_2 + D_i/\delta)\}] \qquad (5\text{-}7)$$

$$\delta = \left(\frac{2\nu\omega}{\omega^2 - N^2 \sin^2\alpha}\right)^{1/2} \qquad (5\text{-}7a)$$

where

$$q = \frac{2n\pi}{\ell n \Delta} \qquad , \qquad \Delta = \frac{c + \gamma}{c - \gamma}$$

$$\theta_1 = q\ell n(\tfrac{B}{\xi}) + \omega t \qquad , \qquad \theta_2 = q\ell n(\tfrac{D}{\xi}) + \omega t$$

For the case of small slopes in the sense $\gamma << c$, Wunsch (1969) has shown that $q \approx \frac{n\pi c}{\gamma}$. Furthermore, for distances well away from the corner ($cx >> |z|$) the coefficient A can be written in terms of the input wave motion

$$A \approx \frac{a_0 \omega}{2 k_0} \quad ; \quad \text{also } k_0 = \frac{cn\pi}{h_0} \tag{5-7b}$$

where a_0 and k_0 are the amplitude and wave number of the internal waves over the flat bottom, respectively. This expression is true for an input area whose top and bottom are horizontal and rigid. If the condition that the vertical velocity of the wave motion at the top and bottom of the input channel is approximately equal to zero, then Equation (5-7b) is approximately true for an input channel with nonrigid upper and lower boundaries. It is important to note that these approximations of q and A imply a smooth transition in flow conditions from the input region to that over the slope (i.e., in two dimensions this implies a smooth matching of stream lines at the transition between the two regions).

For conditions of small slope ($\gamma \ll c$) and a smooth bottom transition, several simplifications are possible in Equation (5-7). For small slope, $\gamma \approx \alpha \approx \sin\alpha$ and for high enough wave frequencies, $\omega/N \gg \sin\alpha$. In addition,

$$M \simeq c; \qquad N \simeq c$$

$$F \simeq -\frac{1}{c}; \qquad G \simeq \frac{1}{c}$$

so that

$$u_f \simeq -\frac{a_0 \, \omega n\pi}{k_0 \gamma \xi} \left[\sin\theta_3 - e^{-D_i/\delta} \sin(\theta_3 + D_i/\delta) \right] \tag{5-8}$$

where

$$\theta_3 = q\ln(c\bar{\xi}) + \omega t \quad ; \quad \delta \simeq \left(\frac{2\nu}{\omega}\right)^{1/2}$$

Since $k_0 = \frac{cn\pi}{h_0}$ and $h = -\gamma x \approx -\gamma \bar{\xi}$ for small γ,

then

$$u_f \simeq \frac{a_0 \omega}{c(\bar{h}/h_0)} \left[\sin\theta_3 - e^{-D_i/\delta} \sin(\theta_3 + D_i/\delta) \right] \tag{5-9}$$

with $n = 1$.

After a short amount of manipulation it can be shown that the maximum
value of the terms inside the brackets on the right side of Equation (5-9)
can be approximated as $\sqrt{2}$ D_i/δ to order $(D_i/\delta)^2$. For waves of 1-hour
period, $\omega \simeq 1.7 \times 10^{-3}$ rad/sec, and for $\nu \simeq 10^{-2}$cm^2/sec, $\delta \simeq 10$ cm.
Typical sediment diameters on the outer shelf are on the order of 10^{-1} cm,
indicating that the above approximation is reasonable to about one percent.
Since for incipient motion conditions it is the maximum value of the velocity
at $\bar{\eta} = D_i$ that is the important quantity, then from Equation (5-9)

$$|u_f|_{max} \simeq \frac{a_o \omega}{c(h/h_o)} \sqrt{2} \ D_i/\delta \qquad (5\text{-}10)$$

for the following assumptions:

      (1) small slopes such that $\gamma \ll c$ and $\alpha \ll \phi$;

      (2) $D_i \ll \delta$.

It is also worth recalling here that the results of the laboratory experiments
described in the earlier chapters for the subcritical case ($\gamma < c$) suggest that,
at least for the conditions tested, the velocity field in the boundary layer was
adequately described by the linear theoretical solutions along the slope to the
point of breaking. For any particular case in which $\gamma \ll c$ is not valid, but
$\gamma < c$ still holds, the complete expression for u_f (Equation (5-7)) must be
used in Equation (5-4). However, it has been shown (Figure 79) that $\gamma \ll c$
is reasonable for several average oceanic conditions.

If Equation (5-10) is applied to Equation (5-6a), then

$$D_i = 0.216 \left[\frac{c(h/h_o)}{a_o \omega} \right]^2 \ \frac{g \delta^2}{C_D} \qquad \text{(downslope incipient motion)} \qquad (5\text{-}11)$$

This equation shows that in order to determine D_i some estimate of boundary
layer thickness δ (or equivalently, viscosity ν) must be made. Owing to the
difficulties in obtaining oceanic measurements of this quantity, this choice is
not simple. However, a lower bound can be estimated: the value of δ obtained

from Equation (5-7a) with $\nu = \nu_k$, where ν_k is the kinematic viscosity $(\nu_k \approx 10^{-2} \text{ cm}^2/\text{sec})$. The variation in ν_k for sea water is shown by Higgins (1962); typically ν_k varies from about $0.008 \text{ cm}^2/\text{sec}$ at 30°C to about $0.015 \text{ cm}^2/\text{sec}$ at 0°C (salinity about 35‰). Although coefficients of viscosity have been suggested by other authors to describe mixing processes that have scales larger than molecular, the current state of knowledge of the oceanic boundary layer induced by internal waves does not justify an a priori assumption of $\nu > \nu_k$. The problem of selecting a representative value of ν was discussed at the end of the previous section in this chapter. The basis for other choices of viscosity here lies in an "intuitive feeling" that natural oceanic boundary layers are turbulent. The actual viscosity is probably a result of several processes at work, including internal waves. It is worth recalling, however, that the experimental runs with linear, smooth slopes showed no appreciable net transport of fluid in the boundary layer outside of the breaking zone for $\gamma < c$. In the discussion of net Lagrangian motion in Chapter 4, this observed absence of net transport was interpreted to mean that there was no measureable mixing induced by the internal waves along the slope up to positions near the breaking zone. The turbulent dissipation of the high-frequency waves for $\gamma < c$ in the breaking zone and the mixing induced by the vortex instability for $\gamma \geq c$ are two possible instances for which a choice of $\nu > \nu_k$ might be made, at least for the laboratory conditions.

The other apparent difficulty in the direct application of Equation (5-6a) or Equation (5-6b) to oceanic conditions is the choice of the drag coefficient C_D. Considerable experimental evidence shows that C_D is largely dependent on a suitable Reynolds number R_D for solid bodies immersed in a moving fluid (Prandtl, 1952; Batchelor, 1967). Usually the relationship between C_D and R_D is given for a steady flow past a smooth and regular body such as a sphere in an unbounded fluid. In the case of an irregularly shaped particle resting on a rough bed in an oscillatory flow, the relationship between C_D and R_D is not well known. Eagleson et al (1958) showed

measurements from which the drag coefficients for spheres rolling down a smooth, inclined boundary immersed in water or oil were evaluated from the relation

$$C_D \, \rho_f \frac{\pi D^2}{8} \, v_s^2 = F_G \sin \alpha$$

where v_s is the measured translational velocity of the sphere of diameter D. Their results are shown in Figure 81. Line A in this diagram is the conventional curve for $C_D \propto R_D^{-1}$ for spherical particles moving in an unbounded fluid (Batchelor, 1967). Eagleson et al (1958) later extended these results experimentally to account for the presence of a rough bottom. Figure 82 shows that for constant values of particle diameter D, decreasing roughness size κ (i.e., increasing ratio D/κ) causes a reduction in the drag coefficient determined for a smooth bottom from Figure 81. In their studies of incipient motion of bed particles due to surface waves, Eagleson and Dean (1959) chose $C_D = 19.2/R_D$ with $D/\kappa \simeq 1$ and $R_D = u_f D/\nu$. On the basis of a large number of experiments in which C_D was computed from an equation similar to Equation (5-4) for various measured values of u_f, D_i, ϕ, α, and s_s/s_f, Eagleson and Dean (1959) concluded that there was no qualitative disagreement between the values of C_D obtained in this way with those values obtained from Figures 81 and 82. It is not obvious, however, that their results show conclusively that the two methods of computing C_D are equivalent for incipient motion of the particles. On the other hand, their results are quite convincing that the two methods are in agreement for discrete particles that are already in motion.

In view of the apparent importance of the local particle Reynolds number R_D on the value of C_D, it is useful to establish some upper bound on R_D for the oceanic problem. Sediments on the outer shelf have median diameters on the order of 10^{-2} cm. Lacking specific measurements of
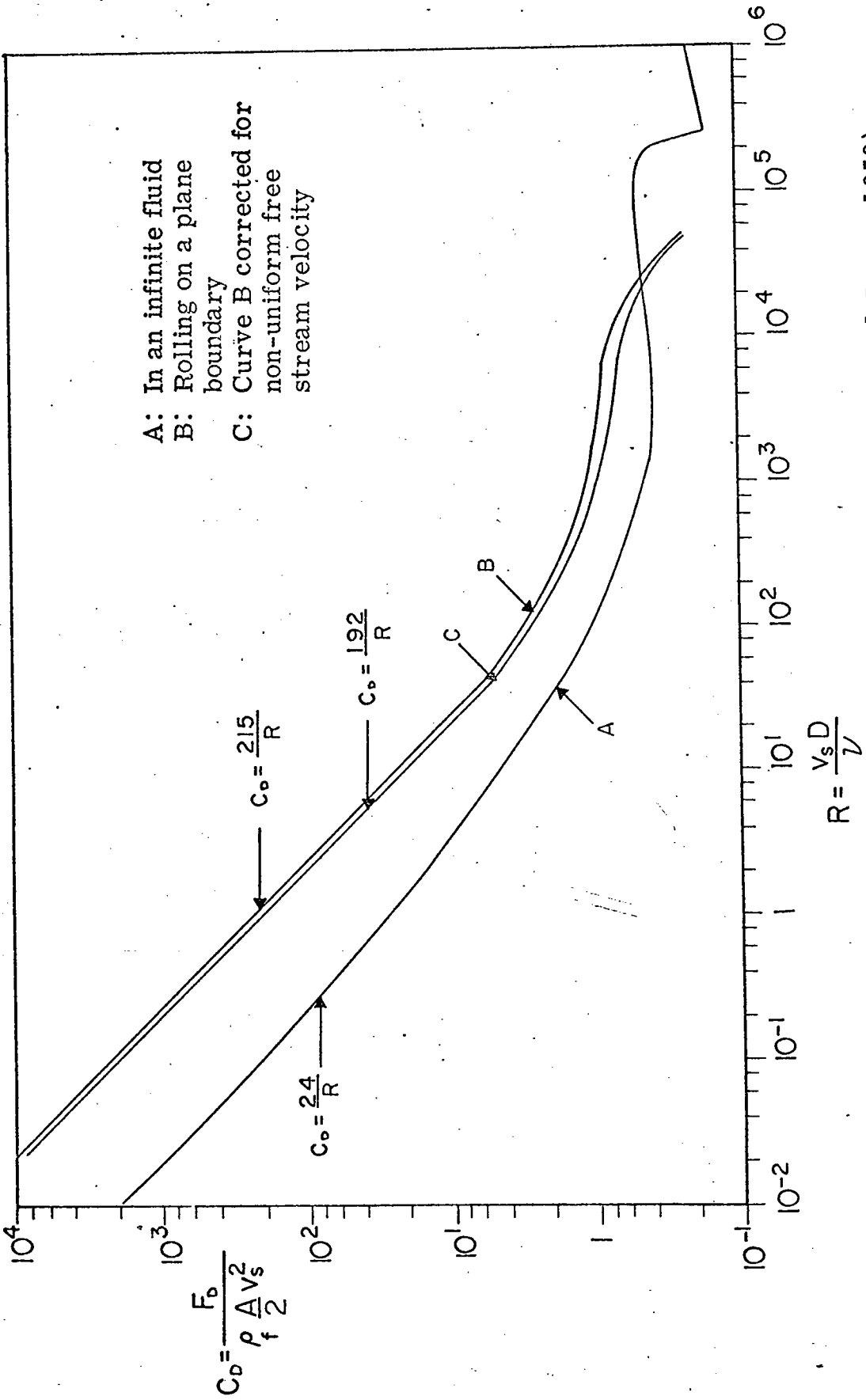
FIG. 81. Resistance coefficients C_D for spheres (after Eagleson and Dean, 1959).

A: In an infinite fluid
B: Rolling on a plane boundary
C: Curve B corrected for non-uniform free stream velocity

$C_D = \dfrac{215}{R}$

$C_D = \dfrac{192}{R}$

$C_D = \dfrac{24}{R}$

$R = \dfrac{V_s D}{\nu}$

$C_D = \dfrac{F_D}{\rho_f \dfrac{A}{2} V_s^2}$
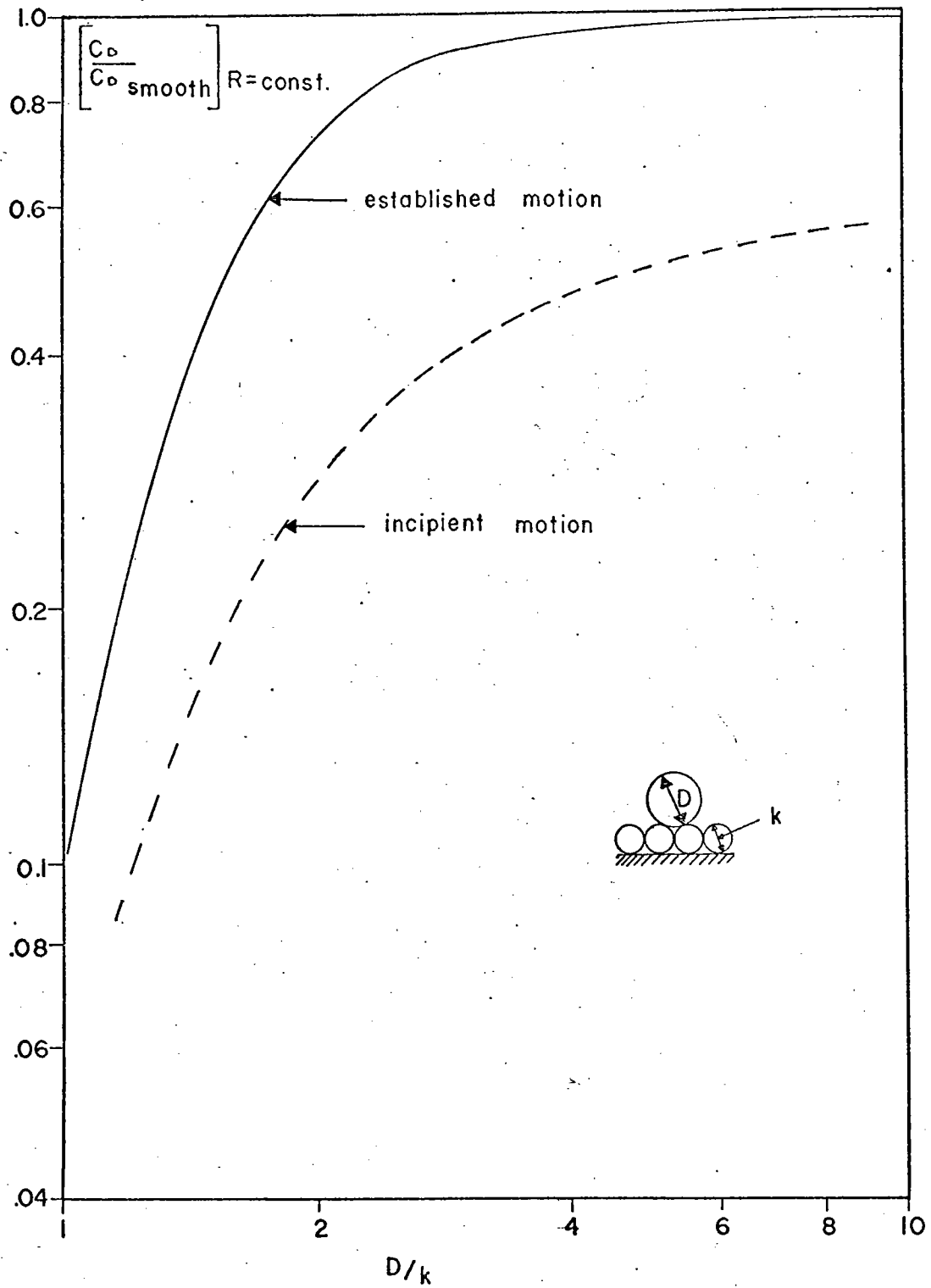
FIG. 82. Effect of bed-particle geometry on the resistance
coefficients for spheres (after Eagleson and Dean, 1959).

internal-wave velocities in the bottom boundary layer, a value of 100 cm/sec is selected as a crude upper estimate.[*]

If $\nu = \nu_k \simeq 10^{-2}$ cm^2/sec, then $R_D \simeq 100$. For larger values of ν or smaller u_f, R_D becomes less than 100. This upper bound suggests that, according to Figure 81, $C_D \approx 192/R_D$ for a hydraulically smooth bottom. If the additonal assumption that $D/\kappa \approx 1$ is made, then $C_D = 192/R_D$ (Figure 82). If this value of C_D is applied to Equation (5-11) with $R_D = \dfrac{u_f D_i}{\nu}$ and $\nu \simeq \delta^2 \omega/2$, then

$$D_i = 31.36 \; \frac{a_o \omega^2}{g\,c\,(h/h_o)} \tag{5-12}$$

for incipient downslope motion on small slopes.

It is obvious from Equation (5-12) — and not unexpected — that the local incipient diameter is a function of the boundary layer thickness (or alternatively, the viscosity ν) as well as the local depth and input wave conditions. The value of D_i increases linearly with decreasing depth, suggesting progressive sorting of sediment. Equation (5-12) predicts that sediment particles having diameters smaller than D_i will initially move downslope so that there should be a trend toward smaller mean diameters in the seaward direction. Since the model does not describe the subsequent history of bottom particles once they are initially moved from their roughness hollows, it is not possible from this analysis to trace their net motion after initial movement. However, one might speculate that once the particles are set into motion they might be advected to different locations as bed load

---

[*] A few values of instantaneous near-bottom velocities on the continental margins are available. For example, Emery and Ross (1968) reported a maximum value of 70 cm/sec on the continental slope south of Martha's Vineyard; the flow direction was parallel to the bottom contours.

if there is net motion of the surrounding fluid. The net motion of the fluid need not depend on mixing induced by internal waves, but can be caused by other currents. It is emphasized that this analysis pertains to initiation of motion of noncohesive bed particles for the conditions assumed; subsequent motion as established bed load or suspended load is only speculative.

The inverse relationship between the ratios D_i/δ and h/h_o can be conveniently illustrated for different choices of a_o, N, and ω; Figure 83 is an example of this relationship. Each straight line in the diagram represents a particular input wave amplitude a_o for internal waves that are assumed to be normally incident to the slope. The larger values of a_o are permitted only for h_o large in the sense $a_o/h_o \ll 1$. (The linear internal wave theory used in this analysis is valid only for small-amplitude waves.) Finite-amplitude effects have not been considered explicitly. Consequently, the results are valid upslope to a point where the Stokes parameter ϵ becomes order one; the exact value of ϵ for this limiting condition is not precisely defined. A discussion of ϵ for the small-slope approximation is given in Chapter 4. The experiments show that for $\gamma < c$, the high-frequency waves induce a zone of breaking for values of $\epsilon \geq 0.5$. A value of $\epsilon \geq 0.5$ might be used to establish a limiting depth ratio h/h_o for this model; i.e., at depth ratios shallower than h/h_o the linear analysis is invalid. If $a_o = mh_o$ where $m \ll 1$ and positive, then from Equation (4-14)

$$h/h_o = (\frac{m}{\epsilon} c\pi)^{1/2} \tag{5-13}$$

where

mode n = 1.

For example, for relatively high-frequency, first-mode internal waves, such that $\omega \simeq N/2$ and $a_o = 0.01 h_o$ (m = 0.01), it follows from Equation (5-13) that

$$h/h_o \simeq \left(\frac{1.8 \times 10^{-2}}{\epsilon}\right)^{1/2}.$$

If $\epsilon = 0.1$, $h/h_0 \simeq 0.4$; if $\epsilon = 0.5$, $h/h_0 \simeq 0.2$. Figure 83 shows the limiting depth ratios derived in these examples.

Before discussing the results of this model in terms of oceanic conditions it is instructive to show that the form of Equation (5-12) is in some sense compatible with the familiar Shields parameter S,

$$S = \frac{\tau_c}{(s_s/s_f - 1)\, \rho_f g\, D_s} \tag{5-14}$$

where D_s is equivalent to D_i and τ_c is the shear stress necessary to produce initial motion of noncohesive bed particles in a steady flow. Shields (1936) presented experimental results relating this parameter to a particular Reynolds number. Others (for example, Vanoni, 1964) provided subsequent experimental results that established a single curve relating this Shields parameter S to the particle Reynolds number R^*_D, where

$$R^*_D = \frac{u^* D_s}{\nu}, \text{ with } u^* = \sqrt{\tau/\rho_f}$$

The diagram in Figure 84 shows the classical Shields curve with some later experimental results plotted on it; the Shields parameter is the ordinate, and the particle Reynolds number is the abscissa. Two basic problems arise in the application of this curve to the present problem: (1) the experimental measurements represented by the curve were made for boundary layers that were fully turbulent; and (2) in most cases the mean flow conditions were steady (channel flow). White (1940) derived a similar semi-empirical result for the critical stress at the bed for steady flow conditions and a laminar boundary layer:

$$S = 0.18 \tan \phi \tag{5-15}$$

where S is given by Equation (5-14). According to White, $\tan \phi$ is about unity which gives $S \approx 0.18$, as compared to about 0.03 to 0.06 for S obtained by Shields (Figure 84). White found, however, that the value of S
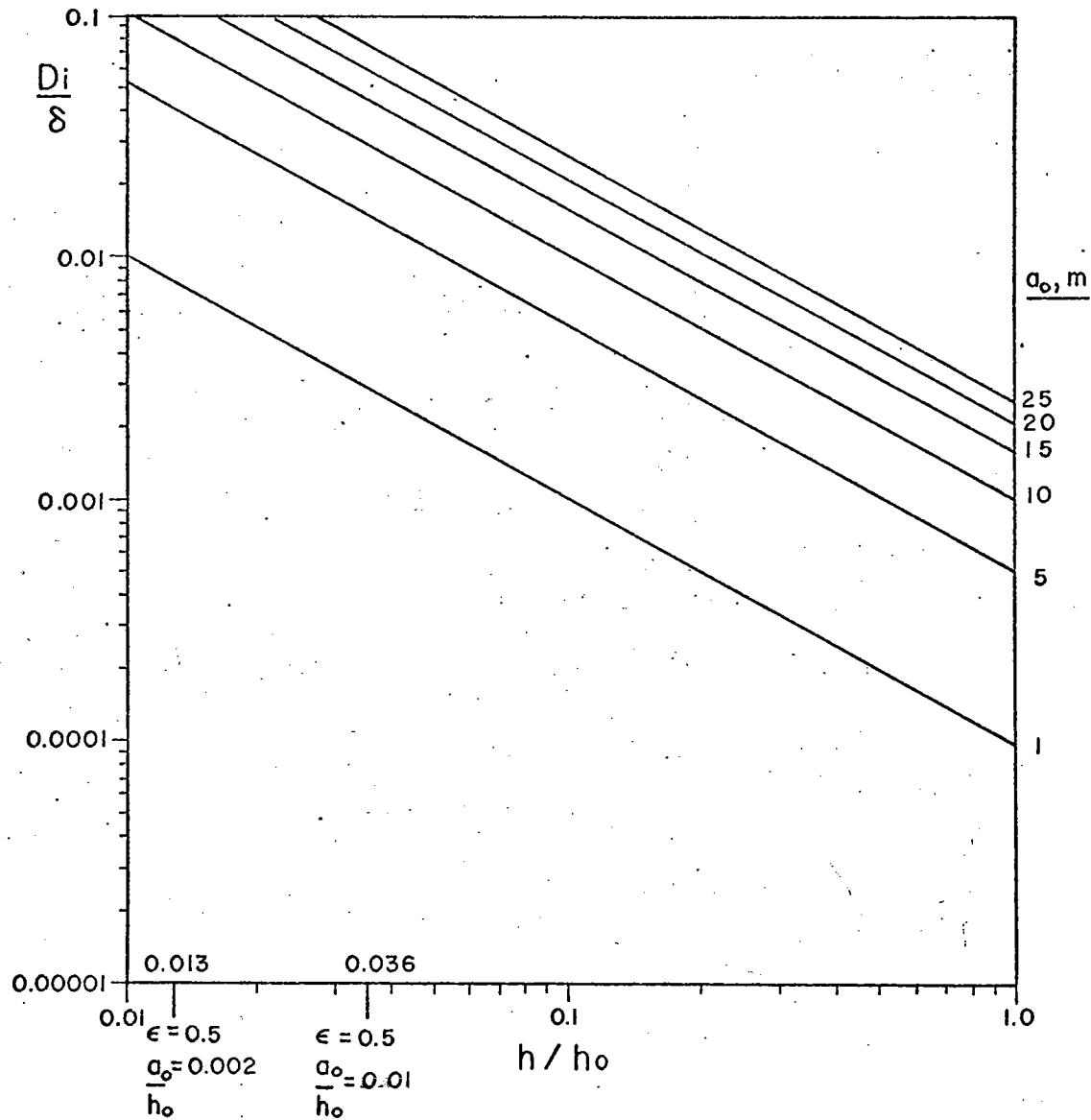
FIG. 83. Ratio of incipient diameter D_i to boundary-layer thickness δ for various positions on the slope, given by h/h_o, and for selected amplitudes a_o of the incident internal waves.

SANDS IN TURBULENT BOUNDARY LAYER

SHIELDS CURVE

$\dfrac{\tau_o}{(\gamma_s - \gamma)d_s}$

$\dfrac{u_* d_s}{\nu}$

Sym	Description	γ_s-g/cm^3
○	AMBER	1.06
◐	LIGNITE (SHIELDS)	1.27
◑	GRANITE	2.7
◒	BARITE	4.25
○	SAND (CASEY)	2.65
◇	SAND (KRAMER)	2.65
⊗	SAND (U.S.W.E.S.)	2.65
◉	SAND (GILBERT)	2.65
●	SAND (VANONI)	2.65
◐	GLASS BEADS (VANONI)	2.49
□	SAND (WHITE)	2.61
○	SAND IN AIR (WHITE)	2.10
△	STEEL SHOT (WHITE)	7.9

FULLY DEVELOPED TURBULENT VELOCITY PROFILE

TURBULENT BOUNDARY LAYER
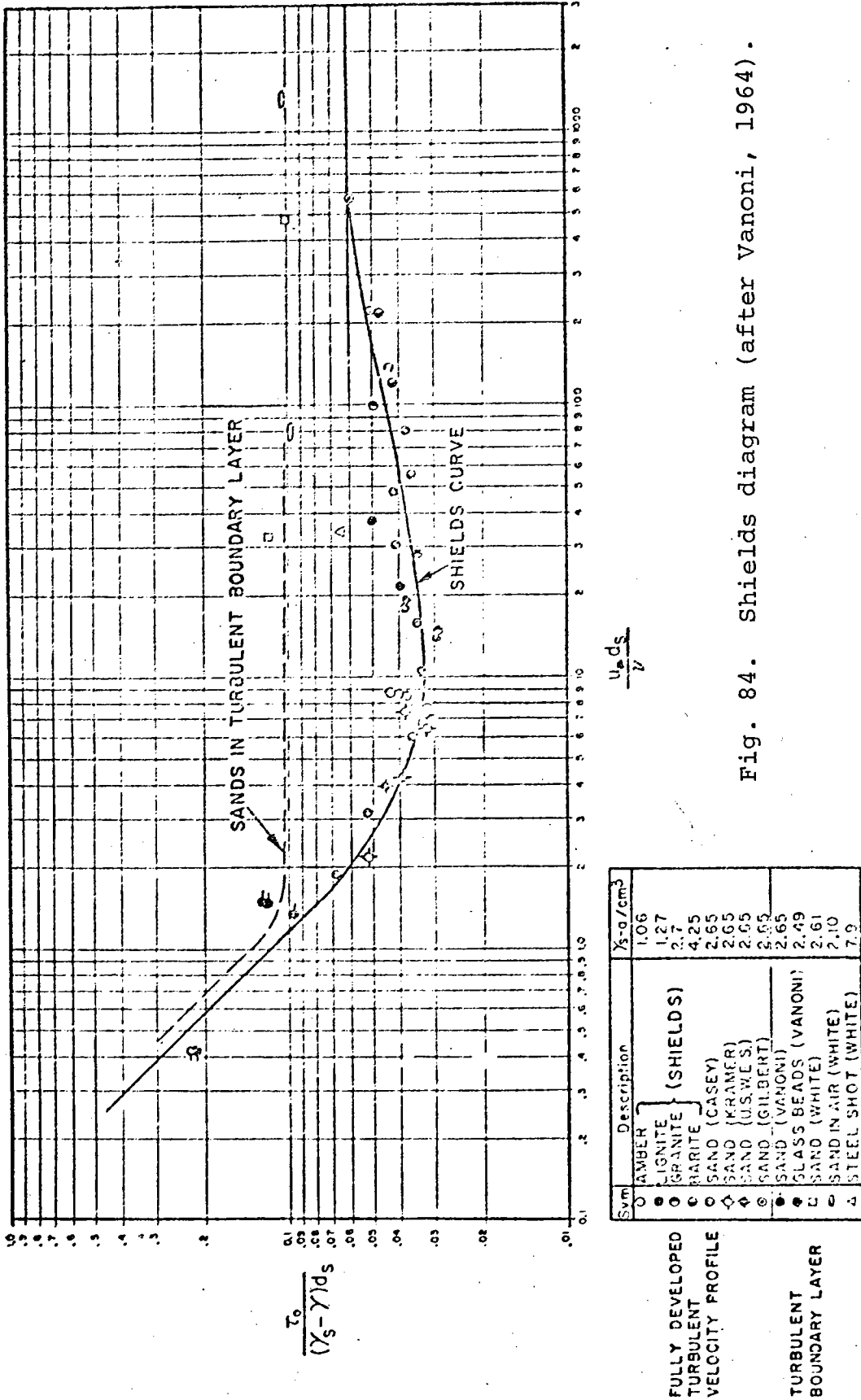
Fig. 84. Shields diagram (after Vanoni, 1964).

for turbulent flow in the boundary layer was about one-half that for laminar conditions. The remaining discrepancies in the results of White for turbulent flow with those of Shields were attributed to the more intense turbulence in the flows with fully developed velocity profiles which Shields used (Vanoni, 1964). The difference between the two results according to Vanoni was that for both turbulent and laminar flow conditions in the boundary layer, White found that τ_c was apparently independent of R^*_D. By contrast, Figure 84 shows that τ_c is dependent on R^*_D to values of R^*_D near 10^3 where the Shields parameter approaches a constant value of about 0.06.

The mean conditions of steady flow that are implicit in Figure 84 are not unreasonable for low-frequency internal wave phenomena, since the advective accelerations are small, as was assumed in the earlier model. The compatibility of the earlier model with White's equation for laminar flow conditions (Equation (5-15)) can be demonstrated simply. If the bed shear stress is written as

$$\tau = \mu \; \partial u / \partial \overline{\eta}$$

and if $\partial u / \partial \overline{\eta}$ is approximated by a linear fit:

$$\partial u / \partial \overline{\eta} \sim \Delta u / \delta \simeq a \omega / c \delta$$

where $\Delta u \approx a \omega / c$, then for $\delta = (2\nu/\omega)^{1/2}$ (i. e., small slopes) and $\mu = \nu \rho_f$ the bed shear stress can be rewritten approximately

$$\tau = \nu \rho_f \; a\omega / \delta = \delta/2 \; a\omega^2 / c. \tag{5-16}$$

On small slopes it was shown earlier that

$$a = a_o h_o / h \qquad \text{(correct to first order in } \epsilon \text{)}. \tag{5-17}$$

Combining Equations (5-16) and (5-17) it follows that

$$\tau \simeq \delta \; \frac{a_o \omega^2}{2c \; (h/h_o)} \tag{5-18}$$

Applying this expression for bed shear stress into White's result for incipient motion in a laminar boundary layer (Equation (5-15)) an expression is obtained for D_i/δ:

$$D_i/\delta = K \frac{a_o \omega^2}{gc(h/h_o)}$$

$$K = \frac{2.78}{(\rho_s - \rho_f)\tan\phi}$$

(5-19)

The functional form of this result is equivalent to Equation (5-12). A closer comparison between this equation and Equation (5-12) is not justified because: (1) Equation (5-17) does not include a Reynolds number dependence; (2) Equation (5-19) assumes a linear velocity profile in the boundary layer; and (3) Equation (5-19) does not specify the point of application of the effective velocity acting on the bed grains.

A brief summary of the preceding analysis might be helpful here. The foregoing model deals with conditions of incipient motion of noncohesive bed particles induced by internal gravity waves shoaling over a small linear slope. The static equilibrium of these particles on the bed was defined in terms of an incipient diameter D_i. The analysis predicts that the net instantaneous hydrodynamic and gravitational moments acting on the particle about the contact points with other bed particles will cause those particles with diameters less than D_i to move downslope initially. Equation (5-12) relates D_i to the internal wave parameters (a_o, ω, c), a local depth ratio (h/h_o), and the boundary layer thickness (δ). It is also shown that Equation (5-12) is compatible with the results of Shields (1936) and White (1940).

MODEL ANALYSIS AND SPECULATION

As defined above, the criterion in Equation (5-12) essentially defines the condition of neutral equilibrium set up by instantaneous hydrodynamic forces of internal waves and that of gravity acting on discrete bed particles that are resting on a rough bed. A different dynamic balance is

needed to define a condition of equilibrium for particles that have already been placed in motion. This balance must depend on the net transport currents influencing the particle motion, including any net currents that might be induced by the internal waves, and the downslope pull of gravity. However, as was indicated in Chapter 4, steady transport of water particles induced by internal waves, near a sloping boundary in a stably stratified fluid, other than that caused by diffusion, theoretically cannot occur in a plane normal to the depth contours unless other processes of mixing are active. Consequently, it is not possible to predict a type of oscillating equilibrium for onshore-offshore motion of sedimentary particles for which $D < D_i$. In the case of surface waves, Ippen and Eagleson (1955) and Eagleson and Dean (1959) have shown that a balance between the forces on a particle due to the mass transport current in the bottom boundary layer, directed upslope, and the downslope component of gravity creates a situation where sediment particles of increasing size in the onshore direction are in oscillating equilibrium. The diameter of the local equilibrium size is often referred to as the "null" or "equilibrium" diameter D_e. The location of this type of equilibrium for a particular sediment size is called the "null" point. Miller and Zeigler (1964) and Eagleson and Johnson (1966) discuss sediment sorting by surface waves and give some comparisons with field data. The only available direct evidence for net fluid transport induced by internal waves on a slope are the laboratory results that were presented in Chapter 4.

In view of the absence of other evidence for the existence of mass transport by shoaling internal waves, only the effects of the incipient condition which was derived in the preceding section are considered here. Curves similar to that shown in Figure 83 can be used to determine the hypothetical distribution of D_i along a linear bottom slope if δ is known. Suppose that the initial size-frequency distribution of noncohesive bed particles is given by the solid curve in Figure 85 at each position along the slope. After the internal waves have acted to produce incipient motion of sediment having
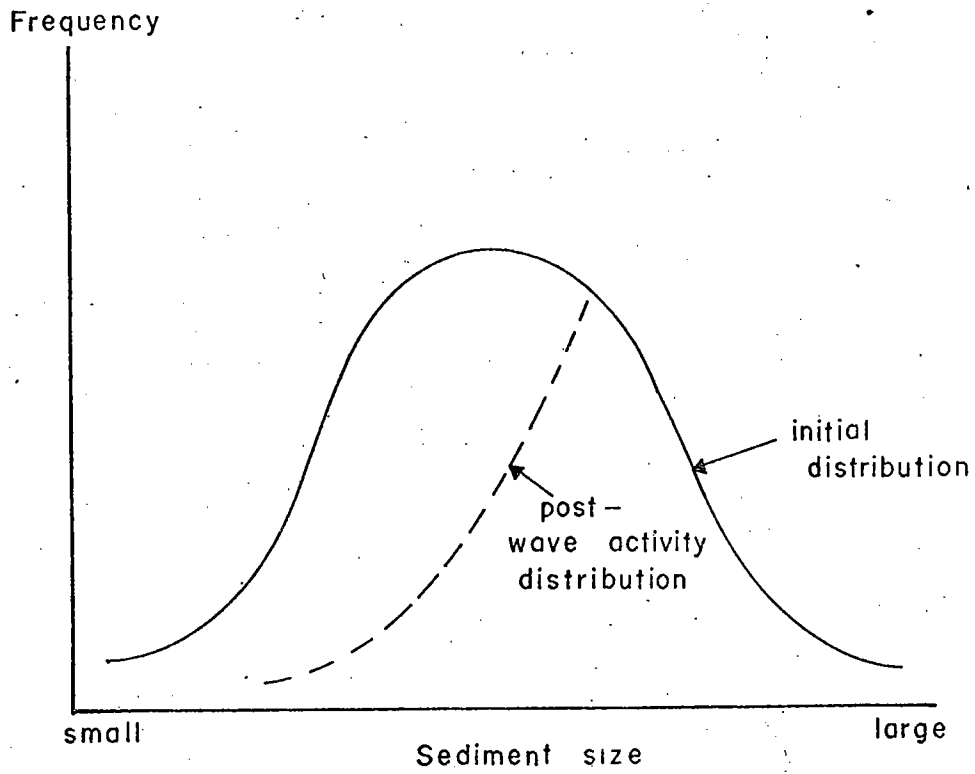
FIG. 85. Hypothetical size-frequency distribution of
sediments on an oceanic slope.

diameters less than D_i at each depth according to Equation (5-12), the final shape of the size-frequency distribution at each location might eventually have a spike at D_i and appear as shown by the broken line in Figure 85. The sediment size at which the spike occurs decreases in the offshore direction.

It is unreasonable to require this simple analysis, with Equation (5-12) as its tidy result, to explain the complicated sedimentary pattern found on the continental margins. Instead, it is instructive to postulate various simple models to determine at what locations and for which hydrodynamic conditions, if any, the predicted values of D_i according to Equation (5-12) might exceed the observed natural sediment diameters.

Models are constructed for three provinces defined by the idealized bottom geometry and the simplified distribution of Brunt-Vaisala frequency shown in Figure 78. Each layer (i.e., the three fluid layers intersecting the shelf A, slope B, and rise C) with constant N is assumed to support small-amplitude, single-frequency internal waves of the first mode that propagate shoreward at approximately normal incidence to the slopes. Furthermore, only examples that satisfy the condition $\gamma << c$ were considered, except for the hypothetical instance of waves with semi-diurnal frequency over the continental shelf and continental rise. In these cases, it is shown that the ratio γ/c is on the order of one-tenth. Values of the pertinent hydrodynamic parameters are listed on each diagram. In addition, since the depth range over which the analysis is valid is limited to small values of ϵ (as discussed in the initial section of this chapter), the depth ratios h/h_0 at which $\epsilon = 0.1$ and $\epsilon = 0.5$ are indicated on each diagram. It should be recalled that the experiments for $\gamma < c$ showed breaking of internal waves at $\epsilon \geq 0.5$. On this basis, it was suggested that the linear solutions might be invalid if local values of ϵ exceed 0.5. The sources for the sediment data are listed in each diagram; the approximate locations of the sampling areas for each source are shown in Figure 76.

Figure 86 treats a continental-shelf model with relatively high-frequency internal waves ($\omega \simeq N/2$, $N = 6$ cph); the pertinent assumptions in the model are specified in the figure. The ordinate is mean diameter D_m (for actual sediment data) or incipient diameter D_i (computed from Equation (5-12)); the horizontal axis is the depth ratio h/h_o. As mentioned above, values of h/h_o computed from Equation (5-13) for two selected values of ϵ and for the particular wave conditions (a_o, ω, c) of the model are marked long the horizontal axis. The variations of D_i with h/h_o are shown as theoretical stright-line curves for selected values of H:

$$H = \frac{a_o \nu^{1/2}}{A_o \nu_k^{1/2}}$$

where a_o is input wave amplitude in meters,

ν is viscosity in cm^2/sec,

$A_o = 1$ m,

$\nu_k = 10^{-2}$ cm^2/sec.

$(A_o \nu_k^{1/2} = 10$ $cm^2 \cdot sec^{-1/2}$.)

For example, the curve in Figure 86 labeled $H = 5$ represents $a_o \nu^{1/2} = 50$ $cm^2 \cdot sec^{-1/2}$, or if $\nu = \nu_k$, then $a_o = 5$ meters. This kind of log-log plot simplifies presentation of the analytical results; the theoretical curves are straight lines (Equation (5-12)), and D_i can readily be obtained for various combinations of a_o and ν (or δ). The field data of mean sediment diameters in Figure 86 show a general trend toward decreasing sizes in an offshore direction. This trend reverses for $h/h_o > 0.4$ in Stetson's data and for $h/h_o > 0.5$ in Hollister's data.

Interpretation of the relationship between the actual mean values D_m and the theoretical distributions of D_i was described earlier and will be summarized here. D_i represents the maximum sediment diameter that is in

Dm
or
Di

0.5

H=50

H=10

H=5

0.1

H=1

0.05

symbol	h/h	ϵ	a , m
a	0.213	0.5	1.0
b	0.480	0.1	1.0
b	0.480	0.5	5.0

0.05   0.1   0.5

h / ho   a   b
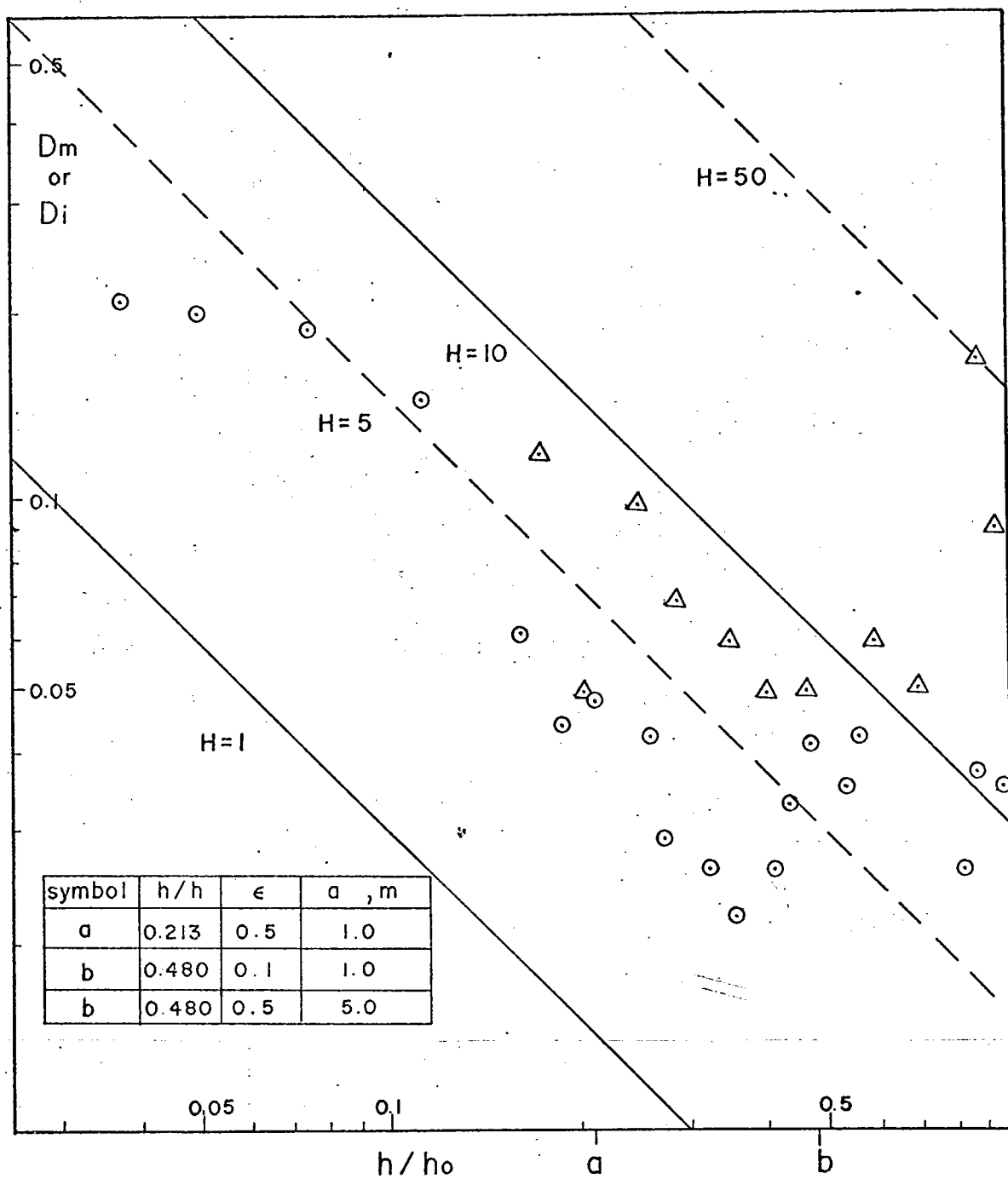
Model parameters

N = 6 cph
ω = 3 cph
c = 0.577
f = 0.062 cph
A_o = 1 m
ν_κ = 10^{-2} cm^2/sec

$$H = \frac{a_o \, \nu^{1/2}}{A_o \, \nu_\kappa^{1/2}}$$

$$c = \left[\frac{\omega^2 - f^2}{N^2 - \omega^2} \right]^{1/2}$$

Sediment data

⊙   Hollister

△   Stetson # 4

FIG. 86.   Continental shelf model; relatively high frequency
waves.

neutral equilibrium at slope positions given by h/h_o for hypothetical internal-wave types and idealized bottom conditions. The analytical model predicts initiation of motion of bed particles in a downslope direction if $D_m < D_i$.

In Figure 86 incipient motion of measured sizes D_m is predicted for $H \geq 50$ (for example, $a_o = 5m, \nu = 1 \text{ cm}^2/\text{sec}$) and $h/h_o > 0.48$ (for the cut-off condition imposed by $\epsilon = 0.5$). If $H = 5$ ($a_o = 5m$, $\nu = \nu_k$) and if $\epsilon = 0.5$ is the limiting value for the linear analysis, then all values of D_m from Stetson's data for $0.25 < h/h_o < 0.45$ could be placed into motion by the waves. It might be noted here that the nonlinear effects which are significant farther upslope (where ϵ is order one, say) could make the case for possible sediment movement even stronger. For instance, the experiments for $\gamma < c$ showed that the measured velocities in the boundary layer near the zone of breaking were significantly larger than corresponding measurements taken farther downslope. Consequently, one might expect that the presence of nonlinearities in the velocity field might increase the values of D_i for positions well upslope. The consideration here of a strictly linear analysis is in this sense a "worst" case: if initiation of motion of measured diameters is predictable from the linear model, then the inclusion of non-linear effects strengthens the argument. We might also recall that values of $\nu > \nu_k$ are included mainly on the supposition that the oceanic boundary-layer dynamics might involve an eddy viscosity.

Figure 87 is another shelf model similar to Figure 86 except that the internal-wave frequency is assumed to be semi-diurnal. In this model, the requirement $\gamma/c << 1$ is necessarily relaxed to $\gamma/c < 1$ ($\gamma/c \simeq 0.01$). The case for incipient motion of the measured sediment sizes is not as convincing as that given in Figure 86. The theoretical curves indicate that D_m is less than D_i for relatively small-amplitude waves ($a_o \leq 5m$) only if $\nu \geq 1 \text{ cm}^2/\text{sec}$ (see $H = 50$, for example). The values of D_i along theoretical curves $H = 1$ and $H = 5$ are below the mean diameters; this suggests that waves of 5-meter amplitudes with $\nu = \nu_k$ will not move the measured mean sizes.

symbol	h / ho	ϵ	a_o , m
a	0.038	0.5	1.0
b	0.085	0.1	1.0
b	0.085	0.5	5.0
c	0.190	0.1	5.0

Model parameters

N = 6 cph

ω = 0.083 cph

c = 0.01

f = 0.062 cph

A_o = 1 m

ν_κ = 10^{-2} cm²/sec

$$H = \frac{a_o \nu^{1/2}}{A_o \nu_\kappa^{1/2}}$$

$$c = \left[\frac{\omega^2 - f^2}{N^2 - \omega^2}\right]^{1/2}$$

Sediment data

⊙   Hollister

△   Stetson # 4
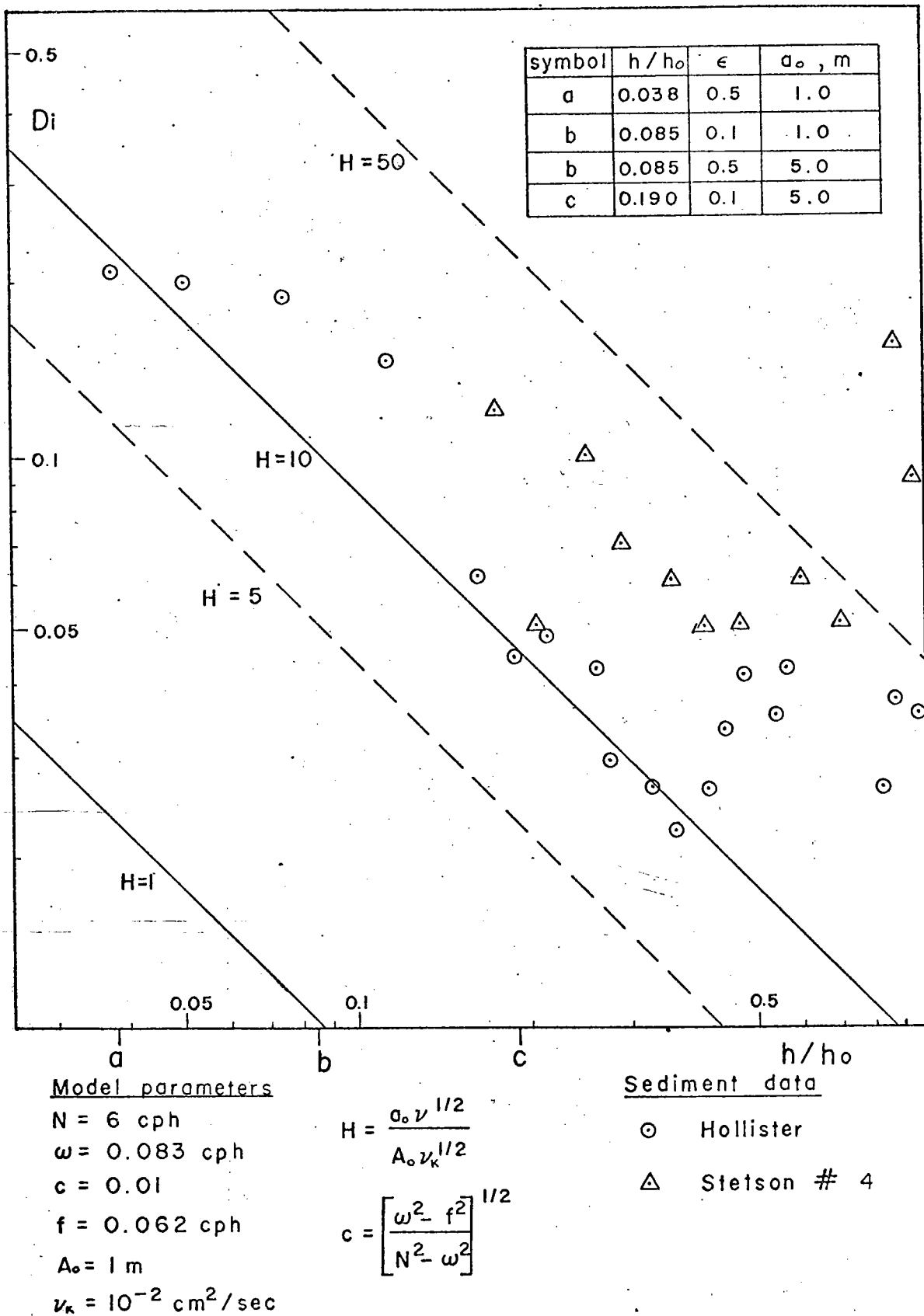
FIG. 87.   Continental shelf model; wave of tidal frequency
            (semi-diurnal).

The continental slope model in Figure 88 assumes relatively high-frequency waves ($\omega = N/2$; $N = 3$ cph) because critical conditions ($\gamma \simeq c$) are approximately achieved along the slope for waves of lower frequencies, such as the frequency of the semi-diurnal tide. The data shown in this figure were obtained from various sources; the lines of sample locations are shown in Figure 76. Initial movement is predicted for sediment along the lower extremity of the slope ($h/h_o \geq 0.8$) for $H = 10$. For $H = 50$ ($a_o = 5$m, $\nu = 1$ cm^2/sec), initiation of sediment motion is possible for each of the measured values along the slope.

A smaller number of data points are shown in the continental rise model in Figure 89. The available values of mean diameter tend to be in the range of fine to very fine silt; the ordinate (D_i or D_m) has been scaled accordingly. It is worth recalling the earlier discussion of sedimentary types on the continental rise. Several previous workers (Heezen, et al 1966, for example) noted that clean quartzose sands and coarse silts inter-bedded with the clays can be locally dominant. These larger sizes are not represented in the data plotted in Figure 89. It is obvious from Pratt's data however, that the mean diameters found on the lower parts of the rise are generally larger than farther upslope. The computed incipient diameters exceed the mean diameters for $H = 5$ ($a_o = 5$m, $\nu = \nu_k$) on the upper rise. Initial movement of the larger measured sizes on the lower rise requires larger wave amplitudes (or larger viscosity), such that $H \geq 50$. The effects of cohesive forces acting on the smaller sizes (very fine silts and clays) have not been considered; these forces might inhibit initial movement and thereby require larger values of H for incipient motion.

The results of this section can be summarized briefly. It has been shown that, within the constraints of the models, the predicted values of incipient diameters D_i can exceed the values of mean diameters D_m measured at various positions on the continental margin southeast of New England. The condition for incipient motion of bed particles induced by internal waves shoaling over a small slope whose average gradient is linear is given by

symbol	h/h_o	ϵ	a_o, m
a	0.051	0.5, 0.1	1, 5
b	0.115	0.1	1
c	0.163	0.5	10
d	0.257	0.1	5
e	0.364	0.1	10
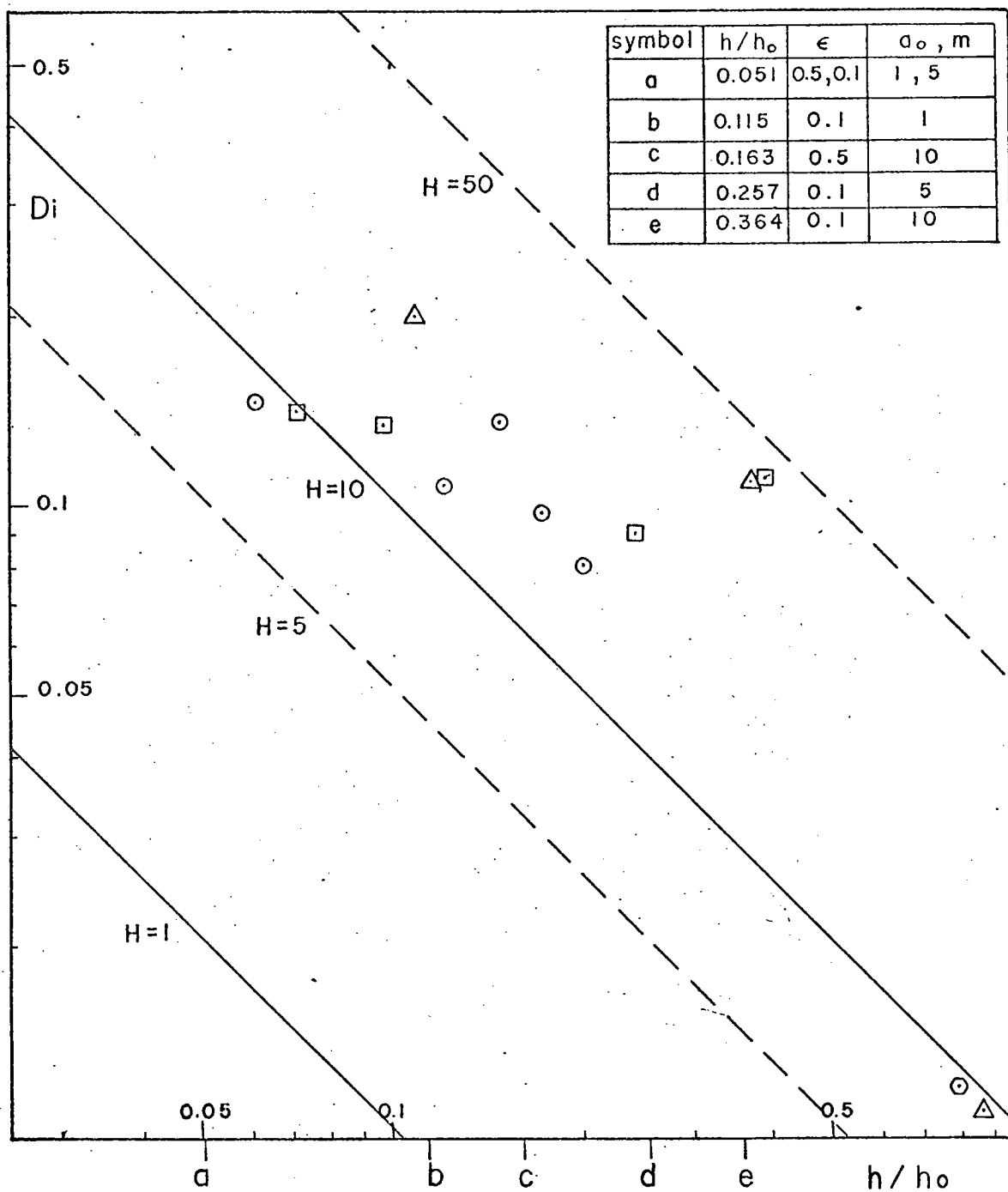
Model parameters

$N = 3$ cph

$\omega = 1.5$ cph

$c = 0.5768$

$f = 0.062$ cph

$A_o = 1$ m

$\nu_\kappa = 10^{-2}$ cm^2/sec

$$H = \frac{a_o \nu^{1/2}}{A_o \nu_\kappa^{1/2}}$$

$$c = \left[\frac{\omega^2 - f^2}{N^2 - \omega^2}\right]^{1/2}$$

Sediment data

⊙   Stetson # 5

▣   Stetson # 6

△   Pratt

⊙   Emery and Ross
      (average of 3
         samples)

FIG. 88. Continental slope model; relatively high-frequency waves.

Di

H = 50

H = 10

H = 5

H = 1

0.5

0.1

0.05
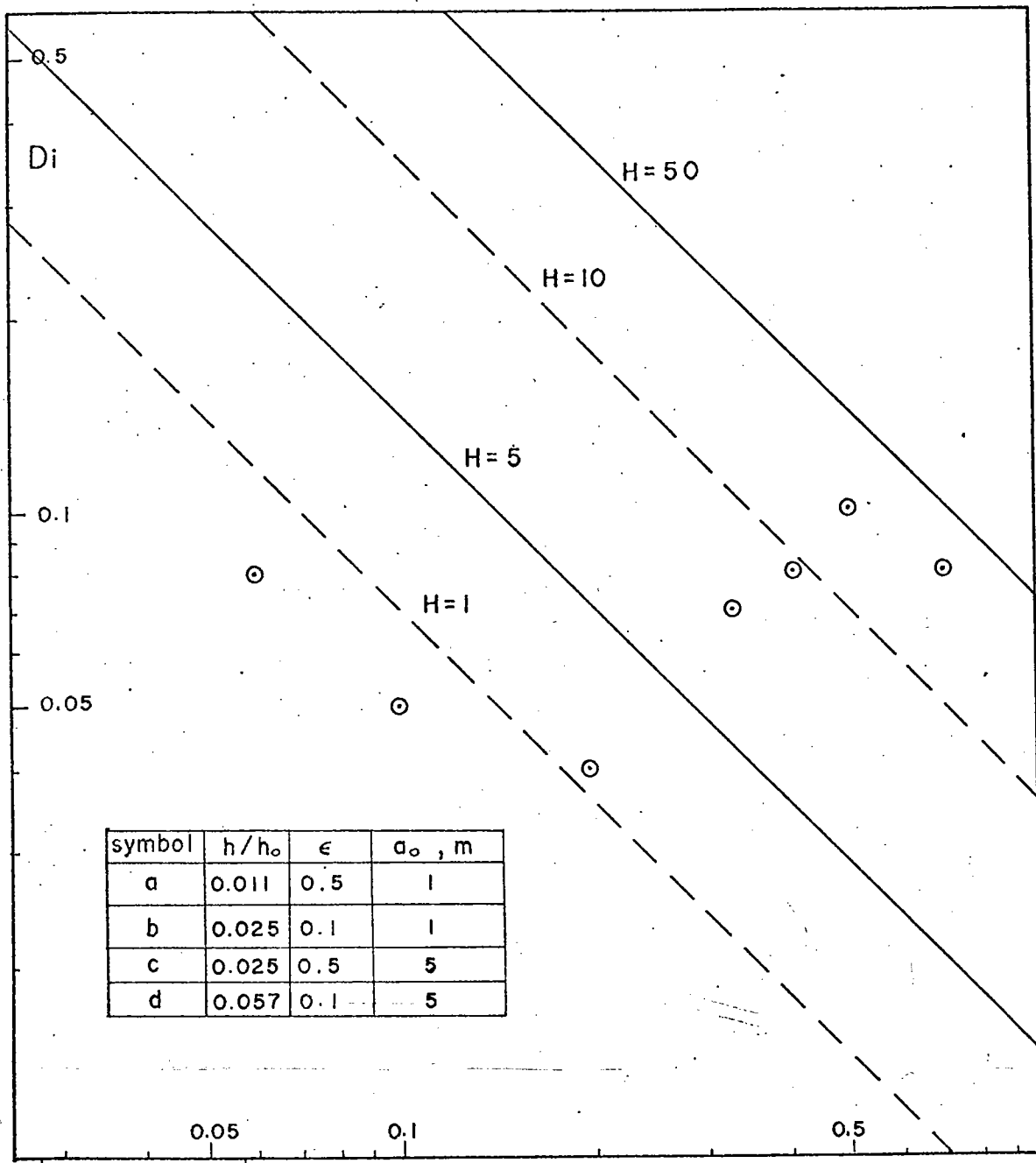
symbol	h/h₀	ε	a₀ , m
a	0.011	0.5	1
b	0.025	0.1	1
c	0.025	0.5	5
d	0.057	0.1	5

0.05   0.1   0.5

b,c   d

h/h₀

Model parameters

Sediment data

$N = 1$ cph
$\omega = 0.083$ cph
$c = 0.056$
$f = 0.062$ cph
$A_o = 1$ m
$\nu_\kappa = 10^{-2}$ cm²/sec

$$H = \frac{a_o \nu^{1/2}}{A_o \nu_\kappa^{1/2}}$$

$$c = \left[\frac{\omega^2 - f^2}{N^2 - \omega^2}\right]^{1/2}$$

⊙   Pratt

FIG. 89.   Continental rise model; waves of tidal frequency (semi-diurnal).

Equation (5-12). It is obvious from Equation (5-12) that larger values of wave amplitude and viscosity produce larger incipient diameters at specified values of h/h_0. Incipient motion of the measured sediment is predicted for specific instances in the models considered above:

(1) on the outer continental shelf ($h > 50$ m, say) with $N = 6$ cph, $\omega = 3$ cph, and $H \geq 5$;

(2) on the outer continental shelf with $N = 6$ cph, semi-diurnal frequencies, and $H \geq 50$;

(3) on the lower continental slope ($h/h_0 \geq 0.8$), for $N = 3$ cph, $\omega = 1.5$ cph and $H = 10$, or on the middle sections of the continental slope with $H = 50$;

(4) on the upper and middle sections of the continental rise for $N = 1$ cph, $\omega = 0.083$ cph, and $H \geq 5$, or on the lower rise with $H \geq 50$. The internal wave amplitudes suggested in the discussion of the various models are representative in that they fall within the range measured in the ocean. The various proposed values of viscosity ν (or boundary layer thicknesses δ) are speculative.

The available data for specific sediment distributions on the continental margins do not correspond in a simple way to the predicted distributions; the natural setting is too complex to fit these idealized models. However, what is not answerable at this time is whether or not the internal waves do in fact initiate motion of bottom sediment: for certain conditions, the models predict that they can. It must be noted that an additional attribute of the sediments on the slope and rise that is probably important in increasing the local forces necessary to dislodge the grains is the existence of cohesive forces acting between particles of clay and very fine silt sizes. The incipient-diameter criterion in Equation (5-12) assumed noncohesive bed particles. Other factors, such as bed roughness scales greater than granular, stirring by bottom organisms, bed fluidization, grain angularity, and packing of bed grains, are probably significant locally in the transport

of bed particles. Their effects are difficult to treat analytically; future field studies might establish their actual importance.

In the light of the experimental results presented above, the effects of two other phenomena induced by internal waves must be considered. Breaking internal waves of high frequency were observed to produce turbulent conditions and increased instantaneous velocities near the bottom. The breaking often generated filimentous horizontal layers which penetrated the adjacent fluid interior. Secondly, experimental runs with $\gamma \geq c$ showed a vortex instability along the slope; the mixing in the vortices caused a vertical structure of alternating horizontal streamers and layers within which the net fluid transport was away from and toward the slope, respectively. If these processes occur in nature, there are no definitive field measurements of either process, speculation about their possible impact for sediment processes on the continental margins raises some interesting questions.

Wherever the breaking might occur on the slope, [*] sediment that is well-sorted and coarse relative to nearby material probably will be associated with this zone. The finer materials might be winnowed out and transported from the area by currents. Hogg and Wunsch (1970) have shown that for sufficiently large values of eddy viscosity and slightly oblique incidence, in theory the breaking internal waves can generate "longslope" currents. Hence, a littoral drift of fine materials similar to that observed for surface waves and supplementing the effects of the contour currents (Heezen, et al 1966) might be possible. If the position of breaking along the slope is a function of time, i.e., if the stratified layer containing the waves shifts its vertical position over a time scale of days or longer, as seasonal or local

---

[*] The laboratory measurements suggest that the breaking occurs well up-slope (for $\gamma \leq c$). In fact, when the stratified section was beneath a less strongly stratified or homogeneous layer, the breaking occurred near or at the base of this upper layer.

thermoclines might, then a time-sequenced winnowing out of fine materials might occur along the bottom over a wide offshore traverse. Deposition of recent sediments entering the area from the continental sources might be prevented, and local size-frequency distributions might be skewed toward the coarser sizes. A dynamic process like this might help to explain the observed scarcity of recent sediments on the outer shelf.

Finally, speculation is ventured for the effects of breaking internal waves at the edge of the continental shelf. Suppose that relatively large-amplitude, high-frequency internal waves were generated at infrequent intervals (for example, by the passage of severe surface storms) in the seasonal thermocline when the upper extent of the thermocline was at the approximate depth of the shelf edge. Sudden substantial increases in bottom turbidity due to the suspension of bed materials by breaking of these large-amplitude waves might increase the density of the water along the shelf-slope transition to values high enough to generate density currents. This mechanism might provide a means of continued eroding the slope face at irregular times and places by relatively weak small-scale turbidity currents.

The vortex instabilities and steamers that were created in the laboratory, generally for $\gamma \geq c$, might also provide a means of increasing suspension of bottom materials, by increased turbulence within the eddies near the bed, and by transporting fine suspended materials away from the slope. The net transport in the streamers might move the finer sediment (clay and very fine silt) away from the continental slope to deeper sites of deposition on the rise or abyssal plain.

None of these mechanisms have been observed in the ocean. The case for increased mixing along the oceanic slopes is not new; Munk (1966) and Wunsch (1970) have called attention to this process. It is hoped that these experiments have illuminated some of the hydrodynamic features of shoaling internal waves, and strengthened the case for internal waves as geological agents on the oceanic slopes.

REFERENCES

Abou-Seida, M.M., 1964, Sediment transport by waves and currents: University of California at Berkley, Hydraulic Engineering Laboratory, Rept. HEL 2-7.

Albertson, M.L., Barton, J.R., and Simons, D.C., Fluid Mechanics for Engineers, Prentice-Hall Inc., Englewood Cliffs, New Jersey, 1960.

Barnes, N.F., 1954, Optical techniques for fluid flow: J. Soc. Motion Pictures and Television Engineering, 5, High Speed Photography.

Batchelor, G.K., 1967, An Introduction to Fluid Dynamics: Cambridge University Press, London.

Bohlen, W.F., 1969, Hotwire anemometer study of turbulence in open-channel flows transporting neutrally buoyant particles: Massachusetts Institute of Technology, Department of Earth and Planetary Sciences, Experimental Sedimentology Laboratory, Rept. 69-1.

Bagnold, R.A., 1963, Part I. Mechanics of marine sedimentation: The Sea, 3, (M.N. Hill, ed.), Interscience, New York, 507-528.

Bagnold, R.A., 1966, An approach to the sediment transport problem from general physics, U.S. Geol. Surv. Prof. Paper 422-I.

Boston, N.E.J., 1964, Observations of tidal periodic internal waves over a three-day period off Panama City, Florida: Texas A. and M. University, Department of Oceanography and Meteorology, A & M Project 286-D, Ref. 64-20T.

Bowin, C.O., Chase, R.L., and Hersey, J.B., 1967, Geological applications of sea-floor photography: Deep Sea Photography, (J.B. Hersey, ed.), Johns Hopkins University Press, Baltimore.

Cairns, J.L., 1967, Asymmetry of internal tidal waves in shallow coastal waters: J. Geophys. Res., 72(14), 3563-3565.

Carruthers, J. N., 1963, History, sand waves and near-bed currents of La Chappelle Bank: Nature, 197(4871), 942-946.

Carstens, M. R., Neilson, F. M., and Altinbilek, H. D., 1969, Bed forms generated in the laboratory under an oscillatory flow: analytical and experimental study: U.S. Army, Corps of Engineers, Coastal Engineering Research Center, Tech. Memo. 28.

Cartwright, D., 1959, On submarine sand waves and tidal lee-waves: Proc. Roy. Soc. London, A, 253, 218-241.

Chepil, W. S., 1959, Equilibrium of soil grains at the threshold of movement by wind: Proc. Soil Sci. Soc. Amer., 23, 422-428.

Defant, A., 1961, Physical Oceanography, 2, Pergamon Press, Oxford.

Donahue, J. G., Allen, R. C., and Heezen, B. C., 1966, Sediment size distribution profile on the continental shelf off New Jersey: Sedimentology, 7, 155-159.

Eagleson, P. S., and Dean, R. G., 1959, Wave-induced motion of bottom sediment particles: Proc. Amer. Soc. Civ. Engrs., J. Hydraulics Div., 85, HY10, 53-79.

Eagleson, P. S., Dean, R. G., and Peralta, L. A., 1958, The mechanics of the motion of discrete spherical bottom sediment particles due to shoaling waves: U.S. Army, Corps of Engineers, Beach Erosion Board, Tech. Memo. 104.

Edgerton, H. E., Handbook of High Speed Photography: General Radio Company, West Concord, Massachusetts.

Emery, K. O., 1966, Atlantic continental shelf and slope of the United States: geologic background: U.S. Geol. Surv. Prof. Paper 529-A.

Emery, K. O., 1956, Deep standing internal waves in California Basins: Limnol. Oceanogr., 1, 35-41.

Emery, K.O., Uchupi, E., Phillips, J.D., Bowin, C.O., Bunce, E.T., and Knott, S.T., 1970, Continental rise off eastern North America: Bull. Amer. Ass. Petrol. Geol., 54(1).

Emery, K.O., 1960, The Sea off Southern California: Wiley, New York.

Emery, K.O., 1965, Characteristics of continental shelves and slopes: Bull. Amer. Ass. Petrol. Geol., 49(9), 1379-1384.

Emery, K.O., and Ross, D.A., 1968, Topography and sediments of a small area of the continental slope south of Martha's Vineyard: Deep-Sea Res., 15, 415-422.

Ewing, M., and Thorndike, E.M., 1965, Suspended matter in deep ocean water: Science, 147(3663), 1291-1294.

Fofonoff, N.P., 1966, Internal waves of tidal period: Woods Hole Oceanographic Institution, unpublished manuscript.

Fofonoff, N.P., 1968, Current measurements from moored buoys, 1959 - 1965: Woods Hole Oceanographic Institution, Ref. 68-30.

Fofonoff, N.P., 1969, The role of the NDBS in future natural variability studies of the North Atlantic: Proc. of the First U.S. Coast Guard National Data Buoy System Scientific Advisory Meeting, U.S. Coast Guard Academy, New London, Connecticut, May 12-14, 50-61.

Fofonoff, N.P., 1969, Spectral characteristics of internal waves in the ocean: Deep-Sea Res., 16 (Supplement), 58-71.

Fortuin, J.M.H., 1960, Theory and application of two supplementary methods of construction of density gradient columns: J. Polymer Sci., 44(44), 505-515.

Garrison, L.E., and McMaster, R.L., 1966, Sediments and geomorphology of the continental shelf off New England: Marine Geol., 4(4), 273-289.

Gaul, R.D., 1961, Observations of internal waves near Hudson Canyon: J. Geophys. Res., 66(11), 3821-3830.

Gibson, C.H., and Schwarz, W.H., 1963, Detection of conductivity fluctuations in a turbulent flow field: J. Fluid Mech. 16(3), 357-364.

Goddet, J., 1960, Etude du debut d'entrainment des materiaux mobiles sous l'action de la houle: La Houille Blance, 15(2), 122-135.

Haurwitz, B., Stommel, H., and Munk, W.H., 1959, On the thermal unrest in the ocean: The Rossby Memorial Volume, (Bolin, B., ed.), Rockefeller Institute Press, 79-94.

Heezen, B.C., Hollister, C.D., and Ruddiman, W.F., 1966, Shaping of the continental rise by deep geostrophic contour currents: Science, 152(3721), 502-508.

Heezen, B.C., Thorp, M., and Ewing, M., 1959, The floors of the oceans; I. The North Atlantic: Geol. Soc. Amer. Spec. Paper 65, 122 p.

Higgins, L.L., 1963, Measurement of temperature, salinity, and velocity of water through electrolytic conductivity measurements: Space Technology Laboratory, Tech. Rept. 8609-01000-RU-000.

Hogg, N.G., and Wunsch, C.I., 1970, Isopycnal displacement and Lagrangian current generation by internal waves: Trans. Amer. Geophys. Union, 51(4) (abstract).

Hulsemann, J., 1968, Morphology and origins of sedimentary structures on submarine slopes: Science, 161.

Ichiye, T., 1966, Turbulent diffusion of suspended particles near the ocean bottom: Deep-Sea Res., 13, 679-685.

Inman, D.L., and Bowen, A.J., 1963, Flume experiments on sand transport by waves and currents: Proc. Eighth Conf. on Coastal Engng., 137-149.

Inman, D.L., 1963, Part II. Mechanics of marine sedimentation: The Sea, 3, (M.N. Hill, ed.) Interscience, New York.

Ippen, A.T., and Eagleson, P.S., 1955, A study of sediment sorting by waves shoaling on a plane beach: U.S. Army, Corps of Engineers, Beach Erosion Board, 63.

Johnson, J.W., and Eagleson, P.S., 1966, Coastal processes: Chapter 9 in Estuary and Coastline Hydrodynamics, (A.T. Ippen, ed.) McGraw-Hill, New York.

Jost, W., 1960, Diffusion, Academic Press, New York.

Kalinske, A.A., 1947, Movement of sediment as bed in reviers: Trans. Amer. Geophys. Union, 28 615-620.

Keller, J.B., and Mow, V.C., 1969, Internal wave propagation in an in-homogeneous fluid of non-uniform depth: J. Fluid Mech., 38(2), 365-374.

Kelley, R.E., 1970, Wave induced boundary layers in a stratified fluid: J. Fluid Mech., 42(1).

Krauss, W., 1966, Interner Wellen: Part II: Gebrüder Borntraeger, Berlin.

LaFond, E.C., 1961a, Boundary effects on the slope of internal temperature waves: Indian J. Meteorol. Geophys., 12, 335-338.

LaFond, E.C., 1961b, Internal wave motion and its geological significance: Mahadevan Volume, Osmania University Press, 61-77.

LaFond, E.C., 1962, Internal waves, Part I: The Sea, (M.N. Hill, ed.) Interscience Publishers, New York and London, 731-751.

LaFond, E.C., 1965, The U.S. Navy Electronics Laboratory's oceanographic research tower: U.S. Navy Electronics Laboratory Rept. 1342.

LaFond, E.C., and Lee, O.S., Internal waves in the ocean: Navigation, 9 231-236.

Lee, O.S., 1961a, Effect of an internal wave on sound in the ocean: J. Acoust. Soc. Amer., 33(5), 677-680.

Lee, O.S., 1961b, Observations on internal waves in shallow water: Limnol. Oceanogr., 6(3), 312-321.

Longuit-Higgins, M.S., 1969, On the reflexion of wave characteristics from rough surfaces: J. Fluid Mech., 37(2), 231-250.

Magaard, L., 1962, Zur Berechnung interner Wellen in Meeresräumen mit nicht-ebenen Böden bei einer speziellen Dichteverteilung: Kiel. Meeresforsch, 18, 161-183.

Manohar, M., 1956, Mechanics of bottom sediment movement due to wave action: U.S. Army, Corps of Engineers, Beach Erosion Board, Tech. Memo. 75.

Martin, S., Simmons, W.F., and Wunsch, C.I., 1969, Resonant internal wave interactions: Nature, 224(5223), 1014-1016.

Miller, R.L., and Zeigler, J.M., 1958, A model relating dynamics and sediment pattern in equilibrium in the region of shoaling waves, breaker zone, and foreshore: J. Geol., 66(4).

Miller, R.L., and Zeigler, J.M., 1964, A study of sediment distribution in the zone of shoaling waves over a complicated bottom topography: Papers in Marine Geology: Shepard Commemorative Volume, (R.L. Miller, ed.), Macmillan, New York, 133-153.

Mowbray, D.E., 1967, The use of schlieren and shadowgraph techniques in the study of flow patterns in density stratified fluids: J. Fluid Mech., 27(3), 595-608.

Mowbray, D.E., and Rarity, B.S.H., 1967, A theoretical and experimental investigation of the phase configuration of internal waves of small amplitude in a density stratified liquid: J. Fluid Mech., 28(1), 1-16.

Munk, W., 1941, Internal waves in the Gulf of California: J. Marine Res., 4(1), 81-91.

Munk, W.H., 1966, Abyssal recipes: Deep-Sea Res., 13, 707-730.

Northrup, J., 1951, Ocean-bottom photographs of the neritic and bathyal environment south of Cape Cod, Massachusetts: Bull. Geol. Soc. Amer., 62, 1381-1384.

Oster, G., 1965, Density gradients, Sci. Amer., 213(2), 70-76.

Oster, G., and Nishijima, Y., 1964, Moire patterns: their application to refractive index and refractive index gradient measurements: J. Opt. Soc. Amer., 54(1), 1-15.

Owen, D.M., and Emery, K.O., 1967, Current markings on the continental slope: Deep-Sea Photography, Johns Hopkins University Press, Baltimore.

Pao, Y-H., 1968, Undulance and turbulence in stably stratified media: Boeing Scientific Research Laboratories, Document DI-82-0742.

Pao, Y-H., 1968, Vortex streets in stably stratified fluids: Boeing Scientific Research Laboratories, Document DI-82-0736.

Phillips, O.M., 1966, The Dynamics of the Upper Ocean: Cambridge University Press, London.

Prandtl, L. 1952, Essentials of Fluid Dynamics: Hafner Publishing Co., New York.

Pratt, R.M., 1968, Atlantic continental shelf and slope of the United States - Physiography and sediments of the deep sea basin: U.S. Geol. Surv. Prof. Paper 529-B.

Raudkivi, A.J., 1967, Loose Boundary Hydraulics, Pergamon Press, New York.

Revelle, R.R., 1939, Sediments of the Gulf of California (abstract); Geol. Soc. Amer. Bull., 50(2), 1929.

Robinson, R.M., 1970, The effects of a corner on a propagating internal gravity wave: J. Fluid Mech., 42(2), 257-267.

Sandstrom, H., 1966, The importance of topography in generation and propagation of internal waves: Ph.D. dissertation, University of California, San Diego, Department of Oceanography.

Sato, S., Ijima, T., Tanaka, 1963, A study of critical depth and mode of sand movement using radioactive glass sand: Proc. Eighth Conf. on Coastal Engng, 304-323.

Schlichting, H., 1955, Boundary Layer Theory, McGraw-Hill, New York.

Schlee, J., 1969, Atlantic continental shelf and slope of the United States: sediment texture of the northeastern part: unpublished manuscript.

Shields, A., 1936, Anwendung der Ähnlichkeits-Mechanik und der Turbulenzforschung auf die Geschiebebewegung: Preussische Versuchsanstalt für Wasserbau und Schiffbau, Berlin, Mitteilungen, No. 26.

Stetson, H.C., 1938, The sediments of the continental shelf off the eastern coast of the United States: Papers in Phys. Oceanog. Meteorology, 5(4).

Stetson, H.C., 1949, The sediments and stratigraphy of the East coast continental margin; Georges Bank to Norfolk Canyon: Papers in Phys. Oceanog. Meterol., 11(2).

Stokes, R.H., Mills, R., 1965, Viscosity of Electrolytes and Related Properties: Pergamon Press, Oxford.

Stride, A.H., and Cartwright, D., 1958, Large sand waves near the edge of the continental shelf: Nature, 81, 41.

Stride, A.H., and Tucker, M.J., 1960, Internal waves and waves of sand: Nature, 188(4754), 933.

Summers, H.J., and Emery, K.O., 1963, Internal waves of tidal period off Southern California: J. Geophys. Res., 68(3), 827-839.

Tareyev, B.A., 1965, Internal baroclinic waves in a flow around irregularities on the ocean floor and their effect on sedimentation processes: Oceanology, 5(1), 31-37.

Thorpe, S.A., 1968, A method of producing a shear flow in a stratified fluid: J. Fluid Mech., 32(4), 693-704.

Thorpe, S.A., 1969, Experiments on the instability of stratified shear flows: immiscible fluids: J. Fluid Mech., 39(1), 25-48.

Thorpe, S.A., 1966, Internal Gravity Waves: Ph.D. Dissertation, Trinity College, Cambridge.

Uchupi, E., 1963, Sediments on the continental margin off eastern United States: Art. 94 in U.S. Geol. Surv. Prof. Paper 475-C, 132-137.

Uchupi, E., 1968, Atlantic continental shelf and slope of the United States - Physiography: U.S. Geol. Surv. Prof. Paper 529-C.

Ufford, C.W., 1947, Internal waves in the ocean: Trans. Amer. Geophys. Union, 28(1), 79-86.

Ufford, C.W., 1947, The theory of internal waves: Trans. Amer. Geophys. Union, 28(1), 96-101.

Vanoni, V.A., 1964, Measurements of critical shear stress for entraining fine sediments in a boundary layer: California Institute of Technology, W.M. Keck Laboratory of Hydraulics and Water Resources, Rept. KH-R-7.

Vincent, G.E., 1958, Contribution to the study of sediment transport on a horizontal bed due to wave action: Proc. Sixth Conf. on Coastal Engineering, 326-354.

Voorhis, A.D., 1968, Measurements of vertical motion and the partition of energy in the New England slope water: Deep Sea Res., 15, 599-608.

White, C.M., 1940, The equilibrium of grains on the bed of a stream: Proc. Roy. Soc. London, A, 174(958), 322-338.

Wunsch, C., 1968, On the propagation of internal waves up a slope: Deep Sea Res., 25, 251-258.

Wunsch, C., 1969, Progressive internal waves on slopes: J. Fluid Mech., 35(1), 131-144.

Wunsch, C., 1970, On oceanic boundary mixing: Deep Sea Res., 17, 293-301.

Zeilon, N., 1912, On tidal boundary waves and related hydrodynamical problems: Kgl. Svensk. Vetakad. Handl., 47, 1-46.

Zeilon, N., 1934, Experiments on boundary tides: Goteborg Kgl. Vetakad. Vittershets-Samhall. Handl., B, 3(10), 1-8.

REFERENCES

(ERRATA)

American Optical Company, informal table 53. Sodium Chloride, 1969.

Ives, David J.G., and Janz, George J., 1961, Reference Electrodes, Academic Press, New York.

Wolbarscht, M.L., MacNichol, E.F., and Wagner, H.G., 1960, Glass insulated platinum microelectrodes, Science, 131, 1309-1310.

APPENDIX A

The use of conductivity cells in A.C. circuits to detect fluctuations of conductivity in electrolyte solutions has been briefly summarized by Gibson and Schwarz (1963). In this section we describe only the particular sensors and circuitry that were used during the set of experiments discussed in the text.

DESCRIPTION

The sensor is a single-electrode, platinum conductivity probe whose construction is shown diagrammatically in Figure 4. The rounded platinum tip and the L shaped glass housing minimized flow disturbances induced by the probes. The probe assembly was oriented so that the horizontal portion of the glass housing containing the probe tip was approximately parallel to the crests of the internal waves (i.e., perpendicular to the side walls of the tank). This prevented the wake of the vertical shaft from washing by the electrode and introducing spurious values. The electrical path was between this electrode and the solution ground (a large copper strip placed along the tank bottom beneath the slope). The platinum tip was normally platinized by a method similar to that described by Wolbarscht et al (1960): (1) the probe was immersed in a 1 percent solution of Chloroplatinic acid to which lead acetate (80 percent by weight) had been added; (2) current from a 10 v D.C. source in series with a 10,000 ohm resistor was passed between the probe (cathode) and a platinum wire (anode) either for about 15 seconds or until a thin stream of bubbles was emitted from the probe tip. The result was a thin grayish-black coating on the platinum probe. The effects of this coating on probe performance are discussed in Ives and Janz (1961); essentially, the platinization minimizes drift in the output of the sensor.

The probe is the active arm in an A.C. Wheatstone Bridge (Figure A1). Potential imbalances across the bridge caused by fluctuations of conductivity at the probe are amplified, detected (diode rectification), and

recorded by the A-D conversion described in Chapter 2. The high excitation frequency (60 kc) and low excitation voltage (0.5 v rms) inhibited polarization of the electrolyte at the probe tip. This was essential in order to minimize signal drift and capacitance problems.

PERFORMANCE

Four complete circuits like that shown in Figure A1 were used. It was found that the levels of signal output changed by as much as 15 percent when probes were interchanged, owing to nonuniformities and irregular platinization of the probe tip; this usually necessitated a calibration check before each experiment. Normally this calibration consisted of recording output voltage as a function of probe depth before each run. This provided an updated sensititivity value that could be checked with previous values. If it was observed that sensitivity changed markedly ($>$ 10 percent) between runs, the probe tip was checked for fouling and cleaned as necessary. The cleaning process is like that described by Ives and Johns (1961). Prior to initial platinization, or when the platinized coating was cleaned off with a soft tissue, the following procedure was used:

(1) wash in warm concentrated HNO_3 for 30 seconds,

(2) wash in distilled water,

(3) polish platinum tip with glass rod,

(4) treat polished electrode with warm 50 percent solution of Aqua Regia (4 Volumes H_2O, 3 Volumes HCl, 1 Volume HNO_3) for 15 seconds,

(5) wash in distilled water,

(6) wash in warm HNO_3 for 30 seconds,

(7) wash in distilled water,

(8) dry in air,

(9) place in distilled water when not in use.

Normally, the output signal was acceptable up to three hours of continuous use; however, shortly thereafter degradation of the signal to noise ratio
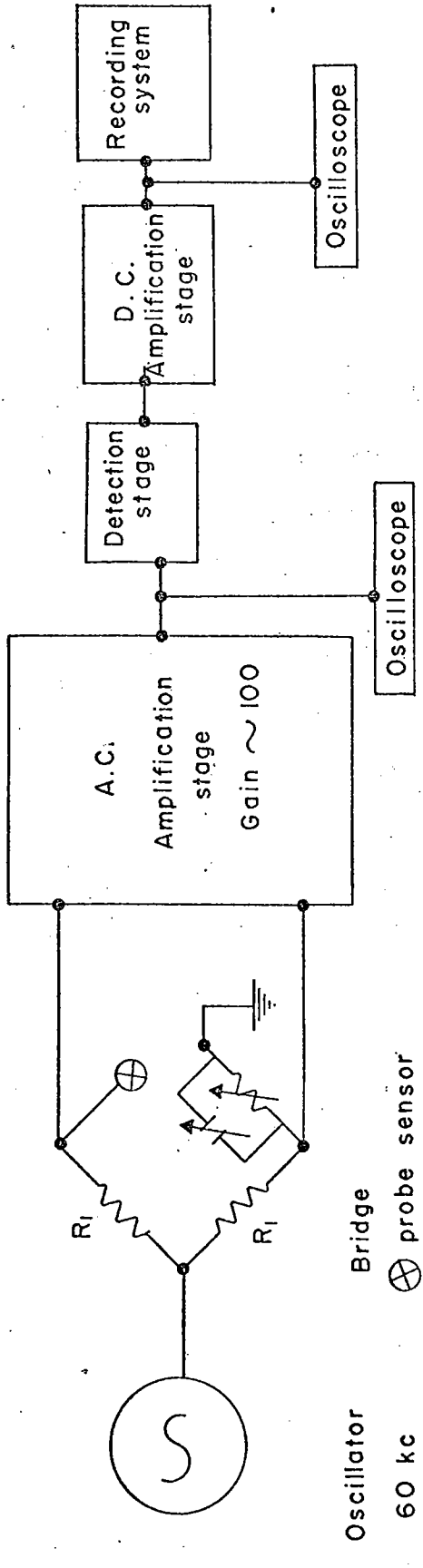
Fig. A1.   Circuit schematic for conductivity sensor

and erratic output values necessitated cleaning of the probe tip (steps (5) through (7) above.

The following list summarizes the average performance of the probes determined from experimental data and calibration tests. The length units are presented for convenience and are based on:

$$\rho = \rho_0 (1 - \beta z)$$

where

$\beta = 0.001$ g/cc/cm

(1) sensitivity: 0.3 volt/0.001 g/cc (0.3 v/cm)

(2) resolution: 0.5×10^{-4} g/cc (0.5 mm)

(3) accuracy: 5 percent of maximum vertical displacement of probe relative to stratified fluid at rest for displacements ≤ 0.5 cm.

(4) linearity: 2 percent of maximum vertical displacement of probe relative to stratified fluid at rest for displacements ≤ 0.5 cm.

(5) drift: variable, depending on quality of platinization. (Typically 20 millivolts/hour.)

It might be useful to present functional relationships between some of the physical variables for sodium chloride solutions that were assembled during this study. Several sources were used to obtain the relationships (L. L. Higgins, 1962; International Critical Tables, 1929; American Optical Company, 1969).

(1) $n = 1.3330 + 0.244 (\rho - 1)$; $T = 20°C$
     (accurate to approximately 1 percent)

(2) $S = 1.39 (\rho - 1) \times 10^3$; $T = 20°C$
     (accurate to approximately 1 percent)

(3) $\sigma = 1.902 (\rho - 1)$; $T = 20°C$
     (accurate to approximately 5 percent)

where

        n is index of refraction,

        ρ is density on g/cm^3

        S is salinity in $^{\circ}/_{\circ\circ}$,

        σ is electrical conductivity in $(ohm\text{-}cm)^{-1}$.

APPENDIX B

TABLE B1

Group	N sec^{-1}	N cps	ω_c sec^{-1}	ω_c cps	T_c sec	h_o cm	α deg	γ (tan α)
1	0.776	0.123	0.199	0.038	31.51	31.55	14.9	0.266
2	0.990	0.157	0.248	0.039	25.35	31.60	14.5	0.259
3	0.970	0.154	0.456	0.073	13.80	31.80	28.0	0.532
4	0.988	0.156	0.494	0.079	12.72	31.65	30.0	0.577
5	0.945	0.151	0.473	0.075	13.29	33.35	30.0	0.577
6	0.952	0.152	0.235	0.038	26.69	33.45	14.3	0.255
7	0.972	0.154	0.497	0.079	12.7	33.5	30.0	0.577

TABLE B2.

Ref. No.	ω cps	T sec	k_O cm^{-1}	c	q
1-2	0.129*	7.76	0.142	1.426	17.105
2-3	0.129	7.76	0.150	1.522	8.614
3-4	0.109	9.14	0.095	0.962	4.532
4-2	0.102*	9.85	0.084	0.843	9.913
5-5	0.102*	9.85	0.083	0.883	4.020
6-3	0.098*	10.24	0.081	0.822	4.075
7-4	0.098	10.24	0.079	0.793	3.627
8-5	0.098*	10.24	0.080	0.853	3.818
9-6	0.098	10.24	0.080	0.848	10.124
10-1	0.094*	10.67	0.116	1.168	13.546
11-2	0.094	10.67	0.074	0.743	8.625
12-3	0.094*	10.67	0.075	0.764	3.656
13-1	0.094*	10.67	0.116	1.168	13.546
14-4	0.090*	11.13	0.070	0.697	2.897
15-4	0.086	11.64	0.065	0.653	2.506
16-5	0.086	11.64	0.046	0.486	--
17-4	0.082*	12.19	0.061	0.612	2.085
18-5	0.082*	12.19	0.061	0.650	2.227
19-4	0.078*	12.80	0.057	0.573	1.537
20-4	0.072*	13.86	0.051	0.515	--
21-4	0.066*	15.06	0.046	0.462	--
22-5	0.066*	15.06	0.046	0.488	--
23-6	0.062	16.00	0.043	0.453	4.922
24-2	0.062*	16.00	0.042	0.420	4.366
25-1	0.055*	18.28	0.051	0.517	5.518
26-4	0.055*	18.28	0.037	0.373	--
27-5	0.055	18.28	0.037	0.393	--
28-3	0.051	19.69	0.035	0.350	--
29-4	0.051*	19.69	0.034	0.343	--
30-3	0.049	20.51	0.033	0.335	--
31-6	0.047*	21.33	0.031	0.325	2.971
32-6	0.043*	23.26	0.028	0.296	2.407
33-4	0.039*	25.60	0.025	0.256	--

TABLE B3

(1)	(2)	(3)	(4)	(5)	(6)	(7)	(8)	(9)	(10)	(11)	(12)	(13)	(14)
Exp. Group No.	ω cps	T sec	x_c cm	z_c cm	x_c/x_o	$\dfrac{c_x^2}{c_x^2-z^2}$ cm^{-1} ($\times 10^2$)	k_w/k_{w_o}	$1/q\,k_m$ cm^{-1} $a_o=0.1$cm ($\times 10^2$)	$1/q\,k_m$ cm^{-1} $a_o=0.2$ cm ($\times 10^2$)	$1/q\,k_m$ cm^{-1} $a_o=0.4$ cm ($\times 10^2$)	$1/k_o\,k_m$ $a_o=0.1$ cm	$1/k_o\,k_m$ $a_o=0.2$ cm	$1/k_o\,k_m$ $a_o=0.4$ cm
1	0.094	10.67	130.6	9.5	1.101	--	--	--	--		--	--	
			100.6	9.5	0.848	0.885	1.032	0.749	0.769		0.872	0.895	
			80.6	9.5	0.680	1.129	1.319	1.032	1.047		1.203	1.219	
			70.3	9.5	0.593	1.347	1.585	1.318	1.275		1.535	1.485	
			70.9	9.5	0.598	--	--	--	--		--	--	
			55.9	9.5	0.471	1.632	1.902	1.485	1.340		1.730	1.561	
			45.6	9.5	0.385	2.046	2.396	2.007	1.858		2.339	2.165	
			40.6	9.5	0.342	2.415	2.843	2.888	3.077		3.364	3.584	
	0.055	18.28	130.6	9.5	1.101	--	--	--	--		--	--	
			100.6	9.5	0.848	0.905	0.989	0.826	0.832		0.887	0.932	
			80.6	9.5	0.680	1.167	1.283	0.903	1.062		0.968	1.139	
			70.3	9.5	0.593	1.414	1.570	1.350	1.274		1.376	1.293	
			70.9	9.5	0.598	--	--	--	--		--	--	
			55.9	9.5	0.471	1.758	1.933	1.597	1.629		1.713	1.748	
			45.6	9.5	0.385	2.313	2.560	2.036	2.222		2.067	2.384	
			40.6	9.5	0.342	2.860	3.209	2.795	2.501		2.998	2.683	
2	0.102	9.85	132.6	6.6	1.085	--	--			--			--
			102.6	6.6	0.840	0.868	1.046			0.856			1.613
			82.6	6.6	0.676	1.101	1.328			1.019			1.206
			72.6	6.6	0.594	1.307	1.586			1.207			1.428
			72.6	6.6	0.594	--	--	--		--	--		--
			57.6	6.6	0.471	1.580	1.905	1.470		1.486	1.738		1.757
			47.6	6.6	0.389	1.962	2.372	1.945		2.059	2.300		2.435
			41.6	6.6	0.340	2.323	2.817	2.199		2.586	2.601		3.058
			51.0	6.6	0.417	--	--	--	--		--	--	
			43.3	6.6	0.354	2.196	2.658	2.438	2.268		2.884	2.682	
			37.1	6.6	0.304	2.891	3.150	3.908	2.628		4.464	3.108	
			32.3	6.6	0.264	3.?51	3.698	2.926	3.754		4.4??	4.4??	

TABLE B3 (Cont)

(1) Exp. Group No.	(2) ω cps	(3) T sec	(4) x_c cm	(5) z_c cm	(6) x_c/x_o	(7) $\dfrac{c_x^2}{c_x^2-z^2}$ cm^{-1} ($\times10^2$)	(8) k_w/k_{w_o}	(9) $1/q\,k_m$ cm^{-1} a_o=0.1 cm ($\times10^2$)	(10) $1/q\,k_m$ cm^{-1} a_o=0.2 cm ($\times10^2$)	(11) $1/q\,k_m$ cm^{-1} a_o=0.4 cm ($\times10^2$)	(12) $1/k_o\,k_m$ a_o=0.1 cm	(13) $1/k_o\,k_m$ a_o=0.2 cm	(14) $1/k_o\,k_m$ a_o=0.4 cm
2 (cont)	0.062	16.00	132.6	6.6	1.085	--	--	--	--		--	--	
			102.6	6.6	0.840	0.881	1.046	0.727	0.874		0.770	0.926	
			82.5	6.6	0.676	1.128	1.349	1.208	1.127		1.279	1.193	
			72.3	6.6	0.594	1.355	1.618	1.492	1.406		1.579	1.488	
			72.8	6.6	0.596	--	--	--	--		--	--	
			57.9	6.6	0.474	1.654	2.060	1.462	1.641		1.548	1.737	
			48.0	6.6	0.393	2.101	2.618	2.361	2.165		2.499	2.292	
			42.9	6.6	0.351	2.516	3.144	3.117	2.906		3.299	3.076	
			51.0	6.6	0.418	--	--	--	--		--	--	
			43.3	6.6	0.355	2.416	3.008	3.021	2.807		3.198	2.972	
			37.1	6.6	0.304	2.967	3.691	3.114	2.951		3.296	3.124	
			32.3	6.6	0.265	3.668	4.536	4.530	3.240		4.796	3.440	
3	0.094	10.67	54.1	5.5	0.905	--	--		--			--	
			33.8	5.5	0.565	2.490	1.393		2.407			1.167	
			25.5	5.5	0.426	3.679	2.110		3.214			1.556	
			21.0	5.5	0.351	4.827	2.789		--			--	
			26.3	5.5	0.440	--	--		--	--		--	--
			21.7	5.5	0.363	4.644	2.686		4.648	4.377		2.251	2.121
			16.7	5.5	0.279	6.268	3.209		7.167	7.517		3.471	3.641
			11.6	5.5	0.194	10.686	5.776		12.240	12.283		5.933	5.954
	0.129	7.76	26.3	5.5	0.440	--	--		--			--	
			21.7	5.5	0.363	4.309	2.524		4.108			2.354	
			16.7	5.5	0.279	5.512	3.209		5.477			3.138	
			11.6	5.5	0.194	7.916	4.530		7.031			4.028	
4	0.098	10.24	48.3	11.1	0.853	--	--						
			32.3	11.1	0.571	3.034	1.537						
			25.5	11.1	0.450	4.707	2.437						
			20.5	11.1	0.362	7.366	3.748						

TABLE B3 (Cont)

(1) Exp. Group No.	(2) ω cps	(3) T sec	(4) x_c cm	(5) z_c cm	(6) x_c/x_o	(7) $\dfrac{c_x^2}{c_x^2-z^2}$ cm^{-1} ($\times 10^2$)	(8) k_w/k_{w_o}	(9) $1/q\,k_m$ cm^{-1} $a_o=0.1$ cm ($\times 10^2$)	(10) $1/q\,k_m$ cm^{-1} $a_o=0.2$ cm ($\times 10^2$)	(11) $1/q\,k_m$ cm^{-1} $a_o=0.4$ cm ($\times 10^2$)	(12) $1/k_o\,k_m$ $a_o=0.1$ cm	(13) $1/k_o\,k_m$ $a_o=0.2$ cm	(14) $1/k_o\,k_m$ $a_o=-.4$ cm
4 (cont)	0.086	11.64	48.3	11.1	0.853		--						
			32.3	11.1	0.571		1.605						
			25.5	11.1	0.450		2,788						
			20.5	11.1	0.362		5.207						
	0.090	11.13	46.8	10.3	0.837		--						
			30.8	10.3	0.545		1.637						
			24.8	10.3	0.425		2.769						
			19.0	10.3	0.336		4.854						
	0.078	12.80	46.8	10.3	0.827		--						
			30.8	10.3	0.545		1.739						
			24.0	10.3	0.425		3.391						
			19.0	10.3	0.336		9.706						
5	0.098	10.24	47.4	11.0	0.427	--	--		--			--	
			37.2	11.0	0.335	2.328	1.443		2.349			1.116	
			28.5	11.0	0.257	3.739	2.001		3.372			1.602	
			23.0	11.0	0.207	5.388	2.885		6.267			2.977	
	0.082	12.19	47.4	11.0	0.427	--	--		--			--	
			37.2	11.0	0.335	2.905	1.502		2.312			0.840	
			28.5	11.0	0.257	4.409	2.235		3.232			1.174	
			23.0	11.0	0.207	7.467	3.721		5.441			1.981	

TABLE B3 (Cont)

(1)	(2)	(3)	(4)	(5)	(6)	(7)	(8)	(9)	(10)	(11)	(12)	(13)	(14)
Exp. Group No.	ω cps	T sec	x_c cm	z_c cm	x/x_o	$\dfrac{c_x^2}{c_x^2 - z^2}$ cm^{-1} ($\times 10^2$)	k_w/k_{w_o}	$1/q\,k_m$ cm^{-1} $a_o = 0.1$ cm ($\times 10^2$)	$1/q\,k_m$ cm^{-1} $a_o = 0.2$ cm ($\times 10^2$)	$1/q\,k_m$ cm^{-1} $a_o = 0.4$ cm ($\times 10^2$)	$1/k_o\,k_m$ $a_o = 0.1$ cm	$1/k_o\,k_m$ $a_o = 0.2$ cm	$1/k_o\,k_m$ $a_o = 0.4$ cm
6	0.062	16.00	177.9	9.5	1.357	--	--		--			--	
			112.9	9.5	0.861	0.744	0.964		0.741			0.858	
			82.9	9.5	0.632	1.103	1.381		1.110			1.285	
			62.9	9.5	0.480	1.540	1.930		1.605			1.858	
	0.047	21.33	177.9	9.5	1.357	--	--		--			--	
			112.9	9.5	0.861	0.764	0.912		0.859			0.835	
			82.9	9.5	0.632	1.173	1.414		1.074			1.046	
			62.9	9.5	0.480	1.102	2.063		1.521			1.480	
	0.043	23.26	177.9	9.5	1.357	--	--		--			--	
			112.9	9.5	0.861	0.773	0.911		0.857			0.743	
			82.9	9.5	0.632	1.192	1.430		1.256			1.089	
			62.9	9.5	0.477	1.799	2.132		1.506			1.306	

TABLE B4

Expt. Group	ω cps	T sec	x_c cm	z_c cm	x_c/x_o	$(\rho_w/\rho_o)^2$	$(a_m/a_o)^2$ $a_o=0.1$cm	$(a_m/a_o)^2$ $a_o=0.2$cm	$(a_m/a_o)^2$ $a_o=0.4$cm
1	0.094	10.67	130.6	9.5	1.101	0.716	--	2.642	
			100.6		0.848	1.716	3.016	3.242	
			80.6		0.680	3.261	3.666	4.474	
			70.3		0.593	4.488	3.045	5.123	
			70.9		0.598	4.410	3.038	5.202	
			55.9		0.471	6.060	4.246	7.996	
			45.6		0.385	4.791	3.782	3.412	
			40.6		0.342	2.544	1.412	2.679	
	0.055	18.28	130.6		1.101	0.704	--	0.884	
			100.6		0.848	1.780	0.723	0.867	
			80.6		0.680	3.650	1.268	1.602	
			70.3		0.593	5.380	2.712	6.550	
			70.9		0.598	5.260	--	--	
			55.9		0.471	8.735	1.633	3.687	
			45.6		0.385	9.758	0.802	1.357	
			40.6		0.342	8.678	0.837	1.221	
2	0.102	9.85	132.6	6.6	1.085	0.735	--	--	--
			102.6		0.840	1.901	--	1.614	1.723
			82.6		0.676	4.081	--	4.202	3.782
			72.6		0.594	6.258	--	8.062	11.820
			72.6		0.594	6.258	4.410	8.108	11.238
			57.6		0.471	12.428	6.083	15.490	14.774
			47.6		0.389	19.295	9.378	21.441	25.845
			41.6		0.340	23.432	--	25.005	24.242
			51.0		0.417	16.479	14.210	--	24.370
			43.3		0.354	22.419	10.942	14.205	23.332
			37.1		0.304	24.437	10.138	25.256	19.539
			32.3		0.264	19.940	6.214	14.178	10.839
	0.062	16.00	132.6	6.6	1.085	0.729	--	--	
			102.6		0.840	1.942	0.843	1.715	
			82.5		0.674	4.354	1.956	5.083	
			72.3		0.591	6.974	2.001	7.272	
			72.8		0.596	6.8071	--	--	
			57.9		0.474	14.670	4.954	10.724	
			48.0		0.393	25.431	12.842	25.578	
			42.9		0.351	33.443	1.471	26.616	
			51.0		0.418	21.520	6.122	19.504	
			43.3		0.355	32.771	12.645	13.248	
			37.1		0.304	43.212	4.571	12.368	
			32.3		0.265	47.519	2.082	11.488	

TABLE B4 (Cont)

Expt. Group	ω cps	T sec	x_c cm	z_c cm	x_c/x_o	$(\rho_w/\rho_o)^2$	$(a_m/a_o)^2$ $a_o=0.1$cm	$(a_m/a_o)^2$ $a_o=0.2$cm	$(a_m/a_o)^2$ $a_o=0.4$cm
3	0.094	10.67	54.1	5.5	0.905	1.427		2.728	3.034
			33.8		0.565	8.702		11.192	6.322
			25.5		0.426	24.331		23.630	22.024
			21.0		0.351	46.975		33.112	71.648
			26.3		0.440	21.816		21.608	25.424
			21.7		0.363	42.216		42.892	44.450
			16.7		0.279	91.863		52.984	60.728
			11.6		0.194	175.545*		73.624*	86.540
	0.129	7.76	26.3		0.440	17.754		16.136	
			21.7		0.363	30.243		42.114	
			16.7		0.279	48.736		56.270	
			11.6		0.194	26.475		20.924	
4	0.098	10.24	48.3	11.1	0.853	1.770			
			32.3		0.571	6.238			
			25.5		0.450	10.014			
			20.5		0.362	17.103			
	0.086	11.64	48.3		0.853	1.877			
			32.3		0.571	8.990			
			25.5		0.450	22.063			
			20.5		0.362	83.440			
	0.090	11.13	46.8	10.3	0.827	2.071			
			30.8		0.545	9.424			
			24.0		0.425	20.394			
			19.0		0.336	57.874			
	0.078	12.80	46.8		0.827	2.279			
			30.8		0.545	16.582			
			24.0		0.425	74.749			
			19.0		0.336X	1946.208			
5	0.098	10.24	47.4	11.0	0.427	2.038		1.485	
			37.2		0.335	4.535		3.221	
			28.5		0.257	9.121		11.402	
			23.0		0.207	12.364		15.100	
	0.082	12.19	47.4		0.427	2.241		1.881	
			37.2		0.335	6.078		8.563	
			28.5		0.257	18.656		19.068	
			23.0		0.207	50.672		37.403	

TABLE B4 (Cont)

Expt. Group	ω cps	T sec	x_c cm	z_c cm	x_c/x_o	$(\rho_w/\rho_o)^2(a_m/a_o)^2$ $a_o=0.1\,cm$	$(a_m/a_o)^2$ $a_o=0.2\,cm$	$(a_m/a_o)^2$ $a_o=0.4\,cm$
6	0.062	16.00	177.9	9.5	1.351	0.318	--	
			112.9		0.861	1.713	2.227	
			82.9		0.632	4.777	4.292	
			62.9		0.480	9.839	7.008	
	0.047	21.33	177.9		1.357	0.318	--	
			112.9		0.861	1.784	1.747	
			82.9		0.632	5.729	4.472	
			62.9		0.480	15.146	4.090	
	0.043	23.26	177.9		1.357	0.295	--	
			112.9		0.861	1.820	1.364	
			82.9		0.632	6.260	7.346	
			62.5		0.477	18.788	6.042	

TABLE B5 (1) $\gamma > c$

(1) Exp. Group	(2) ω cps	(3) T sec	(4) x_c cm	(5) x_c/x_o	(6) z_c cm	(7) h cm	(8) z_c/cx_c	(9) k_m/k_o $a_o=0.2$ cm	(10) k_m/k_o $a_o=0.4$ cm	(11) $\dfrac{c^2 x}{(cx)^2 - z^2} \times 10$, cm^{-1}	(12) a_m/a_o $a_o=0.2$ cm	(13) a_m/a_o $a_o=0.4$ cm	(14) ϵ_m $a_o=0.2$ cm	(15) ϵ_m $a_o=0.4$ cm
3	0.051*	19.7	54.1	0.90	5.5	28.8	0.293			0.202	0.817	0.903		
			33.8	0.56	5.5	17.9	0.466	2.510	3.521	0.378	0.539	0.414		
			28.7	0.48	5.5	15.3	0.550	4.840	5.581	0.499	0.861	0.918		
			25.5	0.43	5.5	13.6	0.618	6.541	9.933	0.636	1.594	1.674		
			21.0	0.35	5.5	11.2	0.753	18.208	19.799	1.097	--	--		
			19.1	0.32	5.5	10.2	0.827	16.863	18.882	1.656	4.781	6.076		
			14.4	0.24	5.5	7.6	1.097	14.176	14.242	3.401	4.480	9.362		
			26.3	0.44	5.5	14.0	0.600	16.919	16.290	0.595	1.434	1.529	0.13	0.51
			21.7	0.36	5.5	11.5	0.726	13.721	14.419	0.980	3.214	3.533		
			16.7	0.28	5.5	8.9	0.947	15.670	16.290	5.682	5.756	9.201		
			11.6	0.19	5.5	6.2	1.361			-1.009	1.455	4.922		
4	0.073*	13.8	48.3	0.85	11.1	26.8	0.432	2.690		0.255	0.181		0.51	
			32.3	0.57	11.1	17.9	0.646	5.042		0.532	0.477			
			25.5	0.45	11.1	14.1	0.819	11.411		1.189	0.112			
			20.5	0.36	11.1	11.4	1.018			-12.892	18.898			
	0.066*	15.1	48.3	0.85	11.1	26.8	0.493	3.046		0.273	1.521		0.51	
			32.3	0.57	11.1	17.9	0.737	3.671		0.677	1.485			
			28.3	0.50	11.1	15.7	0.842	4.526		1.212	1.976			
			25.5	0.45	11.1	14.1	0.934	8.157		3.044	3.705			
			22.1	0.39	11.1	12.3	1.078	12.984		-2.780	14.721			
			20.5	0.36	11.1	11.4	1.161			-1.402	25.292			
	0.055*	18.3	48.3	0.85	10.3	26.8	0.594	4.599		0.330	4.156		0.60	
			32.3	0.57	10.3	17.9	0.902	0.995		1.742	5.976		0.26	
			25.5	0.45	10.3	14.1	1.160	18.191		-1.225	10.140			
			20.5	0.36	10.3	11.4	1.960			--	3.665			

TABLE B5 (1) $\gamma > c$ (Cont)

(1)	(2)	(3)	(4)	(5)	(6)	(7)	(8)	(9)	(10)	(11)	(12)	(13)	(14)	(15)
Exp. Group	ω cps	T sec	x_c cm	x_c/x_o	z_c cm	h cm	z_c/cx_c	k_m/k_o $a_o=0.2$ cm	k_m/k_o $a_o=0.4$ cm	$\dfrac{c^2_x}{(cx)^2-z^2}$ $\times 10$, cm^{-1}	a_m/a_o $a_o=0.2$ cm	a_m/a_o $a_o\ 0.4$ cm	ϵ_m $a_o=0.2$ cm	ϵ_m $a_o=0.4$ cm
4 (cont)	0.051*	19.7	48.3	0.85	11.1	26.8	0.673			0.378	0.910			
			32.3	0.57	11.1	17.9	1.006	3.486		-24.134	5.195			
			25.5	0.45	11.1	14.1	1.274	4.904		- 0.627	2.010		0.19	
			20.5	0.36	11.1	11.4	1.586	17.776		- 0.322	1.591			
	0.039*	25.6	48.3	0.85	11.1	26.8	0.935			1.647	0.574			
			32.3	0.57	11.1	17.9	1.398	6.306		- 0.324	4.046			
			25.5	0.45	11.1	14.1	1.770	2.685		- 1.836	8.052		0.37	
			20.5	0.36	11.1	11.4	2.202	24.317		- 1.266	9.238			
5	0.066*	15.1	47.4	0.84	11.0	27.4	0.472			0.272	1.176			
			37.2	0.66	11.0	21.5	0.602	0.706		0.422	1.867			
			28.5	0.50	11.0	16.5	0.786	6.647		0.917	1.306		0.28	
			23.0	0.41	11.0	13.3	0.973	7.300		8.325	17.794			
	0.055	18.3	47.4	0.84	11.0	27.4	0.595			0.327	3.531			
			37.2	0.66	11.0	21.5	0.759	2.114		0.633	4.568			
			28.5	0.50	11.0	16.5	0.990	5.577		18.007	8.450		0.38	
			23.0	0.41	11.0	13.3	1.228	14.578		0.859	12.363			

TABLE B5 (2) $\gamma = c$

(1)	(2)	(3)	(4)	(5)	(6)	(7)	(8)	(9)	(10)	(11)	(12)	(13)	(14)	(15)
Exp. Group	ω (cps)	T (sec)	x_c (cm)	x_c/x_o	z_c (cm)	h (cm)	z_c/cx_c	k_m/k_o $a_o=0.2$ cm	k_m/k_o $a_o=0.4$ cm	c^2x $(cx)^2 - z^2$ $\times 10^2$ cm^{-1}	a_m/a_o $a_o=0.2$ cm	a_m/a_o $a_o=0.4$ cm	ϵ_m $a_o=0.2$ cm	ϵ_m $a_o=0.4$ cm
3	0.073*	13.80	54.1	0.90	5.5		0.191	--	--	1.918	0.876	0.916		
			33.8	0.56	5.5		0.306	1.961	2.912	3.263	0.912	1.002		
			25.5	0.43	5.5		0.405	4.351	3.884	4.690	1.211	1.018		
			21.0	0.35	5.5		0.492	8.632	6.211	6.280	1.687	2.345		
			26.3	0.44	5.5		0.393	--	--	4.495	1.206	1.107		
			21.7	0.36	5.5		0.476	7.456	6.062	5.957	1.566	1.987		
			16.7	0.28	5.5		0.618	10.450	11.421	9.695	2.015	3.014	0.13	0.38
			11.6	0.19	5.5		0.890	12.011	14.121	41.548	1.122	1.631		
4	0.079*	12.72	48.3	0.85	11.1		0.398	--	--	2.460	0.721	--		
			32.3	0.57	11.1		0.595	2.342	--	4.795	0.864	--		
			25.5	0.45	11.1		0.754	5.012	--	9.087	0.854	--	0.26	
			20.5	0.36	11.1		0.938	11.028	--	40.500	4.321	--		

BIOGRAPHICAL SKETCH

The author was born, August 4, 1940, and raised in Erie, Pennsylvania. After receiving an A. B. degree in geology from Princeton University in June, 1962, he entered the Naval Officers Candidate School in Newport, Rhode Island. Following commissioning into the U.S. Navy in December, 1962, he spent three years aboard the U.S.S. Saint Paul where he served as an engineering and a weapons officer. During this time he married the former Virginia Louise Beardsley in San Diego, California. He did graduate study in oceanography at the U.S. Naval Postgraduate School in Monterey, California for one year before transferring to M.I.T. in September 1966.

The author is a Lieutenant on active duty in the U.S. Navy, a member of the American Geophysical Union, and a member of the Society of Sigma Xi. He has two children, David Scott (5) and John Daniel (3).